Vertical Axis Wind Turbine Optimization for Ship Propulsion

using a free wake vortex model

Master of Science Thesis

Laurens-Jan Lagendijk

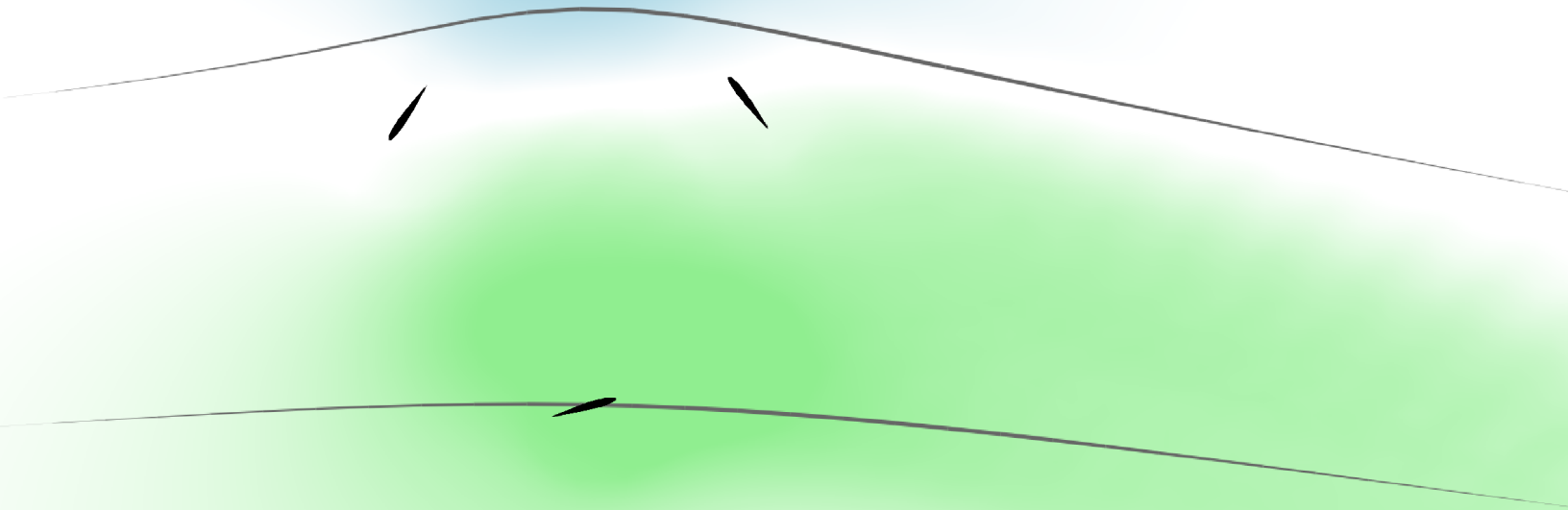

TU Delft

ECONOWIND

Vertical Axis Wind Turbine Optimization for Ship Propulsion

USING A FREE WAKE VORTEX MODEL

---

by

Laurens-Jan Pieter Lagendijk

in partial fulfilment of the requirements for the degree of

Master of Science
in Aerospace Engineering,
Aerodynamics and Wind Energy track

at the Delft University of Technology,
to be defended publicly on Wednesday September 28, 2022 at 9:00 AM.

Student number:	4511808	
Supervisor:	Dr. ir. D.A.M. De Tavernier	TU Delft
Thesis committee:	Prof. dr. D.A. Von Terzi	TU Delft
	Prof. dr. ir. L.L.M. Veldhuis	TU Delft
	Ir. F. Nieuwenhuis	Econowind

TU Delft

ECONOWIND

Abstract

The global emission of harmful greenhouse gasses has to be reduced. Commercial shipping contributes to these emissions by using fossil fuel as the only energy source to provide propulsion and power auxiliary systems. In order to reduce fuel consumption, much research is focused on increasing the efficiency of the propulsion system and reducing the required power consumption. In recent years an increasing amount of research focuses on utilizing wind energy as an alternative energy source. This is a renewable source of energy which is plentiful at sea. This thesis focuses on the novel concept of using a Vertical Axis Wind Turbine (VAWT) as a means of ship propulsion and power generation.

Existing Wind Assisted Ship Propulsion (WASP) systems can only be utilized in conditions when the ship is in transit and when the apparent wind conditions are favorable. The VAWT concept has the ability to generate power in wind conditions where conventional sailing systems are not functional, including when the ship is in port. This system can also be used as a thrusting device when the wind conditions are favorable for sailing systems. Therefore this system can be used more frequently which is beneficial for the overall power savings. The use of a VAWT for WASP in combined operation as a thruster and a power generator does currently not exist. Therefore the design of the rotor has to be investigated and optimized in order to evaluate effective designs for different conditions and to compare this device to existing sailing concepts.

The aerodynamic performance of the VAWT will be evaluated using numeric simulation models. This model will be coupled to an optimization algorithm in order to find the optimal design parameters for different wind conditions and modes of operation.

This project will result in a better understanding of the working principles of VAWT used for WASP and the potential energy saving of optimized designs for the operational modes as a generator, thruster and combined-operation.

There is a large opportunity for capturing wind energy at sea. This project has the potential to add a new method of ship propulsion to reduce shipping emissions and reducing the cost of ship operation. When one or multiple of these systems can be applied on a large share of the worldwide shipping fleet, this research can contribute to the reduction of commercial shipping emissions.

Preface

This report is written for the Master Thesis project of Laurens-Jan Lagendijk, at Delft University of Technology in the Netherlands, Faculty of Aerospace Engineering, for the track in Aerodynamics and Wind Energy. The opportunity for this project is provided by Econowind. Most of the project guidance is provided by TU Delft. This report provides insight into the working principles of Vertical Axis Wind Turbines used for ship propulsion and describes the optimization of such a turbine for a variety of wind conditions. The structure of the report is informative whereby the report explains the working principles of different concepts. The report is written for employees of Econowind, staff members of the TU Delft at the Faculty of Aerospace Engineering, and other people involved in the project.

I would like to thank Frank Nieuwenhuis, the managing director of Econowind for the opportunity to work on this topic. I also want to thank Dominic von Terzi for his interesting insights during the progress meetings. I would like to thank Delphine de Tavernier for her guidance and remarks during the weekly meetings and her expertise in the field of vertical axis wind turbines which helped me to understand the working principles.

Contents

List of Figures

List of Tables

Nomenclature

Symbol	Description	Unit
AR	Blade aspect ratio	–
A_{θ_p}	Pitch amplitude	°
$A_{sail,potential}$	Potential side projected sail area	m^2
A	Swept area	–
C_D	3D drag coefficient	–
C_L	3D lift coefficient	–
$C_{P',thruster}$	Equivalent power coefficient from forces in thrust direction	–
$C_{P',turbine}$	Equivalent power coefficient from produced power	–
$C_{P'}$	Equivalent power coefficient	–
C_P	Power coefficient	–
$C_{d,turbine}$	Drag coefficient of the entire turbine	–
C_d	2D drag coefficient	–
$C_{l,turbine}$	Lift coefficient of the entire turbine	–
C_l	2D lift coefficient	–
$C_{res,turbine}$	Resultant force coefficient of the entire turbine	–
$C_{s,air}$	Speed of sound in air	–
$C_{s,turbine}$	Side force coefficient of the entire turbine	–
$C_{t,turbine}$	Thrust force coefficient of the entire turbine	–
C	Admiralty constant	$m/kg^{1/3}$
$F_{c,blade}$	Centrifugal force on the blade	N
$F_{d,turbine}$	Drag force of the entire turbine	N
$F_{l,turbine}$	Lift force of the entire turbine	N
$F_{res,turbine}$	Resultant force of the entire turbine	N
$F_{s,turbine}$	Side force of the entire turbine	N
$F_{t,turbine}$	Thrust force of the entire turbine	N
H	Blade span	m
M_{blade}	Blade mass	kg
M	Mach number	–
N_{blades}	Number of blades	–
$N_{vortices}$	Number of vortices in the simulation timestep or at the end of the simulation	–
N	Number of dimensions of the optimization problem	–
P_1	Penalty function value for the minimum chord length constraint	–
P_2	Penalty function value for the maximum chord length constraint	–
P_3	Penalty function value for the maximum absolute pitch amplitude	–
P_4	Penalty function value for the maximum apparent wind speed on the blades	–
P_5	Penalty function value for the maximum absolute pitch phase	–
P_6	Penalty function value for the severe stall constraint	–
P_7	Penalty function value for the minimum power production constraint	–
P_B	Engine brake power	W
P_i	Constraint specific penalization value	–
P_r	Power provided or required by the turbine	W
$P_{t,eq,thruster}$	Equivalent propulsion power of the VAWT used as a thruster	W
$P_{t,eq,turbine}$	Equivalent propulsion power of a VAWT used as a turbine	W
P_{total}	Total penalization value applied to the objective	–
$R_{vortex\ core}$	Vortex rigid core radius	m

Symbol	Description	Unit
Re	Reynolds number	–
R	Turbine radius	m
U_R	Reduced wind speed at the turbine	m/s
U_∞	Far field wind speed	m/s
U_a	Unperturbed apparent wind speed, same as U_∞ when stationary	m/s
U_{blade}	Speed over the blade due to rotation of the turbine	m/s
U_{cut-in}	Far field wind speed above which the turbine is used	m/s
$U_{cut-out}$	Far field wind speed above which the turbine no longer is used	m/s
U_e	Wind speed at the end of the streamtube	m/s
$U_{induced,min}$	Minimum velocity induced by the vortex	m/s
U_{rated}	Far field wind speed above which the produced power is no longer increased	m/s
U_{rel}	Relative speed over the blade	m/s
U_s	Ship speed	m/s
U_{wind}	Wind speed in an earth fixed reference frame	m/s
V_I	Virtual incidence	°
V_c	Virtual camber	–
X	Vector of design parameters	–
Δ	Ship displacement	kg
Γ	Vortex strength	m^2/s
$\alpha_{L=0}$	Angle of zero lift	°
$\alpha_{stall,ref}$	Reference stall angle	°
α	Angle of attack	°
β_a	Apparent wind direction with respect to the heading	°
β_t	True wind direction with respect to the heading	°
η_D	Efficiency of the main drive(s)	–
λ_1	Dominant eigenvalue	–
λ_s	Leeway angle	°
λ	Tip speed ratio	–
ν	Kinematic viscosity	m^2/s
ω	Angular velocity	rad/s
ϕ	Blade pitch angle	°
ρ	Air density	–
σ	Turbine solidity	–
θ_p	Pitch angle, clockwise positive w.r.t. blade direction	°
θ	Azimuth angle	°
$\tilde{f}$	Penalized objective function	–
a	Axial induction factor	–
c	Chord length of the blades	m
e	Span efficiency factor	–
f	Objective function	–
k	Weibull shape parameter	–
n	Size of the comparison matrix	–
p_1	Penalty factor for the minimum chord length constraint	–
p_2	Penalty factor for the maximum chord length constraint	–
p_3	Penalty factor for the maximum absolute pitch amplitude	–
p_4	Penalty factor for the maximum apparent wind speed on the blades	–
p_5	Penalty factor for the maximum absolute pitch phase	–
p_6	Penalty factor for the severe stall constraint	–
p_7	Penalty factor for the minimum power production constraint	–
p_i	Penalty factor	–
pd	Probability density	–
p	Static pressure	Pa
r	Euclidian distance to the vortex core	m
$t_{simulation,timestep}$	Simulation time for one timestep	s
v	Normalized principal eigenvector associated with the largest eigenvalue	–
$x_{drop\,vortices}$	x-position from where the vortices can be dropped	m
$x_{freesteram\,wake}$	Freestream wake extend which determined the total runtime of the model	m

Symbol	Description	Unit
x_{vortex}	Vortex x-position	m
y_{vortex}	Vortex y-position	m
DWT	Deadweight Tonnage, measure for the carrying capacity of a ship	t
GT	Gross Tonnage, measure for overall internal ship volume	–

Acronyms

AHP	Analytic Hierarchy Process
BEM	Blade Element Momentum
CFD	Computational Fluid Dynamics
CI	Consistency Index
CR	Consistency Ratio
DMST	Double Multiple StreamTube
DNV GL	Det Norske Veritas, Germanischer Lloyd
EEDI	Energy Efficiency Design Index
EEXI	Energy Efficiency Existing Ship Index
HAWT	Horizontal Axis Wind Turbine
IMO	International Maritime Organization
ISA	International Standard Atmosphere
LHS	Latin Hypercube Sampling
MADM	Multiple Attribute Decision Making
MEPC	Marine Environment Protection Committee
MNMS	Modified Nelder-Mead Simplex
MST	Multiple StreamTube
NMS	Nelder-Mead Simplex
RI	Random Index
SOG	Speed Over Ground
STOL	Short Take-Off and Landing
STW	Speed Through Water
TSR	Tip Speed Ratio
VAWT	Vertical Axis Wind Turbine
VTOL	Vertical Take-Off and Landing
WASP	Wind Assisted Ship Propulsion

Chapter 1

Introduction

For many centuries wind energy has been used in various applications, from grinding grain with traditional style windmills to draining the polders of the Netherlands and ship propulsion using sails. Nowadays wind turbines are mainly used to produce renewable energy as the world has to limit emissions and transition away from the use of fossil fuels, to reduce the effects of climate change.
The Paris Agreement [65, Article 2a] aims to limit global warming to well below $2[^{\circ}C]$ and pursues efforts to limit the temperature increase to $1.5[^{\circ}C]$ compared to pre-industrial levels. To achieve this, the maritime transport industry can contribute to reducing emissions as the commercial shipping industry is almost entirely powered by fossil fuels. According to the International Maritime Organization (IMO) [30, p. 112], the share of CO_2 emissions from shipping contributed 2.89% of the total global emissions in 2018. The absolute CO_2 emissions from shipping are projected by the IMO [30, Fig. 1, p. 26-27] to increase by 2050 for various long-term economic and energy scenarios.
Wind energy is plentiful at sea, therefore many developments are ongoing on the utilization of wind as an additional propulsion method for commercial shipping. These developments are additionally driven by changing regulations for the energy efficiency of ships (Energy Efficiency Design Index (EEDI) and Energy Efficiency Existing Ship Index (EEXI)). Because of these regulations, ship emissions have become a more significant design consideration which provides additional incentive to explore the use of alternative energy sources such as wind energy.

Wind Assisted Ship Propulsion (WASP) is being applied to some early adopting commercial cargo ships as a renewable propulsion system. These existing systems work on principles similar to sailing whereby lift-generating devices are used to provide a thrust force to propel the ship. As every sailor knows, this concept is limited to favorable apparent wind directions and speeds. Due to the speed of the ship, the apparent wind encountered by the ship is mainly upwind. Therefore conventional sailing solutions can only be used in a fraction of the time at sea. The utilization of these systems is also limited by the time which cargo ships are stationary, in port, or at anchor because in these conditions thrusting devices cannot be used.
Most WASP research focuses on improving the performance of sailing systems which have the downside of limited usability. It is proposed that substantial energy savings can be obtained by increasing the utilization of the WASP system. To provide power when the ship is stationary or experiencing a headwind, a wind turbine system can provide a solution. However, a conventional wind turbine is not able to provide thrust when the wind conditions are favorable for sailing. The turbine concept described in this study combines the possibilities of using a Vertical Axis Wind Turbine (VAWT) to generate power in combination with the ability to provide thrust like a cyclogyro in favorable wind conditions. This work investigates a VAWT application of combining energy generation and thrusting on board cargo ships in one system. This WASP system can be used in many different wind conditions, at sea as well as in port. Therefore it contributes to the energy transition and provides new insights for possible applications of VAWTs.

This novel concept might provide a solution for a cost-effective WASP system. This study investigates the potential performance of a VAWT used as a power generation system, propulsion system, and a system combining both modes of operation. The objective is to optimize such a system and evaluate the potential energy saving.

The working principles of WASP systems will be explained to provide an overview of existing concepts. The operational profile and wind conditions of seagoing cargo ships are also evaluated. A dedicated model is developed and validated to be used for the optimization study. The results of this study are compared to existing WASP concepts. Through these steps, this study investigates a novel VAWT concept that can be used for energy generation and wind-assisted ship propulsion.

1.1 Research questions

Main research question: What is the potential energy saving of a VAWT used for wind-assisted ship propulsion on seagoing cargo ships?

1. What is a suitable formulation of the optimization problem?
   (a) What are suitable optimization objectives for the different operational modes?
   (b) What are suitable design constraints?
   (c) Which parameters are fixed and which are used to optimize the design?
2. What is a suitable and efficient optimization method?
   (a) What is a suitable and efficient optimization algorithm?
   (b) What is a suitable starting point of the optimization process?
   (c) When should the optimization process be terminated?
3. What are the optimized designs for different modes of operation?
   (a) What is the potential energy saving of a VAWT only used as a turbine?
   (b) What is the potential energy saving of a VAWT only used as a thruster?
   (c) What is the potential energy saving of a VAWT only used in a combination of operational modes?
4. How does the resulting design depend on the optimization input?
   (a) What is the influence of the different design parameters?
   (b) What is the sensitivity of the operational conditions on the resulting design?

1.2 Research aims

Research aim: To optimize the aerodynamic performance of a VAWT used for wind-assisted ship propulsion using a validated lifting line model and an appropriate optimization method.

This aim will be realized through multiple sub-steps which will be the deliverables of this study.

1. A validated lifting line VAWT model.
2. A formulation of the optimization problems.
3. A suitable and efficient optimization method.
4. Optimized designs for different modes of operation.
   (a) VAWT design optimized for energy generation.
   (b) VAWT design optimized for thrusting.
   (c) VAWT design optimized for both energy generation and thrusting.
5. Comparison of the resulting designs to existing concepts.
   (a) Comparison to the aerodynamic performance of a Horizontal Axis Wind Turbine (HAWT) of similar size.
   (b) Comparison to another WASP system.

6. A report to explain the methods and decisions and to present the results.

Chapter 2

Wind assisted ship propulsion

Cargo ships require a propulsion system, traditional ships used sails to provide propulsion. When steam and combustion engines were invented, the shipping industry gradually shifted from wind propulsion to fossil fuels as the main source of energy. Nowadays, commercial cargo ships use combustion engines to power a propeller that propels the ship. This has the benefit of being less dependent on the environmental and wind conditions however this method of propulsion requires fuel which is a substantial part of the operational cost and emits harmful emissions. In modern shipping, it is not feasible to use only sails as a means of propulsion. However, both propulsion systems can be combined to reduce fuel cost and emissions. Combining these systems where part of the propulsion is provided by the propeller and partially by a wind propulsion system is called WASP. Many different WASP systems have been invented to provide propulsion on commercial cargo ships. This chapter describes the working principles of WASP propulsion by explaining some basic sailing concepts and existing systems. The operational profile and wind conditions are also discussed.

2.1 Sailing

Sailing systems can be used to provide propulsion when a ship is in transit at sea and when the apparent wind conditions are such that a thrust force can be provided. This depends on the apparent wind direction and the force characteristics of the wind propulsion system.
The horizontal force produced perpendicular to the flow direction is referred to as the lift force. Usually, this force acts vertically, however a sailing system can be seen as a vertically oriented wing used to produce a force in the horizontal plane. The sailing system is oriented such that the lift force contributes to the positive thrust force.
If the wind conditions are such that a net positive thrust force or propulsion can be produced, the wind conditions are called favorable. For lifting systems this is the case for all wind conditions, except for upwind conditions. Some WASP systems require power to operate. The maximum upwind angle (close-hauled conditions) for which positive thrust can be generated is influenced by the lift-to-drag ratio and the power demand to operate the system.

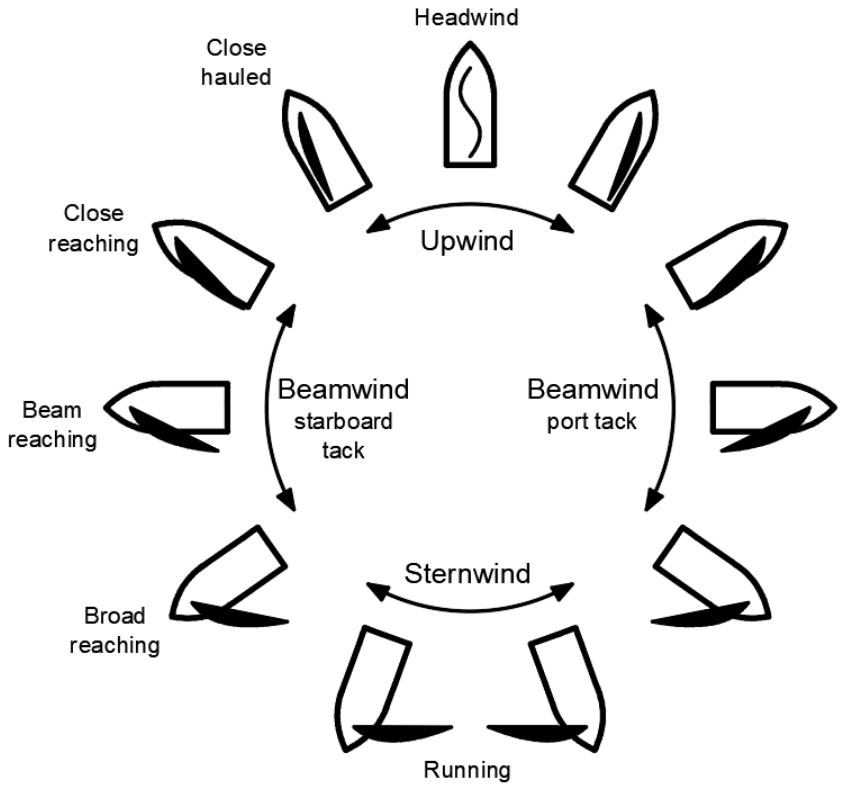

Figure 2.1: Courses with respect to the true wind direction, inspired by Santos et al. [21]

In some wind conditions, the WASP system also generates an aerodynamic sideforce which can be undesirable as this induces a leeway angle λ_s which increases the induced resistance of the ship. Sailing ships can efficiently counteract this sideforce using a keel which generates an opposed hydrodynamic force. General cargo ships without a keel are not efficient lifting bodies to generate this sideforce. However because WASP only provides propulsion assistance, these forces are considered to be relatively small. Therefore the effect of sideforce can be neglected according to the Marine Environment Protection Committee (MEPC) guidelines which state that secondary effects of wind-assisted propulsion systems which might increase the ship resistance can be ignored.
The forces as shown in Figure 2.2 act above the deck area. Therefore these forces generate moments that can influence the stability of the ship and cause pitch and yaw motions. The longitudinal ship stability is considered substantially large such that the thrust force does not have a substantial influence. The transverse stability could induce a heeling angle as described by Van der Kolk [87]. According to the IMO guidelines from the MEPC [8], all secondary effects such as leeway, rudder angle, heel, and reduced propeller efficiency can be ignored without significantly reducing the accuracy of the performance prediction. These guidelines provide an overview on how to treat innovative energy technologies such as WASP to calculate the regulatory energy efficiency of new ships (EEDI) and existing ships (EEXI). Therefore this study does not consider these secondary effects.

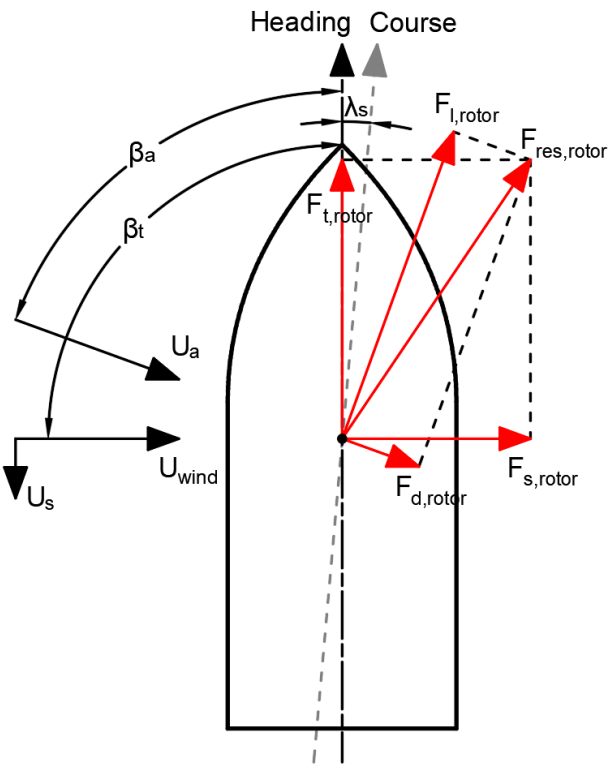

Figure 2.2: Schematic ship wind and force diagram, modified from Lagendijk [56]

The thrust- and sideforce can be evaluated using Equation 2.1.

$$\begin{bmatrix} F_{t,turbine} \\ F_{s,turbine} \end{bmatrix} = \begin{bmatrix} sin(\beta_a) & -cos(\beta_a) \\ cos(\beta_a) & sin(\beta_a) \end{bmatrix} \cdot \begin{bmatrix} F_{l,turbine} \\ F_{d,turbine} \end{bmatrix} \tag{2.1}$$

2.2 Wind propulsion systems

This section describes existing WASP technologies, from state-of-the-art sailing technologies to wind turbine concepts and a new VAWT concept which provides the opportunity to combine both turbine and thruster modes of propulsion.

2.2.1 Sailing systems

Many wind-powered propulsion systems have been developed. Over the past years, there has been increasing interest in wind-powered propulsion systems. WASP is an emerging technology with many developments and the potential to grow as only a small fraction of commercial ships use wind propulsion. Some WASP systems are currently operating on existing ships. These systems range in complexity. The most well-known systems are traditional sail cloth designs. Advances in aerodynamics have resulted in more complex designs such as rigid wings, multi-element wings, suction sails, Magnus rotor sails, kites, and many more.

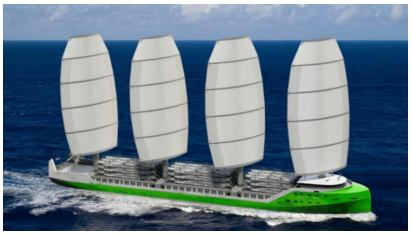

Figure 2.3: Dynarig, with permission from Dykstra Naval Architects [1]

Figure 2.4: Rigid wingsail, from Bordogna [2, Fig. 1.3]

Figure 2.5: Two element wing, from Econowind [66]

Figure 2.6: Suction sails, from Econowind [66]

Figure 2.7: Flettner rotors, from Wikimedia [83]

Figure 2.8: Skysails kite sail system, from Bordogna [2, Fig. 2.2]

All these systems mainly use a lift force to provide propulsion. Therefore these systems can generate thrust when the ship is in transit in favorable wind conditions. However, the performance of these systems is limited by the ability to provide thrust in different wind conditions such as a headwind. Weather routing can be used to adjust the course such that favorable wind conditions are encountered. This is commonly seen on sailing yachts which use zig-zag maneuvers (tacking) to move upwind. Weather routing might not be feasible for commercial ships as these can be confined to shipping routes and tacking lengthens the voyage distance which is undesirable. As only a minority of the propulsion is provided by the WASP system, the additional propulsive power might not be sufficient to compensate for the additional distance.

2.2.2 Wind turbine ship propulsion

In order to be able to produce power independent of the apparent wind direction, wind turbine systems have been proposed as a means to provide power for ship propulsion [72][68][5][4]. A benefit of a wind turbine system is the ability to generate electric power in upwind conditions and when the ship is not moving. This power can be used for ship propulsion when the ship is in transit or to power auxiliary systems when the ship is in port.

Both vertical- and horizontal-axis wind turbines have been proposed by Bose [4]. This study also concludes that such a system theoretically can provide propulsion in any apparent wind direction, including headwind conditions. Bose [4, p. 157] also compared the performance of wind turbine propulsion to a sailing propulsion by means of Dynarigs as shown in Figure 2.3. This study concludes that turbine systems perform better in a headwind and traditional sailing systems are better on most other courses. A more recent study (2011) of Bøckmann [5] investigates ship propulsion by means of a HAWT. This study concludes that for the same size system and a ship moving at half the wind speed, turbine propulsion is weakly preferred over wingsail propulsion. Both these studies note that the preferred system depends on the encountered wind conditions.

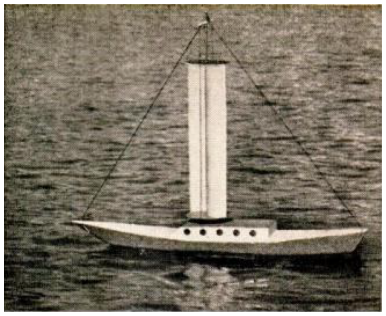

Figure 2.9: Savonius drag driven turbine (1963), from Clough [72]

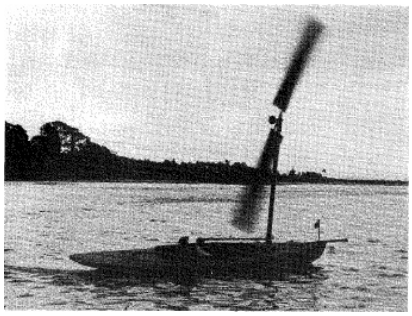

Figure 2.10: The Brabazon turbine boat (1980), from Rainey [68]

Figure 2.11: HAWT impression (2011), from Bøckmann [5]

It is interesting to note that sailing WASP systems as described in subsection 2.2.1 perform relatively better on ships with a low main drive efficiency (η_D). This is because, for the same propulsive power from a WASP propulsion system, a ship with a worse drive efficiency can reduce the engine power more to attain the same total propulsive power.
When a wind turbine is used for WASP, this system generates electric power which is used to drive the conventional propulsion system, usually to power a propeller. Therefore these systems benefit from a high main drive efficiency (η_D). The effect of efficiency of the main drive(s) for wind turbine ship propulsion is in more detail discussed in subsection 3.6.2.

2.2.3 VAWT thruster concept

All previously mentioned systems have one mode of propulsion, either thrusting with a sailing system or power generation with a turbine system. As the preferred system depends on the encountered wind conditions, it would be advantageous to be able to have one system which can combine both modes of operation. This study investigates the possibilities of such a system based on a novel application of a VAWT concept. The configuration of the VAWT is already incorporated in the name which refers to the blades rotating around a vertical axis. The VAWT concept has been around for a long time, the oldest known wind turbines where drag driven vertical axis machines known as Panemone windmills which were used to mill grain in Persia as early as 200 BC as discussed by Eldridge [11].

Cyclorotor is an overreaching term covering aerodynamic devices which operate with an axis of rotation perpendicular to the flow direction and spanwise oriented blades parallel to the axis of rotation. These systems can be used to provide thrust in any direction when powered. When subjected to an airflow, this system can be used as a wind turbine and as a lifting device when rotating without being driven. This study focuses on the possibility of using a cyclorotor to provide thrust to a ship or generate power depending on the apparent wind conditions. Systems combining both these modes of operation for ship propulsion have not been found in literature.
When a cyclorotor is used to generate power, for this study, it is referred to as a VAWT. When the cyclorotor is used to provide a thrust force for ship propulsion, it is referred to as a thrusting VAWT.
The same concept of a thrusting VAWT is often referred to under different names depending on the application. Some examples of similar powered and free running or driven VAWTs systems are: a cyclogyro, cycloidal rotor, cycloidal propeller, Giro-mill, Voith-Schneider Propeller, Cyclocopter, wheel orthopter. Some of these systems will be discussed in subsection 3.7.1.

The current sailing systems as described in subsection 2.2.1 are often limited in size because the large size of these systems obstructs the field of view from the bridge. The requirements of the field of view are provided in ship specific class regulations such as the regulations from Bureau Veritas [10, p. 17] and Det Norske Veritas, Germanischer Lloyd (DNV GL) [76]. These regulations specify sightline requirements to ensure the helmsman has a good overview around the ship from the bridge deck. One additional benefit of the VAWT system is the semi-transparent appearance when rotating and the relatively small blades when not in operation. Therefore the field of view obstruction for VAWT systems is smaller, this could allow for larger WASP systems to be installed.

2.3 Ship operational profile

The operational profile of the ship consists of information such as the fraction of time in port, at sea, and the characteristic speed at which the ships are operating when in transit. This profile influences the wind conditions encountered in these specific situations and determines the potential power which can be provided by the VAWT system. Therefore it is important to evaluate how frequently certain conditions are expected to be encountered.
Shipping companies do not generally disclose the operational profile of their ships as this is commercially sensitive information. The results of some ships are listed in Table 2.1 and the Fourth greenhouse gas study of IMO provides an overview for different ship types and the change between 2014 (IMO3) and 2020 (IMO4) [30]

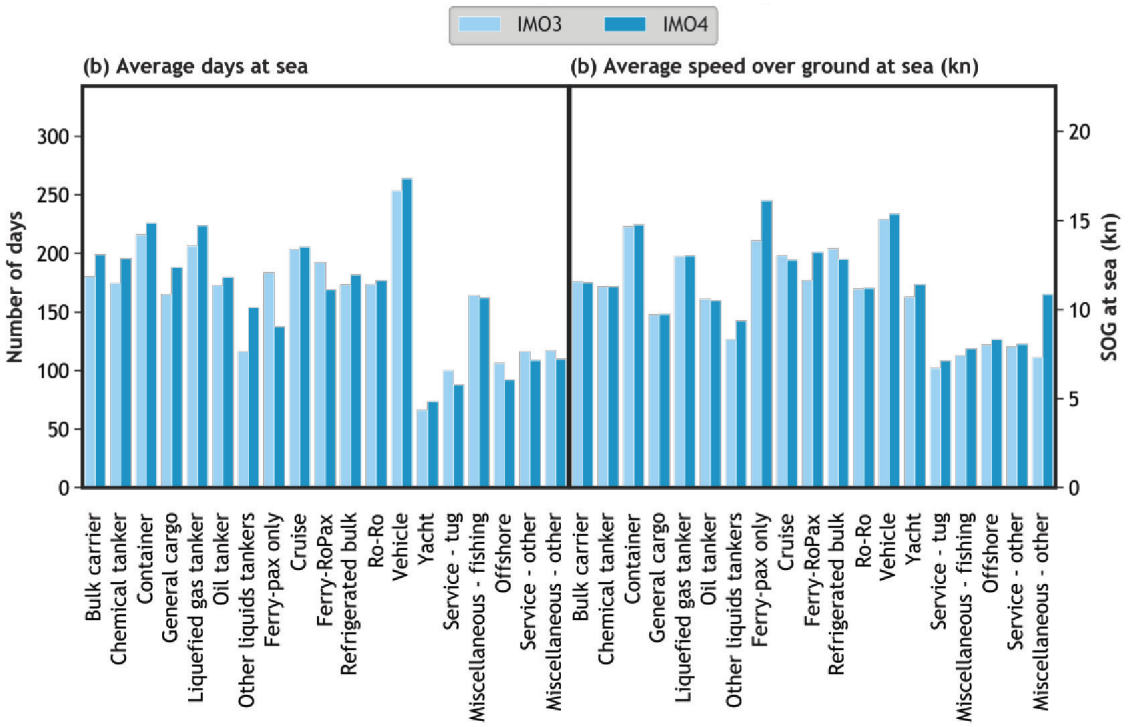

Figure 2.12: Comparison of operational profiles for different ship types, annual days at sea and Speed over Ground (SOG) from Faber et al. [30, Fig. 111]

The fraction of time that a ship spends in transit at sea depends on the ship type. Charlotte Banks et al. [17] found larger tankers to spend less than average time in port. Johnson [48] presents the operational profile of ships in the region of the North- and Baltic sea with a voyage duration of fewer than 4 days. This is comparable to some ships currently operating with WASP systems. The general operational profile of these ships is, 50% of the time at sea and 40% of the time in port. This is also found for many ship types in Figure 2.12. Therefore these conditions are considered as the reference operational profile for this study.

Table 2.1: Operational profiles of various ship types

At sea	Manouvering	Port	Anchored	Other	Ship type	#Ships	Source
47%	13%	40%	-	0%	Dry bulk carrier ≈5000 GT	1	[48]
48%	8%	44%	-	0%	Dry bulk carrier ≈5000 GT	1	[48]
72%	8%	19%	1%	0%	LNG carrier	40	[14]
75%	-	25%	-	0%	Bulk carrier	4	[17]
43%	-	54%	-	3%	Handysize tanker	1	[17]
57%	-	42%	-	1%	Aframax tanker	4	[17]
67%	-	32%	-	1%	Suezmax tanker	5	[17]
67%	-	33%	-	0%	Post Panamax Container ship	2	[17]
71%	-	29%	-	0%	Post Panamax plus Container	4	[17]

Over the past years, ships have started operating at an average speed slower than the design speed, to reduce fuel consumption. This is called slow steaming. The ship speed varies per ship type and size as shown in Figure 2.12. The average speed ranges from $10 - 14[kts]$ for many ship types as found by Faber [29, p. 59]. Container ships and ferries generally move considerably faster.
This study considers ships which operate at a speed of $U_s = 6[m/s] \hat{=} 11.7[kts]$. This provides a reasonable reference speed for many ship types.
The propulsive power of the ship depends on the Speed Through Water (STW). For this study, the effect of sea currents is neglected as this speed is considered to be small with respect to the wind speed and the ship speed. Therefore difference between Speed Over Ground (SOG) and STW are neglected and the ship speed is referred to as U_s.

2.4 Wind conditions

The potential power provided by WASP propulsion systems depends on the apparent wind conditions. These conditions are site-specific and vary in time. The temporal variation can be described using site-specific, probabilistic wind conditions. The apparent wind conditions both at sea and in port have to be evaluated as these wind conditions can be different.

2.4.1 Wind at sea

To provide a global prediction for the potential benefit of WASP, the MEPC guidelines [8] provide a reference wind probability distribution along the main global shipping routes. This matrix is included in Appendix A.

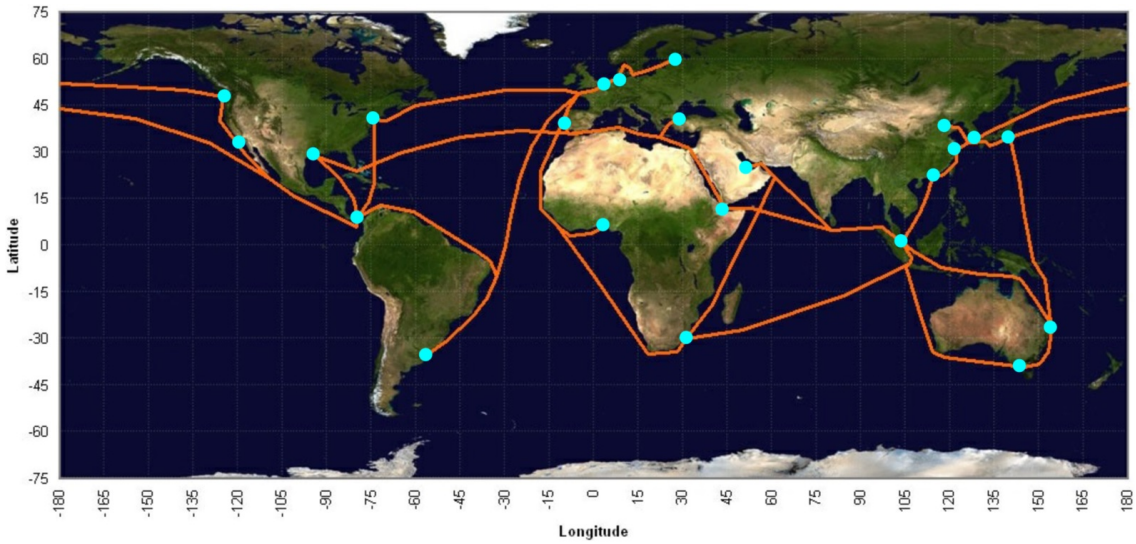

Figure 2.13: Main global shipping routes used for the global wind statistics from MEPC [8], modified to include major ports along these routes

The wind probability distribution along these routes defines the true wind conditions relative to the course along the shipping route. Therefore the course information is already incorporated in this distribution whereby a wind angle of zero does not represent north, rather it represents a headwind along the shipping route. This distribution is symmetric around beam reaching wind. This indicates the distribution is produced for two-way legs of the shipping routes. Head- and stern wind are more frequently encountered, this is explained in the MEPC guideline [8]. The cause for these wind conditions is because most shipping routes run parallel to coastlines and wind directions tend to follow the coastline. Most shipping routes are also orientated around equal latitudes (east-west). This is also the case for global trade winds and therefore results in more head- and stern wind. The wind probability is symmetric for port and starboard. Therefore the directional distribution is only shown from $\beta_t = 0 - 180[^\circ]$.

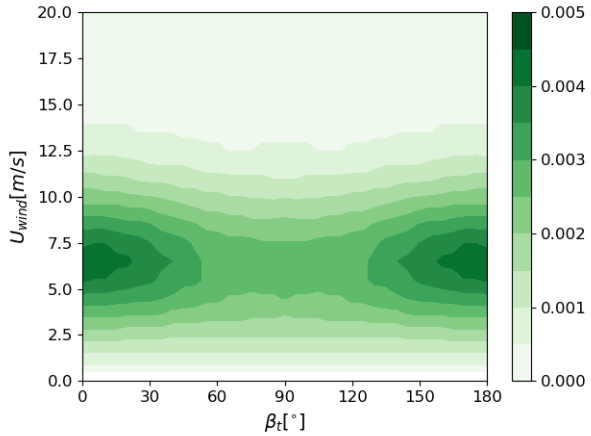

Figure 2.14: Wind conditions probability density from the global wind statistics matrix from MEPC [8] for $U_s = 0[m/s]$ along the shipping routes

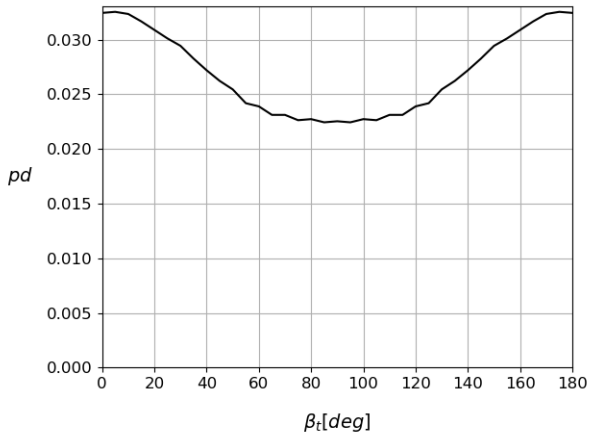

Figure 2.15: Probability density distribution of the true wind direction along the main global shipping routes of Figure 2.13

A Weibull probability density function is fitted through the wind statistics data to obtain the probability distribution. This distribution is commonly used for wind speed probability distributions and is found to be better suited compared to the Rayleigh distribution [49]. This has also been concluded from measurements in Bahrain by Hennessey [50] and in Northern Morocco by Bidaoui [25]. A Weibull distribution with a shape

parameter of $k = 2$ results in a Rayleigh distribution. The Weibull distribution has one more fitting variable which makes it more customizable to suit the specific climate and landscape surface conditions as stated by Bussel [86].

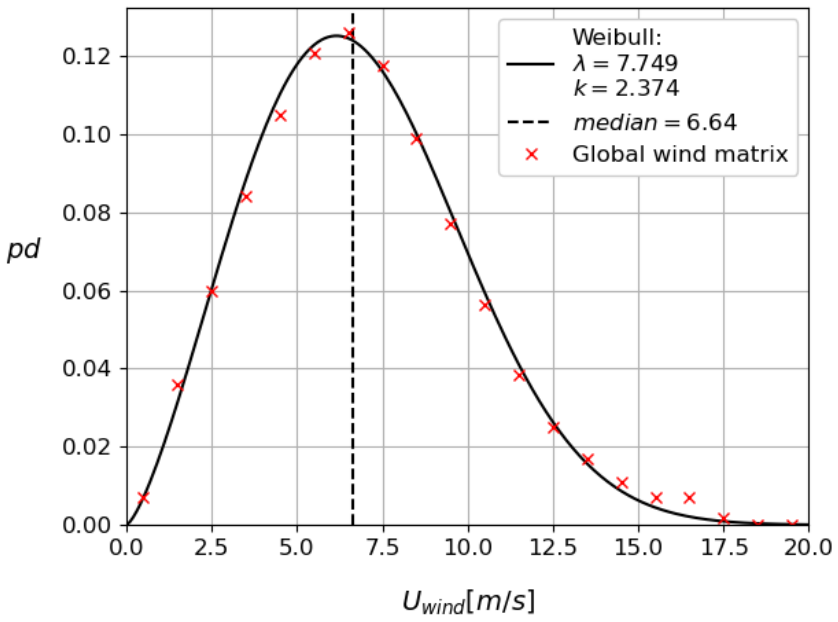

Figure 2.16: Probability density distribution of true wind speed along the main global shipping routes

2.4.2 Apparent wind at sea

The wind conditions experienced onboard the ship are called the apparent wind conditions. These conditions are influenced by the true wind conditions (conditions in an earth-fixed reference frame) and the speed of the ship (SOG). The speed of the ship increases the apparent wind velocity encountered in headwind conditions however the ship speed can also reduce the apparent wind speed in downwind conditions.

$$\overrightarrow{U_a} = \begin{bmatrix} U_s \\ 0 \end{bmatrix} + \overrightarrow{U_{wind}} \tag{2.2}$$

$$U_a = \sqrt{(U_s + U_{wind} cos(\beta_a))^2 + (U_{wind} sin(\beta_a))^2} \tag{2.3}$$

Fitting the Weibull distribution through the statistics from the wind matrix does not provide a perfect fit because this distribution is disturbed by the ship speed component. However, the fit is close enough to show the increase in median apparent wind speed of 28% with respect to the median true wind speed from Figure 2.16.

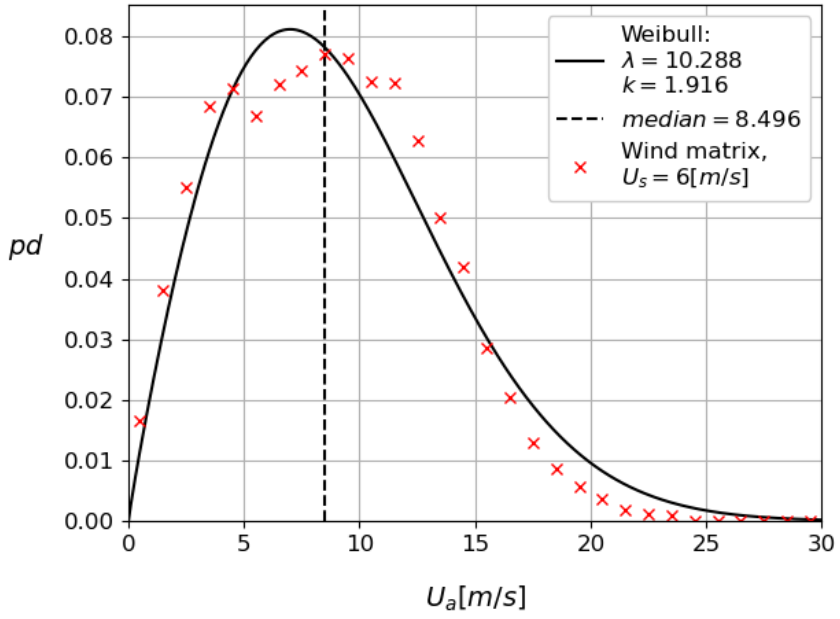

Figure 2.17: Probability density distribution of the apparent wind speed along the main global shipping routes, for a ship speed of $U_s = 6[m/s]$

For larger ship speeds, the probability distribution shifts more to a headwind. This happens because the apparent wind due to the ship speed always contributes to the apparent wind speed as an additional headwind component. This is shown in Figure 2.18 where the data is scattered due to numerical discretization however a fourth-order polynomial provides a smooth fit for the probability distribution of the apparent wind angle for different ship speeds. The β_a distribution in Figure 2.18 for a ship speed of $U_s = 0[m/s]$ is the same as the β_t distribution of Figure 2.15 which is to be expected. The probability around $\beta_t = 180[^\circ]$ is also reduced for larger ship speeds because when the true wind speed in stern wind conditions is lower than the ship speed, this wind direction becomes a headwind. It should also be noted that the probabilities consider the averages over a range of 5 degrees.

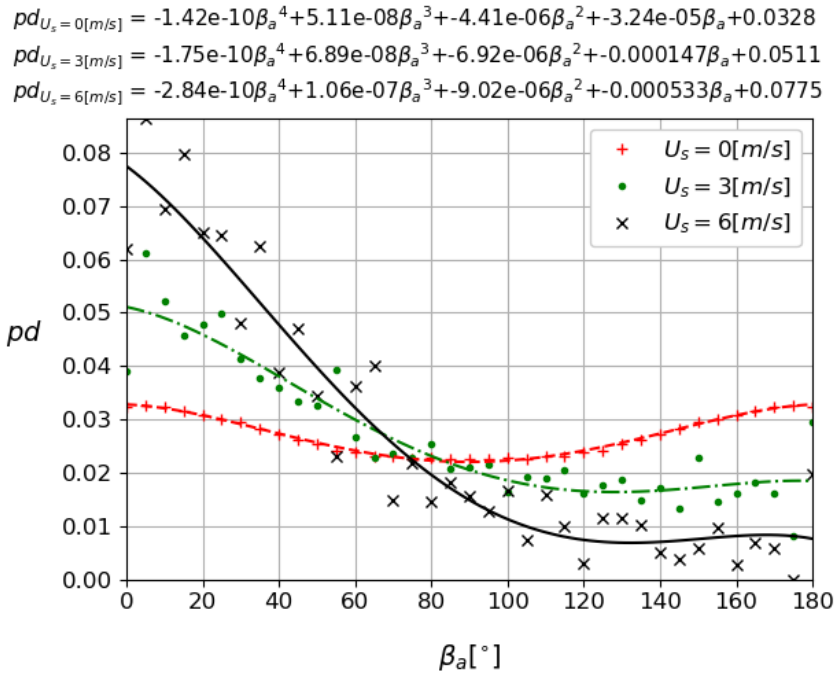

Figure 2.18: Probability density distribution of the apparent wind direction along the main global shipping routes, for variable ship speeds

It is interesting to note that a change of the ship course does not establish the same change in apparent wind direction due to the apparent wind component from the ship speed which remains aligned with the course. This makes weather routing as discussed in subsection 2.2.1 less effective for faster moving ships.

2.4.3 Wind in port

The VAWT can also be used to provide power when the ship is in port. To obtain reference wind conditions in ports, the average wind conditions in major ports along the main global shipping routes as indicated in Figure 2.13 are used. These 23 ports are listed in Table 2.2. The wind statistics at these large ports are obtained using the Marin Blueroute web application [63]. This application uses ERA-5 hindcast data from 1989-2019 at a vertical height of 10$[m]$. The directional resolution of this data is large, however, the wind speed resolution is limited to 5 wind speeds. The wind conditions for different ports are included in Appendix B.

Table 2.2: Ports main global shipping routes

Continent	Port	Country
Europe	St. Petersburg	Russia
	Hamburg	Germany
	Rotterdam	The Netherlands
	Lisbon	Portugal
	Istanbul	Turkey
Africa	Lagos	Nigeria
	Durban	South Africa
	Djibouti	Djibouti
Americas	New york	USA
	Houston	USA
	Seattle	USA
	Los Angeles	USA
	Panama	Panama
	Buenos Aires	Argentina
Asia	Singapore	Singapore
	Tianjin	China
	Shanghai	China
	Hongkong	China
	Busan	South-Korea
	Tokio	Japan
	Doha	UAE
Oceania	Melbourne	Australia
	Brisbane	Australia

The prevailing wind direction varies for the different ports however directional information is not necessary as the orientation of the ship can vary and the turbine can use a yaw mechanism to pitch the blades appropriately and capture wind energy from every direction.
The probabilities of all ports are averaged to obtain the average global wind statistics in port conditions. From this distribution, it can be concluded that the median wind speed at sea is 39% larger compared to the median wind speed in port. The median apparent wind speed for a ship moving at $U_s = 6[m/s]$ is 78% larger compared to the median wind speed in port. This indicates that substantially more wind power is available at sea.
The Weibull shape parameters (k) for values larger than 1 provide a measure for the variation in wind conditions. Therefore it can be concluded that the true wind conditions are more variable at sea compared to the wind conditions in port.

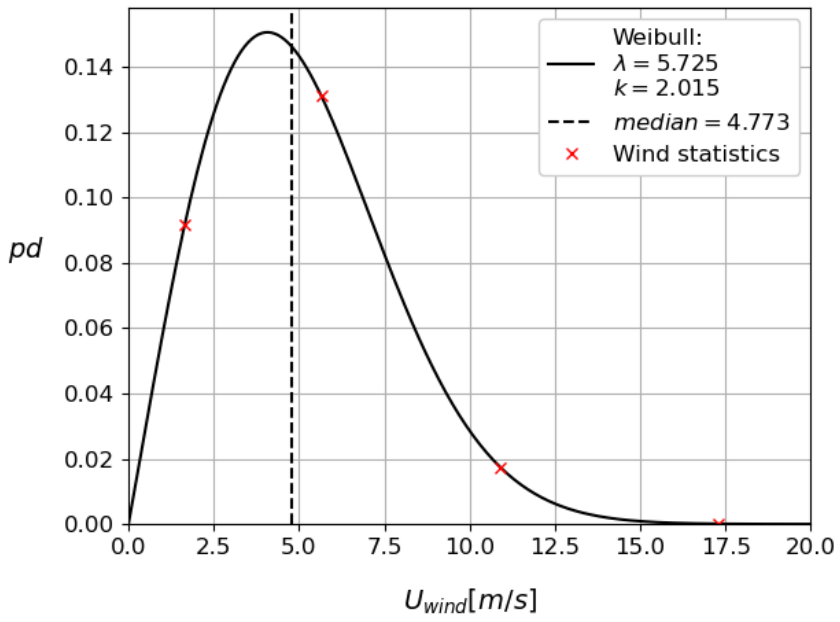

Figure 2.19: Wind speed probability density distribution in port conditions

2.4.4 Wind variation

The wind conditions experienced by the VAWT can be influenced by many effects other than the true wind speed and the ship speed.
The vertical wind profile is influenced by the planetary boundary layer. This causes vertical variations in the flow conditions as described by Burton [40, p. 18]. This boundary layer causes increasing wind speeds at larger altitudes. This is known as wind shear. Because the ship speed is a constant component and the wind speed varies vertically, the apparent wind direction also varies vertically whereby the apparent wind is closer to a headwind at a lower altitude. This vertical change in apparent wind direction occurs when the ship is moving and is known as wind veer. These vertical variations are specific to the wind conditions, the sea state, and ship speed. It requires 3D models to capture these vertical variations of the apparent wind profile.
The VAWT will be installed above the deck area. At this location, the wind conditions are distorted due to the ship's structure. These interactions were studied by Moat [13] to evaluate the flow patterns using Computational Fluid Dynamics (CFD) simulations. This study found separation regions with reduced flow speed may form around sharp corners such as the edge of the hatch covers. There can also be regions of accelerated flow above the deck. These interactions depend on the ship's geometry and the apparent wind direction.

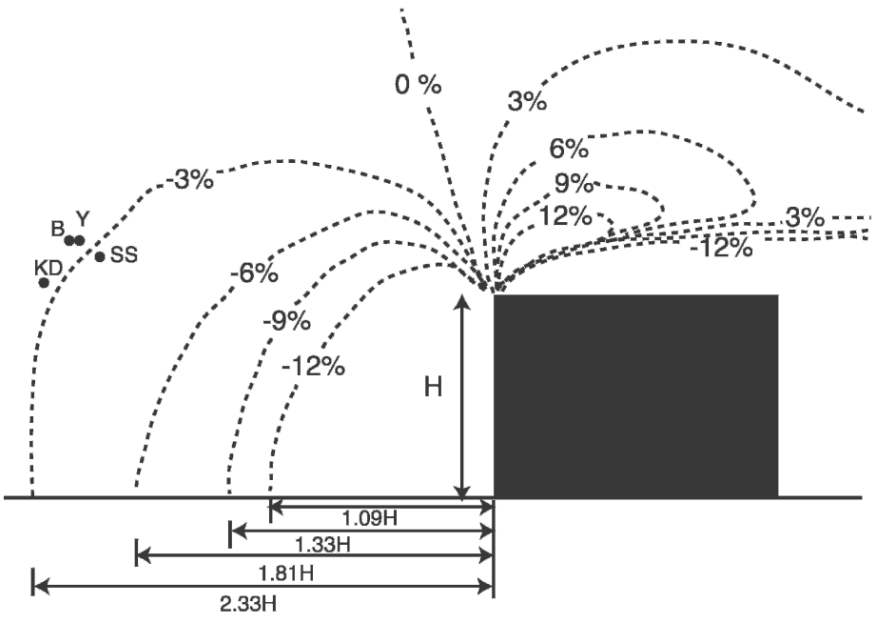

Figure 2.20: Wind speed distortion around a block for beam reaching wind conditions, from Moat et al. [13]

Ship motions such as rolling and pitching can also result in temporal variations in the wind conditions on the VAWT. These effects are more severe at large vertical locations because this is further from the center of rotation. The influence of effects from ship motions depends on the sea state and the ship's responses and seakeeping characteristics. This effect is therefore ship specific and depends on the sea state.
Temporal variations such as turbulence also causes variation in the flow conditions. Gusts are also an example of variable flow conditions as described by Burton [40, p. 18].
When multiple VAWTs are operating in close proximity, the interaction between the turbines can influence the flow conditions on each turbine. This is particularly the case for downwind interactions.
The described flow variations are complex to model and often depend on the ship geometry, wind conditions, and sea state. These variations are considered to be beyond the scope of this research. Therefore this study considers undisturbed steady uniform flow conditions of only one VAWT.

2.5 Ship size

WASP is effective when a substantial fraction of power can be provided by the wind propulsion system. The required engine power of the ship (P_B) can be estimated using the admiralty coefficient formula as described by Schneekluth [74, p. 184]. This shows the required propulsive power depends on the ship displacement (Δ), the ship speed (U_s), and the admiralty constant (C) which is a ship type specific parameter.

$$P_B = \frac{\Delta^{\frac{2}{3}} U_s^3}{C} \tag{2.4}$$

This formula shows the engine power is related to the ship displacement (Δ) to the power $\frac{2}{3}$. The engine power, therefore, scales quadratically with the length of the ship of uniform scaling. If the side projected area is a measure of the available wind propulsion power, this also scales squared with the length of the ship. Therefore a relatively similar sized WASP system can provide a similar fraction of propulsion power on different size ships. The size of the swept area of the VAWT should therefore be the same fraction of the potential sail area to provide the same fraction of propulsive power. Therefore even the largest ships can benefit from WASP systems as long as the swept area of the system is suitably large with respect to the ship size.

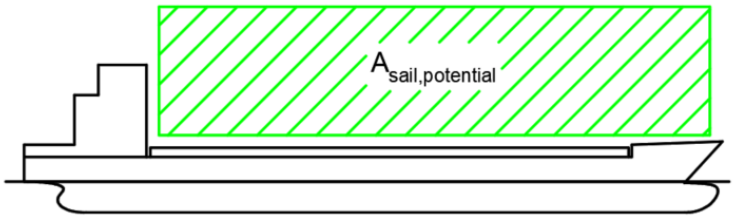

Figure 2.21: Potential side projected sail area

Chapter 3

VAWT for ship propulsion

The VAWT concept can be used to capture wind energy and can be used to provide a thrust force for ship propulsion. The design of a VAWT is considerably different from the design of a HAWT. The use of a VAWT enables the combination of power generation and thrusting. This chapter describes the working principles of a VAWT and the most influential aerodynamic effects for both the turbine and thruster modes.

3.1 Capturing wind energy

Wind energy is a freely available source of energy. The challenge is capturing this energy from moving air and using it in a useful way. The power which can be extracted from the wind has a cubic relation with the wind speed as shown in Equation 3.1. The principles described in this section are based on the concepts as explained in the Wind Energy Handbook by Burton [40].
The wind speed is influenced by the planetary boundary layer (friction layer) which describes the wind speed profile close to the earth's surface as stated by Kaltschmitt [36, p. 52-55]. The wind speed is usually faster at sea because there is less surface friction over the sea surface. Because of this surface friction, the wind speed is also larger at larger altitudes due to the earth's boundary layer. For offshore windfarm applications, a reference wind speed at 10 meters above the surface is used as the reference velocity as described by Heier [45, p. 44]. The velocity at different heights in the lowest part of the atmospheric boundary layer can be determined using the log law which is an empiric relation.
The increased wind speed is a reason for building wind farms offshore. One downside is the need to transport the energy to the consumers through a system of transformers and cables. Ships also spend approximately half the time at sea as explained in section 2.3. Ships could therefore make use of this freely available source of energy. One benefit of capturing wind energy onboard a ship is that the energy is consumed locally, either for propulsion or to provide electric power to auxiliary systems.
As explained by Leishman [58] the power which extracted from moving air can be expressed as a function of the power coefficient (C_P), the air density (ρ), the swept area ($A = 2RH$) and unperturbed far-field wind speed (U_∞). U_∞ is the same as U_a when the ship is in transit. Depending on the operational mode, $U_a = U_{wind}$ when ship is stationary.

$$P = C_P \frac{1}{2} \rho A {U_\infty}^3 \tag{3.1}$$

The power coefficient is a measure of how much wind energy a turbine can extract. This parameter is influenced by the wind turbine design and operation, this is discussed in more detail in subsection 3.1.2. The air density and wind speed are site-specific probabilistic properties. The power output is linearly proportional to the swept area.

3.1.1 Actuator surface

Moving air contains kinetic energy. This energy can be extracted from the swept area occupied by a wind turbine device. This extraction process is often modeled using an actuator surface. This theory is based on

the conservation of momentum and conservation of mass. This provides insight into the energy extraction process. The streamlines moving through the actuator surface are referred to as the streamtube. Energy can be extracted by slowing the flow speed inside the streamtube. This is indicated by an induction factor a. The induced wind speed at the turbine can be expressed as a function of the far field wind speed and the induction factor as shown in Equation 3.2. This reduction in speed cannot be done instantaneously because of continuity. Equation 3.4 indicates that reducing the flow speed requires an increase of the streamtube area and therefore the streamtube expands as the flow slows down. Mass is conserved as the mass flow rate along different downstream locations along the streamtube is constant. Because the velocities are relatively low as explained in section 4.1, the flow may be assumed to be incompressible and the density is assumed to be constant. Therefore the volume flow is constant through the streamtube. Bernoulli [47, p. 207] showed that the sum of dynamic and static pressure along a streamline is constant. Therefore the static pressure increases when the flow slows down. Due to the actuator providing a force resisting the flow, the static pressure jumps over the actuator surface this provides resistance against the flow and indicates the energy extraction. The force opposing the flow can be calculated as pressure jump times the swept area. The extracted energy can be calculated by this force with the local flow speed through the actuator surface, as indicated by Equation 3.6.

$$U_R = U_\infty(1 - a) \tag{3.2}$$

$$U_e = U_\infty(1 - 2a) \tag{3.3}$$

$$U_\infty A_\infty = U_R A = U_e A_e \tag{3.4}$$

$$p_t = p + q = p + \frac{1}{2}\rho U^2 \tag{3.5}$$

$$P = \Delta p A \overrightarrow{U_R} \cdot \hat{n}_A = F_d U_R \tag{3.6}$$

The static pressure (p) far upstream and downstream are the same however this changes near the actuator surface, with a jump at the actuator surface. This static pressure causes the expansion shape of the stream tube.

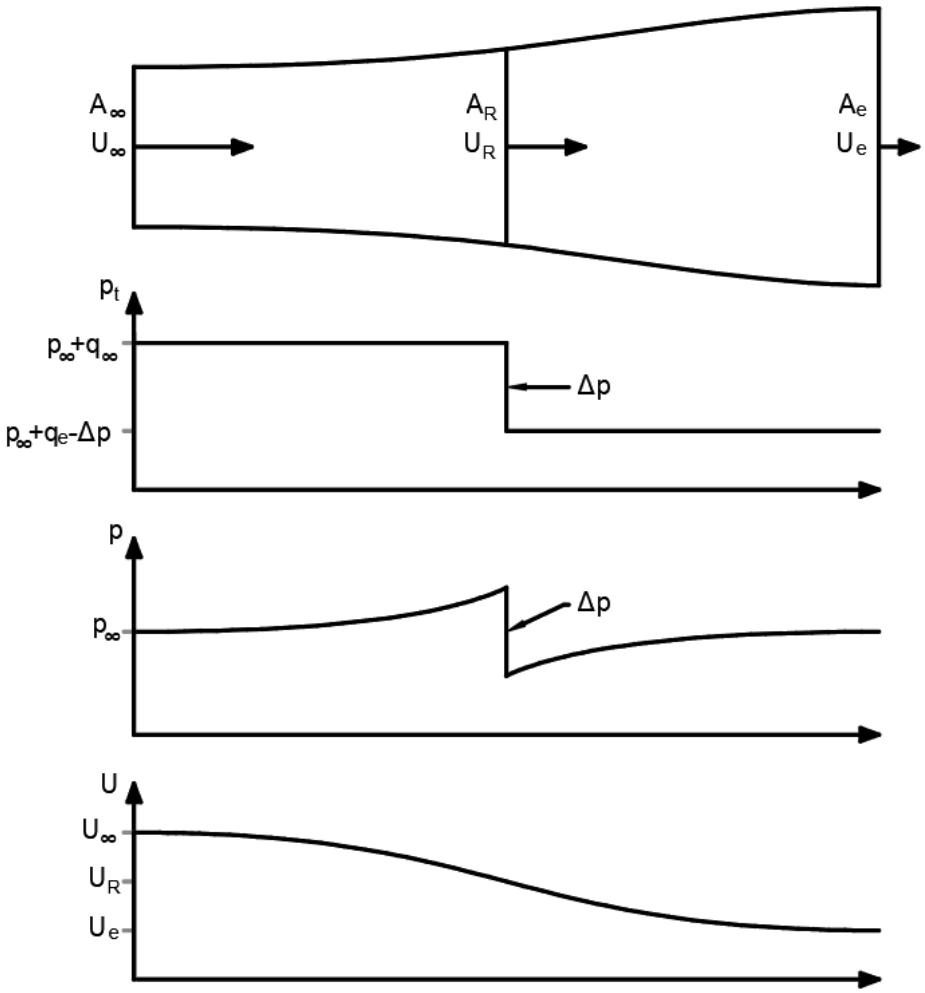

Figure 3.1: Actuator surface stream tube, pressure and velocity variation, inspired by Ferreira [41]

Because a VAWT has an upwind and a downwind side on which energy can be extracted, an actuator cylinder model is often used to model VAWT performance. The basic concept and conservation equations of this model are the same, section 4.2 elaborates further on momentum models to model VAWTs.

3.1.2 Betz limit

Extracting energy from an airflow means extracting kinetic energy and therefore slowing down the flow. Not all energy can be extracted from the flow as this would mean the air is stationary after the turbine which does not allow for flow to pass through the turbine.
To extract more energy, the pressure drop (Δp) and the wind speed at the turbine (U_R) should be increased. However because an open flow is considered, continuity will require the streamtube to expand if the pressure jump is increased. This expansion will also result in an upstream contraction which reduces the flux through the actuator surface and consequently the flow speed at the actuator surface. Therefore more resistance means a larger fraction of kinetic energy is extracted from the flow passing through the actuator surface however this also reduces the flow passing through the turbine.
The optimum balance is found for the induction factor where C_P is maximum. As shown by figure Figure 3.2 maximum power can be extracted at $a = 1/3$ for a HAWT. This strikes the optimum balance between providing a force opposing the flow and streamtube contraction to allow flow through the swept area. As indicated by the power coefficient, a maximum of $16/27 \approxeq 59.3\%$ of the kinetic energy can be extracted. This is known as the Betz limit. Which is obtained at a drag (often referred to as thrust) coefficient of $C_{d,turbine} = 8/9$. Momentum theory is no longer valid for $a > 0.5$ because this results in reversed flow far

field down the stream tube ($U_e < 0$).
As shown in Figure 3.2, there is a single optimal induction factor. This indicates that the actuator surface should be uniformly loaded for HAWTs. Approaching uniform loading is also found to be optimal by Madsen [24] for VAWTs.
Based on actuator cylinder models, Madsen [24] concludes that the maximum C_P for VAWTs can exceed the Betz limit close to uniform loading. This is also found by Chen [19] for a study based on unsteady 2D CFD simulations.

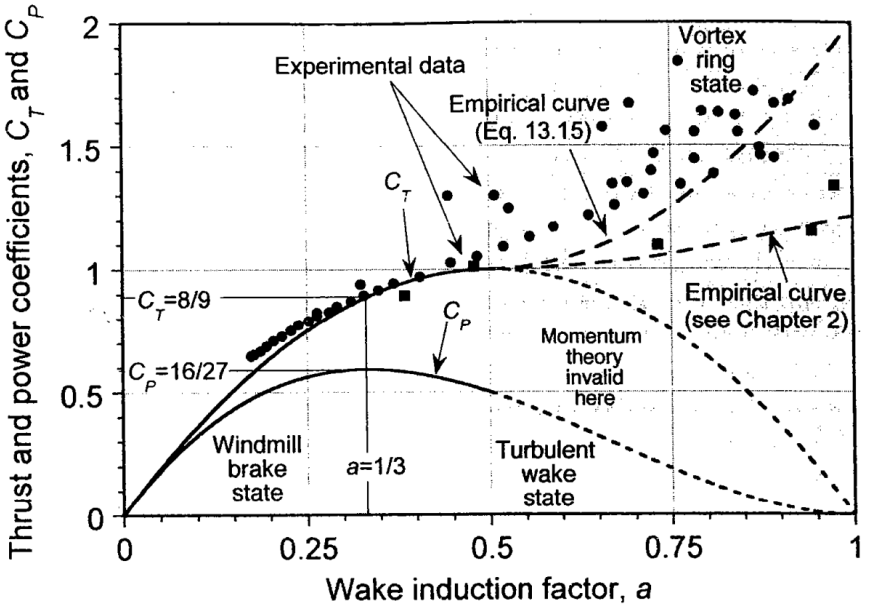

Figure 3.2: Momentum theory for different induction factors for a HAWT actuator surface. Measurements from multiple sources including Lock (1925). From Leishman [58, p. 730]. C_T is in this figure refers to $C_{d,turbine}$

This study considers the application of lift-driven turbines, these are fundamentally able to extract a larger fraction of the wind energy. Drag machines such as cup anemometers are limited because the cup-blades cannot move faster than the wind speed. Whereas for lift-driven machines, the relative velocity on the blades is usually faster than the wind speed. Therefore drag driven wind turbines are fundamentally able to extract less energy compared to lift-driven turbines as stated by Manwell [62, p. 115]. The power coefficient for drag-driven devices can be expressed as Equation 3.7. For a reasonably large drag coefficient of 1.2 this results in $C_{P,drag} \approx 0.18$ which is only 30% of the Betz limit for lift driven devices as found by Kabalc [51, p. 278]. Therefore lift driven VAWT concepts are generally able to produce more power.

$$C_{P,drag} = \frac{4}{27} C_d \tag{3.7}$$

3.1.3 Power curve

Any wind turbine should be able to operate in a range of wind conditions. At low wind speeds, the aerodynamic torque from the turbine might not be sufficient to overcome the friction to rotate the turbine. Even if the turbine can be rotated, the turbine has to rotate slowly in these wind conditions. Therefore the generator efficiency might be outside the efficient operating range as found by Bai [18]. Therefore wind turbines are usually not used below a certain far-field wind speed called the cut-in speed (U_{cut-in}).
As indicated by Equation 3.1 the power has a cubic relation with the wind speed. Therefore much power can be obtained in strong winds. However, the turbine should not fail structurally or exceed the maximum electrical load of the generator. This maximum load is attained at the rated wind speed. At lower than rated wind speeds, the turbine is aiming for maximum efficiency. To be able to use the turbine at large wind speeds. The operational parameters can be adjusted to purposefully operate the turbine less efficiently (at

lower C_P) to retain a constant power beyond the rated wind speed. Therefore the power is usually kept constant above the rated wind speed (U_{rated}) in order not to surpass the generator's operational range. As the power remains constant above the rated wind speed, Equation 3.6 can be rewritten as Equation 3.8. This shows the drag force is inversely proportional with U_R. When the turbine is operating above the rated wind speed and the power is fixed at the rated power. This means that the drag force on the turbine decreases inversely proportional to the induced wind speed. Therefore maximum aerodynamic loading occurs at the wind speed where rated power is just attained, at the rated wind speed as stated by Loenbaek [33].

$$F_d = \frac{P}{U_R} \tag{3.8}$$

As the wind speed increases, the rotational speed of the turbine also has to increase to attain similar operational conditions on the blades. Due to the rotation of the blades, these experience an acceleration in radial direction. In the turbine fixed reference frame, this acceleration is experienced by the blades as a centrifugal force ($F_{c,blade}$) which only exists in the inertial frame of reference. This radially outward pointing force is proportional to the square of the rotational velocity. Above some wind speed, the structural loads due to the rotational speed become substantial and the turbine should be stopped above the cut-out wind speed ($U_{cut-out}$). The high rotational speed should also not surpass the operational range of the generator.
When the turbine is stopped, the loads on the stationary blades are minor because the relative wind speed on the blades is low and the blades might be stalled. This substantially reduces the loads on the blades such that the turbine can survive large wind speeds when it is not rotating. Therefore the largest aerodynamic loads are encountered at the rated wind speed.

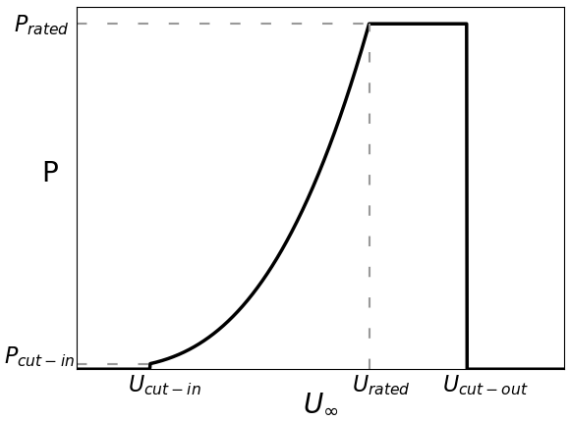

Figure 3.3: Schematic power curve

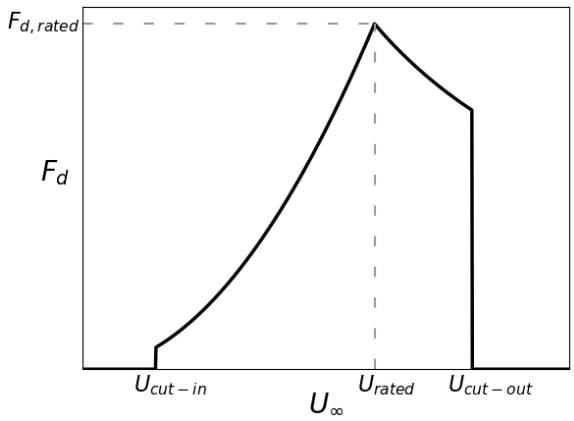

Figure 3.4: Schematic force curve

When operating a wind turbine, the objective is to produce maximum power. Therefore when selecting the cut-in, rated and cut-out wind speeds, the right balance between the structural limits, generator limits and power production has to be found. This depends on the encountered wind conditions and the power curve should match the environmental conditions.

3.2 Turbine type

The design of a VAWT is considerably different from the design of a HAWT. Within the class of VAWTs, multiple turbine types with specific properties have been invented. This section discusses the differences between turbine designs.

3.2.1 Comparison VAWT and HAWT

Wind energy can be extracted by many different wind turbine concepts. The most common type of wind turbine is the HAWT concept. These turbines are being applied all around the world to generate renewable

energy. The scale of these turbines is increasing as this technology is being developed. The wind turbine type investigated in this study is a VAWT which is a cyclorotor type concept. The VAWT concept has benefits and downsides compared to the HAWT concept. Both concepts have specific characteristics which provide specific use cases for both turbine types.

3.2.1.1 Swept area

To produce more power, the swept area of a wind turbine can be increased. However, this also increases the cost of a turbine. The cost of a wind turbine is often related to the blade span. For a HAWT, the swept area scales quadratic ($A = \pi R^2$) with the blade span (R). For a VAWT, the swept area scales linearly with the blade span and the radius ($A = 2RH$). When the blade span of a HAWT is doubled, the power production roughly increases by a factor 4. For a VAWT to attain the same power increase, the radius or the blade span has to increase roughly by a factor 4. Due to this difference in swept area scaling, HAWT turbines have an inherent benefit at large scales, therefore VAWTs are often considered less cost-effective for large turbines as noted by Riegler [71]. Figure 3.5 and Figure 3.6 show the different types of turbines with the same blade span.

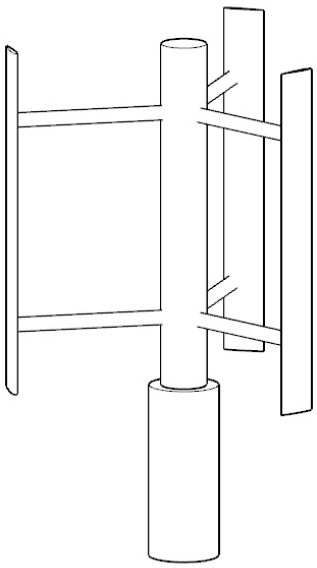

Figure 3.5: H-type VAWT

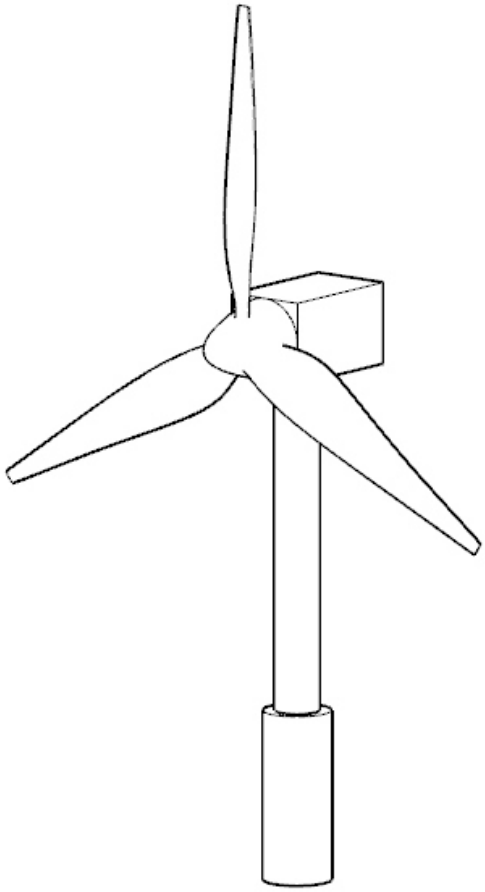

Figure 3.6: HAWT

3.2.1.2 Operating conditions

The blades of the VAWT per definition experience variable operating conditions because the rotation direction is not aligned with the wind direction and because the downwind blades pass through the wake of the upwind blades. This turbine shape means energy can be generated on the upwind as well as on the downwind side. However, this shape also causes interactions and periodic variations in the flow conditions. The unsteady aerodynamics of a VAWT result in a complex flow field. This complexity might have obstructed

the development of VAWTs as stated by De Tavernier [80].
The blades of a HAWT have more constant operating conditions where variations can be caused by wind shear due to the earth boundary layer and wind veer. Yaw angle offsets and interactions with the tower can also result in variable operating conditions for a HAWT. However, because the blades do not pass through each other's wake there is less interaction between the blades of a HAWT.

3.2.1.3 Blade geomertry

Because the operating conditions for a HAWT vary in spanwise direction (radially), the blades have to be twisted and require variable chord along the span. This results in a relatively complex blade shape which is therefore expensive to manufacture. For H-type VAWTs, each spanwise blade section experiences the same operating conditions, apart from the tip effects. Therefore the blade sections do not have to use twist and chord variation. This simpler blade shape makes the the blades less expensive to manufacture as concluded by Sutherland [79].

3.2.1.4 Pitch

As stated by Islam [46, p. 2], VAWTs without pitch variation are omnidirectional and therefore do not require a yaw system to direct the turbine surface into the wind whereas, for a HAWTs, the entire rotor-nacelle assembly has to rotate such that the rotor plane is parallel to the wind direction. VAWTs with pitch variation have to adjust the excenter setting to the wind direction. This is a small operation compared to the yaw system on a HAWT. The excenter setting on a VAWT can also be used to stall the blades and stop the turbine when required, provided that the pitch amplitude is sufficient.

3.2.1.5 Blade support and loading

The blades of both turbine types experience sheer forces and bending moments. For a HAWT this moment can be substantial and requires a thicker blade root near the rotor hub. The H-type VAWT has struts supporting the blades at two locations along the span. This reduces the sheer force and bending moment on the blades. However, the struts and pitch actuation arms provide parasitic drag which lowers the turbine performance.
Fatigue loading can also be critical as these turbines experience many stress cycles over the lifespan of a turbine. The variable operating conditions of VAWTs over the rotation result in periodic load variations which could cause fatigue problems. Because the blades of a VAWT are loaded in two directions, tension-compression cycle fatigue can occur. Due to this cyclic loading, the fatigue equivalent loads are larger for a VAWT as found by Galinos [20].

3.2.1.6 Tip speed ratio

The relative speed on the blades increases over the span for a HAWT. Therefore each blade section is operating under different flow conditions. The blade root operates relatively slow and the blade tip relatively fast. The blades of an H-type VAWT are fully located at the outer radius, therefore these are the fastest moving part of the turbine and the blades operate at the same speed along the span. Therefore VAWTs can generally operate at lower tip speed ratio (λ) and produce less noise as concluded by De Tavernier [80, p. 20].

3.2.1.7 Gearbox and generator location

The gearbox and generator require regular inspection and maintenance. In HAWTs these are located in the nacelle. This, therefore, requires maintenance personnel to climb to the top of the tower. VAWTs can have the gearbox and generator at the turbine foundation and are therefore more easily accessible for maintenance.

3.2.2 VAWT types

Many different types of VAWTs have been invented. The most occurring type is the H-type turbine where the blades are parallel to the axis of rotation. This type is investigated in this study. Other common types are analyzed and discussed by Casini [6]. The Darrieus type is shaped such that the blades are loaded in tension at high rotational speeds. As opposed to the H-type turbine where the blades experience a shear load and a bending moment which is generally undesirable for slender structures. The operating conditions

and load on the blades vary over the rotation. To reduce fatigue loading, the Gorlov type VAWT features twisted blades to reduce the amplitude of the load oscillations.

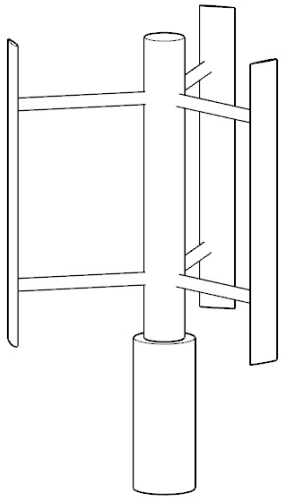

Figure 3.7: H-type

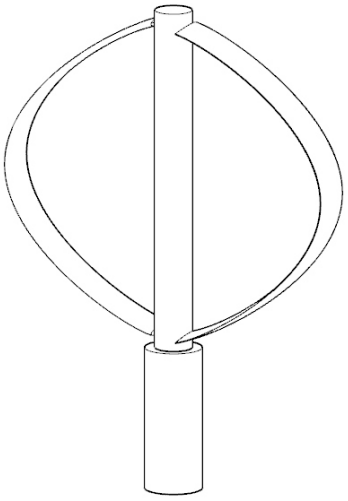

Figure 3.8: Curved Darrieus

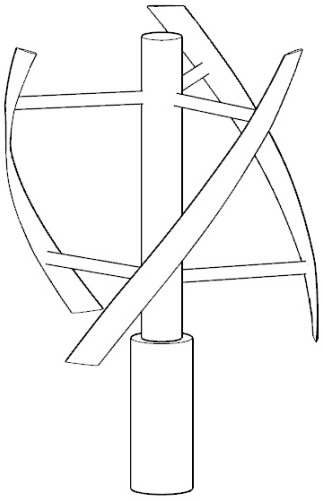

Figure 3.9: Gorlov type

3.3 VAWT working principles

Because the rotation axis of the blades is not aligned with the wind direction, the blades experience variable flow conditions. Therefore the operational conditions depend on the azimuth angle (θ) which can be characterized in four quadrants.

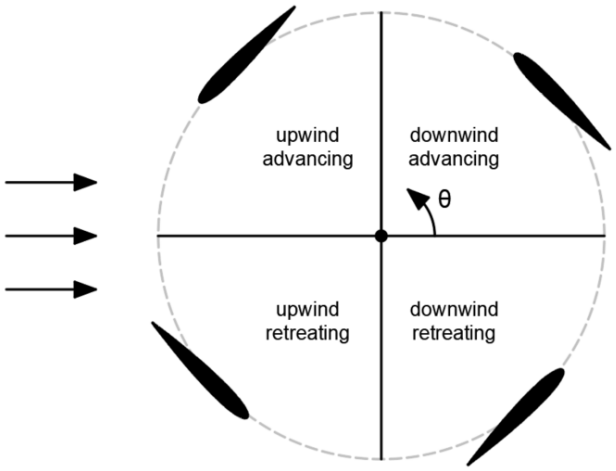

Figure 3.10: VAWT quadrants, inspired by Keijer [54, p. 35]

The blades of a VAWT experience variable operating conditions over the rotation. The relative speed (U_{rel}) on the blades is a combination of the wind speed at the rotor (U_R) and the tangential speed due to the rotation of the blades (U_{blade}). The magnitude of the vector addition defines U_{rel} and the ratio of these wind speeds define the local angle of attack (α).
It is useful to use non-dimensional properties such that the results can be scaled for different turbine sizes. The angular velocity is expressed as ω. The relative rotational speed is characterized by the non-dimensional Tip Speed Ratio (TSR) (λ). Increasing the TSR results in a larger blade velocity, lower angles of attack, and a smaller moment arm of the forces if the lift over drag ratio is constant. It is important to note that some

information is lost by making properties non-dimensional, for instance, the Reynolds number effects are not incorporated in the tip speed ratio.

$$\lambda = \frac{U_{blade}}{U_\infty} \tag{3.9}$$

$$\omega = 2\pi\, RPS = \frac{U_{blade}}{R} \tag{3.10}$$

At low λ or when the turbine is stationary, the angles of attack are large. General airfoils are not suitable to operate at large angles of attack because the airfoil will stall which is detrimental to the lift force which drives the turbine. Therefore lift driven VAWTs with symmetric blades are generally not self-starting.
A VAWT without pitch is omnidirectional, therefore the operating conditions are not influenced by the wind direction.

$$\overrightarrow{U_R} = \begin{bmatrix} U_\infty(1-a) \\ 0 \end{bmatrix} \tag{3.11}$$

$$\overrightarrow{U_{blade}} = U_\infty TSR \begin{bmatrix} sin(\theta) \\ -cos(\theta) \end{bmatrix} \tag{3.12}$$

$$\overrightarrow{U_{rel}} = \overrightarrow{U_{blade}} + \overrightarrow{U_R} \tag{3.13}$$

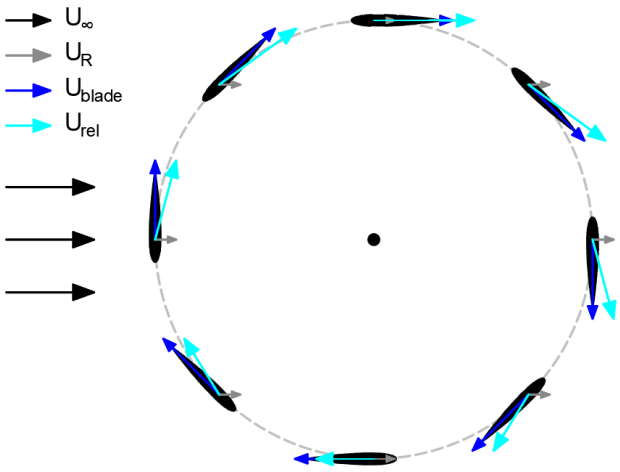

Figure 3.11: VAWT wind speeds, $\lambda = 2.5$

The H-type VAWT is a lift-driven turbine. This means the lift force provides a moment around the rotation arm whereas the drag force reduces the moment arm. Therefore operating the blades at large lift and small drag is desirable. Madsen [24] found an increase of the airfoil drag coefficient of just 0.001 to result in a 1% decrease in the power coefficient. The lift and drag forces on the blades averaged over the rotation are mainly influenced by the angle of attack and relative velocity.

$$\alpha = arccos\left(\frac{\overrightarrow{U_{blade}} \cdot \overrightarrow{U_{rel}}}{\left|\overrightarrow{U_{blade}}\right| \left|\overrightarrow{U_{rel}}\right|}\right) \tag{3.14}$$

$$\hat{U_{rel}} = \frac{\overrightarrow{U_{rel}}}{\left|\overrightarrow{U_{rel}}\right|} \tag{3.15}$$

$$\overrightarrow{F_{d,blade}} = \frac{1}{2}\rho U_{rel}^2 csC_d(\alpha)\hat{U_{rel}} \tag{3.16}$$

$$\overrightarrow{F_{l,blade}} = \frac{1}{2}\rho U_{rel}^2 csC_l(\alpha)\hat{U_{rel}} \begin{cases} \begin{bmatrix} 0 & -1 \\ 1 & 0 \end{bmatrix} & \theta \leq 90, \theta > 270 \\ \begin{bmatrix} 0 & 1 \\ -1 & 0 \end{bmatrix} & 90 < \theta \leq 270 \end{cases} \tag{3.17}$$

$$\overrightarrow{F_{t,blade}} = \overrightarrow{F_{l,blade}} + \overrightarrow{F_{d,blade}} \tag{3.18}$$

$$M_{blade} = r \begin{bmatrix} cos(\theta) \\ sin(\theta) \end{bmatrix} \times \overrightarrow{F_{t,blade}} \tag{3.19}$$

On the retreating side, the relative wind speed is smaller which results in smaller forces however on the retreating side, the moment arm of the force is larger. This makes the moment a function of the azimuth angle.
As found by Kemp [55, P. 10, 17], most literature considers symmetric airfoils. However cambered airfoils are considered to have better self-starting characteristics. Cambered airfoils can also be used to limit the influence of the flow curvature effect as explained in subsection 3.4.2. Cambered airfoils are also better suited to the different operating conditions on the upwind and downwind side however this can also be achieved using active pitching as explained in subsection 3.4.3.

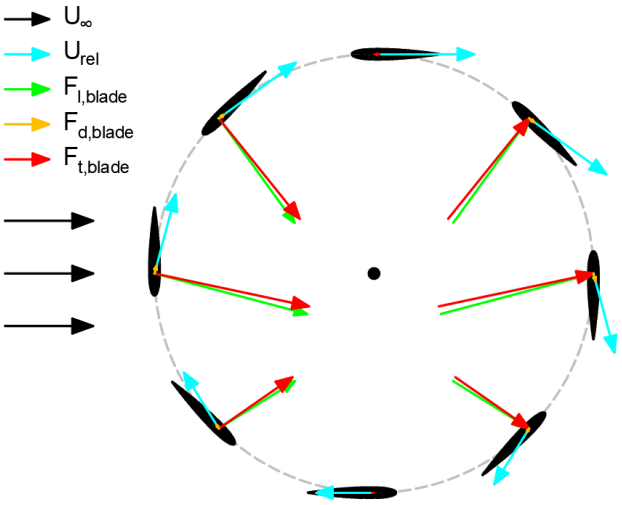

Figure 3.12: VAWT driving forces, Cl/Cd = 20

Besides the operating conditions of the blades, the magnitude of the forces also depends on the chord length of the blades and the number of blades. This is made non-dimensional by division with the turbine diameter which results in the solidity (σ) parameter. Figure 3.13 to Figure 3.15 show VAWTs of equal solidity for a variable number of blades.

$$\sigma = \frac{N_{blades}c}{2R} \tag{3.20}$$

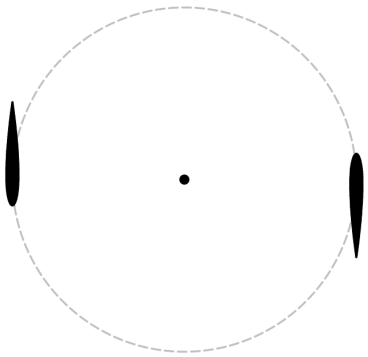

Figure 3.13: $\sigma = 0.6$, $N_{blades} = 2$

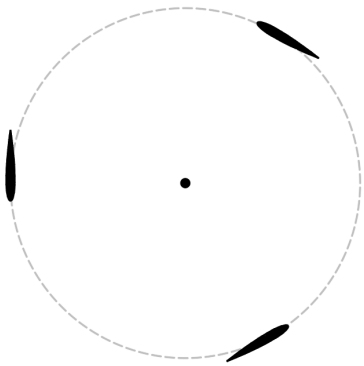

Figure 3.14: $\sigma = 0.6$, $N_{blades} = 3$

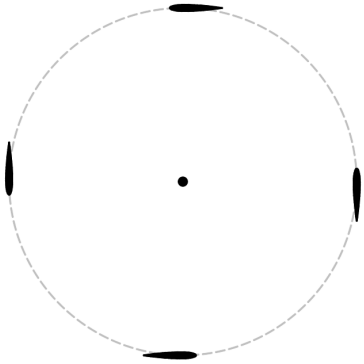

Figure 3.15: $\sigma = 0.6$, $N_{blades} = 4$

Small solidity turbines generate a small force due to the small blades, therefore these turbines operate at larger rotational speeds whereas large solidity turbines have larger forces and therefore operate at lower rotational speeds. This is concluded by Brusca [39] and indicated in Figure 3.16.
The design of the turbine can influence the maximum attainable power coefficient and the TSR range for which high power coefficients can be attained. Figure 3.16 shows large solidity turbines to be more sensitive with a narrow operating range for the TSR.

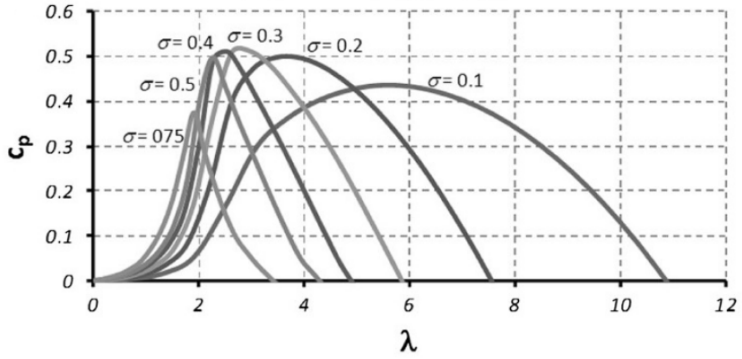

Figure 3.16: Power coefficient for an H-type VAWT, NACA 0018, Re = 5e6, from Brusca [39]

3.4 Influential aerodynamic effects

The blades of a VAWT operate along a circular path in variable relative flow conditions. Therefore the airfoils are subject to additional aerodynamic effects which are more complex compared to a static airfoil in steady flow conditions.

3.4.1 Boundary layer centrifugal effect

The rotation of the blades consists of a combination of a constant tangential blade velocity (U_{blade}) and an acceleration in radial direction. In the rotor fixed reference frame, this acceleration is experienced by the blades as a centrifugal force. Due to viscous effects, a boundary layer is formed around the airfoil. This boundary layer is also influenced by the centrifugal force as explained by Migliore [38]. Particles at the airfoil surface move with the airfoil along the rotational path. Due to this rotational motion, these particles also experience centrifugal body forces causing the wake to be shed radially outward when leaving the trailing edge. These centrifugal forces also affect the pressure gradient normal to the airfoil surface. Migliore [38] found the surface perpendicular pressure gradient in the boundary layer to be at least one order of magnitude larger than usually found in curved flows. This pressure gradient is proportional to TSR^2 as the centrifugal forces also scale quadratically with the angular velocity. This effect might delay separation on the upwind

side and promote separation on the downwind side. The influence of this effect is considered small compared to the other effects however can still have a substantial influence at higher TSR.

3.4.2 Flow curvature effect

The blades on a VAWT follow a curved path. Therefore the blades encounter curvilinear flow which results in a continuous variation of the relative flow conditions along the chord as explained by Burton [61]. This influences the forces generated by the airfoil. As explained by Bianchini [12], a symmetric airfoil in a curved flow operates similarly to a cambered airfoil with additional incidence in a rectilinear flow. These effects are respectively known as virtual camber (V_c) and virtual incidence (V_I). The virtual camber can be seen as a virtual change in airfoil geometry and the virtual incidence can be seen as additional pitch due to the curved flow path.

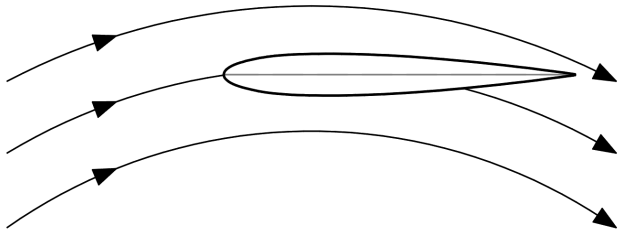

Figure 3.17: Symmetric airfoil in a curvilinear flow, inspired by Akimoto et al. [26]

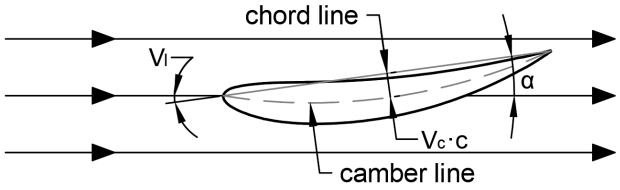

Figure 3.18: Virtual camber and angle of attack in a rectilinear flow, inspired by Akimoto et al. [26]

The influence of the flow curvature effect depends on the blade chord with respect to the turbine radius (c/R), the TSR, the mounting point, and the pitch angle as explained by Li [59, p. 94]. For the same solidity, this effect is therefore more influential for turbines with fewer blades. When the turbine is subjected to a far-field flow, the influence of the flow curvature effect also depends on the TSR (λ). For a small TSR, the blade velocity along the curved trajectory is small with respect to the induced wind velocity which is a rectilinear flow. Therefore the flow curvature effect is more substantial for larger TSR.
Rainbird [31] found that using the experimental polars of the actual blade geometry yields inaccurate results for large c/R ratios. This difference is already apparent for $c/R = 0.25$.

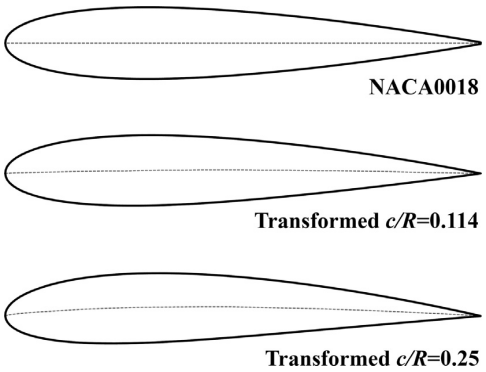

Figure 3.19: Airfoil transformations to compensate for curved flow, from Rainbird et al. [31]

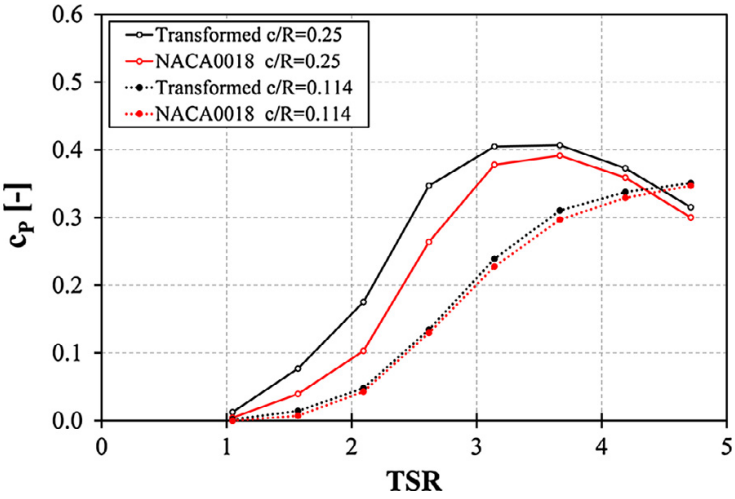

Figure 3.20: Performance deviations due to flow curvature effects, from Rainbird et al. [31]

Because the flow curvature effect can have a substantial influence, large c/R ratios should be avoided or this effect should be accurately modeled. As proposed by Migliore [38], conformal transformation can be used for the aerodynamic analysis of blades in curvilinear flow. If the polar information of the virtual airfoil shape in a rectilinear flow is known, the characteristics of the rotating blade will be known.
It is recorded by De Tavernier [80, p. 39-40] that flow curvature can be compensated for by changing the angle of attack or changing the airfoil camber. Increasing the airfoil camber has the approximate effect of vertically shifting the lift polar whereas the additional virtual incidence influences the location on the lift and drag polars.

3.4.3 Pitch variation

To provide maximum power, the blades should generate a large moment around the rotation axis without a large total drag force ($F_{d,turbine}$) blocking flow to the turbine. This can be achieved by a large lift force and a large moment arm which requires a small drag force. To attain this, the blades should operate at optimal conditions over the entire rotation. For a fixed pitch VAWT, the operating conditions are only influenced by the TSR and the polars resulting from the blade geometry. More design freedom is required to enable the blades to be more effective over a larger part of the rotation. This can be achieved by applying periodic pitch variation over the rotation such that the upwind and downwind turbine loading is uniform, resulting in a constant bound circulation on the upwind and downwind sides with jumps between the upwind and downwind sides as concluded by De Tavernier [80, p. 256]. To achieve this, the angle of attack is more constant over parts of the rotation but not completely constant because the relative velocity varies over the rotation. The optimal pitch variation is therefore not sinusoidal but more like a block-type wave as shown in Figure 3.21.

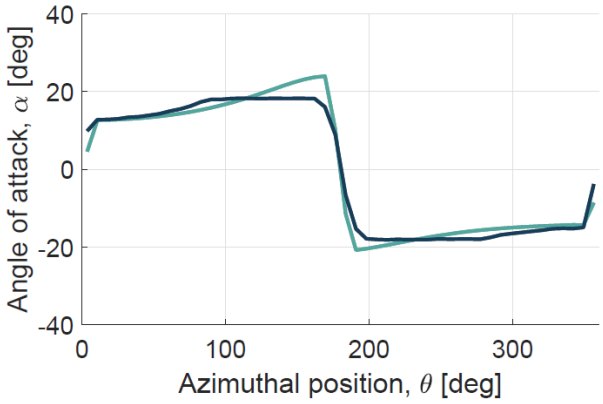

Figure 3.21: Optimised angle of attack for maximum power, from De Tavernier [80]

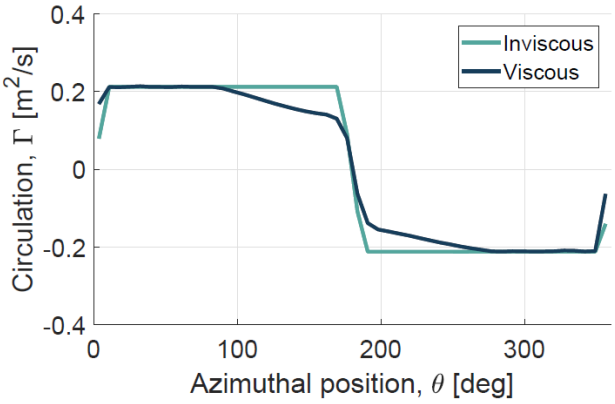

Figure 3.22: Optimised bound circulation for maximum power, from De Tavernier [80]

Elkhoury [34] found that variable pitch VAWTs can attain larger power coefficient and the maximum C_P occurs at lower TSR. Pitching the blades can reduce the angle of attack on the blades and therefore the TSR should be reduced to keep the angle of attack in an efficient operating range (no stall but large lift/drag). Because the turbine now rotates more slowly, the loading is reduced. Therefore the chord of the blades should be increased for efficient operation.
The VAWT concept works without pitch variation as indicated by Figure 3.12. Even without pitch variation, the blades can create a moment around the axis of rotation. This only works if the turbine is rotating at sufficient speed such that the blades work efficiently. Therefore a fixed pitch VAWT with symmetric blades is generally not self-starting. This can be solved by pitching the blades periodically over the rotation such that the angle of attack at low TSR is reduced to reduce stall at startup. This can make the VAWT self-starting.

3.4.3.1 Passive pitch

As described by LeBlanc [57], the pitch angle can be passively driven by the use of the natural aerodynamic loading to pivot the airfoil around the pitch axis. This can be used without additional structures other than pivot points to rotate the blades freely. This can prevent stall and improve performance at lower TSR as described by LeBlanc [57]. Passive pitch systems are limited because these depend on the aerodynamic loading to initiate the pitch. These systems are therefore not suitable to prescribe the exact pitch angle over the rotation.

3.4.3.2 Active pitch

Active pitch systems force the pitch angle over the rotation, as described by LeBlanc [57]. To reduce the required complexity, many active pitch systems use struts and rods to mechanically prescribe the pitch variation. Struts are the main structural connections connecting the blades to the rotation axis. These are found on every H-type VAWT and are used to support the blades and transfer the majority of the blade loads.
Rods are used to prescribe the pitch variation. These are connected to the blades at a different chordwise position. These rods are connected to an eccentric shaft which is used to prescribe the pitch variation. All these horizontal struts and rods have a negative effect on the power coefficient as they experience drag when rotating. The parasitic drag and resulting power loss from these rods is more substantial at large TSR as found by Elkhoury [34].
If the pitch amplitude is sufficient, active pitch can also be used to alter the pitch variation such that the blades do not operate efficiently, or are forced to stall. This increases the drag and is detrimental to the lift which drives the turbine. Therefore the power coefficient can become negative, which can be used to force the turbine to stop using the pitch phase setting. This can be used as an additional safety system in case the generator or the braking system is not able to slow down the turbine.

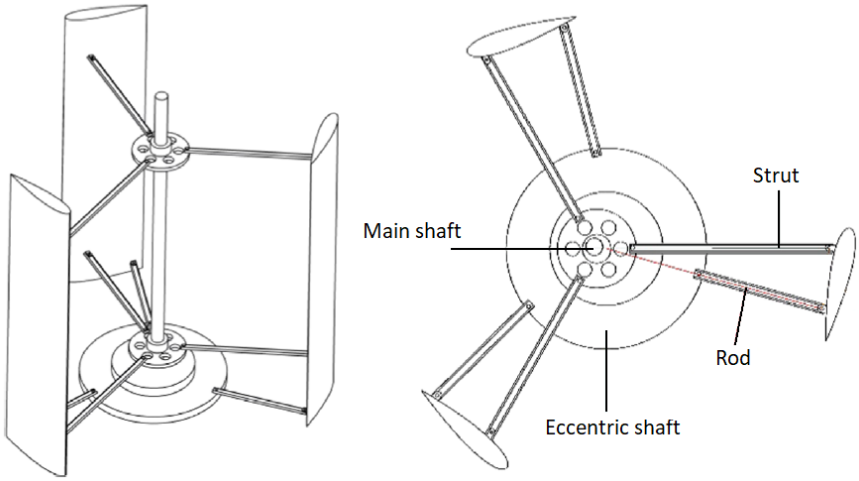

Figure 3.23: Pitch actuation system, modified from Elkhoury [34]

This mechanism uses an excenter to prescribe the pitch variation which is often referred to as sinusoidal pitch variation. This excenter pitch mechanism indeed produces a sinusoidal variation of the pitch angle however Figure 3.24 shows that this pitch is not the same as a symmetric sinusoidal pitch pattern. Figure 3.25 shows that an excenter offset in x-direction does not result in a maximum pitch angle at $\theta = 180[°]$. The excenter offset is phase-shifted resulting in a maximum pitch angle when the excenter rod is near opposite to the excenter direction. The pitch variation curve is also shifted in average amplitude, resulting in different positive and negative pitch amplitudes. The influence of these effects increase for larger pitch amplitude (A_{θ_p}) and a larger c/R ratio. The difference between excenter and sinusoidal pitch can be reduced by adjusting the length of the pitch actuation rods.

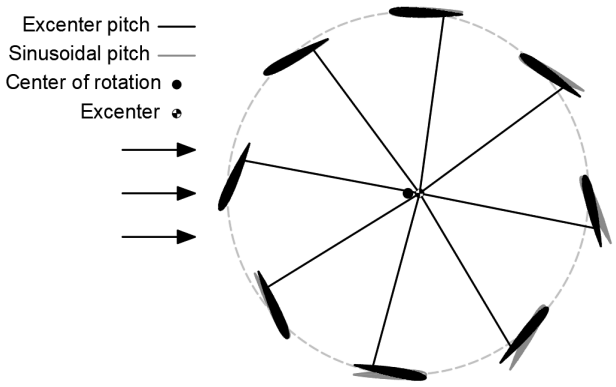

Figure 3.24: Comparison pitch variation, amplitude of $A_{\theta_p} = 24[°]$ at $\theta = 180°$

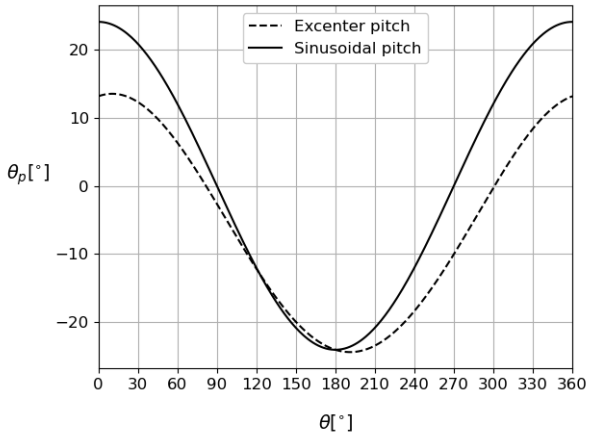

Figure 3.25: Comparison pitch variation, amplitude of $A_{\theta_p} = 24[°]$ at $\theta = 180°$

3.4.3.3 Independent active pitch

The blade pitch can also be controlled per individual blade. An independent active pitch control system is applied by LeBlanc [57]. Independent active pitch control allows the optimal blade pitch to be prescribed per individual blade at any point of the rotation. This is advantageous for the turbine performance however requires a relatively complex pitch actuation system [57].

3.5 Unsteady operation

Many aerodynamic flows are fundamentally unsteady depending on the scale of the flow structures. These flows are often represented as averaged, steady flows for which models (such as turbulence models) are used to capture the influence of the unsteady effects. This can only be used if the operating conditions are steady. For a VAWT, the operating conditions on the blades change over the rotation. These changing conditions result in changing blade loads over the rotation. As used by Ferreira [42], the forces at any azimuthal angle are referred to as the instantaneous forces whereas the rotation averaged forces are referred to as the integral forces. The unsteady aerodynamic effects of the changing operating conditions can influence instantaneous the performance of the turbine.

3.5.1 Step responses

The operating conditions on the blades are continuously changing over the rotation. When an airfoil experiences a change in operating condition, the flow and the resulting forces do not immediately conform to this new operating condition. Instead, the flow will adapt to this new condition in a transient manner. This effect is more severe for more rapid changes.
To explain this behavior, it is insightful to look at Prandtl's lifting-line theory. This states that the lift can be indicated by a single bound vortex (Γ). A change in lift requires a change in bound vorticity. Kelvin's circulation theorem states that this requires a vortex of the opposite strength of the change to be shed in the wake. Therefore the total circulation in the wake is the same but opposite to the bound circulation. In 3D this can be seen as a closed loop with a horseshoe-shaped vortex in the wake. When the angle of attack on an airfoil is increased, this increases the bound vorticity and sheds an opposite vortex with the same strength as the bound vorticity increases. As explained by Leishman [58, p. 431-434], these shed vortices induce velocities on the flow field such that the change in bound circulation and lift is reduced until the vortices are convected away from the airfoil.

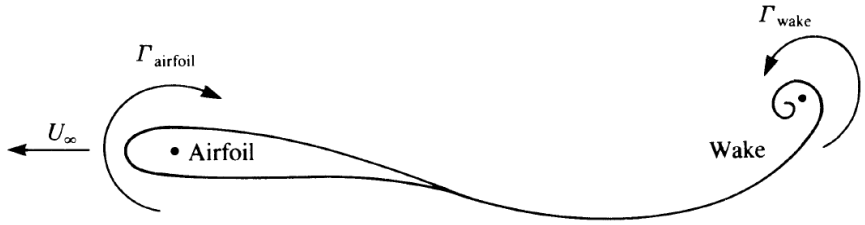

Figure 3.26: Airfoil and wake circulation after a sudden motion, from Katz [53, p. 26]

Therefore an instantaneous change in the angle of attack results in a gradual change in forces. This is both the case for increasing and decreasing lift. On a VAWT, this vortex shedding is a continuous process as the operating condition change continuously over the rotation. This effect can be modeled using Theodorson's theory as explained by Leishman [58, p. 431-434].

3.5.2 Dynamic stall

Because the angle of attack varies over the rotation, depending on the pitch actuation system, the angle of attack of a cyclorotor can momentarily surpass the stall angle and dynamic stall phenomenon can appear.
Dynamic stall can occur when the effective angle of attack due to unsteady motion such as pitching surpasses the static stall angle and when this change in angle of attack is relatively rapid with respect to the flow speed. This results in fundamentally different separation development compared to stall in steady flow conditions. This phenomenon is explained by Burton [58, p. 525-529] and is graphically shown in Figure 3.27. This figure shows substantially larger lift coefficients can momentarily be attained at large angles of attack for which static stall would already have occurred. This increase in lift is accompanied by an increase in drag.
Dynamic flow separation is found to be characterized by a vortex being shed from the leading edge which is convected over the suction side. A vortex contains low pressure at the core which temporarily increases the lift and causes an angle of attack reducing the pitching moment. After a brief increase in lift, this vortex has passed over the airfoil and is shed into the wake. The airfoil forces now follow a hysteresis trend and

will perform as if fully separated. To reattach the flow to the surface, the angle of attack has to be reduced below the static stall angle of attack.
When increasing the angle of attack, circulation is shed into the wake which initially reduces the lift as explained in subsection 3.5.1. This also reduces the adverse pressure gradient. Another contribution is the pitching motion which induces virtual camber similar to the flow curvature effect. The unsteady effects in the boundary layer due to an increase in pitch also contribute to a delay in separation.

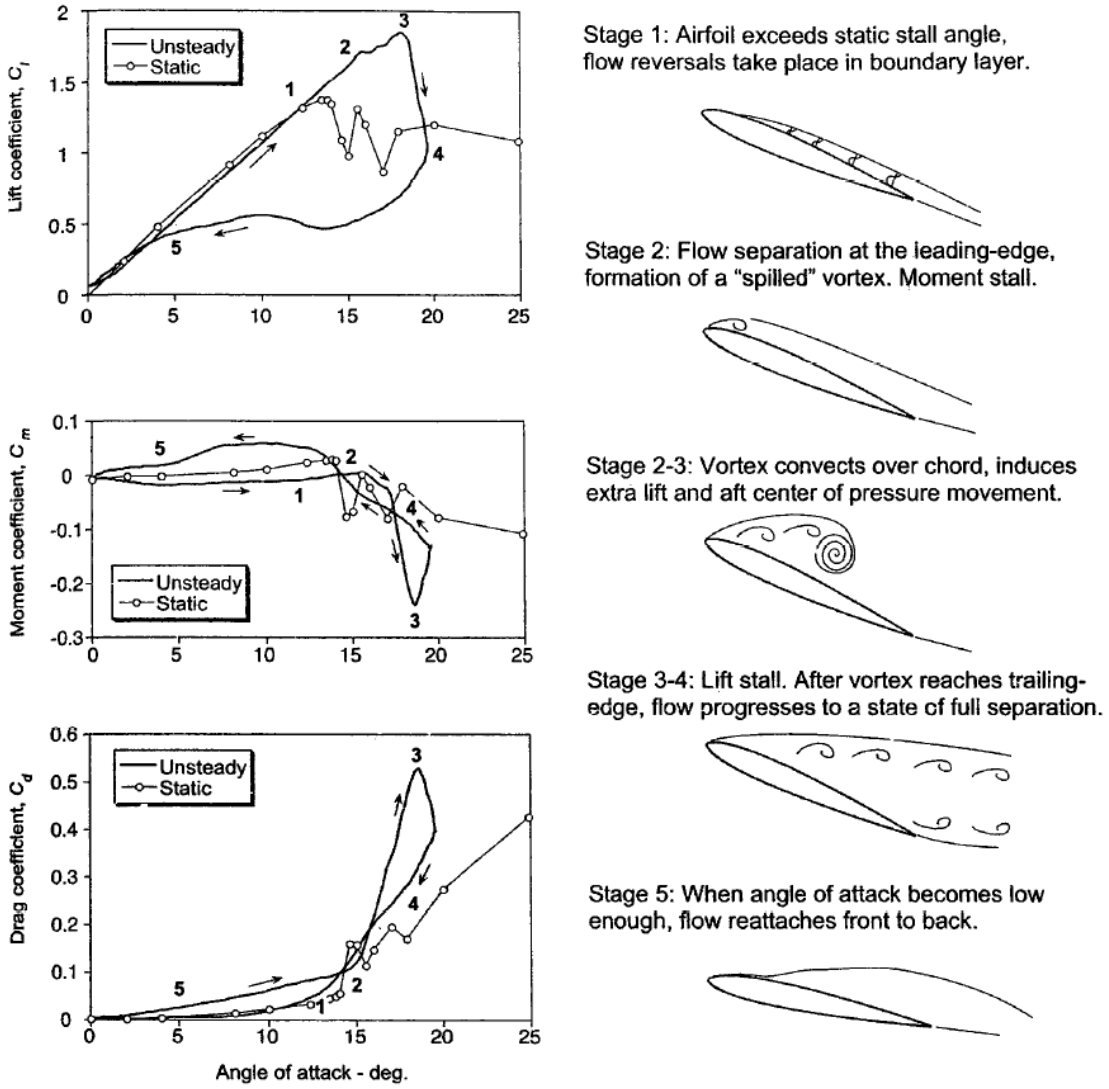

Figure 3.27: Schematic representation of dynamic stall on a 2D oscillating airfoil, from Leishman [58, p. 529]

3.6 VAWT as a turbine

The VAWT can be used to capture wind energy and convert this energy into electrical power. This power can be used for systems onboard the ship or to provide propulsive power.

3.6.1 In port

When a ship is in port, it is not using the propulsion system however many auxiliary processes onboard require power to keep the ship in operation when the ship is not in transit. This power is often provided by generator sets using combustion engines which emit harmful emissions. Even though the wind conditions in port are generally at lower wind velocities as described in subsection 2.4.3, there is still wind energy available

which can be captured by a VAWT to provide a renewable energy alternative to power the auxiliary systems. Because ships operate around 40% of the time in port as discussed in section 2.3, the ability for a wind propulsion system to also be useful in port provides a benefit with regard to current sailing WASP systems.

3.6.2 Ship propulsion

As discussed in section 2.4, the wind conditions at sea are generally stronger. The VAWT can also be used at sea to generate electric power. Conventional sailing WASP systems can only be used up to a certain upwind angle in favorable wind conditions. Figure 2.18 shows that faster moving ships more frequently encounter headwind conditions which are unfavorable for conventional sailing systems. Therefore these systems cannot be used for a substantial fraction of the time at sea. This could be increased if weather routing was applied such that the wind conditions are more favorable for sailing systems. However, this also increases the travel distance which is undesirable. Because the wind propulsion system only provides assisted propulsion, this additional distance might not be worth the benefit of some additional wind propulsion.
This problem could be solved by the VAWT WASP system. This system can produce power in port or in any apparent wind direction at sea, including a headwind. The phase of the pitch variation should be adjusted such that the upwind and downwind sides are loaded, providing torque around the rotation axis.

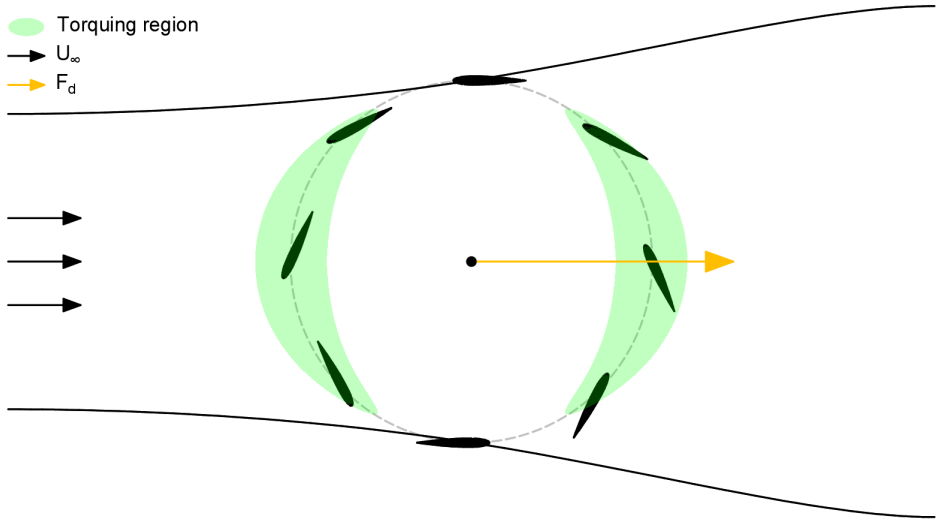

Figure 3.28: VAWT energy harvesting mode

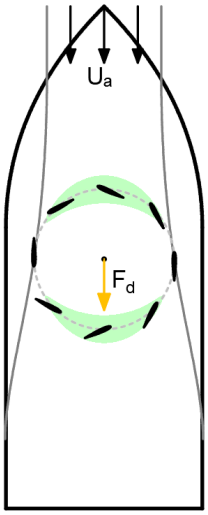

Figure 3.29: VAWT on a ship in a headwind

Headwind conditions often result in larger apparent wind speeds. This enables more power to be extracted however also increases the turbine drag ($F_{d,turbine}$) which can acts as a negative thrust force (F_{thrust}) in apparent headwind conditions. From Equation 2.1 the thrust force can be written as Equation 3.21 over the entire range of $\beta_a = 0 - 360[°]$. This results in a negative thrust for headwind conditions.

$$C_{t,turbine} = C_{l,turbine} sin(\beta_a) - C_{d,turbine} cos(\beta_a) \tag{3.21}$$

The generated power should be greater than the power required to overcome the negative thrust. For instance, if the true wind speed is zero but the ship is in transit, energy can still be extracted from the apparent wind due to the ship's speed. However, this is not efficient as this provides a negative thrust that cannot be compensated by the generated power and therefore reduces the total propulsion efficiency, as no net propulsion benefit can be obtained from the VAWT system.

$$C_P \frac{1}{2} \rho A U_a^3 > -\frac{\rho A C_{t,turbine} U_a^2}{2\eta_D} U_s \tag{3.22}$$

Equation 3.22 can be rewritten as Equation 3.24 to show the condition which has to be satisfied in order to effectively provide propulsive power to the ship. This all depends on the efficiency of the main drive, which is to be set to $\eta_D = 0.7$, as specified by the MEPC guidelines [8].

$$P_{t,eq,turbine} = C_P \frac{1}{2} \rho A U_a^3 + \frac{\rho A C_{t,turbine} U_a^2}{2\eta_D} U_s > 0 \tag{3.23}$$

$$C_P U_a + \frac{C_{t,turbine}}{\eta_D} U_s > 0 \tag{3.24}$$

This shows that the effectiveness of power generation for propulsion depends on the turbine power and drag performance and the difference between the ship speed and the apparent wind conditions. Figure 3.2 shows $C_{t,turbine} > C_P$. Therefore, in the case of a straight headwind ($cos(\beta_a) = 1$), the use of a wind turbine is only effective if the apparent wind speed is sufficiently larger than the ship speed (U_s), this also depends on the apparent wind direction as this influences $C_{t,turbine}$. It is suggested by Bose [4] that high-speed boats in low-speed wind conditions probably perform better with sail systems. It is questionable if this is the case for the statistic wind conditions of high-speed ships as these conditions frequently result in a headwind for which sail systems cannot be used.

3.7 VAWT as a thruster

A cyclorotor can either be used as a VAWT to generate power or to produce thrust. The more effective operational mode when the ship is in transit at sea depends on the wind conditions and the ship's speed.

3.7.1 Cyclogyros

The idea of creating lift using blades parallel to the axis of rotation with pitch variation is as old as 1909 by Samoljot [77]. This concept is known as a cyclogyro. Cyclogyros are already applied in many different applications and concepts [85]. One of the earliest attempted flight machines featured cyclogyros. These concepts could provide Vertical Take-Off and Landing (VTOL) possibilities however these early concepts were not deemed to work.
The Voith-Schneider ship propeller is also a cyclogyro propulsor that is used for maneuverable ships to be able to quickly change the thrust force direction. These ships do not require a rudder to steer as the pitch variation of the cyclogyro can be used to generate a side force. One of the most recent applications is the use in drones whereby cyclogyros allow for forward or backward acceleration without pitching the drone.
Sometimes the turbine is free running and sometimes the turbine is powered to be able to produce larger forces. The solidity of powered cyclogyros is often larger compared to free-running cyclogyros and VAWTs.

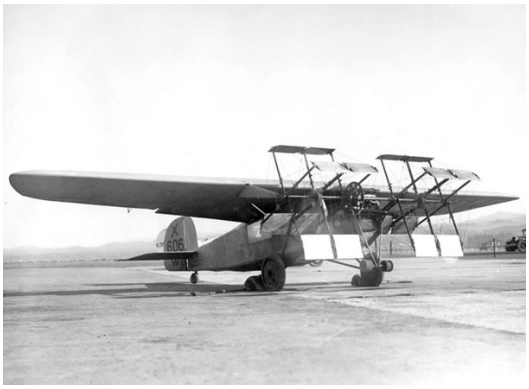

Figure 3.30: Schroeder S1 Cyclogyro (1930), from Schwaiger [75]

Figure 3.31: Rohrbach cyclogyro (1933), from MSW [64]

Figure 3.32: Voith-Schneider propellers on a ferry, from Forns et al. [35]

Figure 3.33: Quadcopter drone with cyclorotors, from Wikimedia [82]

3.7.2 Wind assisted ship propulsion

All WASP systems mentioned in section 2.2 use lift to provide the thrust force. The cyclorotor concept can also be used as a lifting device when the pitch variation of a VAWT is phase shifted such that the advancing and retreating sides are loaded as shown in Figure 3.35.

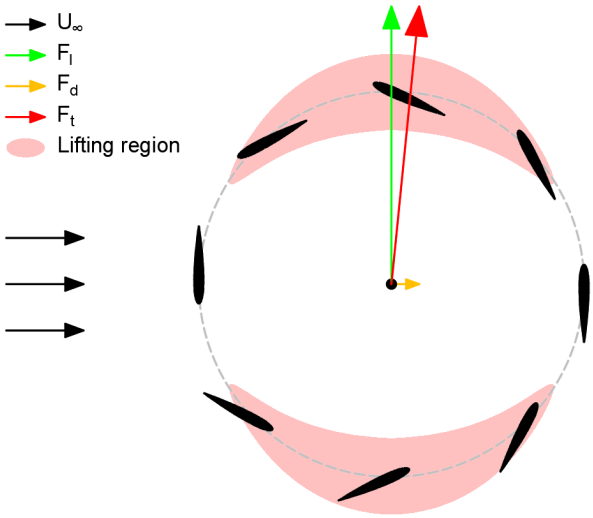

Figure 3.34: Cyclogyro lifting

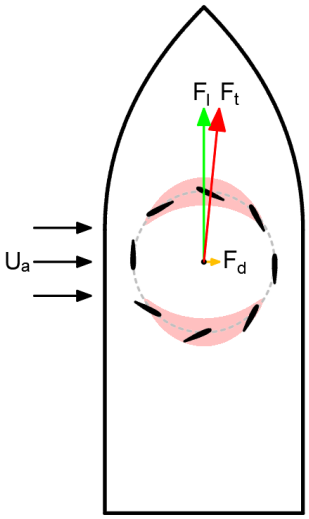

Figure 3.35: Cyclogyro on a ship in a beamwind

As described in subsection 2.4.4, it can be difficult to predict the local wind direction due to the complex flow around the ship structure. This makes it difficult to prescribe the correct angle of attack in the WASP control system.
Sailing systems as described in subsection 2.2.1 are sensitive to the correct angle of attack setting for the local wind conditions as experienced by the propulsion system. An overestimation of the angle of attack can lead to stall which is detrimental to the lift force and increases the drag force. An underestimation does not allow the full potential of the sailing system to be used.
The VAWT system can change the direction of the total force vector by phase shifting the pitch variation. This phase shift is equivalent to a change in the angle of attack. Therefore the VAWT can be less sensitive to the correct estimation of the local angle of attack.
Onboard ships, it can be difficult to accurately measure the local wind direction as this is influenced by flow disturbances by the ship and possible interaction with other wind propulsion systems as investigated by Borren [3]. Therefore it is advantageous that the VAWT system is less sensitive to the correct pitch phase setting as this can be difficult to determine. It is also favorable that pitch variation does not result in sudden stall which is a problem for wing-like WASP systems as these are generally operated near the maximum lift

coefficient. Therefore the wind direction measurement system does not have to be as precise for a VAWT as for a wing-like WASP system.

The direction of the force produced by a VAWT depends on the pitch variation pattern. A VAWT can generate a force without any apparent wind when the turbine is driven. This allows for larger forces to be generated however also requires additional power to operate the turbine which reduces the effective equivalent propulsion power.
When the apparent wind direction is such that the lift force from a VAWT can be used to generate thrust, this mode might be more efficient than producing power as a VAWT. To select what operational mode is most effective, the equivalent power should be compared for different modes of operation.
The equivalent power is defined as the power required from the engine to provide the same thrusting power. This difference is due to the efficiency of the main drive(s) (η_D) such as the propeller efficiency. This method is defined in the MEPC guideline [8].
For the VAWT, the equivalent power is assumed to be equal to the power provided by the turbine. This means electrical losses from the generator and the motors are neglected because these losses are considered to be small.
In driven thruster VAWT mode, it requires power to operate the cyclorotor. This power (P_r) should be subtracted from the equivalent propulsion power.

When a thrusting VAWT is subjected to a flow, the pitch variation can be adjusted such that the upwind and downwind sides operate as a turbine, and the advancing and retreating sides operate to provide a lift force. When the total torque on the rotation axis is zero, the turbine is free running. In this free running VAWT thruster mode, the required rotation power is to be set to $P_r = 0$. This might be a delicate balance to find the exact pitch variation to balance the rotation, therefore the generator can be used as a motor to prescribe the required TSR.

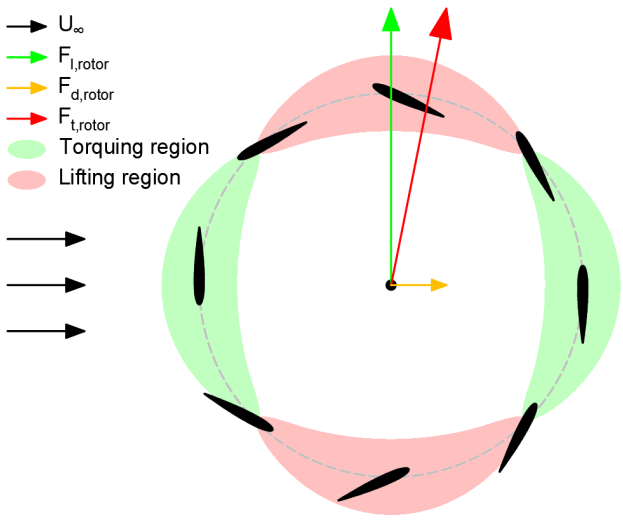

Figure 3.36: Free running clogyro

The equivalent thrust power in thrusting VAWT mode is expressed as Equation 3.25. It is more effective to use the cyclorotor as a VAWT thruster if $P_{t,eq,thruster} > P_{t,eq,turbine}$.

$$P_{t,eq,thruster} = \frac{\rho_{air} A C_{t,turbine} U_a^2}{2\eta_D} U_s - P_r \tag{3.25}$$

Chapter 4

Modeling

Modeling is a way to evaluate the performance and characteristics of a VAWT without actually building and testing many different turbines. The major benefit of modeling over model testing is the possibility to quickly investigate many different configurations. This allows for easier performance evaluation and variation of design and operational parameters to evaluate the performance sensitivities and optimization of the design. Models can be used to investigate performance characteristics which can be used to provide a better understanding of the working principles.
Usually, in aerodynamics, the structures are static or experience small deformations however for VAWTs, the blades rotate which introduces additional dynamic effects and interactions which can be difficult to capture using a model. As stated by Anderson and encountered by Newton, "the analysis of fluid flow is conceptually more difficult than the dynamics of solid bodies" [47, p. 6]. It is important to assess the characteristics of different models and the operational range for which these models provide valid results. For aerodynamic models, the validity depends on the flow regime and the ability to capture influential aerodynamic phenomena as discussed in section 3.4. The model should be able to predict the performance of such a turbine.

4.1 Flow Regime

When models are used to describe physical phenomena, the models are often accurate for a limited range of conditions. Therefore the flow regime should be defined.
As described in subsection 2.4.4 this study considers uniform inflow conditions.
The air density of the undisturbed air is mainly influenced by the air temperature and pressure, humidity can also influence the air density. These properties vary around the world however for simplicity, the air density is assumed to be constant at $\rho = 1.225[kg/m^3]$ as determined by the International Standard Atmosphere (ISA) at mean sea level [7].
The flow over the turbine blades is considered to be incompressible. This is accurate for flows at low Mach number $M < 0.3$ where the isentropic density variation is below 5% as stated by Anderson [47, p. 64, 572].
The Reynolds number (Re) indicates the ratio of inertial forces with respect to viscous forces. Reynolds number effects depend on the size of the turbine and the flow velocity. This can influence the turbine performance as the lift and drag polars are influenced by the Reynolds number of the blades. Different VAWT studies use different definitions for the Reynolds number. This study follows the definition as used by Ferreira [42, p. 83] where the Reynolds number on the blades is defined as Equation 4.1 and the turbine Reynolds number is defined as Equation 4.2. ν is the kinematic viscosity. This study considers Reynolds numbers of the blades from $Re = 1e5$ to $Re = 5e6$. The polar can change substantially within this range therefore the effect of the Reynolds number should be modeled.

$$Re = \frac{c\lambda U_a}{\nu} \tag{4.1}$$

$$Re_D = \frac{DU_a}{\nu} \tag{4.2}$$

4.2 Model descriptions

Many modeling methods for VAWTs have been developed. Every model has benefits and downsides. Models can provide steady or time-varying results. Unsteady models use time-varying results at different azimuthal angles. As stated by Ferreira [15], there can be a noticeable difference between the results of different VAWT models.
This study also investigated the possibility of VAWT used as a thruster to provide propulsion. These turbines can be more heavily loaded compared to VAWTs. The model should therefore be valid for these heavily loaded flow conditions. As described in subsection 3.7.1, cyclogyros generally have a larger solidity and a larger c/R ratio. Therefore the flow curvature effect is more important.
In VAWTs the airfoils are relatively spaced out such that the blade interaction of the bound vorticity is not the most important. However, because the blades operate upwind as well as downwind, the shed vorticity of the upwind blades is convected downwind and can influence the flow conditions on the downwind section of the turbine. Even if the upwind blades are not operating in a stalled condition, the disturbance in the wake can be substantial and must be captured to accurately model the instantaneous blade forces.
Three main modeling categories which could be suitable for modeling the performance of a VAWT are described.

4.2.1 Momentum models

Momentum models consider the turbine as an actuator surface to which loads are applied, similar to the theory described in subsection 3.1.1. The loading of the actuator surface is related to the average blade loading at this location. Therefore the flow solution of these models is steady and no instantaneous results are provided. The steady solution is obtained iteratively to find a balance between the surface loading and the flow field. The loads are obtained using Blade Element Momentum (BEM) theory. These methods do not model the blades, rather they simulate the loading on the blade section. These models can be used for 2D and 3D flows. These are low-fidelity models however these models are computationally inexpensive.

4.2.1.1 Double multiple streamtube model

The Double Multiple StreamTube (DMST) model is widely used in literature. This model discretized the VAWT in upwind and downwind actuator surfaces. According to Ferreira [15] this model does incorrectly assume the upwind streamtube to be fully expanded before the downwind actuator surface. This intuitively makes sense because the turbine diameter is small compared to the length required to fully expand the upwind streamtube. This model therefore tends to tends to overestimate the performance on the upwind side and underestimate the performance on the downwind side. This model also neglects the influence of the downwind side on the upwind side.

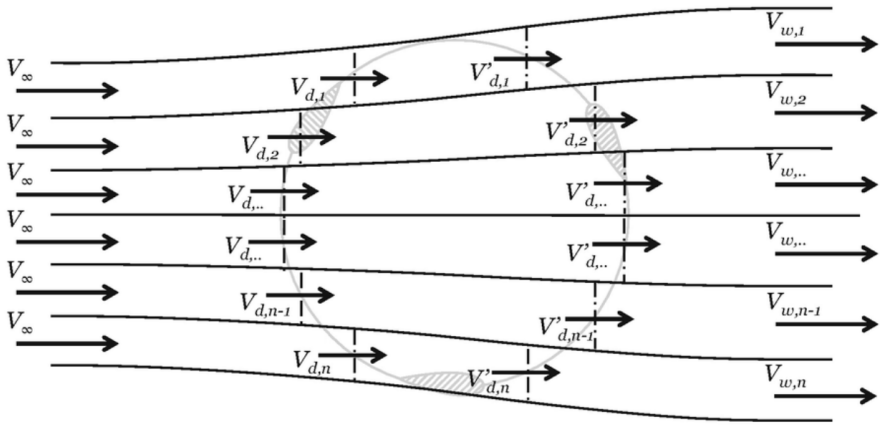

Figure 4.1: Schematic DMST model, from De Tavernier [81, Fig. 6]

4.2.1.2 Actuator cylinder model

The actuator cylinder model is developed by Madsen [60]. This model considers the actuator surface to be shaped as a cylinder covering the circumference of the turbine. This can be represented in 2D and 3D simulations. This model is found by Ferreira [15] to be more accurate compared to the DMST model because the actuator cylinder considers interactions between different upwind and downwind elements and streamtubes.

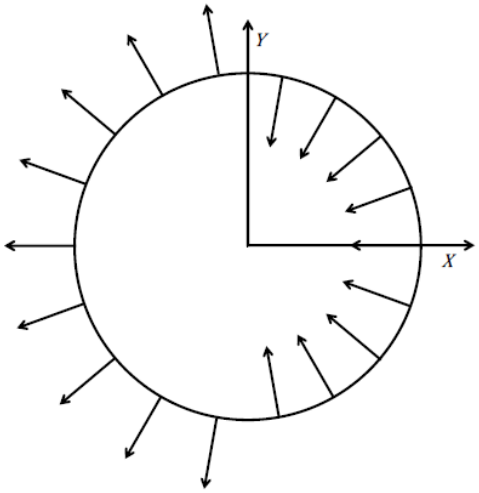

Figure 4.2: Schematic 2D actuator cylinder, from De Tavernier [80]

4.2.2 Potential flow models

Potential flow models use lines of vorticity to shape the flow field. These models are described by Katz [53]. Because the flow is considered incompressible, potential flow can be used to model the flow around a VAWT. Potential flow is incompressible and irrotational and does not capture viscous flow effects. Therefore these effects should be modeled to increase the model accuracy. Potential flow methods can be used for 2D and 3D models. Potential flow models can be used to model unsteady flows and therefore can provide instantaneous results. Therefore these models use temporal discretization to model the performance over the rotation. These models shed vorticity which is convected to form a free wake. Therefore these models include interaction between the blades and the wake of the blades.

4.2.2.1 Lifting line model

Airfoils carrying an aerodynamic loading can be modeled using Prandtl lifting-line theory. This is a model which condenses the airfoil to a single bound vortex. The strength of this vortex is determined using airfoil polars.
Various effects such as viscous effects, dynamic stall, and flow curvature effects can be included in this model by modifying the force polars.
The flow curvature effect is not directly captured by this model. Li [59, p. 91-110] has studied this effect and explains methods on how to incorporate this in the models. Often this effect is modeled using a virtual airfoil with additional virtual camber and a virtual angle of incidence as explained in subsection 3.4.2. This is often modeled using conformal mapping of the airfoil geometry. Because these effects change over the rotation, this would require the evaluation of the virtual airfoil properties at every azimuthal location over the rotation. This is computationally expensive and therefore undesirable for optimization purposes. Li proposed an alternative method of evaluating the angle of attack at the three-quarter chord point. This method still requires the lift force to be applied perpendicular to the angle of attack at the quarter chord point.
The Cactus model is an example of a 3D lifting line model. Deglaire [37] used a vortex model to evaluate the flow around a 2D VAWT.

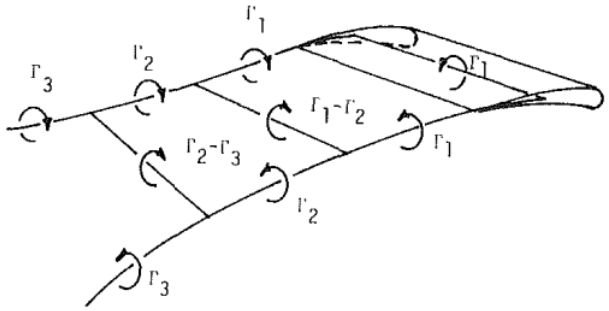

Figure 4.3: Schematic lifting line model, from Strickland [28]

4.2.2.2 Lifting surface model

The lifting line model can be expanded to a lifting surface model whereby this model discretizes the actual airfoil geometry as a flat surface on the camber line. This is also known as a vortex lattice model. This surface contains bound vortices to discretize the airfoil surface. The strength of these bound vortices is such that the collocation point is impermeable. This model neglects the thickness of the airfoil, therefore this model is more suitable for thin airfoils. Because this model contains the camber line geometry, some flow curvature effects are incorporated. This model is somewhat more computationally expansive compared to the lifting line model because the lifting surface is more detailed however the shed wake is similar. This method is used for the analyses of a cyclogyro by Yu [27].

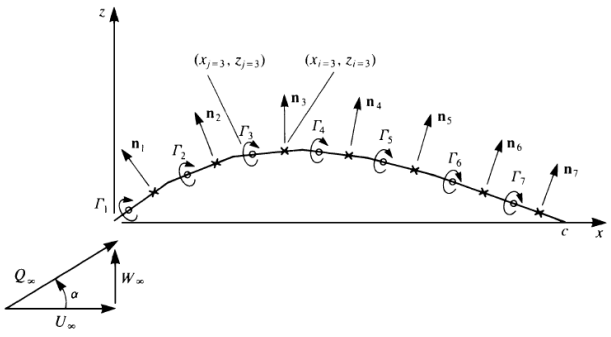

Figure 4.4: 2D lifting surface model, from Katz [53]

4.2.2.3 Panel model

Potential flow methods can discretize the airfoil surface

A panel model is an expansion of the lifting surface model. This model discreteness the actual airfoil geometry such that the thickness is also modeled. The flow curvature effect is implicitly incorporated in this model. This model is somewhat more computationally expansive compared to the lifting line and lifting surface models because the lifting surface is even more detailed however the shed wake is similar. The U2DiVA model as described by Ferreira [15] is an example of such a model.

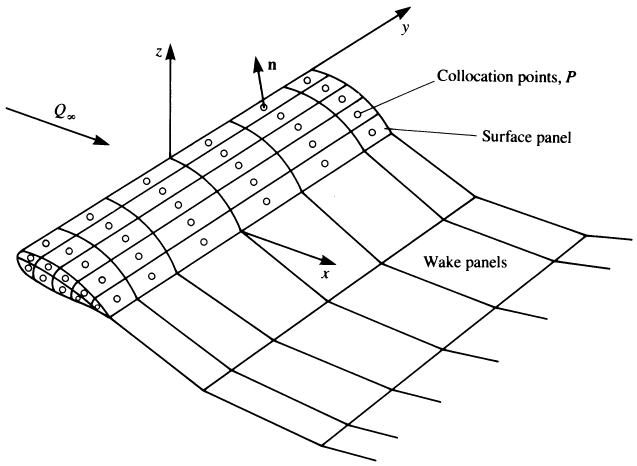

Figure 4.5: Schematic panel model, from Katz [53]

4.2.3 Computational fluid dynamics

CFD is a high fidelity modeling method to numerically solve the Navier-Stokes equations which describe the motions of viscous fluids. This method uses spatial discretization of the fluid volume and therefore requires grids. Because of the rotating blades, CFD simulations can use sliding grids around the turbine as described by Elkhoury [34]. To capture unsteady effects, this method would also require temporal discretization. CFD simulations are often used for the analyses of cyclorotors used for lifting or thrusting as found in multiple studies [32] [69] [16] [22] [70].

4.3 Finite blade length

All flows are fundamentally 3D however these flows are computationally more expensive to analyze, therefore 2D flows are often used to reduce the required computational cost. As noted by Flandro [23, p. 112], 2D results can provide considerable value.
For 3D turbines with finite span, the bound circulation varies over the span. For a constant, non-twisted blade section, this variation is largest at the tips where the pressure difference cannot be sustained and trailing tip vortices are shed into the wake. These tip vortices have a downwash effect resulting in a loss in lift near the tip regions. This is known as the downwash effect [43]. Because this only affects the tip regions, the influence of this effect depends on the aspect ratio. This also influences the gradient of the lift curve. These losses need to be included in the model and can be modeled using Equation 4.4 from [43]. This downwash effect correction reduces the required computational time and enables the use of 2D models for optimization.

$$AR = \frac{H}{c} \tag{4.3}$$

$$C_L = \frac{C_l}{1 + \frac{C_l}{\pi AR}} \tag{4.4}$$

The vortices at the wingtips cause induced drag when the wing produces a lift force. This effect can be predicted using an analytic formula which depends on the aspect ratio (AR) and an efficiency factor (e) [44] [47, p. 440]. This efficiency factor is 1 for an elliptic load distribution.

$$C_D = C_d + \frac{{C_L}^2}{\pi \cdot AR \cdot e} \tag{4.5}$$

4.4 Model selection

Model selection is often subjective as different performance aspects of different models can be hard to quantify. To select a suitable aerodynamic model, qualitative model properties are compared using an Analytic Hierarchy Process (AHP). AHP is an Multiple Attribute Decision Making (MADM) method developed by Saaty [73] and explained by Kana [52]. This method can be used for comparison, quantification, and selection. It can therefore be used to select the appropriate aerodynamic modeling method for this study.

4.4.1 Focus matrix

The focus matrix is used to quantify the requirements of the model and to provide a ranking of the importance of different model properties. This is done by pairwise comparison of the properties of one model to another model based on a 9-point scoring system as defined in Table 4.1.

Table 4.1: Fundamental AHP scale, from Saaty [73]

Intensity	Definition	Explanation
1	Equal importance	Two activities contribute equally to the objective
3	Moderate importance of one over another	Experience and judgment weakly favor one activity over another
5	Essential or strong importance	Experience and judgment strongly favor one activity over another
7	Very strong importance	An activity is strongly favored and its dominance demonstrated in practice
9	Extreme importance	The evidence favoring one activity over another is of the highest possible order of affirmation
2,4,6,8	Intermediate values between the two adjacent judgments	When compromise is needed

The comparison of models focuses on 3 general properties. The first property is accuracy. This property is based on the ability to model influential and unsteady aerodynamic effects such as flow curvature effect, blade interaction, viscous effects (flow separation, boundary layer centrifugal effect), and unsteady effects (step responses, dynamic stall). This accuracy focuses on cases including highly loaded turbines.
The second property is recognition. This is based on how often a model type is used in academic literature for VAWTs as well as heavily loaded rotors such as cyclogyros.
The last property is computational cost. This is based on the time required to run a single simulation. For optimization studies, it is important to be able to run sufficient simulations to map the design space.

The scoring system in the focus matrix is used to indicate how the property in the first column is preferred over the property in the first row. If the property in the first column property is not favored in preference to the property in the first row, the reciprocal of the intensity is put in the matrix. Therefore the entire focus matrix is reciprocal. The filled-in matrix is shown in Table 4.2, for instance, this matrix indicates with the value 5 that computational cost has a strong importance over recognition.

Table 4.2: Focus matrix

Focus	Accuracy	Recognition	Computational cost
Accuracy	1	3	1
Recognition	1/3	1	1/5
Computational cost	1	5	1

4.4.2 Consistency

The comparison matrices should be cardinally-consistent. This means if $A > B$ and $B > C$, then $A > C$ should be true. For a cardinally-consistent matrix, the largest eigenvalue (λ_1) of the matrix should be equal

to the size of the matrix (n). The focus matrix Table 4.2 is not cardinally-consistent, $\lambda_1 = 3.029 \neq n = 3$. To determine if the matrix is sufficiently consistent, the Consistency Index (CI) is evaluated. For the focus matrix, $CI = 0.01453$.

$$CI = \frac{\lambda_1 - n}{n - 1} \tag{4.6}$$

The consistency can be checked based on the Consistency Ratio (CR). This ratio should be smaller than 0.1 to indicate that the consistency should be 10 times better than the random index. This compares the consistency to a Random Index (RI). RI depends on the size of the comparison matrix, for a matrix with $n = 3$, $RI = 0.58$ as is shown in Table 4.3. This results in $CR = 0.02505 < 0.1$. Therefore the focus matrix is considered to be consistent and can be used for the model comparison.

Table 4.3: Random consistency index, from Saaty [73]

n	1	2	3	4	5	6	7	8	9	10
RI	0	0	0.58	0.90	1.12	1.24	1.32	1.41	1.45	1.49

$$CR = \frac{CI}{RI} \tag{4.7}$$

4.4.3 Criteria weights

The normalized principal eigenvector associated with the largest eigenvalue (v) is used to indicate the weights of certain selection criteria. This is called the priority vector. The sum of this vector is always 1. This is used to quantify the relative performance of different models.

$$v_{focus} = \begin{bmatrix} 0.4054 \\ 0.1140 \\ 0.4806 \end{bmatrix} \begin{matrix} \leftarrow \textit{Accuracy} \\ \leftarrow \textit{Recognition} \\ \leftarrow \textit{Computational cost} \end{matrix} \tag{4.8}$$

For this case, accuracy and computational cost are both considered strongly more important than recognition and computational cost is slightly more important than accuracy. Therefore in the selection process, the computational cost is the most important focus in the model selection and is weighted $\frac{0.4806}{0.4054} = 1.186 \widehat{=} 18.6\%$ more compared to model accuracy.

4.4.4 Local priority matrices

The procedure as previously explained in subsection 4.4.1 to subsection 4.4.2. Is also used to construct priority matrices to compare different models for specific focuses. A comparison matrix is provided for each focus based on the properties of the specific models.
This selection only considers 2D models to limit the required computational cost as this is an important selection criterium and 2D results can still provide insight for the comparison of different turbine configurations and optimization.
The actuator cylinder, lifting line, panel model, and CFD are compared as these are common models which have been found in literature.

4.4.4.1 Accuracy

CFD and the panel method are considered less accurate because these methods depend on the accuracy of the simulation to evaluate the loading on the blades. Especially the onset of stall and the loading when stalled are difficult to accurately simulate. The panel method is considered the least accurate because this model does not capture stall if the flow is modeled to be attached to the surface. The lifting line and actuator cylinder methods use experimental polars, these are considered more accurate than the loading resulting from simulations. The actuator cylinder model is considered to be less accurate than the lifting line method because the actuator cylinder is less capable of modeling highly loaded turbines which is required for this study.

Table 4.4: Accuracy comparison matrix, $n = 4$, $\lambda_1 = 4.077$, $CI = 0.03899$, $CR = 0.06723 < 0.1$

Accuracy	Actuator cylinder	Lifting line	Panel model	CFD
Actuator cylinder	1	1/3	5	3
Lifting line	3	1	7	5
Panel model	1/5	1/7	1	1/3
CFD	1/3	1/5	3	1

$$v_{accuracy} = \begin{bmatrix} 0.2622 \\ 0.5650 \\ 0.05529 \\ 0.1175 \end{bmatrix} \begin{matrix} \leftarrow Actuator\ cylinder \\ \leftarrow Lifting\ line \\ \leftarrow Panel\ model \\ \leftarrow CFD \end{matrix} \tag{4.9}$$

4.4.4.2 Recognition

The CFD models are found to be the most recognized because almost all cyclogyro studies use CFD models with one exception for a lifting line model. Therefore this model scores second highest. The actuator cylinder and panel method are both not used for heavily loaded turbines but because the actuator cylinder is common for VAWTs it does score better than the panel method.

Table 4.5: Recognition comparison matrix, $n = 4$, $\lambda_1 = 4.117$, $CI = 0.03899$, $CR = 0.06723 < 0.1$

Recognition	Actuator cylinder	Lifting line	Panel model	CFD
Actuator cylinder	1	1/3	3	1/5
Lifting line	3	1	5	1/3
Panel model	1/3	1/5	1	1/7
CFD	5	3	7	1

$$v_{recognition} = \begin{bmatrix} 0.1175 \\ 0.2622 \\ 0.05529 \\ 0.5650 \end{bmatrix} \begin{matrix} \leftarrow Actuator\ cylinder \\ \leftarrow Lifting\ line \\ \leftarrow Panel\ model \\ \leftarrow CFD \end{matrix} \tag{4.10}$$

4.4.4.3 Computational cost

The actuator cylinder requires the least computational time and scores best. The lifting line method is slightly less computationally expensive than the panel method and CFD scores worst because these unsteady simulations require the most computational time.

Table 4.6: Computational cost comparison matrix, $n = 4$, $\lambda_1 = 4.093$, $CI = 0.03110$, $CR = 0.05361 < 0.1$

Computational cost	Actuator cylinder	Lifting line	Panel model	CFD
Actuator cylinder	1	2	3	9
Lifting line	1/2	1	2	7
Panel model	1/3	1/2	1	7
CFD	1/9	1/7	1/7	1

$$v_{cost} = \begin{bmatrix} 0.4837 \\ 0.2889 \\ 0.1880 \\ 0.03940 \end{bmatrix} \begin{matrix} \leftarrow Actuator\ cylinder \\ \leftarrow Lifting\ line \\ \leftarrow Panel\ model \\ \leftarrow CFD \end{matrix} \tag{4.11}$$

4.4.5 Selection

The normalized principal eigenvectors associated with the largest eigenvalues of the local priority matrices are merged into one local priorities matrix. This matrix is multiplied with the priority vector to obtain the weighted results for the different modeling methods.
The lifting line model is found to be the most suitable method based on combined performance. The actuator cylinder is the second most suitable method. This performance is based on the computational cost which is best for this model.

$$[v_{accuracy} \quad v_{recognition} \quad v_{cost}] \cdot v_{focus} = \begin{bmatrix} 0.3522 \\ 0.3978 \\ 0.1191 \\ 0.1310 \end{bmatrix} \begin{matrix} \leftarrow Actuator\ cylinder \\ \leftarrow Lifting\ line \\ \leftarrow Panel\ model \\ \leftarrow CFD \end{matrix} \tag{4.12}$$

4.5 Vortex model description

This section describes the implementation of a 2D free wake vortex model used to evaluate the instantaneous and unsteady turbine loading and performance. This model describes the flow field around counter-clockwise rotating turbine designs. The output of this model is used for the design optimization algorithm. The resulting optimum designs are only optimal within the scope of the used model and method this optimum may therefore vary depending on the model describing the performance as stated by Papalambros [67, p. 1]

4.5.1 Variable geometry description

The model has many settings which can change the evaluated VAWT configuration and operating conditions. The parameters of the pitch amplitude (A_{θ_p}), the TSR (normalized ω), the solidity and the pitch phase (θ_p) are used to optimize the design. The number of blades is also a variable input of the model. The variable dimension parameters are shown in Figure 4.6.

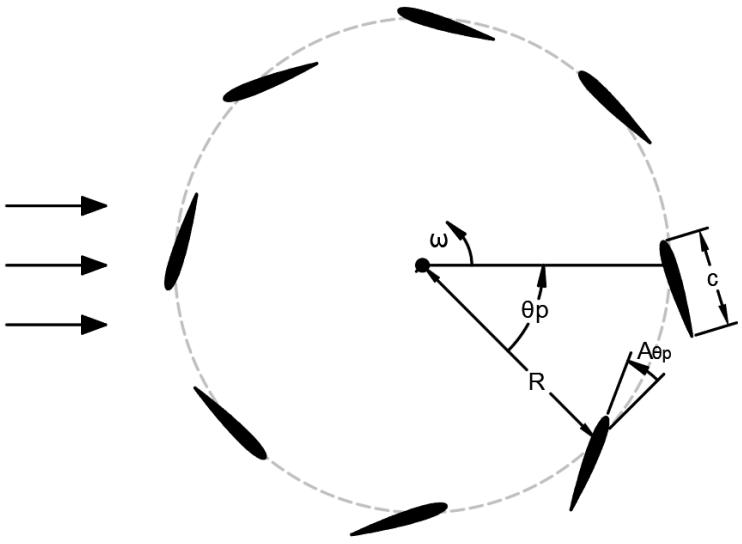

Figure 4.6: Variable design and operational parameters, sinusoidal pitch variation at an amplitude of $A_{\theta_p} = 24[°]$ and a pitch phase of $\theta_p = 45[°]$

4.5.2 Flow diagram

The vortex model is implemented in the Programming language Python, version 3.8.5. The basic working principles of this model are summarized in a schematic flow diagram in figure Figure 4.7. The model uses time-step iterations to develop a quasi-steady, periodically oscillating flow field, and to provide the instantaneous and integral performance parameters such as C_d, C_l, and C_P.

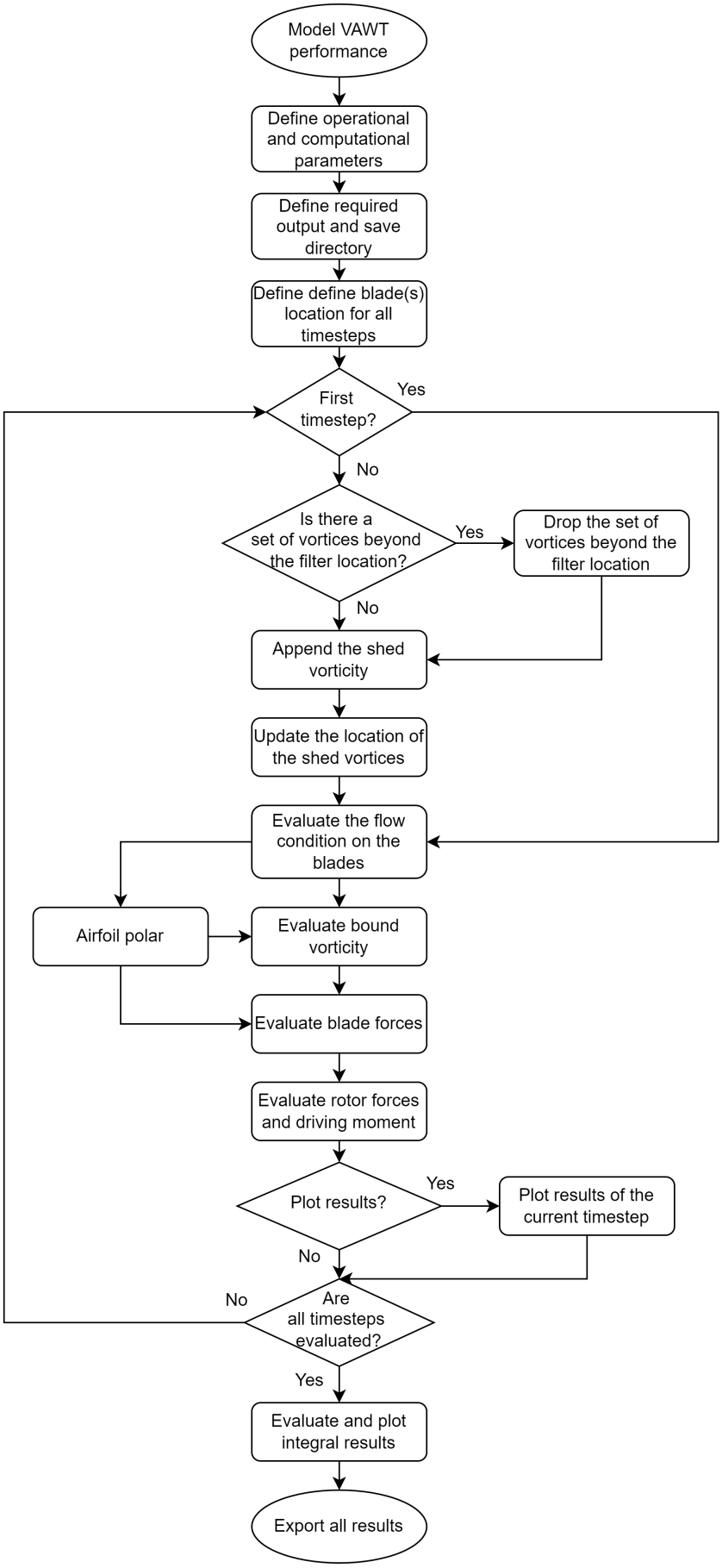

Figure 4.7: Flow diagram of the lifting line vortex model

4.5.3 Lifting line

The vortex model is based on the lifting line theory whereby the lift of an airfoil is proportional to the bound circulation. This bound circulation is determined based on the local flow conditions as experienced by a blade at the quarter chord position and the blade polar which results in the lift. Lifting line theory is used to evaluate the vortex properties which make up the flow field. This theory describes each blade of the VAWT as a single bound vortex for which the strength depends on the flow conditions and the airfoil polar.
The model is unsteady such that instantaneous properties can be evaluated. The influence of step responses as described in subsection 3.5.1 is captured by the vortex model. This is an important effect for modeling the continuous variation in operational conditions over the rotation.
Circulation is conserved as stated by Kelvin's circulation theorem which is explained by Katz [53, p. 25-26]. Therefore every time step, each blade sheds vorticity in its wake with a strength opposite to the change in bound vorticity. This model sheds the trailing vortices at the trailing edge location. Dissipation of the vortex strength is neglected by this model. The bound vorticity in the first time step is generally of substantial strength, therefore the first shed vortex is also substantially strong with an opposite strength. This is the starting vortex. To model a free wake, the influence of all vortices is combined to update the locations of the shed vortices for the next time step.

4.5.4 Vortex description

The vortex model uses the linear summation of the far field wind speed in combination with the summation of the influence from discrete vortices to describe the flow conditions at a specific location.
A vortex induces tangential velocities around the vortex core. This influence decreases inversely proportional with increasing distance from the vortex core as described by Katz and Plotkin [53, fig. 2.11]. r is the Euclidean distance between the vortex core and the position where the flow condition is evaluated as shown in Equation 4.13.

Because the induced velocity magnitude approaches infinity near the location of the vortex core, the induced velocities in a region near the core of the vortex is modeled as a circular rotating rigid body, with increasing velocity away from the core. This method is described by Katz and Plotkin [53, p. 34-35].
The velocities induced by a vortex depend on the strength of the vortex and the distance from the vortex. To reduce computational time, the velocity induced by a vortex is set to zero if the induced velocity is below a specified threshold value with respect to the far-field wind speed.

$$r^2 = (x - x_{vortex})^2 + (y - y_{vortex})^2 \tag{4.13}$$

$$\overrightarrow{U} = \begin{bmatrix} U_x \\ U_y \end{bmatrix} = \begin{cases} [0,0]^T & \text{if } \frac{\Gamma^2}{4\pi^2 r^2} < {U_{induced\,min}}^2 \\ \frac{\Gamma}{2\pi {R_{vortex\,core}}^2} \begin{bmatrix} 0 & -1 \\ 1 & 0 \end{bmatrix} \cdot \begin{bmatrix} x - x_{vortex} \\ y - y_{vortex} \end{bmatrix} & \text{if } r^2 < {R_{vortex\,core}}^2 \\ \frac{\Gamma}{2\pi r^2} \begin{bmatrix} 0 & -1 \\ 1 & 0 \end{bmatrix} \cdot \begin{bmatrix} x - x_{vortex} \\ y - y_{vortex} \end{bmatrix} & \text{otherwise} \end{cases} \tag{4.14}$$

The influence of the vortex, therefore, depends on the distance from the vortex and the magnitude of the induced velocity. This is shown in Figure 4.8.

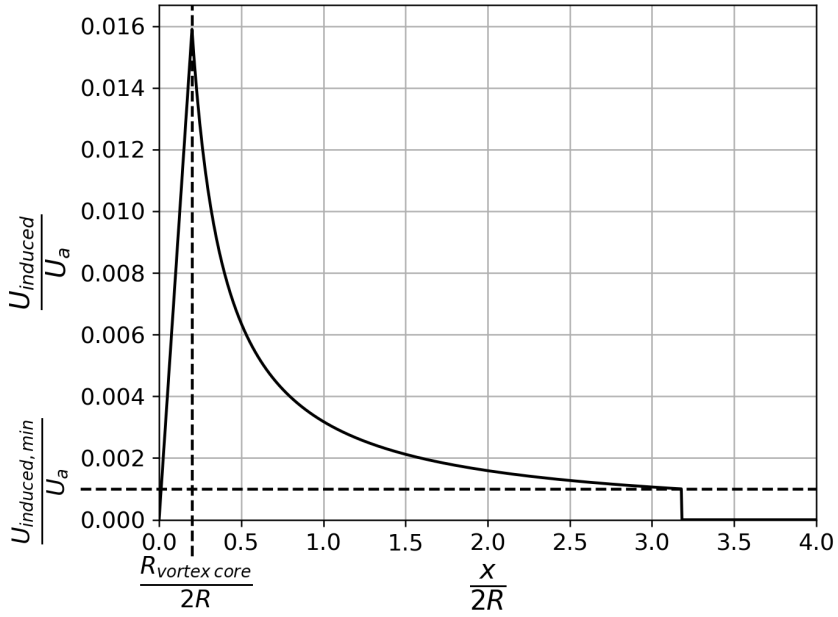

Figure 4.8: Vortex induced velocities at different distances from the vortex core

Counterclockwise vortices are defined by a positive vortex strength and are shown in green. Clockwise vortices have a negative vortex strength and are shown in red. The size of the vortices indicates their strength. This strength is constant over time and therefore no viscous dissipation is included in the model. The strength of the shed vortices indicates the change in bound circulation. As shown in Figure 4.13 this change is strongest around the change between the upwind and downwind sides. This agrees with the findings of subsection 3.4.3.

This method is used to evaluate the flow conditions at the locations of the turbine blades and to evaluate the velocity of the vortices such that the free wake propagation of all vortices can be evaluated. The model uses temporal discretization for an unsteady model which uses the velocity at the vortex locations to update the vortex positions at the next time step as illustrated by Figure 4.9. Because the vortices only induce tangential velocities, the distance between these vortices would remain the same. However, due to temporal discretization, the updated location of the vortices increases over time.

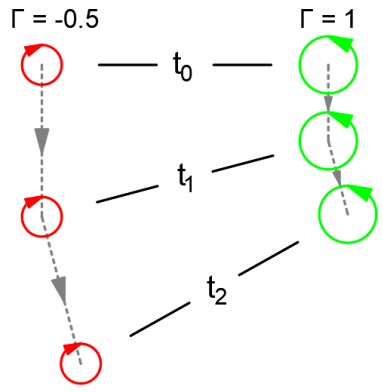

Figure 4.9: Interaction between two vortices over 3 time steps

4.5.5 Airfoil polar

The forces generated by a specific airfoil section depend on the flow conditions. These forces are normalized by the dynamic pressure and the reference blade length to obtain the 2D force coefficients. These coefficients depend on the angle of attack and the Reynolds number experienced by the airfoil. This is expressed in

airfoil polars. This research uses the airfoil polars of a NACA0015 airfoil of which the section is shown in Figure 4.10.

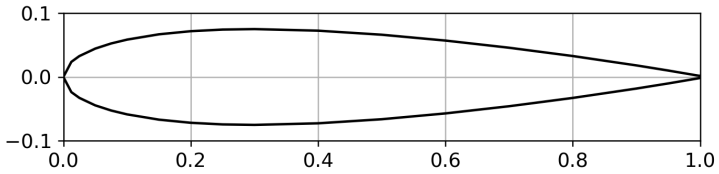

Figure 4.10: NACA 0015 geometry from Airfoil Tools [84]

Because the local Reynolds number and angle of attack change over the rotation, this has to be specified for the specific conditions. Therefore bilinear interpolation between the airfoil polars from Sheldahl [78] is used to find the corresponding lift and drag coefficients for the specific angle of attack Reynolds number. This report presents airfoil polar data for multiple symmetric airfoil sections including the NACA 0015 obtained using wind tunnel tests. This model is tested for a range of Reynolds numbers from 0.35e6 to 0.7e6 and angles of attack up to 180 degrees. These results are extrapolated using a model to include Reynolds numbers between 1e4 and 1e7. As stated by Sheldahl [78, p. 9], "The section data requirements for application to vertical axis wind turbines are broader in scope than are those the aircraft industry usually concerns itself with". Some stall properties of the blades are included in the model by means of the polars which result in increasing drag and reducing lift after the stall angle.

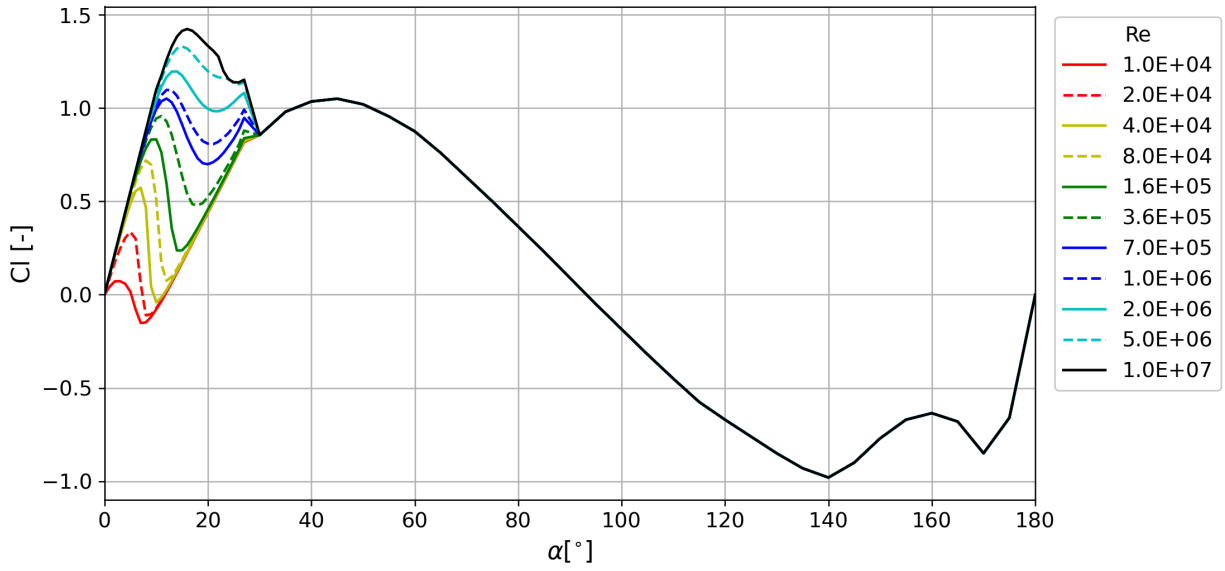

Figure 4.11: Lift polars for NACA 0015, from Sheldahl [78]

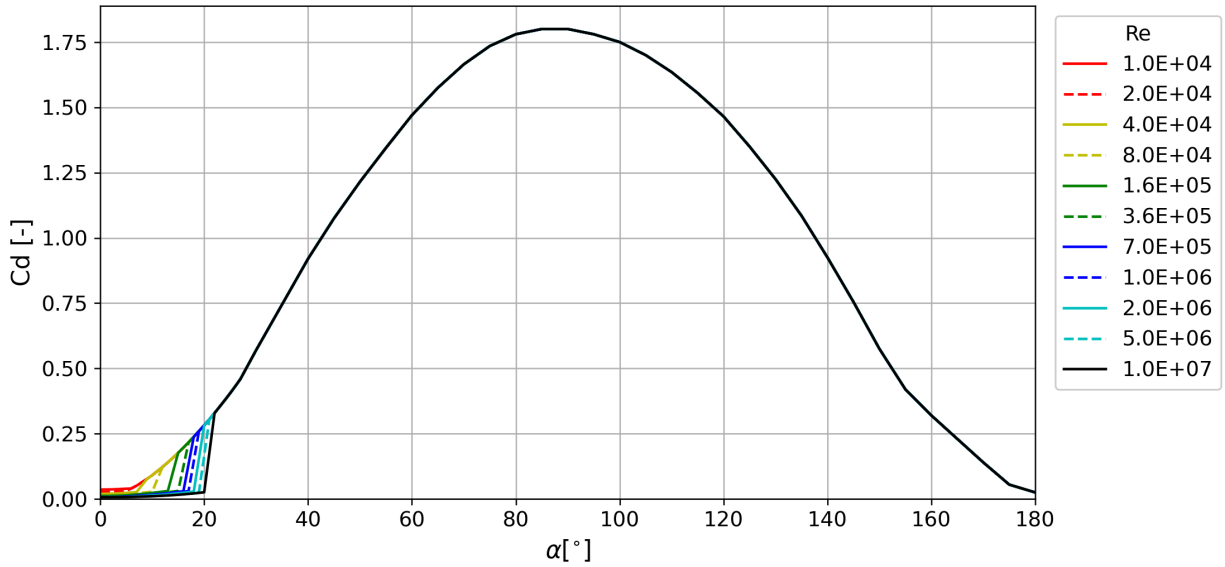

Figure 4.12: Drag polars for NACA 0015, from Sheldahl [78]

4.5.6 Forces

The local flow conditions at the quarter chord location of the blades and the corresponding polar values for this condition are used to evaluate the blade loading and the bound circulation. The forces on the blades are projected on the same timestep such that the moment arm is not influenced by the rotation step size. The bound circulation is updated for the next time step.
The blade and total turbine forces are plotted in the output figures of the flow field. The plotted total force arrows are normalized by the maximum attainable lift force for a lift coefficient of 1 ($\frac{F_{t,blade}}{\frac{1}{2}\rho c1(|U_a|(TSR+1))^2}$), such that this arrow size is appropriate for different turbine configurations and modes of operation. These arrows are plotted on the quarter chord position of all blades and the sum of these forces is plotted in the center of the turbine.

4.6 Model settings

The model uses input settings to evaluate the performance and the flow field. These settings consist of computational settings and operational settings. Both types of input influence the required computational time.

4.6.1 Operational and design parameters

The model is capable of evaluating many different turbine configurations and operating parameters of the turbine. Fixed design settings remain the same during all simulations for the optimization.
The number of blades is fixed at 3 blades. From two bladed simulations, it follows that this results in large oscillations in force amplitude and direction. This is also the case for one blade which has the additional disadvantage of an unbalanced rotation mass. Both one and two-bladed turbines are therefore more susceptible to fatigue problems.
The airfoil section is fixed as a NACA0015. This blade section is frequently used for VAWTs in literature [46][15][37][16].
The turbine has a square swept area with a diameter ($2R$) and blade span (H) of 5[m].
The far-field flow properties are also fixed at the specifications by the ISA [7]. The air density is fixed at $\rho = 1.225[kg/m^3]$ and the kinematic viscosity is fixed at $\nu = 1.460e-5[m^2/s]$. The apparent wind speed for all model simulations is fixed at $U_a = 10[m/s]$. This is a frequently encountered wind speed at sea as shown in Figure 2.17.

The construction parameters are parameters that cannot be adjusted during operation. These are the solidity (σ) and the pitch amplitude (A_{θ_p}).
Operational parameters are parameters that can be adjusted during the operation of the turbine. These are the TSR and the pitch phase (θ_p).
To evaluate the model performance and properties and find suitable computational settings, the reference turbine parameters as shown in Table 4.7 are used. These settings will be referred to as the reference operation parameters. This is a relatively highly loaded condition without pitch. Because this condition is highly loaded, this requires the streamtube-aligned induction to be accurately captured.

Table 4.7: Turbine reference parameters

σ	A_{θ_p}	TSR	θ_p
0.4	0	2.5	0

4.6.2 Computational settings

The computational settings determine the accuracy and the runtime of the model. These settings are normalized such that these are also valid for different turbine designs. These settings are fixed during the optimization. The computational settings are:
The rotational stepsize ($d\theta$). This influences the temporal and spatial discretization of the vortices and determines how many timesteps are required for a single rotation.
The normalized freestream wake extend ($\frac{x_{freesteram\ wake}}{2R}$). This determines the total runtime of the simulation. To make this property non-dimensional it is normalized by dividing by the turbine diameter.
The relative vortex core size ($\frac{R_{vortex\ core}}{2R}$). This is the region around the vortex core where the induced velocities are linear as if this region is rigid as indicated in Figure 4.8. This radius is normalized by the turbine diameter.
The relative minimum velocity induced by a vortex ($\frac{U_{induced,min}}{U_a}$) as indicated in Figure 4.8. This is normalized by the apparent wind velocity.
The normalized downwind location from where vortices are dropped if all vortices from the same time step have passed this location ($\frac{x_{drop\ vortices}}{2R}$). This is also normalized by the turbine diameter to make this setting non-dimensional.

To find appropriate computational settings such that the results of the simulation are sufficiently accurate and the computation time is sufficiently short, a numeric convergence study is done to find appropriate settings. This study is done for the reference operational and design settings as shown in Table 4.7.
This study uses the average properties over the last rotation to determine if the computational settings are sufficiently refined. This convergence study therefore uses integral parameters to select the appropriate computational settings. This only roughly indicates if the results are converged and is therefore less reliable compared to the instantaneous properties. However integral properties also indicate whether the computational settings are sufficiently refined such that the integral results do not change when refining the setting. The validation study in section 4.7 uses instantaneous results to evaluate the validity and specify differences in the results.
The compared integral properties are the drag coefficient, lift coefficient, power coefficient, and the free stream aligned induction at the center of the turbine. The power coefficient is the most significant parameter therefore this is mainly used to determine suitable computational settings as shown in Figure 4.15 to Figure 4.19.

To provide a rough overview of the influence of different computational settings, 32 arbitrary variations of the computational settings are evaluated. From this investigation, a reference computational setting is selected as shown in Table 4.8. This setting is refined by 2 levels for the fine2 setting and 3 levels for the fine3 setting. Based on this investigation, a sufficiently converged setting is selected to be used for the optimization. The fine2 computational setting requires approximately 14 times more computational time to evaluate the model compared to the reference setting and is assumed to be accurate. The converges setting is the least computationally expensive as this requires approximately half the computational time of the reference settings. The difference in computational settings and results is shown in Table 4.8.

Table 4.8: Computational settings

Setting	$d\theta$	$\frac{x_{freestream\ wake}}{2R}$	$\frac{R_{vortex\ core}}{2R}$	$\frac{U_{induced,min}}{U_a}$	$\frac{x_{drop\ vortices}}{2R}$	Runtime [s]
Reference	10	10	0.2	0.001	3	87e1
Fine2	6	14	0.2	0.00001	4	13e3
Fine3	4	16	0.2	0.000001	4.5	61e3
Converged	12	10	0.2	0.001	2.5	43e1

The flow field indicates differences in the simulation such as the number of vortices in the flow and the velocities in the wake. Figure 4.13 shows the results of the fine2 settings after 11 rotations whereas Figure 4.14 shows the results of the converged computational settings after 7.67 rotations. These figures show the wake is further developed for the fine2 settings however this simulation required 22 times more computational time compared to the converged computational settings. The yellow region in the flow field of Figure 4.13 indicates reversed flow in the wake which is not captured for the converge computational settings.
The arrow in the center of the turbine indicates the average force on the turbine over the last rotation. The length of the force arrow indicates $C_d/2$ aligned with the far field flow direction and $C_l/2$ perpendicular to the far field flow direction. Note that the results of the converged computational settings and the fine2 settings agree with respect to the power and drag coefficient however, the converged computational settings result in a lift force of 20% of the drag force whereas the results of the fine2 settings almost only show drag. Therefore the lift of the converged computational settings is considered less reliable compared to the drag and power.

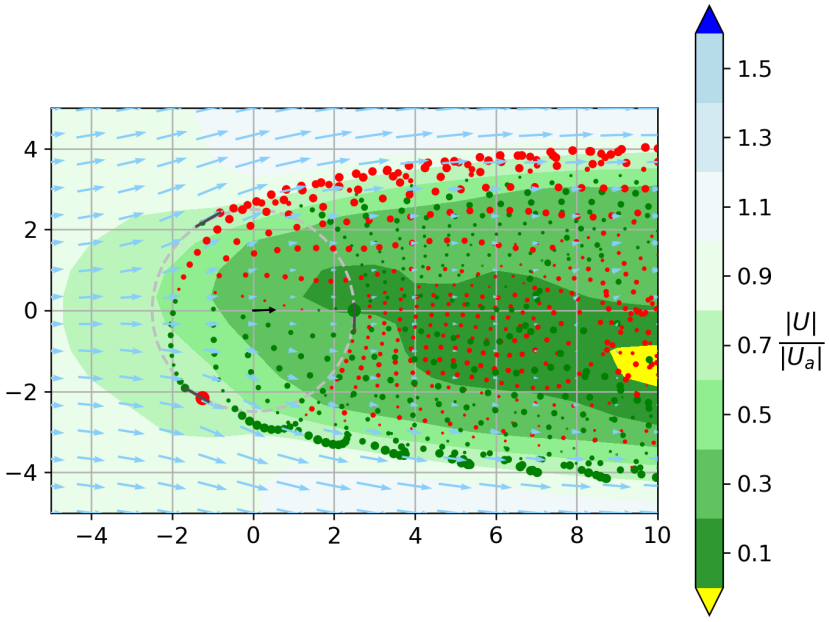

Figure 4.13: Flow field and last rotation averaged force vector for the fine2 computational settings and reference parameters: $\sigma = 0.4$, $A_{\theta_p} = 0[°]$, $TSR = 2.5$, $\theta_p = 0[°]$, results last rotation: $C_d = 1.05$, $C_l = 0.0289$, $C_P = 0.439$

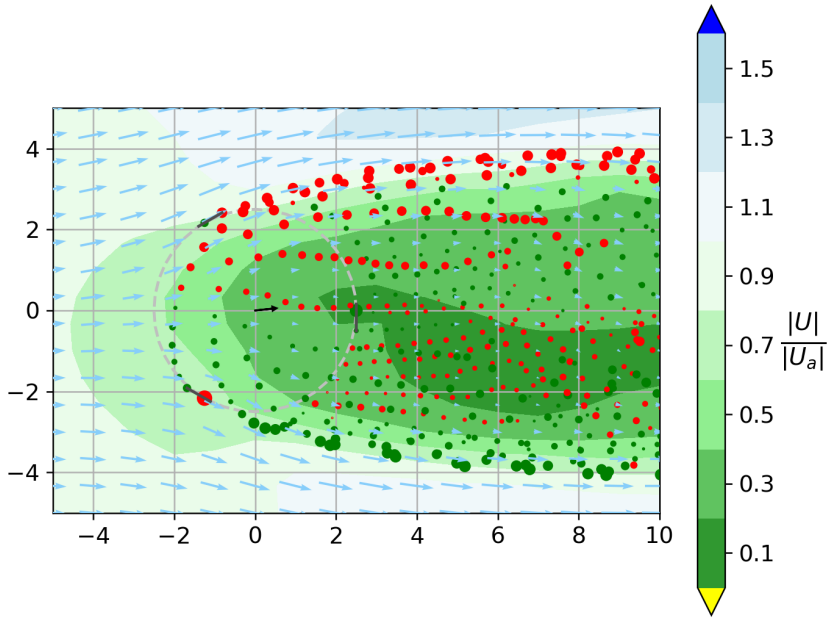

Figure 4.14: Flow field and last rotation averaged force vector for the converged computational settings and reference parameters: $\sigma = 0.4$, $A_{\theta_p} = 0[°]$, $TSR = 2.5$, $\theta_p = 0[°]$, results last rotation: $C_d = 1.06$, $C_l = 0.208$, $C_P = 0.445$

The power coefficient appears to change for all rotational stepsizes ($d\theta$). At small rotational stepsizes, the results diverge because smaller stepsizes result in smaller changes in bound vorticity and consequently smaller shed vortices in the wake. These small vortices induce small velocities and therefore the minimum induced velocity filters more vortex influences to zero. At larger stepsizes, the discretization error increases. The stepsize has a large influence on the computational time as shown in the lowest x-axis. Therefore larger stepsizes are preferred as long as the discretization error is limited. A rotational stepsize of $d\theta = 12[deg]$ appears to be a suitable setting and is used.

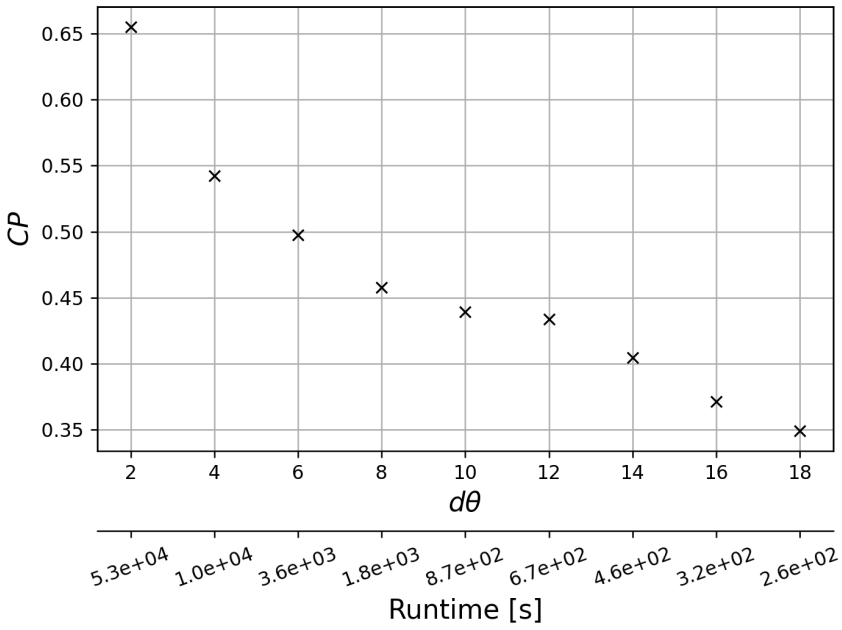

Figure 4.15: Rotational step size influence on computational accuracy

The freestream wake extend determines the total number of timesteps of the simulation. Therefore increasing this setting increases the computational time. Because the starting vortex generally is strong, the simulation requires sufficient time steps such that this vortex is convected away from the turbine and less strong vortices are used to construct a periodically steady wake. If the freestream wake extend setting is too low, the simulation has not converged to repeating oscillatory behavior and constant integral parameters. This is achieved around $\frac{x_{freestream\ wake}}{2R} = 10$. Therefore this setting is selected.

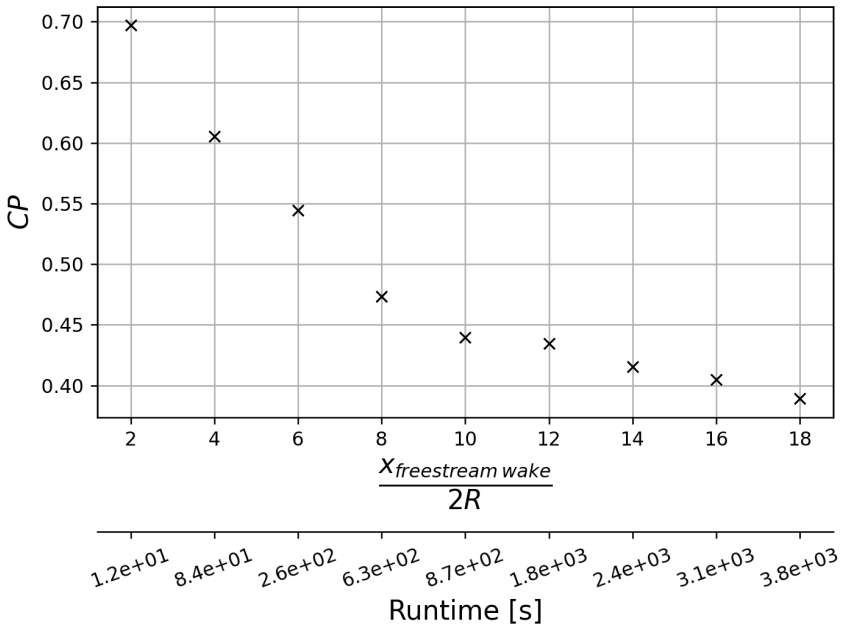

Figure 4.16: Relative freestream wake extend influence on computational accuracy

The vortex core radius determines the distance for which the induced velocities increase linearly with increasing distance as if the vortex core is rigid. This setting has no monotonic influence on computational time. Therefore computational time is not used for the selection of this setting. A small vortex core radius is preferred as this captures the interaction between different vortices however for small vortex core radii, the simulations diverge due to large velocities being induced near the vortex core location. Therefore $\frac{R_{vortex\ core}}{2R} = 0.2$ is selected as this is sufficient to prevent diverging simulations. This setting is not changed for different model refinement settings like fine2 as this can cause diverging simulations.

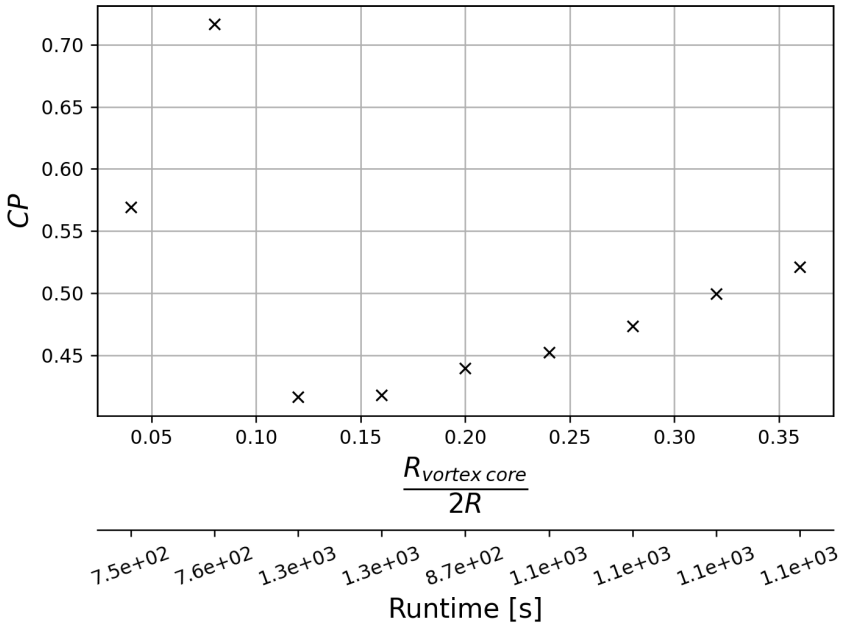

Figure 4.17: Relative vortex core radius influence on computational accuracy

The minimum induced velocity is a computational setting included in the model to reduce computational time by setting induced velocities to zero when the induced velocity is below the minimum threshold. To reduce computational time, this setting should be as high as possible however this reduces the accuracy of the results. Therefore $\frac{U_{induced,min}}{2R} = 10^{-3}$ is used.

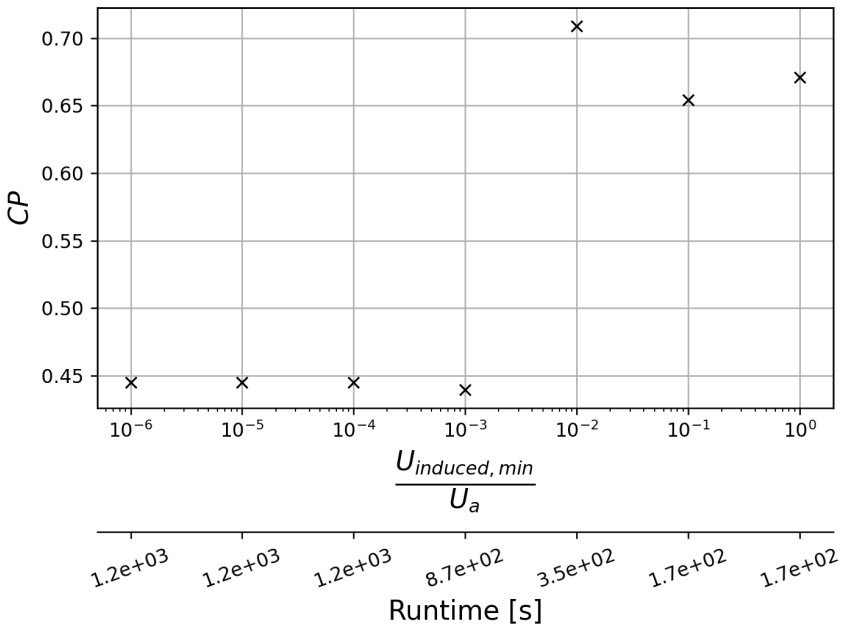

Figure 4.18: Relative minimum induced velocity influence on computational accuracy

To reduce computational time, vortices can be dropped once they pass a normalized downwind location. This can also be seen as a rough form of viscous dissipation. Dropping vortices has a substantial influence on computational time. However, it can also influence the accuracy of the simulation if the wake is not

accurately evaluated sufficiently far downwind. A setting of $\frac{x_{drop\ vortices}}{2r} = 2.5$ is selected as this reduces the computational cost for a relatively small deviation of C_P within 2.8% of the results when no vortices are dropped.

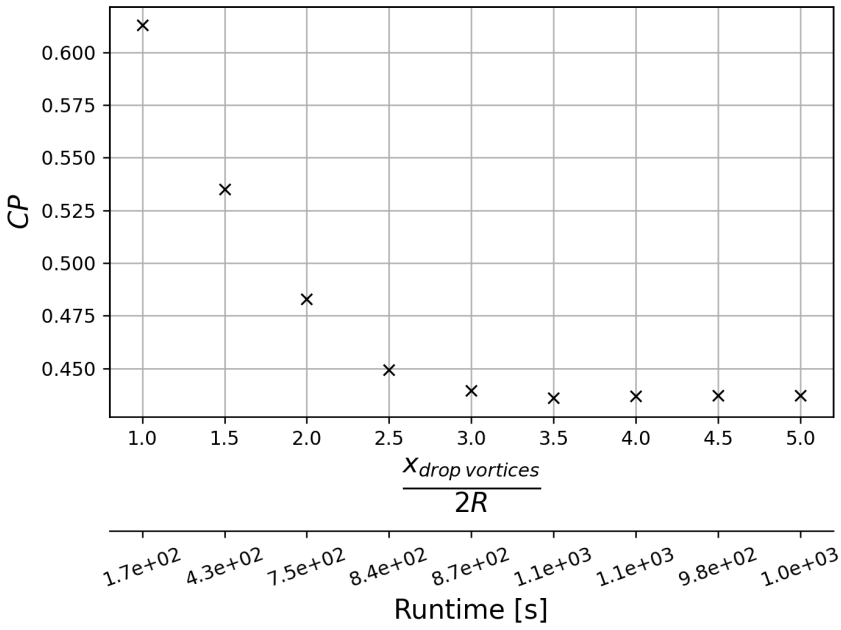

Figure 4.19: Relative vortex dropping distance influence on computational accuracy

4.6.3 Computation time

The computational time is not only influenced by the computational settings but also by the complexity of the simulation. More complex simulations require more vortices to be simulated which all influence the position of the vortices shed in the wake. Therefore the number of vortices is the main parameter to determine the computational time per timestep. This time increases quadratically as evaluated for the fine2 settings and shown in Figure 4.20.

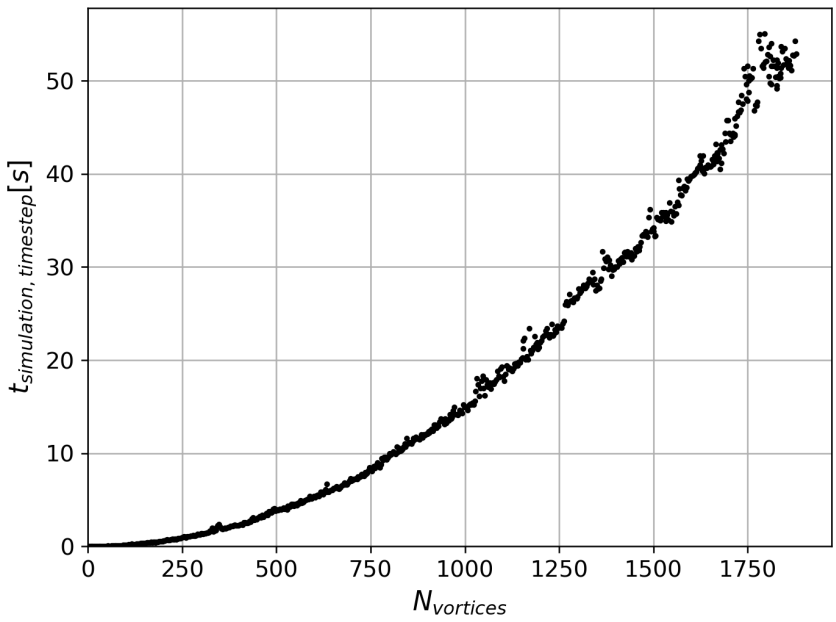

Figure 4.20: Computational time per timestep for the fine2 computational settings

The computational time per timestep increases until vortices reach a location sufficiently downwind such that they are dropped or when vortices are sufficiently far apart such that their influence is filtered to zero by the vortex-induced velocities. The number of vortices generally increases for longer simulations.
The total simulation time is the sum of the computational time of all timesteps. The number of timesteps is therefore also important for the total simulation time. The number of timesteps increases for increasing TSR as this requires more timesteps for the freestream wake to pass the required number of turbine diameters. This increase is linear as indicated by Figure 4.21.

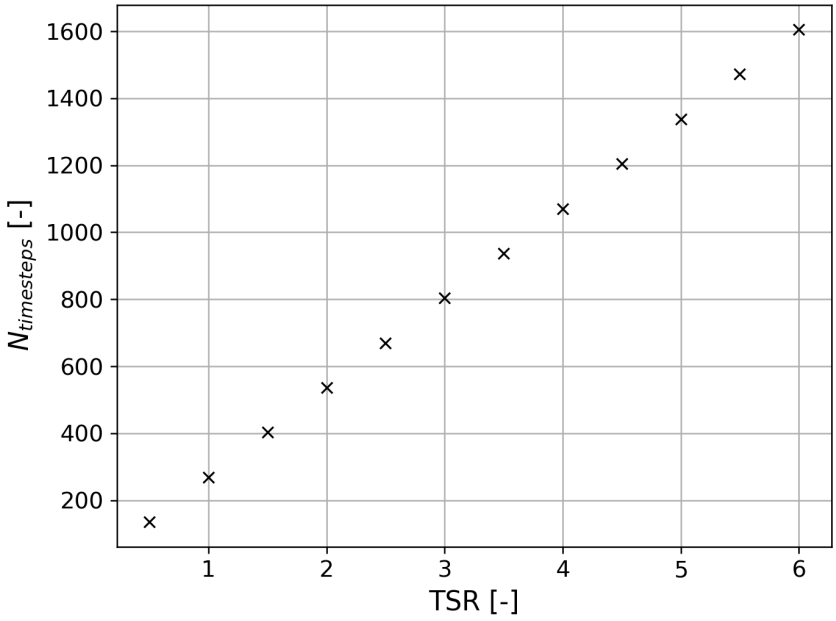

Figure 4.21: Total number of simulated timesteps for different TSR settings, fine2 computational settings

The number of vortices at the end of the simulation also increases for increasing TSR. This is approximately

a linear increase because vortices getting dropped at the downwind side of the domain. This follows from the fact that doubling the TSR would result in twice as many vortices in the domain however the dropping of vortices depends on the development of the wake and this wake development depends on the TSR and can therefore be irregular.

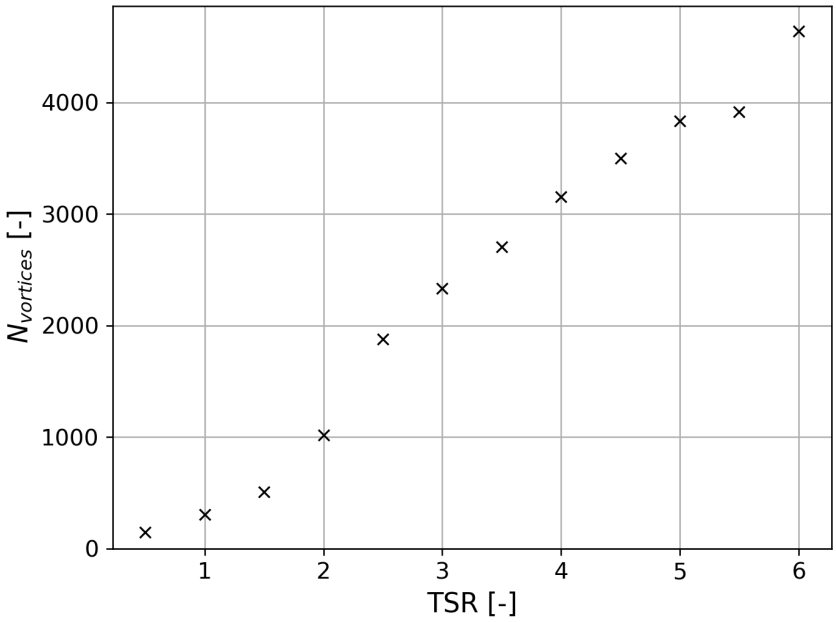

Figure 4.22: Total number of vortices at the end of the simulation for different TSR settings, fine2 computational settings

For increasing TSR, the simulation time increases with a cubic relation as shown in Figure 4.23. This follows from $N_{vortices}$ increasing approximately linearly for increasing TSR and $t_{simulation,timestep}$ increasing quadratic for increasing TSR.

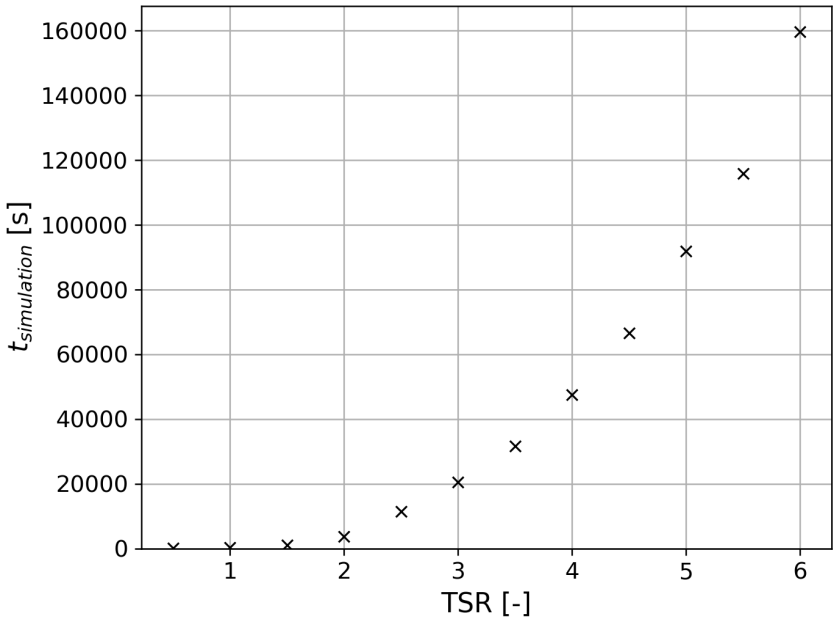

Figure 4.23: Total simulation time for different TSR settings, fine2 computational settings

The induced flow field behind the turbine influences at what rate the vortices are convected beyond the downwind location where vortices are dropped. This flowfield development is influenced by all design parameters as these influence the development of the wake.
The computational time therefore does not only depend on the computational settings, but also on the model input design parameters.

4.7 Validation

To use the model for optimization, the results should be sufficiently reliable. This is evaluated by comparison of the instantaneous and integral results of 6 different VAWT models and different types of models. The first type is momentum models such as the Multiple StreamTube (MST), DMST, and actuator cylinder model. A panel model, U2DiVA, is also compared. Two vortex models are compared, AEDEMA2D which is a 2D model, and Cactus which is a 3D model. The results of these different models are presented by Ferreira et al. [15]. This study compares models and presents the results for two different designs. These results are obtained using the WebPlotDigitizer application to convert the graphs to data points. The design used for validation features two blades and the polar does not include drag or stall. The results of the model is compared to both the converged and the fine2 computational settings.

4.7.1 Instantaneous results

The computational settings are defined based on integral results however a more reliable method to determine if the simulation is accurate is to compare instantaneous results. The instantaneous results are evaluated for a TSR of $\lambda = 4.5$ and two solidities of $\sigma = 0.1, 0.14$. These results are compared to the developed model.

The results are compared over the last rotation of the simulation. The compared parameters are the streamtube aligned induction factor (a), the angle of attack (α), and the normalized tangential force which drives the turbine.
The normalized tangential force is obtained from a calculation based on the streamtube aligned induction, the angle of attack, and the polar to evaluate the force on the blade. This calculation therefore does not include crosswind induction (from the streamtube expansion) to determine the magnitude of the relative wind speed on the blades. This influence is considered to be small with respect to the total relative velocity magnitude. Note that the angle of attack originates from the data and therefore does include the effect of tangential induction. This assumption is used for all models and the difference is evaluated in Figure 4.24 and Figure 4.25. This shows that the difference is sufficiently small to use the calculated results for the validation of the normalized tangential forces.

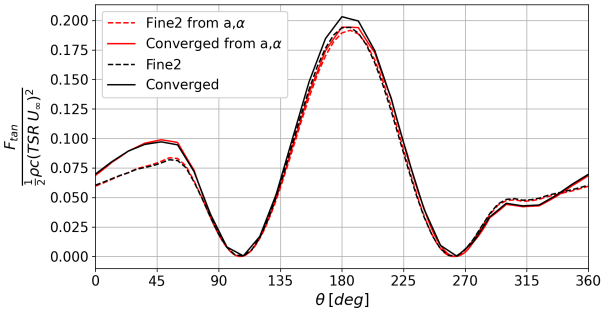

Figure 4.24: Actual and calculated normalized tangential force comparison, $\sigma = 0.1$

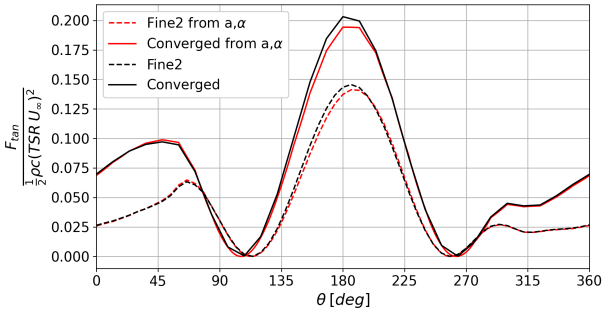

Figure 4.25: Actual and calculated normalized tangential force comparison, $\sigma = 0.14$

The model comparison of instantaneous results for $\sigma = 0.1$ are shown in Figure 4.26 to Figure 4.28.
The streamtube aligned induction agrees with the results from the other models however there is some difference between the converged and the fine2 settings.
The angle of attack from the model agrees with the other models but shows a slight overestimation on the downwind advancing part ($\theta = 0-70[°]$). The calculated and normalized tangential force shows some overestimation in this same region, this difference is most substantial for the converged computational settings.

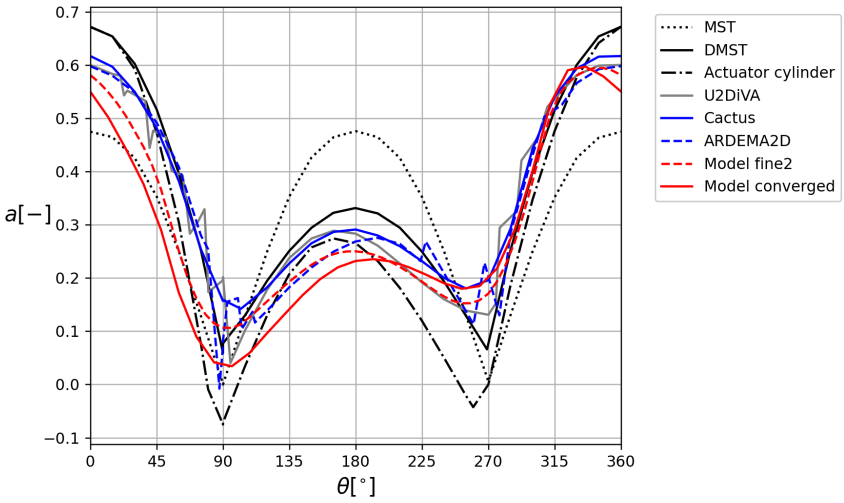

Figure 4.26: Streamtube aligned induction compared to models from Ferreira et al. [15], $\sigma = 0.1$

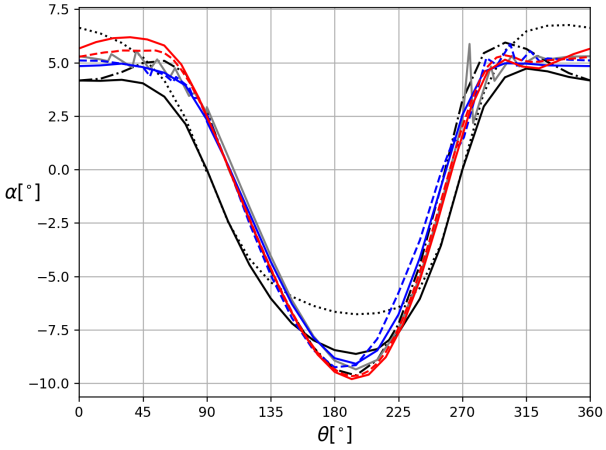

Figure 4.27: Angle of attack compared to models from Ferreira et al. [15], $\sigma = 0.1$

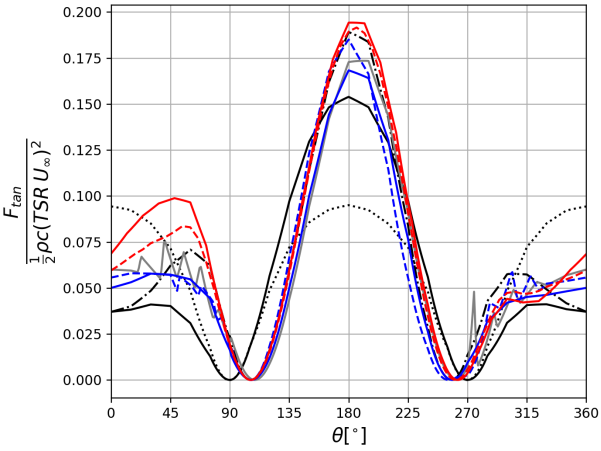

Figure 4.28: Calculated normalized tangential force compared to models from Ferreira et al. [15], $\sigma = 0.1$

The model comparison of instantaneous results for $\sigma = 0.14$ are shown in Figure 4.29 to Figure 4.31.
The streamtube aligned induction agrees with the results from the other models for the fine2 computational settings however the induction is underestimated for the converged computational settings.
The angle of attack from the model agrees with the other models but the results of the converged computational setting show a slight overestimation on the downwind advancing part ($\theta = 0-70[°]$). This is similar to the results of the lower solidity in Figure 4.27. The angle of attack is slightly underestimated for the fine2 computational settings on the downwind retreating part ($\theta = 300-360[°]$). The calculated and normalized tangential force shows some differences in the downwind part.

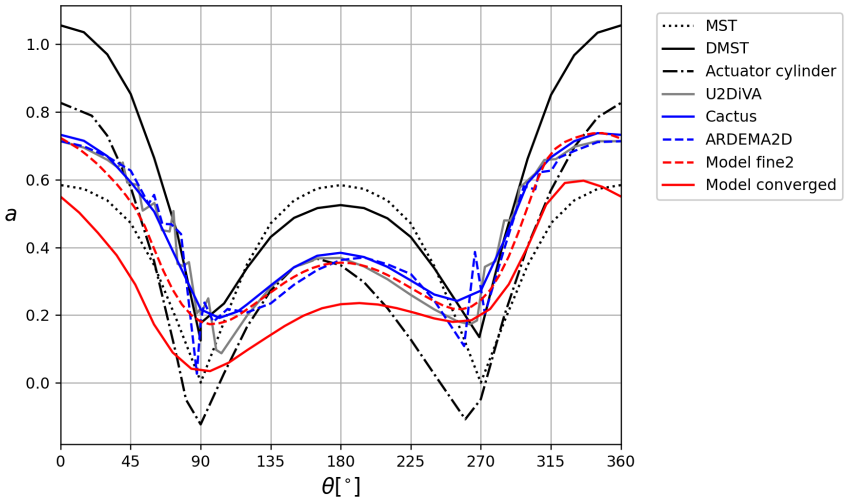

Figure 4.29: Streamtube aligned induction compared to models from Ferreira et al. [15], $\sigma = 0.14$

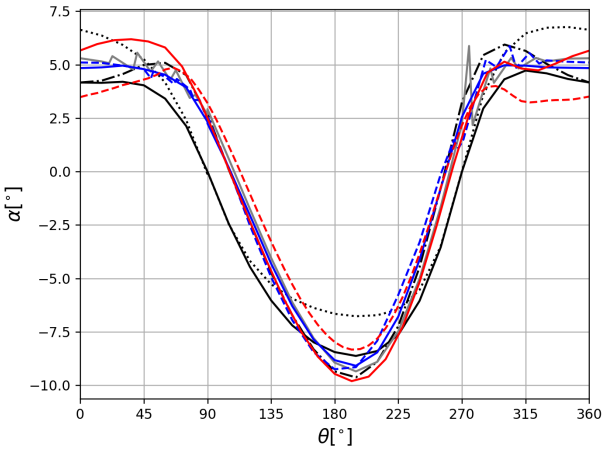

Figure 4.30: Angle of attack compared to models from Ferreira et al. [15], $\sigma = 0.14$

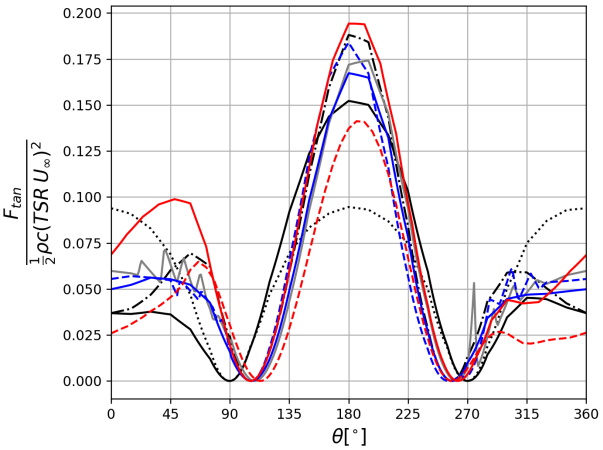

Figure 4.31: Calculated normalized tangential force compared to models from Ferreira et al. [15], $\sigma = 0.14$

The results of both the fine2 and the converged model settings are considered to be sufficiently accurate. The results for the fine2 settings show a strong resemblance to the results from the different models for both turbine solidities. This indicates that the model is valid and differences can occur due to the computational settings. The difference between the developed model and the other models appears to be larger on the downwind side of the turbine compared to the wind side. This is because accurate induction has a larger influence on the downwind side of the turbine and therefore makes the results more sensitive to differences on the downwind part.
From these results it can be concluded that the model is valid however there are discrepancies in the results due to the numerical settings for the used settings.

4.7.2 Integral results

The integral results indicate the average parameters of the turbine over the last rotation of the simulation. These results are used by the optimization algorithm to obtain the best-performing design. The results of the model for the converged and the fine2 computational settings are compared to the results from the Cactus model as presented by Ferreira et al. [15]. The Cactus model is a similar type of vortex model and therefore provides a suitable model for comparison. The drag coefficient and power coefficient are evaluated for design

space with variable TSR and solidity.

The comparison for the power coefficient is made with figures Figure 4.32 to Figure 4.34. These figures show a strong resemblance to the different models and computational settings. The difference is mainly in the maximum attained power coefficient which is higher for the developed model and highest when the coarser converged computational settings are used. All figures indicate C_P values above the Betz limit of $16/27 \approx 0.593$. Even though subsection 3.1.2 describes the possibility for VAWTs to surpass the Betz limit, the vortex model tends to overestimate the maximum power. This overestimation is most substantial for the converged computational settings. This indicates that the overestimation is at least partially due to the numeric settings and discretization errors. It should therefore be noted that results showing a power coefficients above the Betz limit in chapter 5 can be exaggerated due to the model settings.
Figure 4.32 to Figure 4.34 indicate that a lot of power can be attained for a low solidity and a large TSR. This is because drag and stall are not included in the polar for these validation simulations.

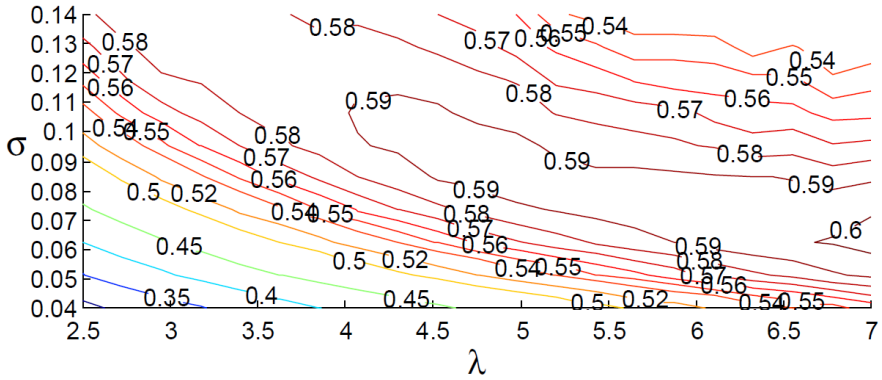

Figure 4.32: Power coefficient (C_P) from the Cactus model as presented by Ferreira et al. [15]

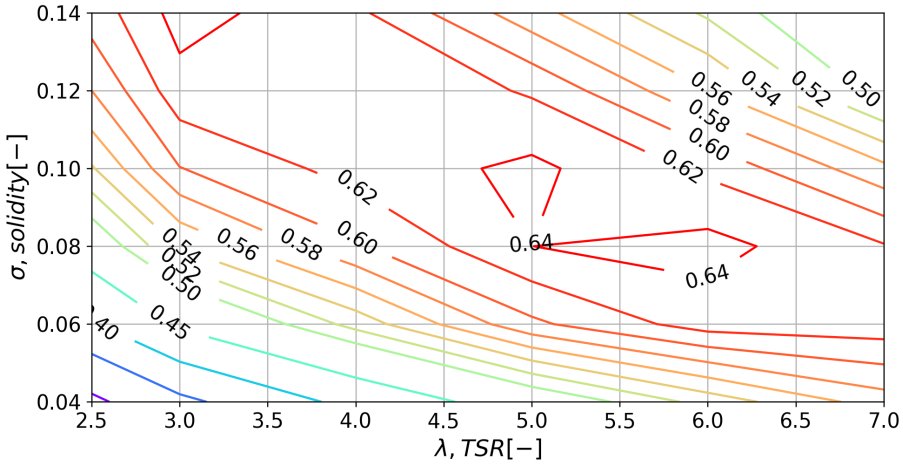

Figure 4.33: Power coefficient (C_P) from the model for the fine2 computational settings

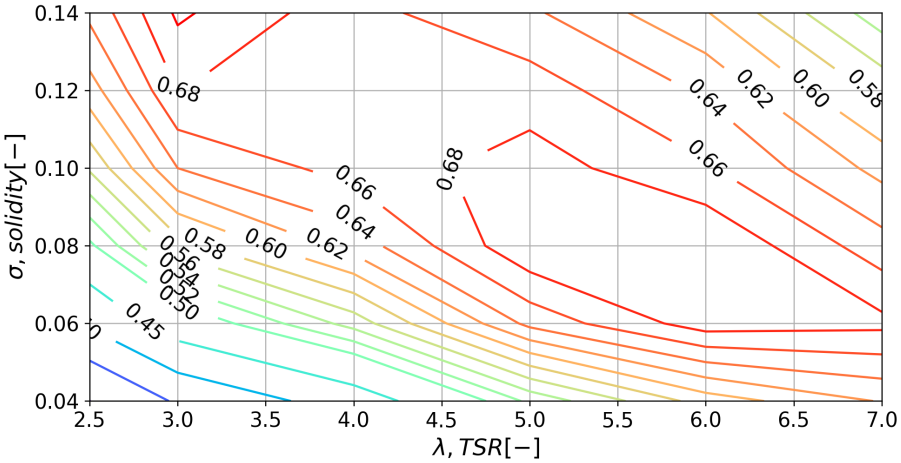

Figure 4.34: Power coefficient (C_P) from the model for the converged computational settings

The comparison for the drag coefficient is made with Figure 4.35 to Figure 4.37. These figures also show a strong resemblance for the different models and computational settings. The maximum drag is found to be largest for the converged computational settings compared to the fine2 settings whereas the Cactus model also indicates maximum drag values below the values for the fine2 setting.

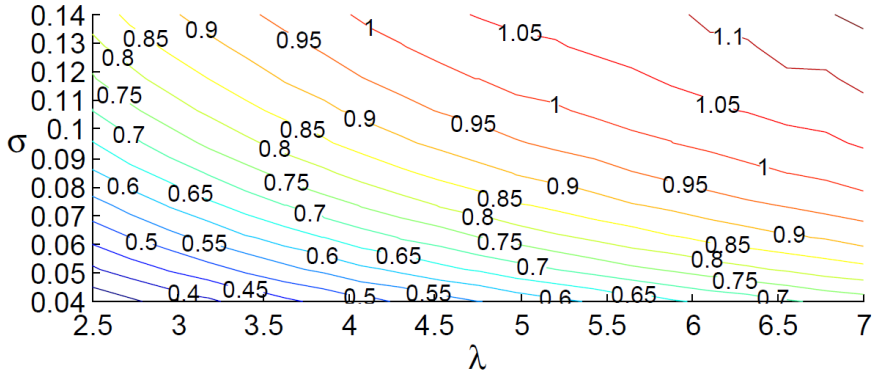

Figure 4.35: Drag coefficient (C_d) from Ferreira et al. [15]

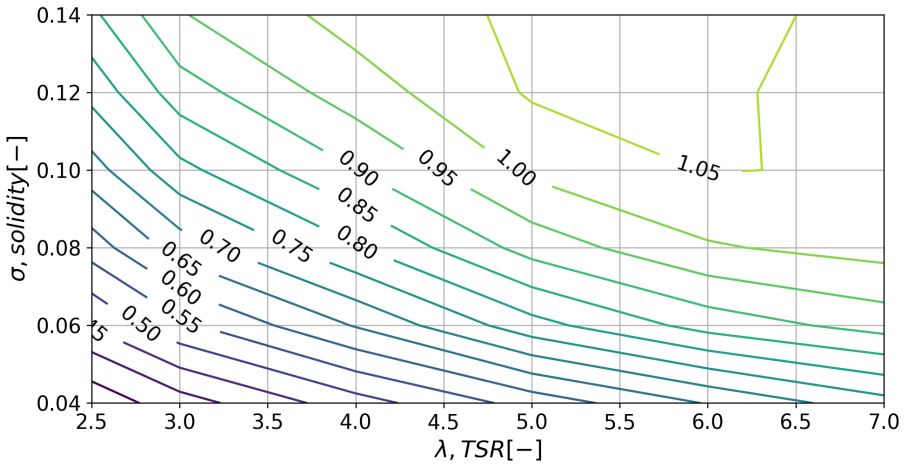

Figure 4.36: Drag coefficient (C_d) from the model for the fine2 computational settings

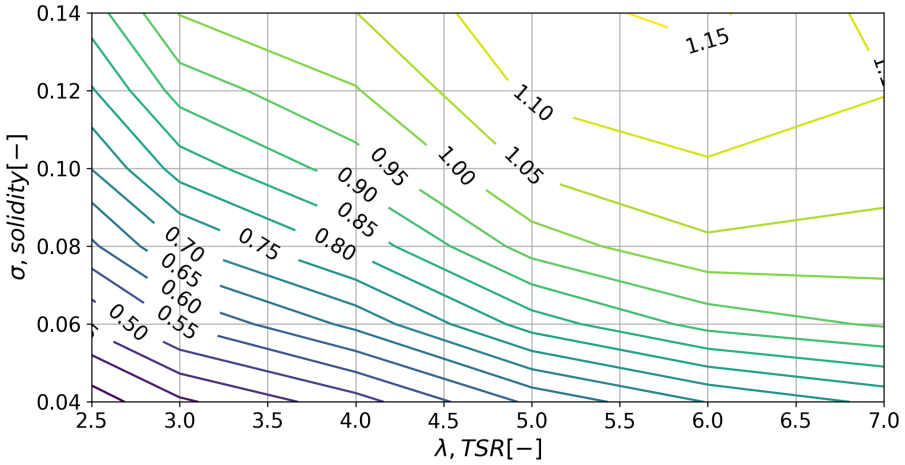

Figure 4.37: Drag coefficient (C_d) from the model for the converged computational settings

The integral results of the model are similar to the results from the Cactus model and are within the variation of results for different models as discussed by Ferreira et al. [15]. Therefore the model is validated and concluded to be sufficiently accurate on the investigated range of operation.
The numeric model settings can result in numeric errors. The operating range of the turbine should also not be too far outside the operating range of the validation cases. The lifting performance is not investigated therefore this performance might be less reliable which should be considered when analyzing the results of the optimization.

Chapter 5

Optimization

The design of aerodynamic structures is a complex process that requires expertise, knowledge, and experience. When designs become more complex with multiple free design variables, it becomes increasingly difficult to design the best-performing structures. To simplify the process of design, models are often used to describe the problem within the limitations of the model. When a model is combined with optimization techniques, this can be used to evaluate the best-performing design. Optimization is a methodology to improve a design based on an objective function to find stationary points in the design space. These stationary points occur at global or local extrema of the objective function. Therefore the optimization problem results in a local or global optimum depending on the characteristics of the optimization problem. The search for an improvement of performance uses the steps as described by Papalambros [67] as the methodology for optimization.

5.1 Problem description

The objective of a VAWT for ship propulsion is to produce maximum power, this can either be electrical power or equivalent propulsive power by means of a thrust force. This power can be provided by extracting kinetic energy from the wind. Therefore the power production is limited by the swept area, the apparent wind speed, and the efficiency of the turbine in terms of power and force production. The most trivial way to increase the performance is to increase the swept area. This is not always possible and increases the cost of construction. Weather routing can be used to provide more favorable wind conditions however this is not considered in this study. This study considers a far-field wind at sea of $U_\infty = 6.64[m/s]$. This speed is obtained from the median wind speed of Figure 2.16 and is also used as the reference wind speed to normalize the performance for different wind conditions. The wind speed in port is $U_\infty = 4.77[m/s]$ as obtained the median wind speed of Figure 2.19.
This optimization problem focuses on improving the efficiency of the turbine by evaluating optimal design parameters. Some parameters are fixed during the optimization. The number of blades is fixed at 3 blades as this is the most well-established configuration of VAWTs. The swept area is fixed at $A = 25[m^2]$ and the diameter is set at $2R = 5[m]$. This results in a virtual span of $H = 5[m]$ which does not influence the results as this optimization uses 2D results. The airfoil section is also fixed as the NACA0015.
The free design parameters determine the efficiency of a turbine. The design parameters which specify the turbine design are the solidity (σ), the pitch phase amplitude (A_{θ_p}), the TSR (λ) and the pitch phase (θ_p) as described in subsection 4.5.1. These parameters are subdivided into construction parameters which consist of the turbine solidity and the pitch amplitude and the operational parameters which can be modified to provide optimum performance in specific encountered wind conditions. When all parameters are used to determine the design, the design space is 4 dimensional. This is therefore a 4D optimization problem.
The design parameters are optimized for conditions when operating at sea and in port. These conditions are weighted as discussed in section 2.3, 50% of the time at sea and 40% of the time in port. The resulting design parameters are weighted according to their probability of occurrence for different apparent wind conditions for a ship speed of $U_s = 6[m/s]$ as specified in section 2.4.

5.1.1 Objectives

The optimal design depends on the specified objective. The objective function is specified as f which can have different subscripts for different objectives when the VAWT is optimized to operate in different modes of operation. The objective functions are formulated such that the optimization is a minimization problem and are non-dimensional such that the results can be scaled.
For any WASP system, the objective is to provide maximum propulsive power for minimum cost. The model enables the evaluation of the performance parameters to evaluate the propulsive power however the cost is not evaluated. Evaluating the cost would be complex and requires multidisciplinary expertise.
The objectives in this optimization use the produced equivalent propulsive power. This power is normalized by the far field power available in the reference swept area ($\frac{1}{2}\rho A {U_\infty}^3$). This results $C_{P'}$ in which is equivalent to C_P on a stationary reference frame. $C_{P'}$ provides insight into comparing the performance of a VAWT on a ship to a stationary wind turbine. The objectives are divided into two parts, the turbine part ($C_{P',turbine}$) and the thruster ($C_{P',thruster}$) part. These separate terms can be used to determine in which conditions it is more effective to use the VAWT as a turbine or as a thruster and to indicate the different contributions to the equivalent propulsive power. The turbine and thruster power contribution are respectively expressed in Equation 5.1 and Equation 5.2. The total equivalent power coefficient expressed in Equation 5.3.

$$C_{P',turbine} = C_P \frac{U_a^3}{U_\infty^3} \tag{5.1}$$

$$C_{P',thruster} = \frac{\left(C_{l,turbine} sin(\beta_a) - C_{d,turbine} cos(\beta_a)\right) U_s U_a^2}{U_\infty^3 \eta_D} \tag{5.2}$$

$$C_{P'} = C_{P',turbine} + C_{P',thruster} \tag{5.3}$$

5.1.1.1 Maximum lift

This study investigates use cases whereby the VAWT is used as a lifting device to provide a thrust force. The maximum attainable lift coefficient is therefore an interesting objective to indicate the lifting performance.

$$f_{max\,lift} = -C_{l,turbine} \tag{5.4}$$

5.1.1.2 Lifting efficiency

Lifting performance can also be expressed as the lift over drag, this ratio is often referred to as the airfoil efficiency. This is important when sailing upwind and is therefore an interesting objective to indicate the lifting performance for upwind conditions.

$$f_{lifting\,efficiency} = -\frac{C_{l,turbine}}{C_{d,turbine}} \tag{5.5}$$

5.1.1.3 Turbine in port

When operating the turbine in port, the objective is to produce maximum electrical power without regard for the produced forces. The power coefficient should therefore be maximized. This objective function is shown in Equation 5.6.

$$f_{turbine,\,port} = -C_P \tag{5.6}$$

5.1.1.4 Combined mode at sea

When the VAWT is in operation at sea, the produced power or thrust force can both be used to provide equivalent propulsion power. What type of propulsion is favored depends on the wind conditions. In stern wind conditions, the drag of the turbine increases the equivalent propulsion power whereas, in upwind conditions, the drag of the turbine reduces the equivalent propulsion power. The lift can provide a thrust force in

between these conditions. Therefore this design is optimized for 13 different apparent wind directions from $\beta_a = -180[°]$ to $180[°]$ in steps of $30[°]$. This results in 13 different optimal designs for every specific wind condition.
What design is optimal for the specific conditions is determined by the objective function. This objective function is a result of Equation 3.21 and Equation 3.23 which describes the equivalent propulsive power. This is normalized by the kinetic power in the true far-field wind flow to make the objective function non-dimensional.

The ship speed is fixed at the previously specified speed of $U_s = 6[m/s]$ as determined in subsection 2.4.2. The far-field wind speed at sea is also fixed at the previously specified $U_\infty = 6.64[m/s]$ this is obtained from the median wind speed of Figure 2.16. Based on these settings, the apparent wind speed can be determined for every wind direction using Equation 2.3.

$$f_{combined,\,sea} = -C_P \frac{U_a^3}{U_\infty^3} - \frac{\left(C_{l,turbine} sin(\beta_a) - C_{d,turbine} cos(\beta_a)\right) U_s U_a^2}{U_\infty^3 \eta_D} \tag{5.7}$$

5.1.1.5 Turbine at sea

When the VAWT is operated as a turbine at sea, the drag force can influence the equivalent propulsive power. Because this mode of operation only considers power generation and drag, the lift force is not incorporated in this objective as this turbine mode does not intend to produce a lift force for propulsion. The objective function is therefore similar to the objective function of Equation 5.7 without the influence of the produced lift force.
The objective for a turbine at sea also depends on the apparent wind direction. Because the ability to produce power is omnidirectional for a VAWT with a variable pitch phase, this design is optimized for 7 different positive apparent wind directions from $\beta_a = 0[°]$ to $180[°]$ in steps of $30[°]$. This results in 7 different optimal designs for every specific wind condition.

$$f_{turbine,\,sea} = -C_P \frac{U_a^3}{U_\infty^3} + \frac{C_{d,turbine} cos(\beta_a) U_s U_a^2}{U_\infty^3 \eta_D} \tag{5.8}$$

5.1.1.6 Thruster at sea

When the VAWT is operated as a thruster at sea, the lift and drag force can be used to provide equivalent propulsive power. Because this mode of operation only considers lift and drag forces, the produced power is not incorporated in this objective. To produce large thrusting forces, the turbine might require power to drive the turbine. This is not investigated in this study as this study considers a free-running turbine. The objective function is therefore similar to the objective function of Equation 5.7 without the C_P term.
The objective for a turbine at sea also depends on the apparent wind direction. Therefore this design is optimized for 13 different apparent wind directions namely, from $\beta_a = -180[°]$ to $180[°]$ in steps of $30[°]$. This results in 13 different optimal designs for every specific wind condition.

$$f_{thruster,\,sea} = -\frac{\left(C_{l,turbine} sin(\beta_a) - C_{d,turbine} cos(\beta_a)\right) U_s U_a^2}{U_\infty^3 \eta_D} \tag{5.9}$$

5.1.2 Constraints

Optimization algorithms often tend to move towards conditions where the model is invalid. Constraints are added to the optimization problem to prevent infeasible designs as the best performing designs.

- P_1 The first constraint prevents a chord length smaller than 8% of the radius of the turbine as shown in Equation 5.12b. This constraint ensures the blades do not become too small and prevents the strength and stiffness would be insufficient. This constraint is set to an arbitrary but reasonable value without modeling the stresses on the blades.
- P_2 The second constraint specifies a chord length no larger than 40% of the radius of the VAWT. This is in order for the blades to be small enough to fit in the structure and for these not to become excessively heavy. The flow curvature effect can also have a substantial influence for large c/R as discussed in

subsection 3.4.2. An additional reason to limit this solidity is that the model simulations can diverge for large solidity in combination with a large TSR. Large blade chords should therefore be prevented. This constraint is normalized by the turbine radius to make the constraint non-dimensional.

P_3 The third constraint specifies the maximum absolute pitch amplitude to be smaller than the reference stall angle of $\alpha_{stall,ref} = 15[^\circ]$. This prevents excessive pitch amplitudes which would already result in stall if the turbine rotates without any wind. Note that also negative pitch amplitudes are allowed. This constraint is normalized by the reference stall angle such that the values of the constraint are in the order of 1.

P_4 The fourth constraint prevents the maximum relative wind speeds on the blades (U_{rel}) to be below 20% of the speed of sound. This is well within the limit where the flow is considered to be incompressible as discussed in section 4.1. The speed of sound is specified by the ISA at mean sea level [7], $C_{s,air} = 340[m/s]$. This limit is used because the airfoil polar does not include the effect of compressibility and such that the speed is reasonable for the turbine to operate on the deck of a ship. This constraint is normalized by the speed of sound to make the constraint non-dimensional.

P_5 The fifth constraint specifies the absolute pitch phase to be up to a maximum of $|\theta_p| \leq 90[^\circ]$. This prevents periodic results with multiples of 180 degrees. This constraint is normalized by the reference stall angle such that the values of the constraint are close to the order of 1.

P_6 The sixth constraint prevents severe stall at any point in the rotation. This is required for the validity of the model because the model does not capture dynamic stall effects. The maximum allowed absolute angle of attack is specified at $|\alpha| = 15[^\circ]$. This constraint is also normalized by the reference stall angle such that the values of the constraint are close to the order of 1.

P_7 The seventh constraint specified that the turbine can only be operated when providing power or in free-running operation. Therefore the case of a driven turbine acting as a thruster is not considered.

5.1.3 Penalization

The constraints are added to the objective function using penalty functions. This does not modify potential interior optima and allows for infeasible designs to be evaluated at the cost of a penalty on the objective. The penalization is only applied if one or more constraints are active. The objective function including penalties is given by Equation 5.10. The penalty values for each constraint (P_i) are summed to the total penalty of all constraints (P_{total}).

$$\widetilde{f} = f + P_{total} \tag{5.10}$$

$$P_{total} = \sum_{i=1}^{7} P_i = \sum_{i=1}^{7} p_i (max(0, g_i))^2 \tag{5.11}$$

Constraint-specific penalty factors p_i are applied in the penalty function such that this function provides smooth yet sufficiently large penalization when the design surpasses the constraint boundary. These factors are provided in Table 5.1. The penalty functions are quadratic, this means the penalty is inherently smooth at the boundary and increases quadratically for increasing constraint values when the constraints are active. The application of the penalty function therefore works like a push in the right direction when the design surpasses a constraint. This smooth application of the penalties improves the efficiency of the optimization algorithm near the constraint boundaries.

Table 5.1: Penalty factors

Penalty factors	p_1	p_2	p_3	p_4	p_5	p_6	p_7
Values	100	20	20	200	0.5	10	10

Figure 5.38 shows that the background contour of the performance is not filled for the combination of large TSR and large solidity. This is because the simulations can diverge for this combination of design

parameters. This can result in $C_P > 1$ which is infeasible. Most of these cases are already penalized, however on rare occasions, the other constraints are inactive for diverged solutions. Therefore an additional penalty is implemented such that the power coefficient is set to a value of $C_P = -10$ for diverged solutions. This prevents the optimization algorithm to move in this direction.

5.1.4 Problem formulation

The optimization problem is formulated in negative null form with inequality constraints as shown in Equation 5.12a to Equation 5.12h. The objective function (f) depends on the mode of operation for which the design is optimized as described in subsection 5.1.1.

$$\min_{\sigma, A_{\theta_p}, TSR, \theta_p} \quad f(\sigma, A_{\theta_p}, TSR, \theta_p) \tag{5.12a}$$

$$\text{s.t.} \quad g_1 = 0.08 - \frac{c}{R} \leq 0, \tag{5.12b}$$

$$g_2 = \frac{c}{R} - \frac{1}{2} \leq 0, \tag{5.12c}$$

$$g_3 = \frac{|A_{\theta_p}|}{\alpha_{stall,ref}} - 1 \leq 0, \tag{5.12d}$$

$$g_4 = \frac{max\left(U_{rel}\right)}{C_{s,air}} - 0.2 \leq 0, \tag{5.12e}$$

$$g_5 = \frac{|\theta_p| - 90}{\alpha_{stall,ref}} \leq 0, \tag{5.12f}$$

$$g_6 = \frac{max(|\alpha|)}{\alpha_{stall,ref}} - 1 \leq 0, \tag{5.12g}$$

$$g_7 = -C_P \leq 0, \tag{5.12h}$$

5.2 Initial problem investigation

To select a suitable optimization method, the characteristics of the optimization problem are investigated. To do this, the turbine performance characteristics and feasible design space are evaluated. This indicates the properties of the optimization problem such as boundedness, linearity, convexity, and monotonicity. These characteristics are used to select a suitable optimization method. The sensitivity of the objective function with respect to the design parameters is also investigated. This indicates the settings to use to investigate the resulting optimum of the optimization.

5.2.1 Design space investigation

The performance parameters of lift (C_l), drag (C_d) and power (C_P) and the feasible region within the design space is investigated. This investigation can be used to indicate incorrect formulations of the optimization problem. The information from this study can also be used to simplify the problem if there are redundant constraints or limit the initial region of investigation to the feasible design region. This investigation provides insight that can be used to select an appropriate optimization method.
To investigate the effect of different design parameters on C_d, C_l and C_P, 2D slices of the 4D design space are evaluated. These 2D slices of the design space are evaluated for all combinations of two design variables which for 4 design variables results in 6 slices. At every grid line crossing including at the edges of the domain, the model is evaluated using the converged computational settings. This is referred to as a function evaluation. These data points are used to make the contour plots of the performance parameters.
The penalty functions are included in these figures to indicate the feasible design region where all constraints are inactive. The distance between the constraint contour ($p_i = 0$) and penalty contour ($p_i = 0.1$) provides a rough indication of the sensitivity of the penalty when surpassing the feasible design domain, whereby a larger distance between these lines indicates a less stringent influence of the constraint.
The fixed parameters in these simulations are the reference parameters as shown in Table 4.7 or use a pitch amplitude of $A_{\theta_p} = 8[^\circ]$ when the effect of pitch is investigated.

All figures of the design space investigation are presented in Appendix C. The most meaningful figures are discussed in this section. These results show that with only 2 design variables, it is already possible to attain large changes in the forces and power coefficients. This indicates that every parameter has a substantial influence on the performance of the turbine. Therefore no design parameters can be set to a fixed value.

5.2.1.1 TSR and solidity

This design space investigation only considers variable TSR and solidity. This investigation considers no pitch variation. Therefore the blades are fixed over the rotation which allows for a simpler geometry. Figure 5.1 shows that the active constraints which indicate the attainable set of design parameters. These are the minimum relative chord length (P_1), the maximum relative speed on the blades (P_4), the maximum angle of attack on the blades (P_6), and the minimum requirement to produce power (P_7).

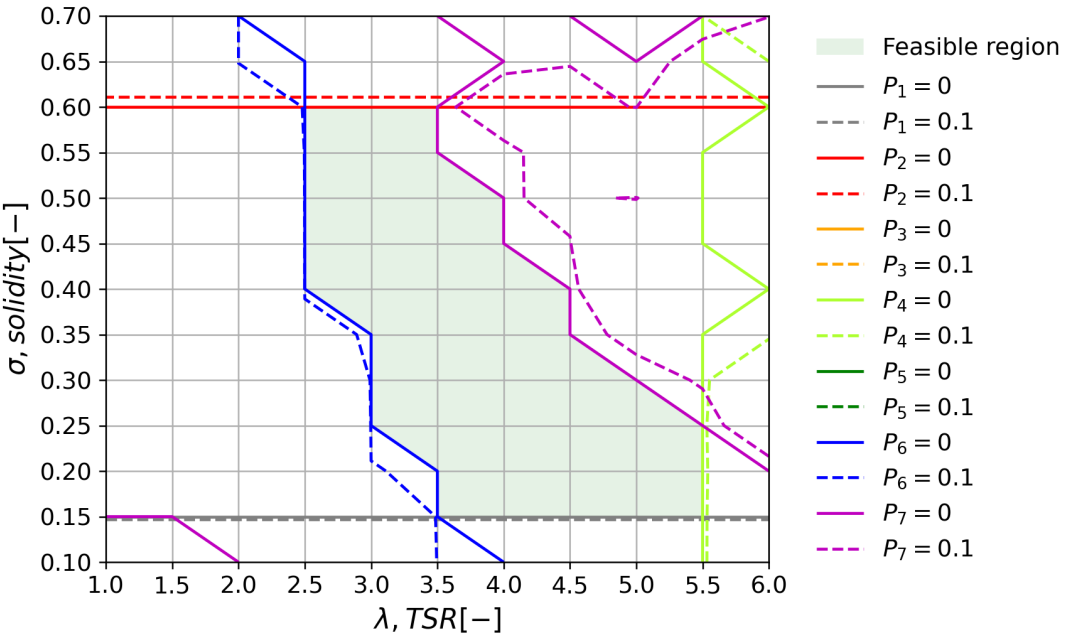

Figure 5.1: Penalties from different constraints, $A_{\theta_p} = 0[^\circ]$, $\theta_p = 0[^\circ]$

The curved diagonal region of largest C_P is clearly visible in Figure 5.2. This trend is also apparent in Figure 4.32 from Ferreira et al. [15]. The highest performance can be attained for a large TSR and a low solidity. However, this combination of design parameters is outside the design space because of the stall constraint (P_6) and the minimum relative chord length constraint (P_1). Therefore to improve the power generating performance of the turbine, pitch variation should be included in the optimization.

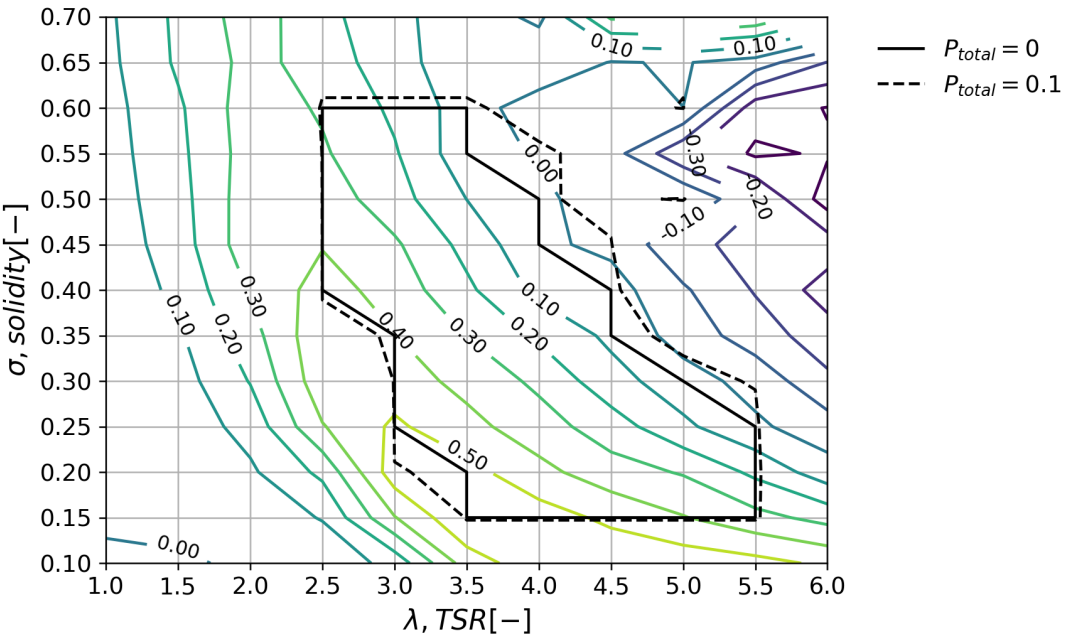

Figure 5.2: C_P for different designs and the total penalty showing the feasible design region, $A_{\theta_p} = 0[°]$, $\theta_p = 0[°]$

5.2.1.2 Solidity and pitch amplitude

This design space investigation only considers variable solidity and pitch amplitude. Figure 5.3 shows that the active constraints which indicate the attainable set of design parameters. These are the minimum relative chord length (P_1), the maximum relative chord length (P_2), the maximum absolute pitch amplitude (P_3), the maximum angle of attack on the blades (P_6) and the requirement to produce power (P_7).

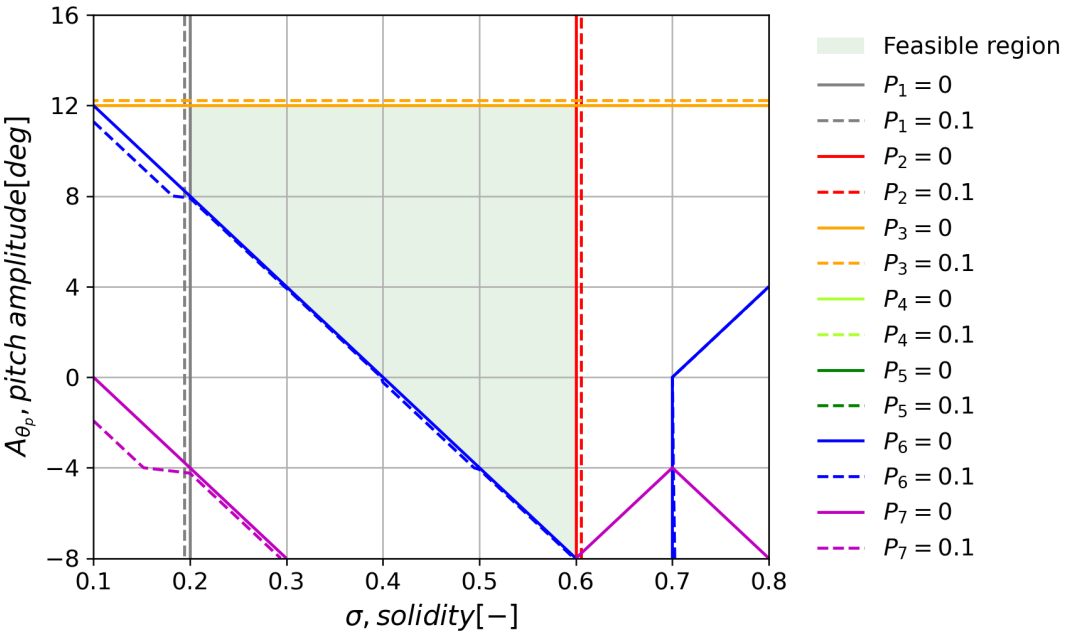

Figure 5.3: Penalties from different constraints, $TSR = 2.5$, $\theta_p = 0[°]$

Figure 5.4 indicates that maximum power can be attained within the feasible domain and that more power can be attained when a positive pitch amplitude is used. This optimum also depends on the fixed design parameters but this indicates that pitch variation can be used to increase the generated power.

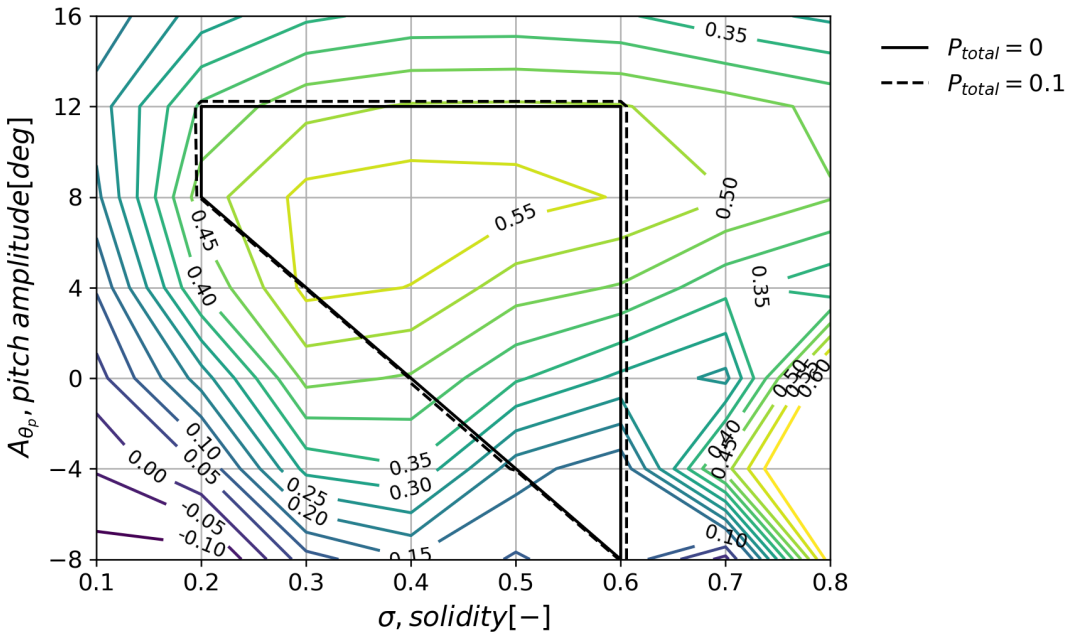

Figure 5.4: C_P for different designs and the total penalty showing the feasible design region, $TSR = 2.5$, $\theta_p = 0[^\circ]$

5.2.1.3 Solidity and pitch phase

This design space investigation only considers variable solidity and pitch phase. Figure 5.5 shows that the active constraints which indicate the attainable set of design parameters. These are the minimum relative chord length (P_1), the maximum relative chord length (P_2), the maximum absolute pitch phase (P_5), the maximum angle of attack on the blades (P_6) and the requirement to produce power (P_7).
The constraint for the minimum power requirement is only active where both constraints of the maximum relative chord length (P_2) and the maximum absolute blade pitch (P_5) and are also active. It therefore depends on the numeric accuracy of the contours if this constraint is active or dominated by the other constraints which might be more strict.

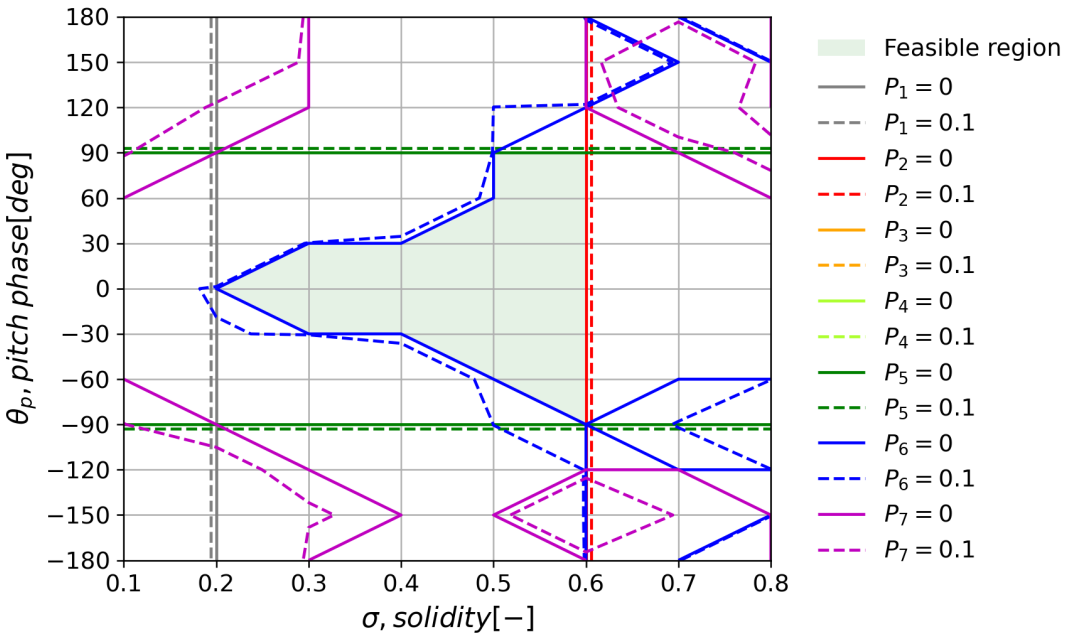

Figure 5.5: Penalties from different constraints, $A_{\theta_p} = 8[^\circ]$, $TSR = 2.5$

The pitch phase setting can be set such that the turbine can be used as a lifting device. This is shown in Figure 5.6. Note that almost no lift is produced when the pitch phase is set to zero. This is because the lift force can mainly be produced on the advancing and retreating sides of the turbine which only operate at a small angle of attack for $\theta_p = 0[^\circ]$. This angle of attack is zero with respect to the far field wind direction at $\theta = 90, -90$. However, due to the expansion of the streamtube, the blades do attain an angle of attack at these locations whereby the force at $\theta = 90$ acts as a positive lift force and at $\theta = -90$ acts as a negative lift force. Because the relative speed over the blades is larger at $\theta = 90$, this can result in a total positive lift force of the turbine when the resistance to the flow causes the streamtube to expand. This effect is therefore more substantial at larger solidities and explains the positive lift at large solidities for $\theta_p = 0[^\circ]$ in Figure 5.6. This indicates the asymmetry due to the rotation direction which is captured by the model.

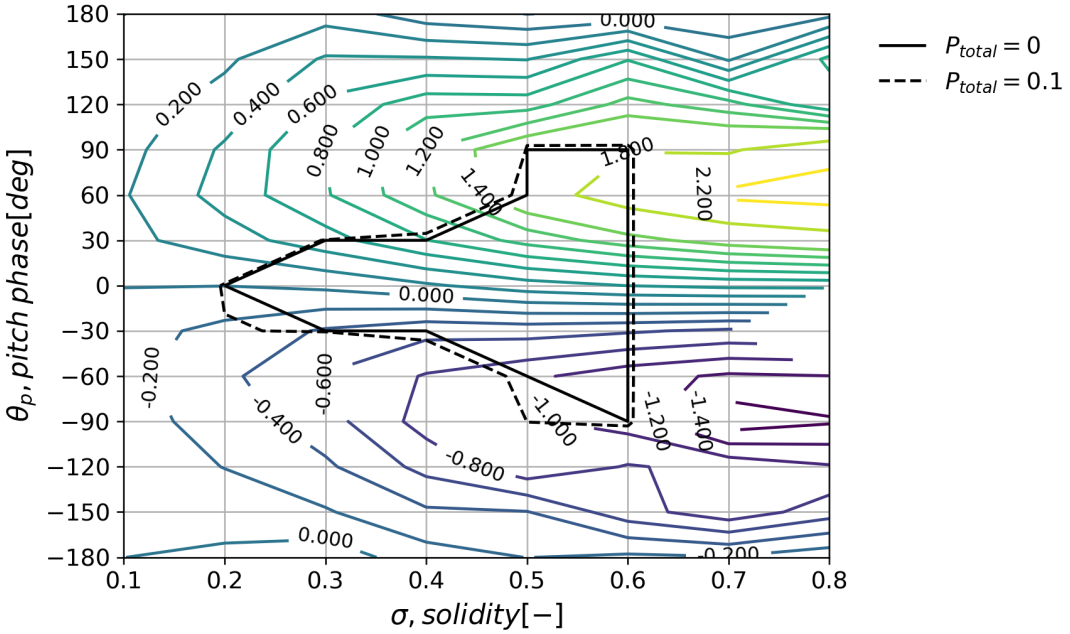

Figure 5.6: C_l for different designs and the total penalty showing the feasible design region, $A_{\theta_p} = 8[^\circ]$, $TSR = 2.5$

The lift coefficient in Figure 5.6 is asymmetric for positive or negative pitch phases. More lift can be attained for a positive pitch phase compared to the absolute lift for a negative pitch phase. This is due to the rotation direction of the turbine as indicated in Figure 5.7 and Figure 5.8 where a large reversed flow region occurs for the negative pitch phase setting.

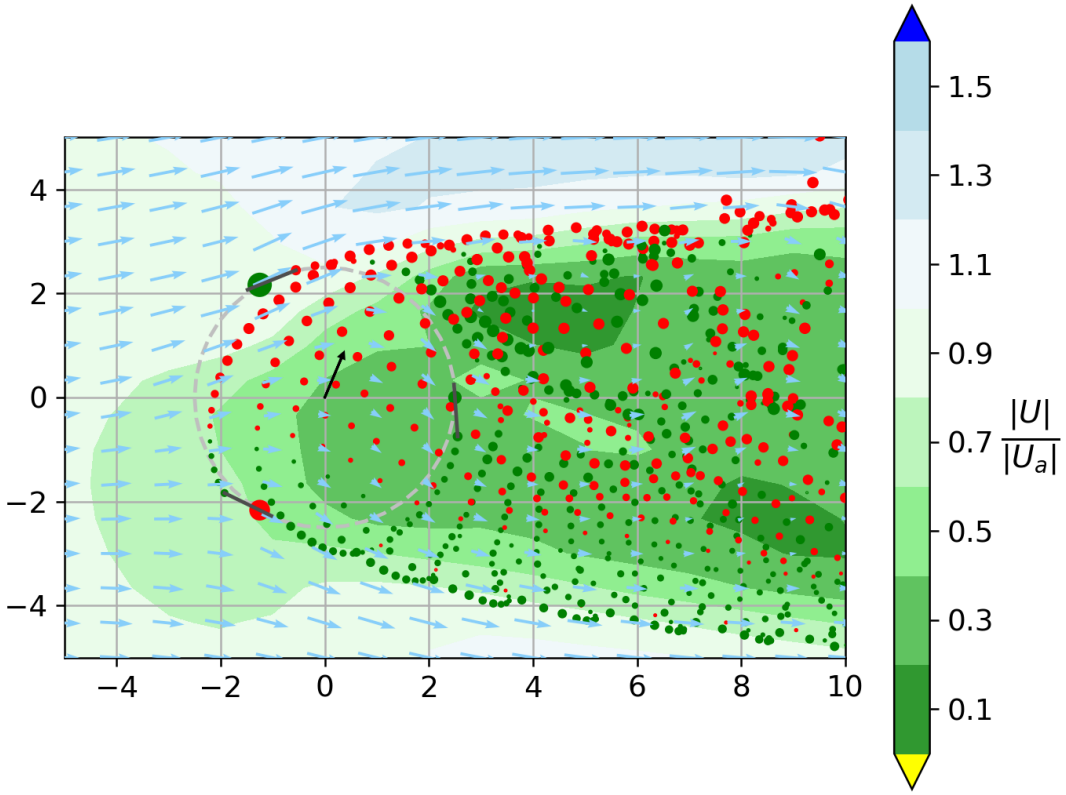

Figure 5.7: Flow field and last rotation averaged force vector for the fine2 computational settings and parameters: $\sigma = 0.6$, $A_{\theta_p} = 8[°]$, $TSR = 2.5$, $\theta_p = 60[°]$, results last rotation: $C_d = 0.727$, $C_l = 1.72$, $C_P = 0.256$

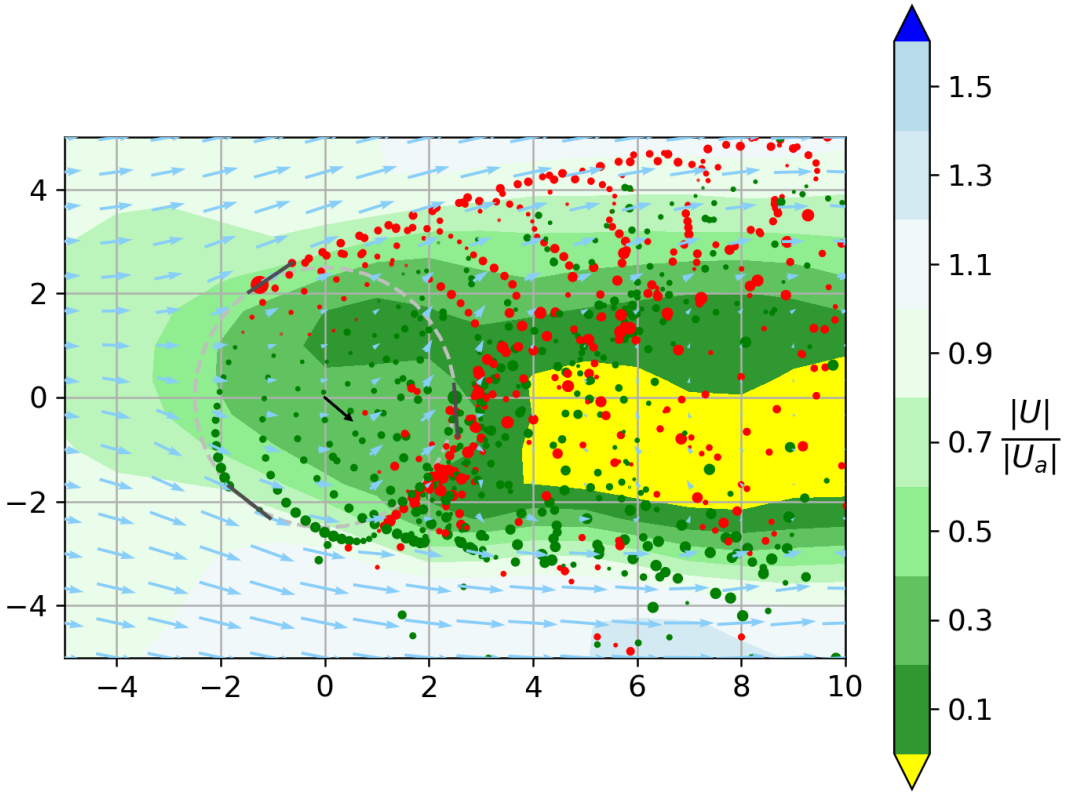

Figure 5.8: Flow field and last rotation averaged force vector for the fine2 computational settings and parameters: $\sigma = 0.6$, $A_{\theta_p} = 8[°]$, $TSR = 2.5$, $\theta_p = -60[°]$, results last rotation: $C_d = 1.02$, $C_l = -0.862$, $C_P = 0.335$

The pitch phase influences the lift force. This influence linearly becomes stronger for larger solidity. The sensitivity of the lift force with respect to the pitch phase can be expressed as a lift gradient ($\frac{dC_l}{d\theta_p}$). The maximum gradient occurs around $\theta_p = 0$, this is shown in Figure 5.6. The gradient at this pitch phase is evaluated using finite difference gradients. The backward difference gradient indicates that the lift is slightly more sensitive for negative changes in the pitch phase compared to the forward difference gradient for positive changes in the pitch phase.
The lift gradient for 2D airfoils without stall is $2\pi \approx 6.28$ when the angle of attack is expressed in radians. This indicates that the turbine is less sensitive to the pitch phase compared to non-stalled airfoils for the angle of attack. This confirms the statement from subsection 3.7.2 that a lifting VAWT is less sensitive for a correct measurement of the wind direction compared to wing-like systems. The pitch phase variation at large pitch phases does not indicate a sudden drop in lift as found on wings that surpass the stall angle.

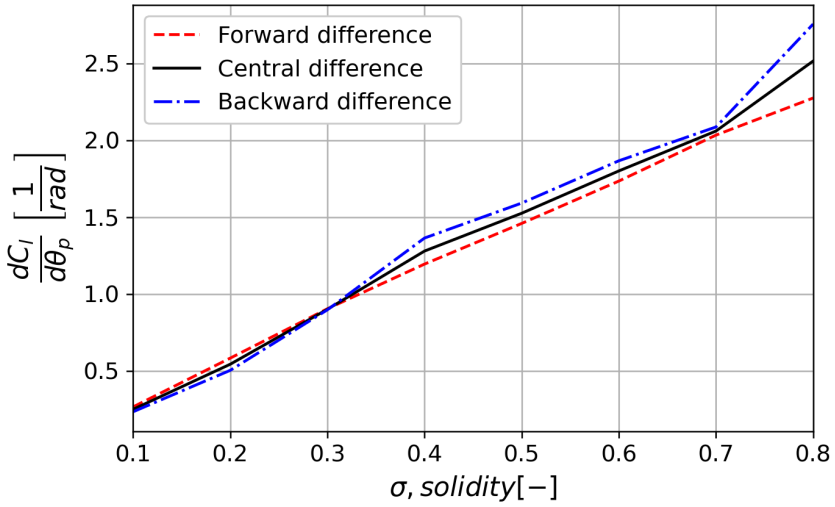

Figure 5.9: Lift coefficient gradient with respect to the pitch phase for $A_{\theta_p} = 8[°]$, $TSR = 2.5$ and $\theta_p = 0$

Maximum power in this investigation can be attained around medium solidity and a neutral or slightly positive pitch phase. The maximum power appears not to be sensitive to a particular solidity. Rather a large range of solidities provides close to maximum power.

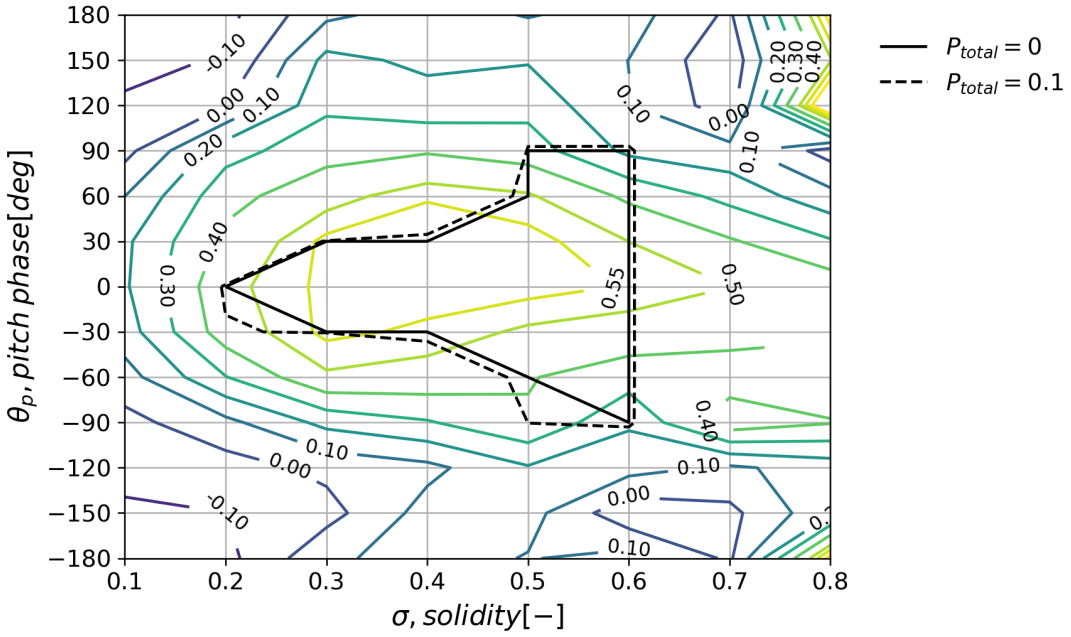

Figure 5.10: C_P for different designs and the total penalty showing the feasible design region, $A_{\theta_p} = 8[°]$, $TSR = 2.5$

5.2.1.4 TSR and pitch amplitude

This design space investigation only considers variable TSR and pitch amplitude. Figure 5.11 shows that the active constraints which indicate the attainable set of design parameters. These are the maximum absolute pitch amplitude (P_3), the maximum relative speed on the blades (P_4), the maximum angle of attack on the blades (P_6), and the requirement to produce power (P_7).

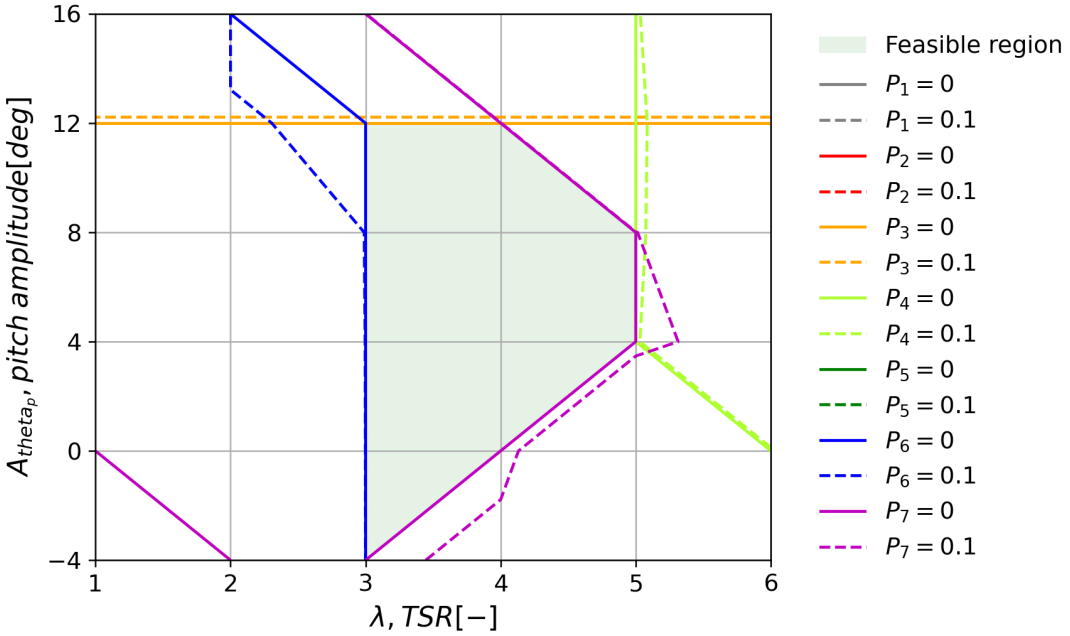

Figure 5.11: Penalties from different constraints, $\sigma = 0.4$, $\theta_p = 0[°]$

Due to the relatively high solidity, maximum power falls partly outside the feasible domain due to stall which occurs at lower TSR. Figure 5.12 indicates that for the fixed design parameters, maximum power can be attained for a pitch amplitude around $A_{\theta_p} = 7[deg]$.

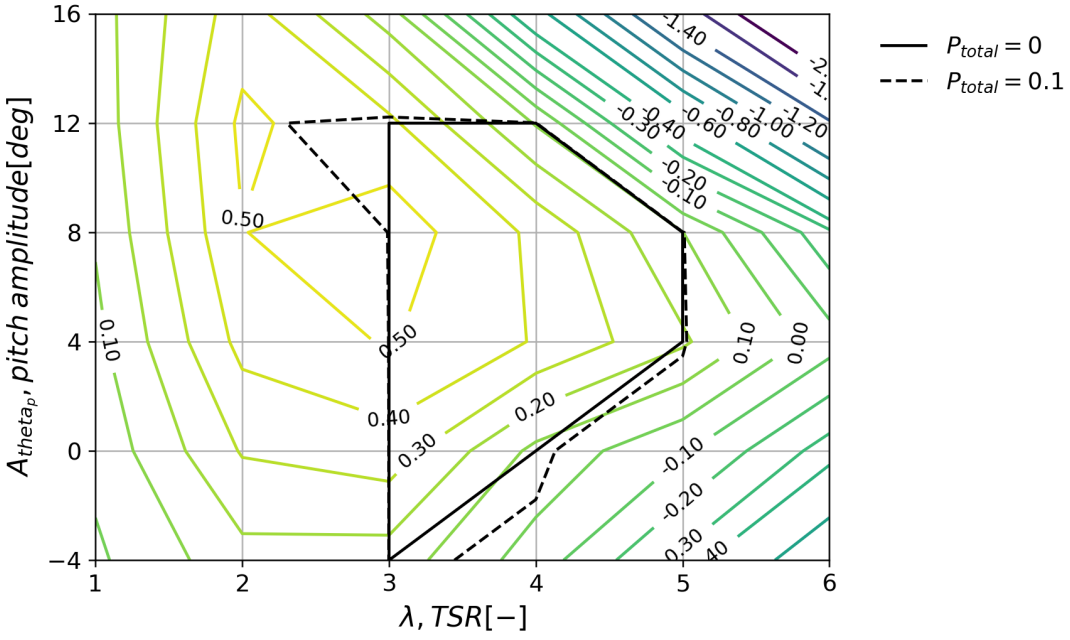

Figure 5.12: C_P for different designs and the total penalty showing the feasible design region, $\sigma = 0.4$, $\theta_p = 0[°]$

5.2.1.5 TSR and pitch phase

This design space investigation only considers variable TSR and pitch phase. Figure 5.13 shows that the active constraints which indicate the attainable set of design parameters are, the maximum relative speed on the blades (P_4), the maximum absolute pitch phase (P_5), the maximum angle of attack on the blades (P_6) and the requirement to produce power (P_7).

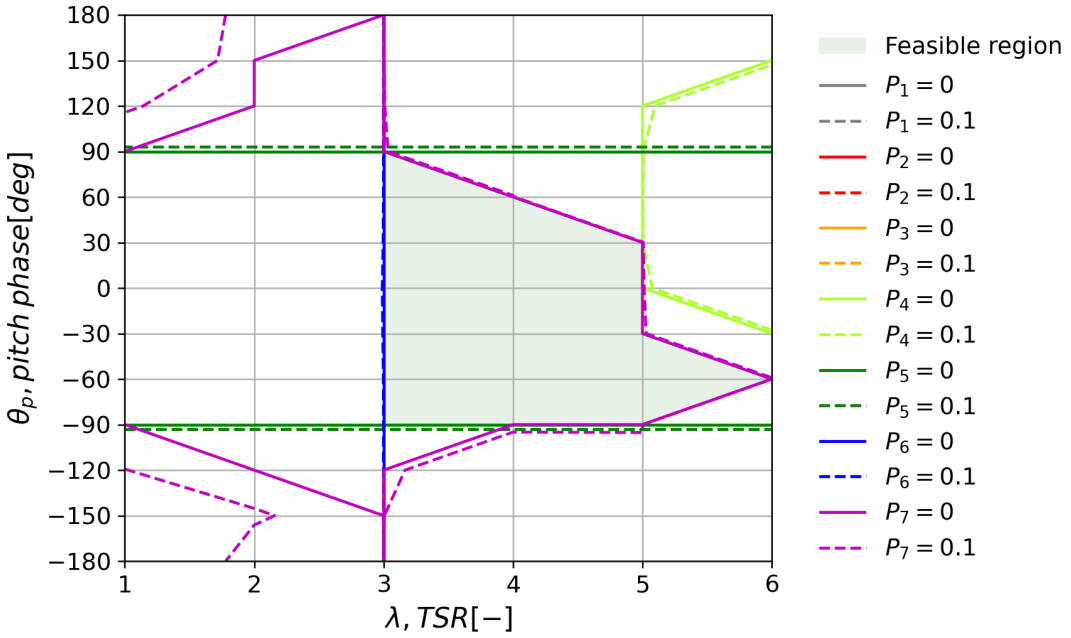

Figure 5.13: Penalties from different constraints, $\sigma = 0.4$, $A_{\theta_p} = 8[^\circ]$

As discussed in subsubsection 5.2.1.3, the pitch phase influences the generated lift as this allows a lift force to be generated on the advancing and retreating sides. The ability to provide lift increases for larger TSR as this increases the relative speed on the blades. Figure 5.14 indicates that a lift coefficient around 3 can be achieved inside the feasible domain, therefore without providing power to the turbine. This indicates that the VAWT concept can be used as an unpowered lifting device.
The lift at $\theta_p = 0$ is small as there is no large streamtube expansion as was found in subsubsection 5.2.1.3.

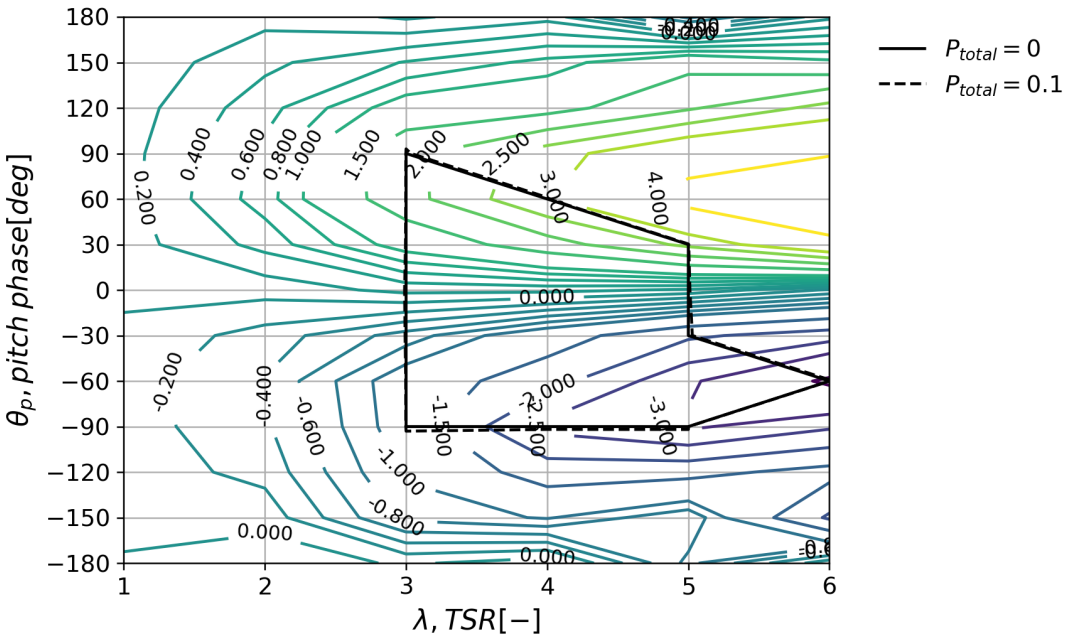

Figure 5.14: C_l for different designs and the total penalty showing the feasible design region, $\sigma = 0.4$, $A_{\theta_p} = 8[^\circ]$

As discussed in subsubsection 5.2.1.3, the lift force is influenced by the pitch phase and the sensitivity of the lift force with respect to the pitch phase can be expressed as a lift gradient ($\frac{dC_l}{d\theta_p}$). Figure 5.6 shows that the maximum sensitivity occurs around $\theta_p = 0$ and increases for larger TSR. The sensitivity at this pitch phase is evaluated using finite difference gradients. The forward and backward sensitivities are the same for lower TSR. At larger TSR, the lift is increasingly more sensitive to positive changes in the pitch phase. Note that this is opposite to the findings in subsubsection 5.2.1.3.
As also discussed in this section, the lift gradient for 2D airfoils without stall is $2\pi \approx 6.28$ when the angle of attack is expressed in radians. Figure 5.6 shows that the lift can be equally sensitive for the pitch phase at high TSR. This provides an additional incentive to limit the TSR of a VAWT such that the performance is less sensitive on the pitch phase setting which depends on the accuracy of the wind measurement.
The region with this high sensitivity falls largely outside the feasible domain and only occurs around the region where $\theta_p = 0$. Therefore the statement from subsection 3.7.2 that a lifting VAWT is less sensitive for a correct measurement of the wind direction compared to wing-like systems is still valid at lower TSR.

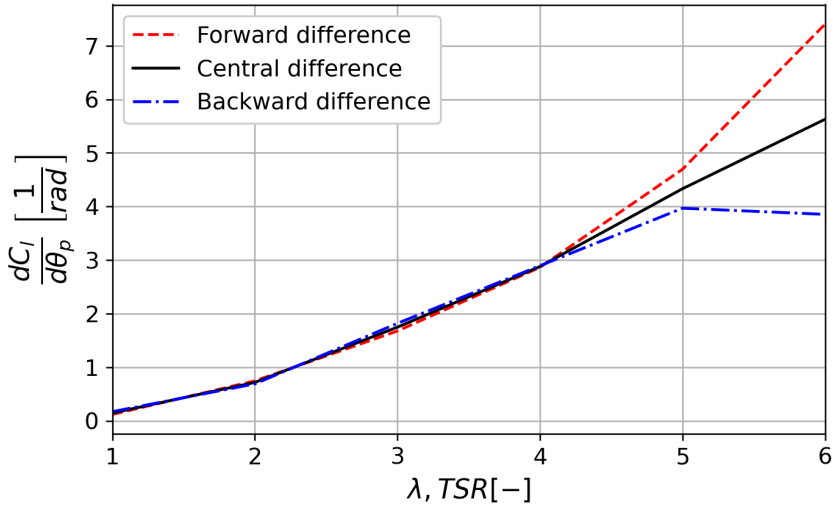

Figure 5.15: Lift coefficient gradient with respect to the pitch phase for $\sigma = 0.4$, $A_{\theta_p} = 8[°]$ and $\theta_p = 0$

The maximum power is not only influenced by the pitch phase but also by the TSR. It is therefore not only important to accurately measure the wind direction but also the wind speed to operate the turbine at a correct TSR.

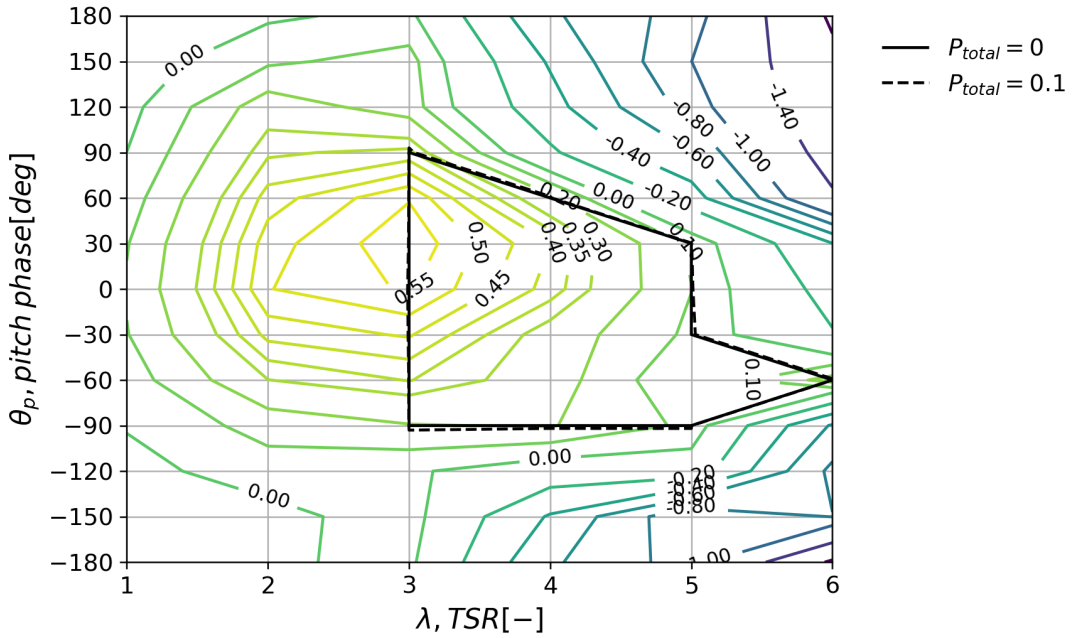

Figure 5.16: C_P for different designs and the total penalty showing the feasible design region, $\sigma = 0.4$, $A_{\theta_p} = 8[°]$

5.2.1.6 Pitch amplitude and pitch phase

This design space investigation only considers variable pitch amplitude and pitch phase. Figure 5.17 shows that the active constraints which indicate the attainable set of design parameters. These are the maximum absolute pitch amplitude (P_3) , the maximum absolute pitch phase (P_5) and the maximum angle of attack on the blades (P_6). The constraint for the requirement to produce power (P_7) is dominated by the other constraints.

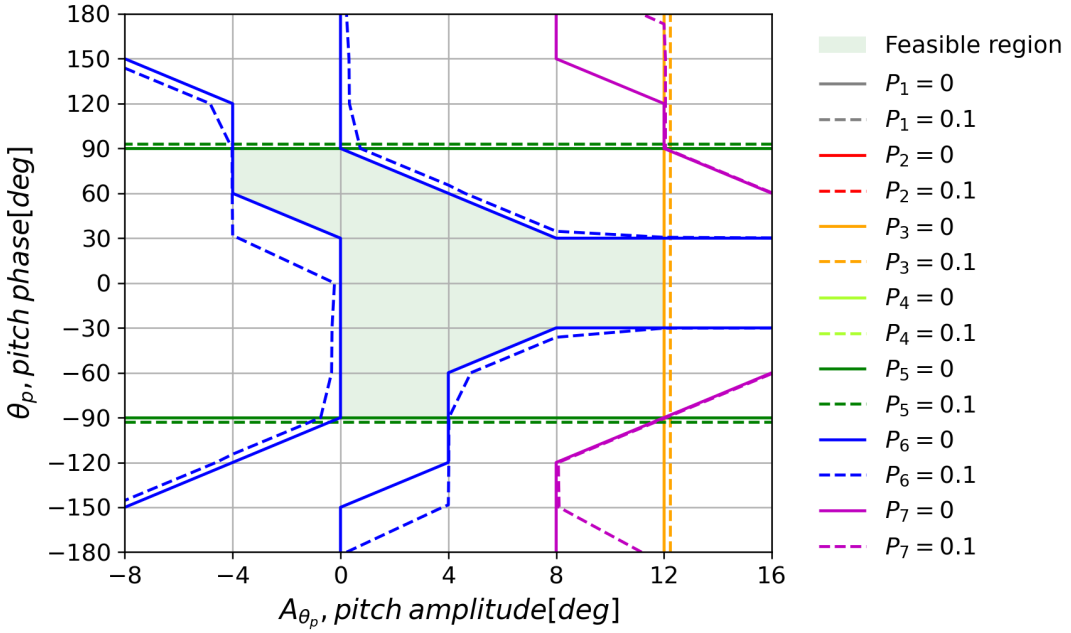

Figure 5.17: Penalties from different constraints, $\sigma = 0.4$, $TSR = 2.5$

For the fixed parameters of this investigation, the produced power is highest for a positive pitch amplitude and pitch phase. The produced power appears relatively insensitive for these exact settings of these parameters.

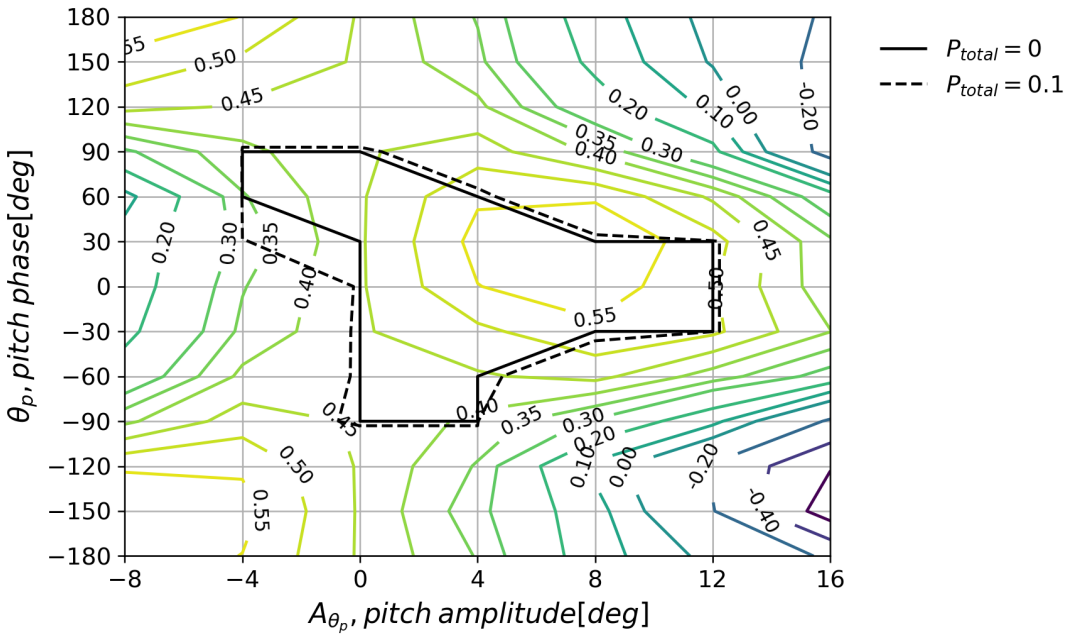

Figure 5.18: C_P for different designs and the total penalty showing the feasible design region, $\sigma = 0.4$, $TSR = 2.5$

5.2.2 Boundedness

The objective functions should be bounded to prevent divergence of the optimization process and to avoid unrealistic solutions. As shown in subsection 5.2.1, the parameters which determine the turbine performance

(C_d, C_l and C_P) are not always well bounded. One example of this is the lift coefficient in Figure 5.14 which increases for increasing the TSR. Therefore not all objective functions without penalization are naturally well bounded. The figures in subsection 5.2.1 show that C_P appears to be well bounded for all 2D slices of the design space. Even if the objective appears to be bounded, this is not necessarily the case because this is based on the 2D slices of the design space. A combination of multiple design variables might lead to an unbound design space. It cannot be concluded from these figures if the higher dimensional design space is properly bounded. Therefore penalty functions are applied to modify the objective function such that the design space is well bounded.

5.2.3 Linearity

The figures in Appendix C show that the performance parameters (C_d, C_l and C_P) are non-linear with respect to the design variables. Therefore the objective functions are non-linear. This means the objective functions can have multiple local optima which might make it more difficult to find the global optimum. It can also not be proven that the solution is a global optimum. This non-linearity has to be considered when selecting the optimization algorithm.
The linearity of the constraints also determines the properties of the optimization problem. The constraint functions are linear for the minimum relative chord length (P_1), the maximum relative chord length (P_2), the maximum absolute pitch amplitude (P_3) and the maximum absolute pitch phase (P_5). The nonlinear constraints are the maximum relative speed on the blades (P_4), the maximum angle of attack on the blades (P_6), and the minimum requirement to produce power (P_7).

5.2.4 Convexity

Convexity indicates the properties of the optimization problem which provides information about the design space and can be used to select an appropriate optimization method.
The objective function is convex if the second derivative of the objective function is never negative with respect to the design variables ($\frac{\mathrm{d}^2 f}{\mathrm{d}X_i^2} \geq 0$). This is not the case for this problem because this is not true for the performance parameters which show local optima in the figures in Appendix C.
A feasible domain is convex if every two points in the domain can be connected by a straight line that lies completely inside the feasible domain. Convex domains are favorable for optimization as it can be hard for algorithms to find all local optima in a non-convex feasible domain. The non-linear constraints result in non-convex feasible domains. Therefore the domain in this study is non-convex as shown in the figures in Appendix C. Therefore there might be multiple local boundary optima.

5.2.5 Monotonicity

The figures in Appendix C show that the partial derivatives of the objective function with respect to the design variables are not always of the same sign. This indicates that the performance parameters and therefore the objective functions are non-monotonic. Therefore local optima can occur in the design space. It is therefore not possible to prove that any found optimum is the global optimum however the initial investigation of the design space can provide guidance for selecting an appropriate region for the starting points.

5.2.6 Sensitivity analysis

To investigate the resulting optimum of the optimization procedure, the partial gradients of the objective function at the optimum point have to be evaluated. When evaluating the partial gradient of the objective function with respect to the design variables, forward finite difference is used. A sensitivity analysis is done to evaluate the appropriate step size such that the gradient is accurate and both the numeric error and the truncation error are low.
The objective functions are a result of the performance parameters. Therefore these parameters are used to determine the sensitivities. The step size used to evaluate the sensitivity gradient should be sufficiently small such that the gradient is evaluated at the point of interest and the truncation error is low. If the selected step size is too small, numeric noise can influence the gradients. The gradient is 0 for step sizes below 1e-16 because this step size is below the floating point accuracy of the model computations. An accurate gradient is obtained for step sizes around the region where the gradient is constant and does not depend on the step size. Figure 5.19 shows only the sensitivities of C_P from step sizes of $dA_{\theta_p} = 10^{-11}$ to 10^{-7} are accurate.

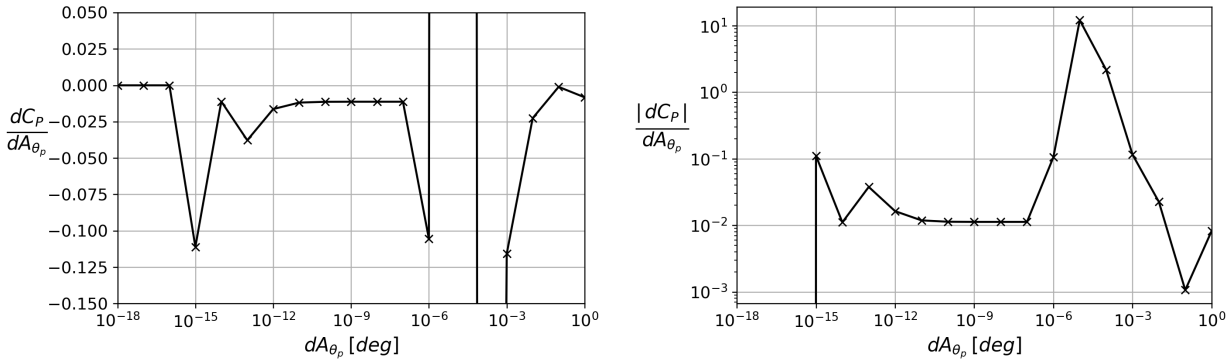

Figure 5.19: Power coefficient response sensitivity of A_{θ_p} at $\sigma = 0.4$, $A_{\theta_p} = 8[deg]$, $TSR = 2.5$, $\theta_p = 0[deg]$

The sensitivity analysis of all design parameter step sizes for all performance parameters is shown in the figures of Appendix D. Based on these figures, the lower and upper bound of accurate gradients is determined. For all design parameters, a step size of 1e-9 is considered to be accurate. Therefore this step size is selected for every parameter as indicated in Table 5.2.

Table 5.2: Parameters step sizes for which the performance sensitivity is constant

	σ	A_{θ_p}	TSR	θ_p
Lower bound	1e-14	1e-11	1e-12	1e-9
Upper bound	1e-8	1e-7	1e-7	1e-7
Selected step size	1e-9	1e-9	1e-9	1e-9

5.2.7 Smoothness

Many physical phenomena show smooth performance variation when changing the design variables. Numeric models can show non-smooth responses with respect to variation of design variables due to discretization errors. For small design variations, numeric noise causes non-smooth responses, therefore the selected step size of subsection 5.2.6 ($1e-9$) is used to investigate the smoothness of design variables.
The smoothness is evaluated for the response parameters C_l, C_d and C_P as a function of the design parameters. This investigation indicates that most responses appear linear on a small domain and are therefore smooth. Only the solidity has non-smooth and sometimes non-monotonic responses as shown in Figure E.2 and Figure E.3. All results of the smoothness investigation are shown in Appendix E. Figure E.12 indicates slight non-smooth however still monotonic responses for C_P.
The design space investigation of section 5.2 shows that all design parameters show smooth responses for large step sizes. Based on these findings, the design space can be considered sufficiently smooth for optimization.

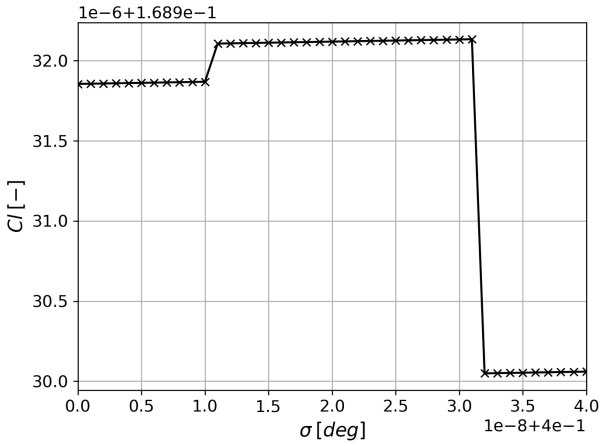

Figure 5.20: Smoothness of C_l as a function of σ for a step size of $\Delta\sigma = 1e-9$

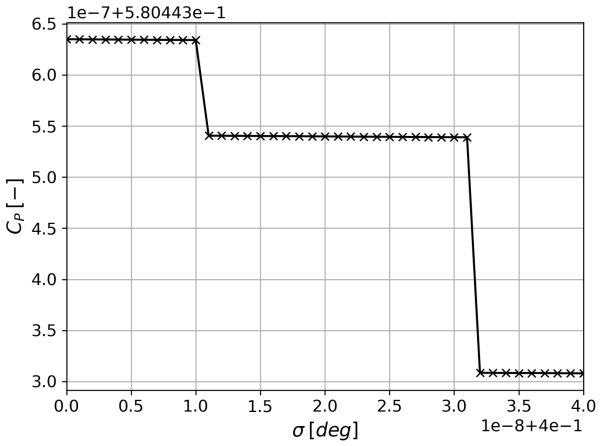

Figure 5.21: Smoothness of C_P as a function of σ for a step size of $\Delta\sigma = 1e-9$

5.3 Optimization procedure

This section describes the steps of the optimization process. The section starts by describing the selection of the start points. Next, the working principles and efficiency of the optimization algorithm are discussed. Finally, the termination criteria and optimum investigation procedure are discussed.

5.3.1 Initial points

The selection of the start point of the optimization is arbitrary however this can have a substantial effect on the required function evaluations and the computational time. It is therefore desirable for the algorithm to start near the optimum location however the starting region should not be selected on a small part of the domain as this is more likely to result in local optima. Because the location of the optimum is unknown, it is unknown where to start. Therefore the design space is mapped using brute force evaluation of some points in the design space. This is an inefficient method for optimization however it can provide rough guidance on where to start the optimization. To efficiently probe the performance in the design space, Latin Hypercube Sampling (LHS) is used. This is a design of experiments method that efficiently distributes the initial points over the design space. LHS is suitable for box-like domains. The limits of the feasible regions of the figures from subsection 5.2.1 are used to limit the domain of the initial sample points as shown in Table 5.3. Therefore some initial points may be infeasible however all points will be near the feasible region.

Table 5.3: Domain of the initial sample points

	σ	A_{θ_p}	TSR	θ_p
Minimum initial value	0.2	-8	3	-90
Maximum initial value	0.7	12	6	90

Optimization is turned on in the LHS function. This provides a better space-filling as described by the Python, Scipy function documentation [9]. LHS is programmed such that the generated start points are reproducible.
To start the optimization, at least one more point than the number of dimensions $(N+1)$ is required to start the algorithm of subsection 5.3.2. The number of initial points should not be too large as the algorithm is more efficient at finding the optimum and the extra evaluated points are likely not to be near the optimum. However, if the number of initial points is too low, the algorithm cannot start at a location near the optimum and the initial step sizes of the algorithm will be large as this is determined by the distance between the points. The number of selected initial points is $3^{N_{dimensions}}$. For 2D optimization, this results in 9 initial

points and for 4D optimization, this results in 81 initial points. This is respectively illustrated in Figure 5.22 and Figure 5.23.

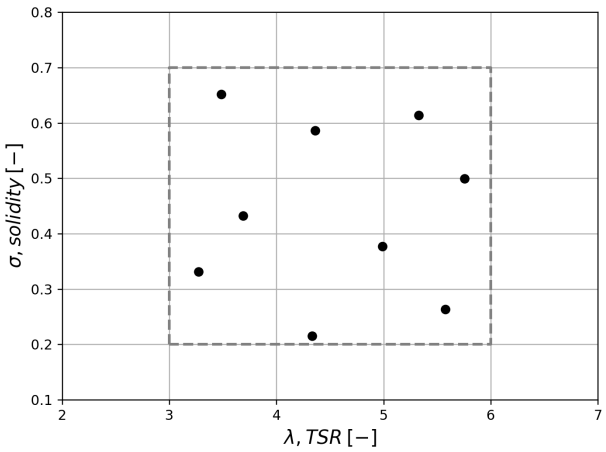

Figure 5.22: LHS initial points 2D design space

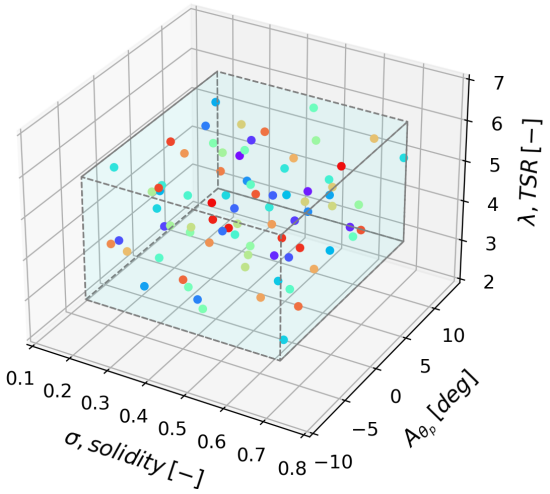

Figure 5.23: LHS initial points 4D design space

The thruster and combined modes do not tend to converge from the LHS start points because the simplex of these points spans a large region. Therefore these modes use the results of the optimized turbine in port, two points optimized for maximum positive or negative lift and two points optimized for maximum positive or negative lifting efficiency. These points provide feasible start points and usually at least one of these points already performs reasonably well for the objective.

5.3.2 Algorithm

The Nelder-Mead Simplex (NMS) algorithm (sometimes referred to as the polytope algorithm) works by reflecting the design coordinates of the worst points over the average design coordinates of the non-worst points. Equation 5.13 is used to evaluate the reflected point which is illustrated in Figure 5.24. This method uses only direct function evaluations (0-th order method) and does not compute gradient information. However, the difference in function values is used to determine a reflection direction which is a coarse estimate for the gradient direction used to evaluate the next design point. The NMS algorithm of Figure 5.24 uses N as the number of design dimensions, i as the index for a specific design parameter and j as the index for the order of the design points whereby $j = 1$ indicates the best design point.

$$X_{r,i} = 2\frac{\sum_{j=1}^{N} X_{i,j}}{N} - X_{i,N+1} \tag{5.13}$$

Modified Nelder-Mead Simplex (MNMS) algorithm uses the same terminology as regular NMS. This modified algorithm is developed to improve the next design point guess by improving the search direction to be closer to the gradient direction. This method uses the function values to determine an improved search direction. This is an operation without the use of the model and does therefore require little computational time. The reflected point for this method is obtained by using Equation 5.14. This method still uses the average of the non-worst points as the origin of the search direction. This is the first term of Equation 5.14. The search direction is determined by the second term in Equation 5.14. This uses a weighted average method analogous to a moment sum where x1-x3 is the lever arm and where f3-f1 is the weight. This sum is divided by the sum of the weights to obtain the total lever arm which is used to determine the location of the reflected point. Examples of this method are shown from Figure 5.25 to Figure 5.31. These figures indicate that the search direction is improved if the difference of non-worst objective values in the simplex is large with respect to the worst point. If this relative difference is small, the modified algorithm works similar to the regular NMS algorithm. The MNMS algorithm can sustain large gradients and therefore makes the optimization process

less sensitive for smooth penalty functions. The MNMS algorithm also works for negative or zero values as respectively shown in Figure 5.30 and Figure 5.31.
Due to the improved search direction, the MNMS is supposedly more efficient and less likely to oscillate during the optimization process.

$$X_{r,i} = \frac{\sum_{j=1}^{N} X_{i,j}}{N} + \frac{\sum_{j=1}^{N} (X_{i,j} - X_{i,N+1})(\widetilde{f}_{N+1} - \widetilde{f}_j)}{\sum_{j=1}^{N} \widetilde{f}_{N+1} - \widetilde{f}_j} \tag{5.14}$$

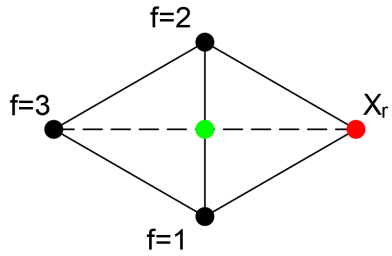

Figure 5.24: Regular NMS reflection

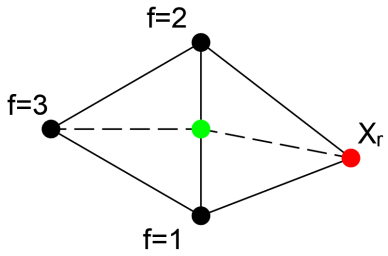

Figure 5.25: MNMS reflection

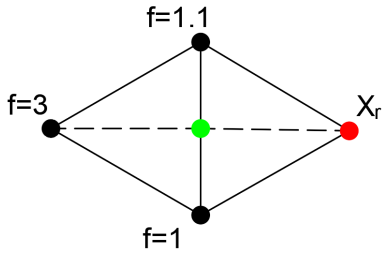

Figure 5.26: MNMS reflection, small difference in non-worst objective values

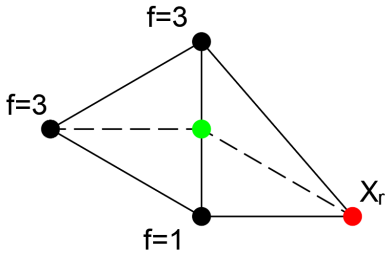

Figure 5.27: MNMS reflection, equal non-best objective values, arbitrary mirror direction

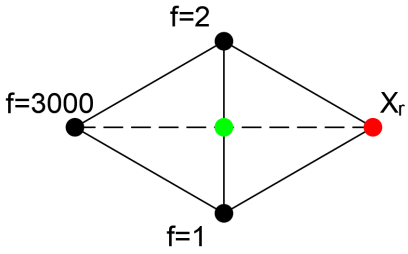

Figure 5.28: MNMS reflection, large worst objective value

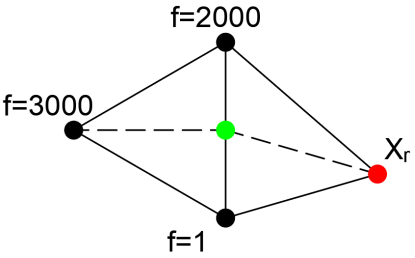

Figure 5.29: MNMS reflection, large non-best objective values

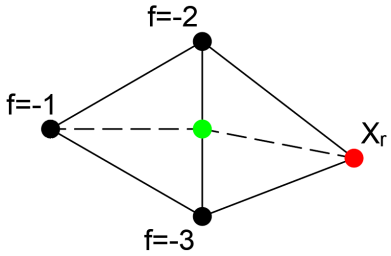

Figure 5.30: MNMS reflection, negative objective values

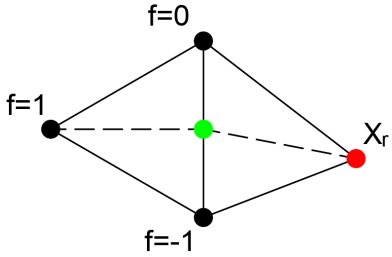

Figure 5.31: MNMS reflection, objective values of different sign

When the search direction is determined and the reflected point is evaluated, an expanded or contracted point can be evaluated along the search direction. This depends on the result of the model function evaluation. The expanded point expands the reflection by a factor of 2 whereby the contracted point contracts the reflection by a factor of 0.5. The expansion and contraction enables adaptive simplex size such that the algorithm can zoom out to move closer to the optimum in fewer function evaluations and zoom in to converge to the optimum. If the reflected or the contracted point fall outside the domain for allowable model input, either

by $\sigma < 0$ or by $TSR < 0$. The worst point is shrunken along the search direction by a factor of 0.25. This is indicated in Figure 5.34.

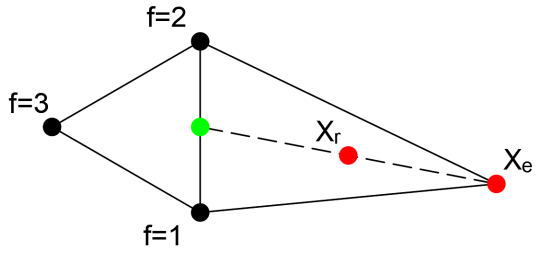

Figure 5.32: MNMS expansion

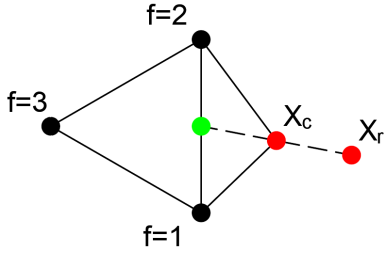

Figure 5.33: MNMS contraction

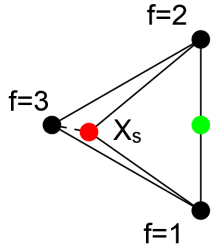

Figure 5.34: MNMS shrinkage

The algorithm which decides to reflect, expand, contract, or shrink the design point is the same for the NMS and the MNMS algorithm. The flow diagram of Figure 5.35 describes the optimization procedure. One iteration of this procedure is referred to as a loop.

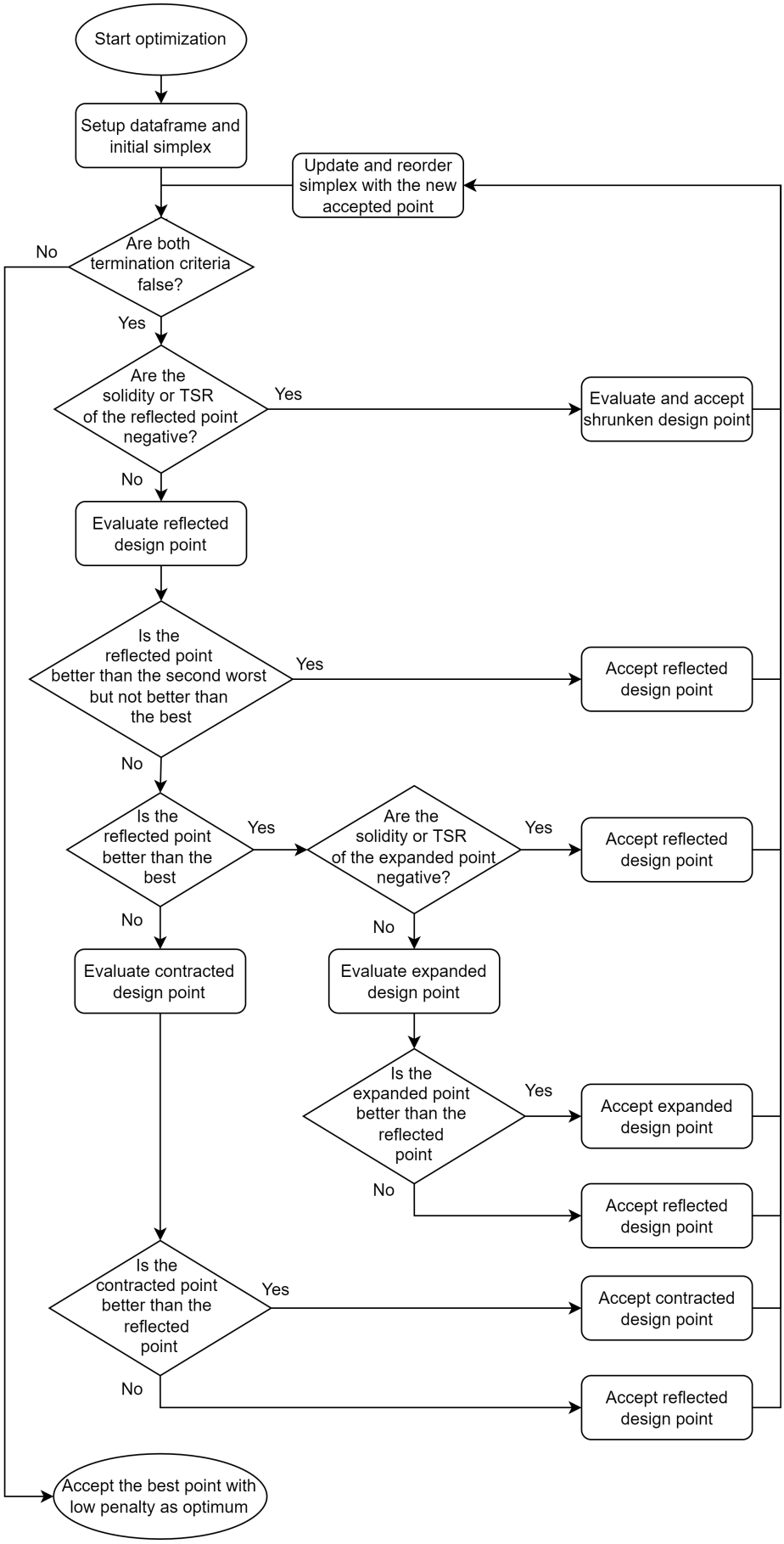

Figure 5.35: Flow diagram of the MNMS algorithm

5.3.3 Termination

The algorithm attempts to improve the objective function to find the best values for the design variables by converging to a steady solution. When the algorithm has converged to a steady solution, the optimization is complete and the algorithm can be terminated.
This convergence is determined based on the standard deviation of the objective values in the simplex as is a usual termination criterion for NMS. If this is below $10e-4$, the optimization is considered to be finished. The evolution of this standard deviation is shown in Figure 5.37.
When progress becomes slow and additional function evaluations do not result in improvement of the objective function, the optimization also is considered to be finished. This is shown in Figure 5.36 where the simulation was terminated because the objective was not improving.
To limit the number of function evaluations, the algorithm can also be stopped after a set amount of function evaluations. Usually, it requires in the order of 100 evaluations for the algorithm to converge to a solution. Therefore this termination limit is usually set around 140 function evaluations.

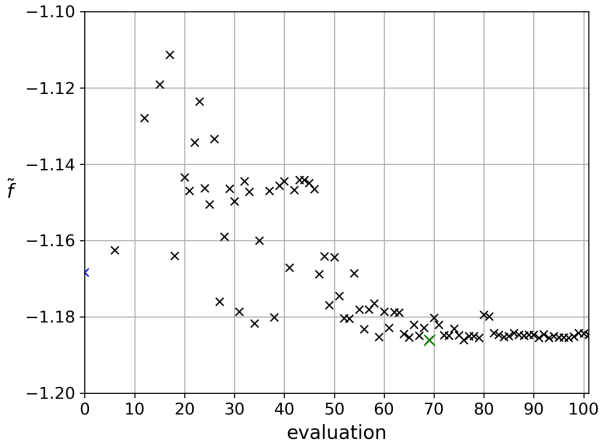

Figure 5.36: Progress of evaluated points for the optimization of a turbine at sea at $\beta_a = 120[°]$

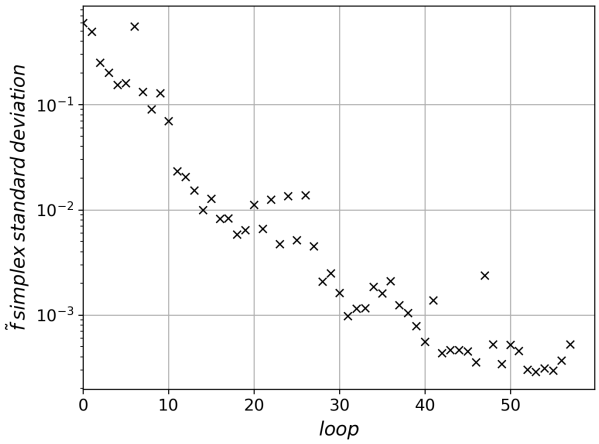

Figure 5.37: Standard deviation development for the optimization of a turbine at sea at $\beta_a = 120[°]$

The best performing point is not always selected as the optimum. If the best performing point is a singular point without the algorithm having converged to a region around this point, a point in a cluster of similar designs is preferred as this is a local optimum of the point cluster. If the best performing point is best even though this point has a severe penalty, a worse performing point with low or no penalty is preferred. Therefore the point with the lowest objective value is not always accepted as the optimum.

5.3.4 Optimum investigation

When an optimum point is selected, the optimality conditions should be true for this point. These conditions indicate that the point should be stationary and the Hessian should be positive definite, meaning the objective function should increase in all possible design directions. The objective function is not known algebraically, therefore the optimality conditions cannot be evaluated directly. Because the selected optimal point is in a cluster of other points of similar designs. These surrounding points can be used to indicate if the design improves in some combinations of design directions. This clustering of evaluated points near the optimum is shown in Figure 5.38. If this indicates that the surrounding points are worse performing, the selected point is assumed to be an actual optimum.
If no penalties are active at the selected optimum, this is referred to as an interior optimum. Otherwise, the point is an exterior optimum with active constraint(s). The possible active constraints should also be investigated. This indicates whether the objective can be improved by constraint relaxation and therefore by changing the formulation of the optimization problem. This also indicates the design direction where more performance can be attained.

5.4 Results

This section describes the results and resulting designs of the VAWT optimization for different modes of operation and computational settings. Per operational mode, the performance of the resulting optimal designs for different wind conditions is weighted according to the probability of occurrence of certain conditions, as described in section 2.3 and section 2.4. This is used to evaluate the average performance at sea, and the total performance which includes the 10% of time when the turbine cannot be used in any mode of operation. The variation in optimum design parameters depending on the wind conditions in different modes of operation is also discussed. All results of optimized designs are presented as tables in Appendix F.

5.4.1 Turbine in port

The turbine in port operational mode is similar to a regular stationary wind turbine. This is therefore a relatively simple optimization problem where the objective is to optimize the power coefficient (C_P). This does therefore not depend on the apparent wind conditions.
As the optimization problem uses a 4D design space, it is hard to visually indicate the optimization algorithm moving through the design space. To provide insight into the optimization process, a simplified problem of a turbine without pitch variation is evaluated. This is a 2D optimization problem with only the solidity and the TSR as design variables. These results and evaluated points are shown in Figure 5.38 where the background shows the contours of the objective function based on grid points from subsection 5.2.1. This figure indicates the evaluated points and the cluster of points as the algorithm converges to the optimum.

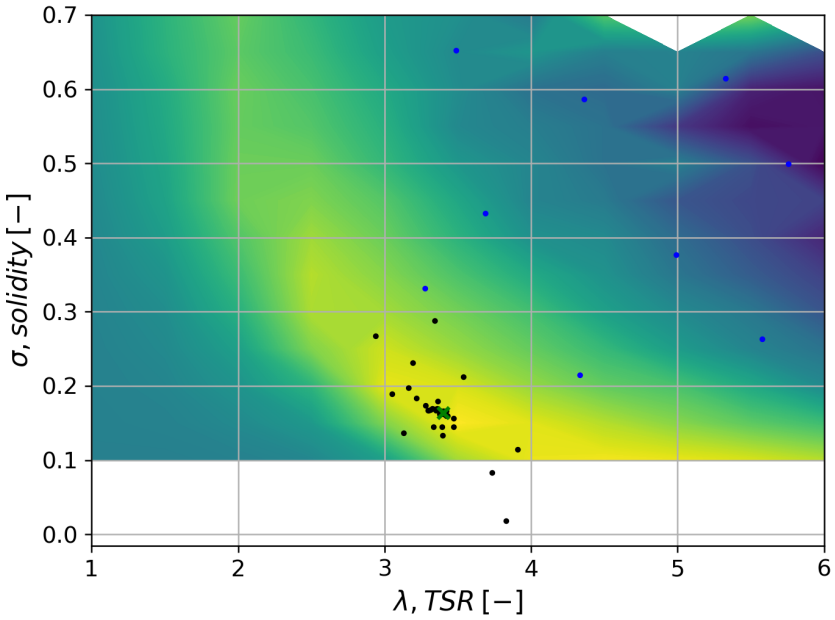

Figure 5.38: The optimization process for a turbine in port without pitch, starting from blue dots as initial points, converging with the black dots for every function evaluation, and resulting in the green x design as optimum

The turbine in port is also optimized with all design variables, including pitch variation. This optimization is 4D as it uses 4 design variables. The design and performance parameters of the best performing designs for both optimized turbines for in port conditions is given in Table 5.4.
No constraints were active at these optima, therefore the resulting optimal points are interior optima. The drag coefficient for both optimized turbines is close to 1 which is to be expected for an optimally operating turbine. The difference in performance for 2D and 4D optimization indicates that pitch variation can increase the power production of a stationary VAWT by 6.13%. Note the lower TSR and larger solidity for the optimal design with pitch variation. The solidity is 87.1% larger compared to the optimal turbine without pitch variation. To reduce the turbine loading for these larger blades, the TSR of the turbine with pitch variation

is 13.1% lower.
The optimal performing turbine for the case with pitch variation results in a configuration that produces lift. This is not required however it is interesting to note that the configuration with maximum power produces a lift force averaged over the rotation whereas the turbine without pitch variation does not generate a substantial lift force. This is also indicated by the average force arraow in the center of the turbines in Table 5.4 and Figure 5.40.

Table 5.4: Results of the optimization of a turbine in port with and without pitch variation

Case	σ	$A_{\theta_p}[^\circ]$	TSR	$\theta_p[^\circ]$	C_d	C_l	C_P	$\frac{U_{rel,max}}{U_\infty}$	$\lvert\alpha_{,max}\rvert\,[^\circ]$	P_{total}	$\tilde{f}$
2D	0.166	0	3.40	0	1.01	0.0187	0.587	4.37	13.4	0	-0.587
4D	0.310	7.14	2.95	56.4	1.06	1.10	0.623	4.13	13.1	0	-0.623

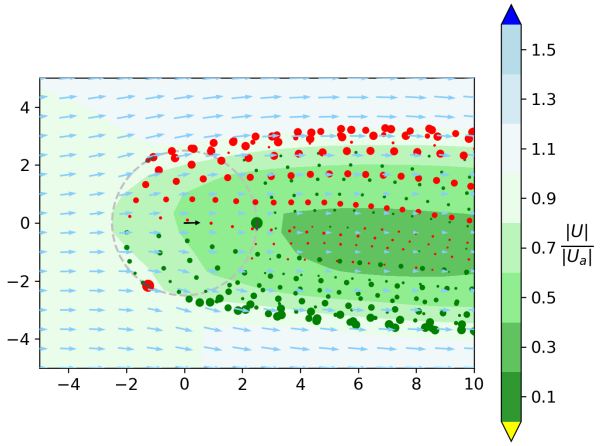

Figure 5.39: 2D optimized turbine in port

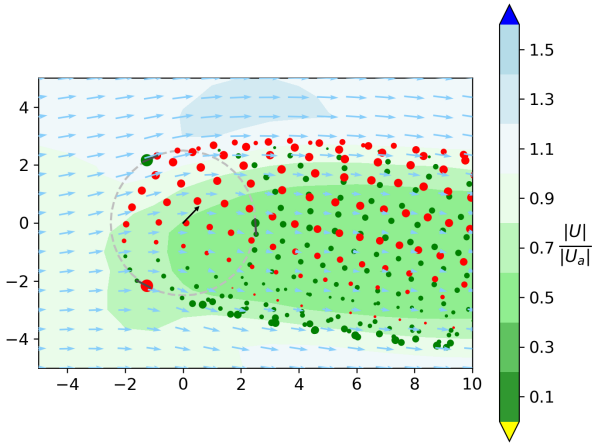

Figure 5.40: 4D optimized turbine in port

The turbine with pitch variation performs better and can operate at a lower TSR. Therefore this is preferred over a turbine without pitch variation. All optimization cases after this use the pitch variation parameters as design parameters.

5.4.2 Maximum lift

The maximum lift coefficient is a characteristic parameter of airfoils. The case of a non-driven turbine used to produce a lift force therefore is an interesting case for optimization. This optimization attempts to achieve maximum lift, regardless of the drag force, whilst operating within the constraints. The turbine should therefore not require power to operate, which is referred to as a driven turbine.
Because the direction of rotation might influence the lifting capabilities, both cases of positive ($C_l{}^+$) and negative lift ($C_l{}^-$) are evaluated. The design and performance parameters of the optimized designs are shown in Table 5.5. Both optimized designs have a penalty for the selected optimum. This indicates that the best points are external optima, slightly outside the feasible design region. For the case of maximum positive lift, the constraint for minimum positive power is active. This indicates that more lift could be provided if the turbine would be driven. The optimized configuration for the case of maximum negative lift has an active constraint for the maximum chord length. This indicates that more lift could be provided if a larger relative blade size would be allowed.
The largest difference between the optimum designs for positive and negative lift is in the solidity whereby the solidity of the negative lift case is 68.1% larger compared to the positive lift case. The other design parameters are similar. The performance for positive lift is slightly larger where positive lift can attain a 11.5% larger lift coefficient compared to negative lift as shown in Table 5.5. Where the case of positive lift requires power to operate, the case of negative lift produces some power. Note that the maximum angles of attack on the blades is different for both cases. It should also be noted that the simulations of the optimized

turbine for negative lift show periodic oscillations in the wake. This makes the operation for negative lift less steady and possibly more sensitive to fatigue.

Table 5.5: Results of the optimization for maximum positive and negative lift

Case	σ	$A_{\theta_p}[^\circ]$	TSR	$\theta_p[^\circ]$	C_d	C_l	C_P	$\frac{U_{rel,max}}{U_\infty}$	$\lvert\alpha_{,max}\rvert\,[^\circ]$	P_{total}	$\tilde{f}$
$C_l{}^+$	0.364	10.9	4.54	57.5	1.00	4.65	-0.00815	6.18	9.15	0.00665	-4.64
$C_l{}^-$	0.612	11.6	4.49	-52.2	1.10	-4.17	0.281	4.62	13.0	0.0277	-4.14

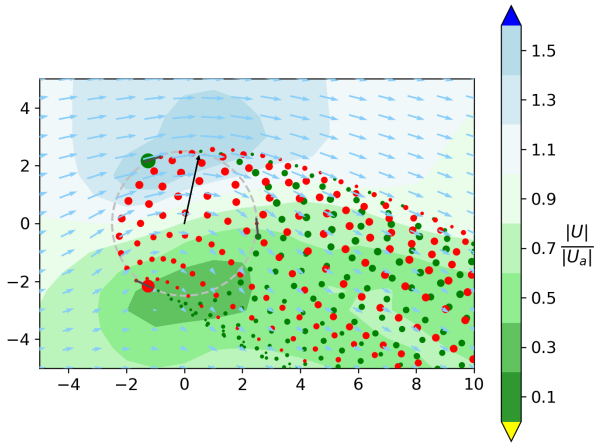

Figure 5.41: Optimized maximum positive lift

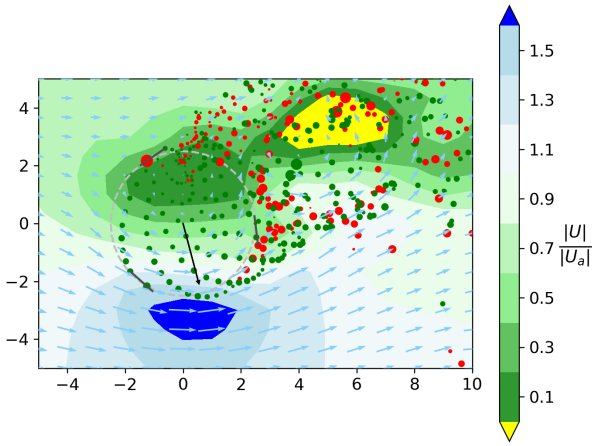

Figure 5.42: Optimized maximum negative lift

The optimization results show that a lift coefficient of $C_l = 4.65$ can be attained for positive lift from an almost non-driven turbine. This is a large lift coefficient, even when compared to multi-element airfoils.

5.4.3 Maximum lift efficiency

Upwind conditions are most frequently encountered when in transit at sea as shown in Figure 2.18. Therefore, lift driven WASP systems require a large lift over drag ratio to effectively operate in close hauled wind conditions. When using a lifting device in upwind conditions, the lift force will mostly be acting as a side force which increases the leeway angle and the induced resistance of the ship's hull which is not considered to be an efficient lifting body. Therefore it is important to have a large lift over drag ratio in upwind conditions when sailing and it is interesting to investigate the maximum lifting efficiency of a VAWT. For reference, the C_l/C_d ratio can reach upwards of $C_l/C_d = 100$ for the 2D NACA0015 polar as can be concluded from subsection 4.5.5.

Because the direction of rotation might influence the lifting capabilities, both cases of positive ($C_l{}^+/C_d$) and negative lift ($C_l{}^-/C_d$) are evaluated. To ensure the optimum converges to a realistic solution, a penalty is applied to the objective for $C_d < 0.1$. The design and performance parameters of the optimized designs are shown in Figure 5.44.

The optimized designs for positive lift efficiency has a penalty for the selected optimum due to a slight negative power coefficient. This indicates that this optimal point is an external optimum and that the positive lifting efficiency could be increased if the turbine was driven. This is logical as driven turbines can produce lift without any drag.

Both optimum designs for positive and negative lift are operating differently. The largest difference is the solidity whereby the solidity of the negative lift case is 118% larger compared to the positive lift case. A similar ratio in solidity differences is found in subsection 5.4.2. The performance for positive lifting efficiency is substantially better compared to negative lifting efficiency. Where the case of positive lift requires some power to operate, the case of negative lift produces power. Note that the maximum angle of attack on the blades is different and relatively low for both cases.

Table 5.6: Results of the optimization for maximum positive and negative lifting efficiency

Case	σ	$A_{\theta_p}[^\circ]$	TSR	$\theta_p[^\circ]$	C_d	C_l	C_P	$\frac{U_{rel,max}}{U_\infty}$	$\lvert\alpha_{,max}\rvert\,[^\circ]$	P_{total}	$\tilde{f}$
$C_l{}^+/C_d$	0.181	13.7	4.32	26.1	0.124	1.38	-0.00415	5.55	7.25	0.172	-11.0
$C_l{}^-/C_d$	0.395	10.4	4.70	-46.2	0.648	-2.77	0.0987	5.23	10.8	0	-4.27

This shows that a lift over drag ratio of $\frac{C_l{}^+}{C_d} = 11.0$ can be attained for positive lift from an almost non-driven turbine.

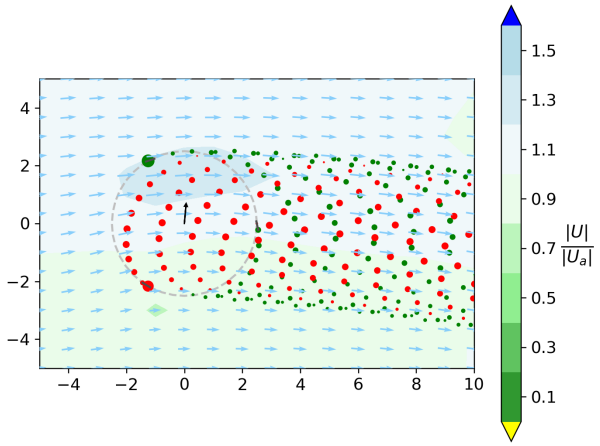

Figure 5.43: Optimized positive lifting efficiency, $\frac{C_{l+}}{C_d} = 11.0$

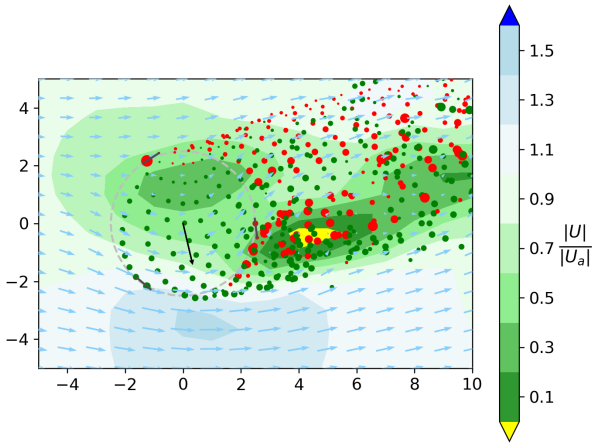

Figure 5.44: Optimized negative lifting efficiency, $\frac{C_{l-}}{C_d} = 4.27$

5.4.4 Turbine at sea

At sea, the VAWT can be used to provide power to the ship's propulsion system. Therefore the VAWT is optimized for the operational mode as a turbine to generate power in different wind conditions at sea. The drag force can benefit the equivalent propulsive power in stern wind conditions or reduce the equivalent propulsive power in headwind conditions. The simulations for port-side or starboard wind are copied as these modes of operation are equivalent irrespective of the apparent wind direction.
Figure 5.45 shows that sufficient power can be generated such that even in a direct headwind ($\beta_a = 180[^\circ]$), the power generation ($C_{P',turbine}$) is larger than the propulsive power required to overcome the drag force ($C_{P',thruster}$). Therefore the equivalent propulsive power is positive such that the ship could provide effective propulsion directly into a headwind.
No constraints are active for all optimized configurations for a turbine at sea. The weighted average power coefficient for the turbine mode at sea is $C_{P'} = 0.544$. This indicates that a VAWT operating as a turbine performs slightly worse compared to an optimized stationary VAWT from subsection 5.4.1.

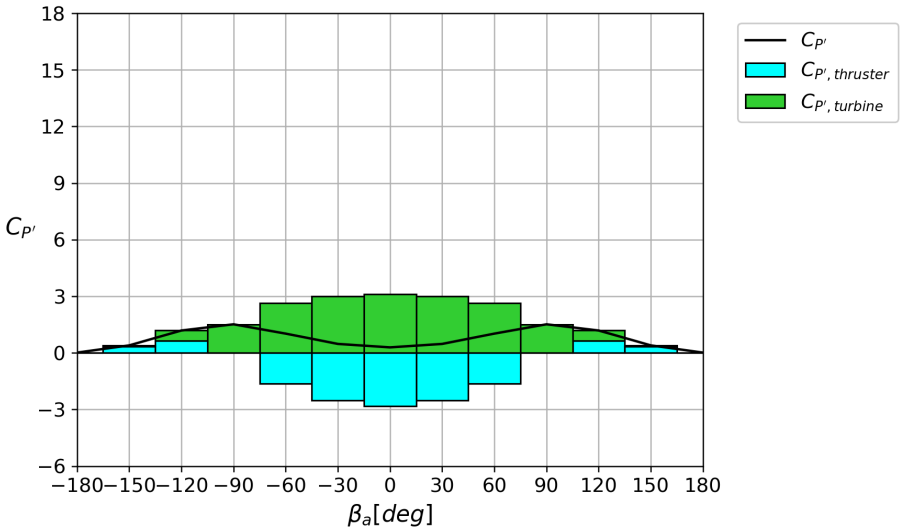

Figure 5.45: Turbine equivalent propulsive power at sea

5.4.5 Thruster at sea

At sea, the VAWT can also be used as a lifting device to provide a thrust force. This thrust force is equivalent to a propulsive power ($C_{P',thruster}$). This mode of operation does not include any power component where the power generated as a turbine can add to the propulsive power. However, the constraint that the turbine is non-driven (P_7) is still applied to the objective.
The VAWT is optimized to operate as a thruster to produce a thrust force in forward direction for different wind conditions at sea. Figure 5.46 shows that most propulsive power can be attained in beam wind conditions from $|\beta_a| = 60\,to\,90[°]$. This is to be expected as these conditions have a large apparent wind speed and the lift force is roughly aligned with the ship's course.
When no positive thrust can be produced, the equivalent power is set to $C_{P'} = 0$. The weighted average power coefficient for the turbine mode at sea is $C_{P'} = 4.79$. Therefore the operational mode of using the VAWT as a thruster at sea performs approximately 9 times better compared to a turbine at sea.

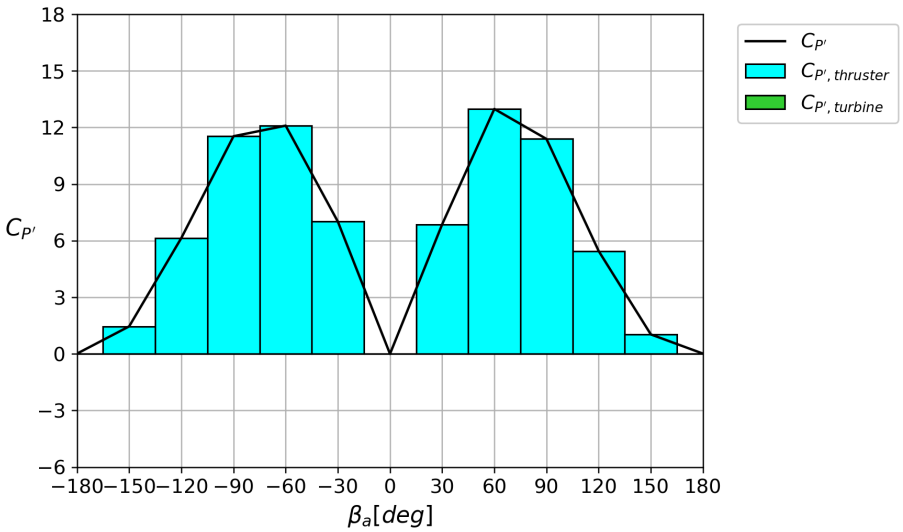

Figure 5.46: VAWT thruster equivalent propulsive power at sea

The constraint for positive power (P_7) is sometimes active for the wind conditions where $\beta_a > 0$. For the

wind conditions where $\beta_a < 0$, the optimum designs are often close to the maximum chord length constraint P_2.

5.4.6 Combined mode at sea

The combined mode combines the operational capabilities of a turbine and a thruster whereby the power production method depends on the apparent wind direction. Figure 5.46 shows that most propulsive power can be attained by operating as a thruster in beam wind conditions. Note that for $\beta_a > 0[^\circ]$. The performance for these wind conditions almost solely uses the thruster mode as the wind from this side requires positive lift which is more attainable for the counter-clockwise rotating turbine as shown by the results of subsection 5.4.2 and subsection 5.4.3.
For $\beta_a \leq 0[^\circ]$, the turbine power is also used to provide propulsion such that even in headwind conditions, the equivalent power coefficient is positive. This is the same condition and objective as the headwind condition in Figure 5.45. However, the result are slightly different designs and some differences in performance. This indicates and confirms that the converged optima can be local optima.

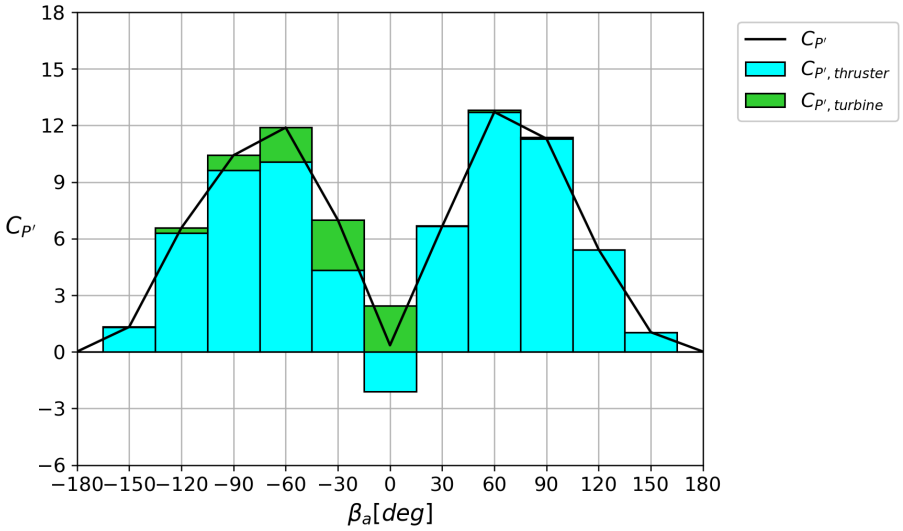

Figure 5.47: VAWT thruster and turbine equivalent propulsive power at sea

For the wind conditions where $0[^\circ] \leq \beta_a > 90[^\circ]$, the constraint for positive power (P_7) is active. This indicates that more equivalent propulsive power could be provided if the turbine was driven. For $\beta_a < 0[^\circ]$, the optimal designs are near the relative chord length penalty limit (P_2). This indicates that the thrust force in these conditions could be increased if a larger relative chord length would be allowed.

5.4.7 Modes design parameters comparison

The design parameters are optimized for different modes of operation. This resulted in many different designs which are suitable to a specific apparent wind condition. Figure 5.48 to Figure 5.51 shows the resulting design parameters for different wind conditions and different modes of operation. These figures can be used to compare the design parameters for different modes of operation.
For $\beta_a > 0[^\circ]$, all modes of operation show that a larger solidity is preferred for more sternward wind conditions. This is because stern wind conditions benefit from a large drag coefficient which can be obtained for a large solidity. The headwind condition shows the turbine and the combined mode at sea. These configurations would be expected to result in the same design because the combined mode cannot use the thrust force in headwind conditions.

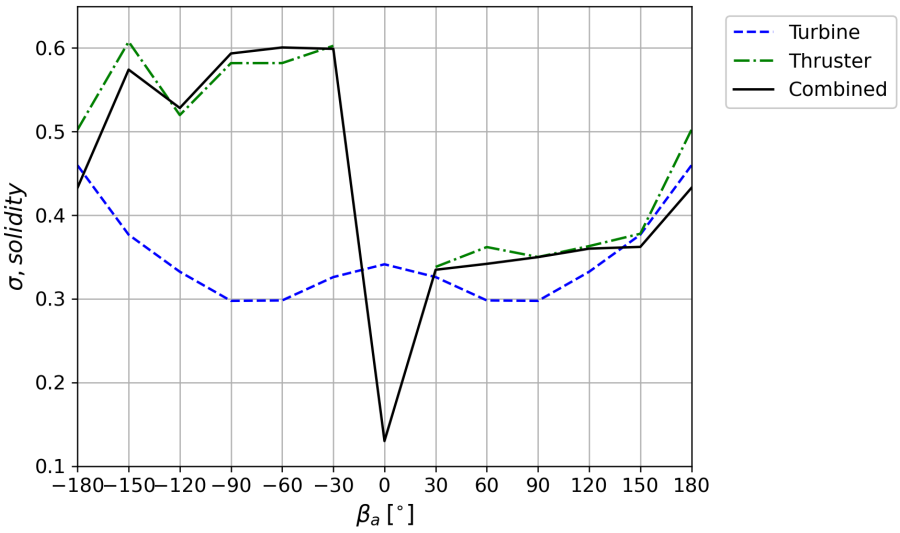

Figure 5.48: Optimized solidity (σ) parameter for different apparent wind directions

All modes require a large pitch amplitude in most wind conditions except stern wind conditions which requires a smaller pitch amplitude. The pitch amplitude for the thruster and the combined mode designs is similar for all conditions at sea. Where these modes show an almost constant optimum pitch amplitude around $A_{\theta_p} = 12[°]$, the thruster configuration shows a gradual reduction in required pitch amplitude for broader wind conditions.

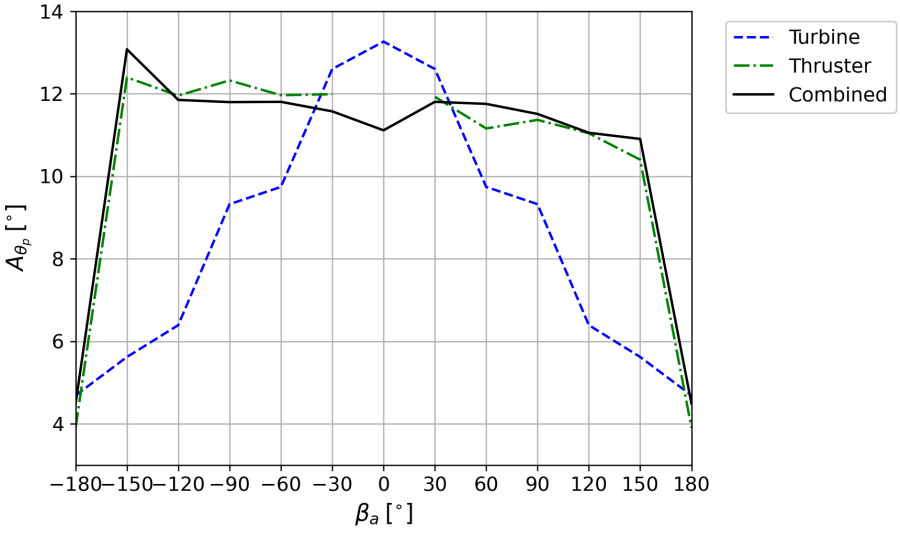

Figure 5.49: Optimized pitch amplitude (A_{θ_p}) parameter for different apparent wind directions

The TSR for the thruster and combined operation mode require a similar TSR whereas the turbine mode requires a lower pitch amplitude. The thruster and combined modes require a larger TSR as this allows for a larger lift production as investigated in subsection 5.4.2. The same TSR is required for all modes of operation in stern wind conditions ($\beta_a = 180[°]$).

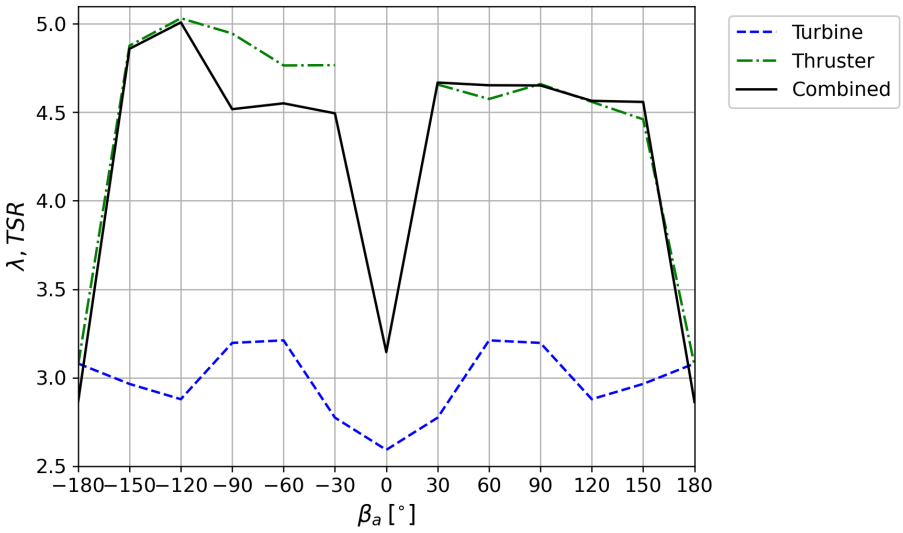

Figure 5.50: Optimized TSR parameter for different apparent wind directions

The pitch phase for both the thruster and the combined mode require a pitch amplitude around $\theta_p \pm 60[^\circ]$ which appears as an odd function with respect to the headwind condition. This is because the direction of the lift force to produce positive thrust, depends on the apparent wind direction whereby the lift force and θ_p are positive for $\beta_a > 0$ and negative for $\beta_a < 0$.
The turbine mode requires a more constant pitch phase as the lift force in this mode of operation does not contribute to the propulsion objective, even though a lift force can be produced when operating at maximum power as concluded in subsection 5.4.1.

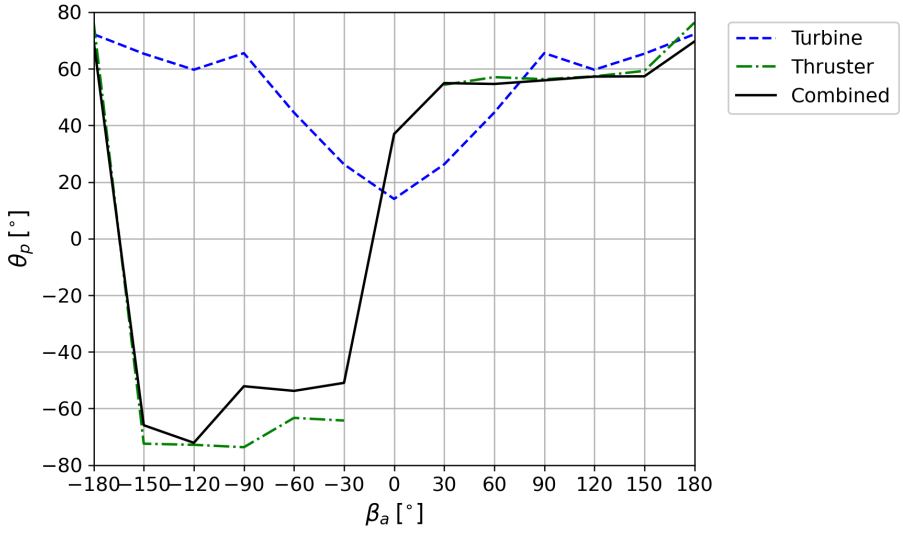

Figure 5.51: Optimized pitch phase (θ_p) parameter for different apparent wind directions

The design parameters are averaged according to the probability of occurrence for the specific wind conditions to obtain the best-performing designs. For the VAWT in turbine and combined mode, this weighted average includes the conditions where the ship is in port and the design of subsection 5.4.1 performs best.

Table 5.7: Weighted averaged design parameters from optimization

Case	σ	$A_{\theta_p}[^\circ]$	TSR	$\theta_p[^\circ]$
Turbine	0.318	9.06	2.98	49.0
Thruster	0.469	11.7	4.72	-5.32
Combined	0.457	11.5	4.53	2.88

The optimum designs do not generally operate with stalled blades ($\alpha_{stall,ref} > 15[^\circ]$) at any point of the rotation. The angle of attack variation for the optimum turbine in port and for the turbine, thruster and combined mode at sea for $\beta_a = 60[^\circ]$ is presented in Figure 5.52. This apparent wind direction is presented as this configuration is representative as it generally provides most performance and occurs relatively frequently. The angle of attack for the thruster and the combined mode at sea are almost similar. This is because both modes of operation use the thrust force to provide the propulsion in this apparent wind condition.

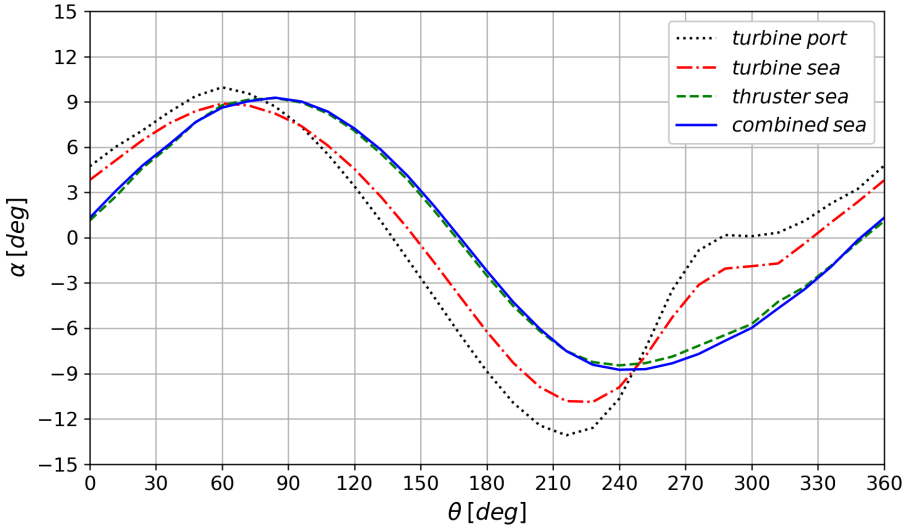

Figure 5.52: Angle of attack variation for multiple optimized designs, in port and at sea for all modes of operation with $\beta_a = 60[^\circ]$

5.5 Fixed construction parameters

The performance diagrams in the previous sections used optimized construction parameters for every wind condition. In reality, the solidity cannot be changed depending on the wind condition and the pitch amplitude is fixed when an excenter rod is used to actuate the pitch as shown in Figure 3.23. Therefore the construction parameters are fixed which reduces the design freedom for optimization. This reduces the performance as only the TSR and pitch phase can be set to the optimal settings.
To find the best performing construction parameters, 2 nested 2D optimization routines should be used to evaluate the actual best performing construction parameters and corresponding operational parameters for every wind condition. This is computationally expensive and is therefore deemed infeasible. Therefore this section investigates the performance which can be attained when the solidity and pitch amplitude are fixed at the weighted averaged optimal values for the combined case as presented in Table 5.7 ($\sigma = 0.457$ and $A_{\theta_p} = 11.5[^\circ]$).
This optimization only uses the operating parameters of the TSR and the pitch phase, therefore this is a 2D optimization problem for every wind direction. For this 2D optimization for headwind conditions ($\beta_a = 0[^\circ]$), only a small positive equivalent propulsive power of $C_{P'} = 0.162$ can be attained. This is only 46.1% of the propulsive power for 4D optimization and is therefore a substantial reduction in performance in upwind conditions. However, it is still possible to provide positive equivalent propulsive power in headwind conditions with the fixed design parameters.

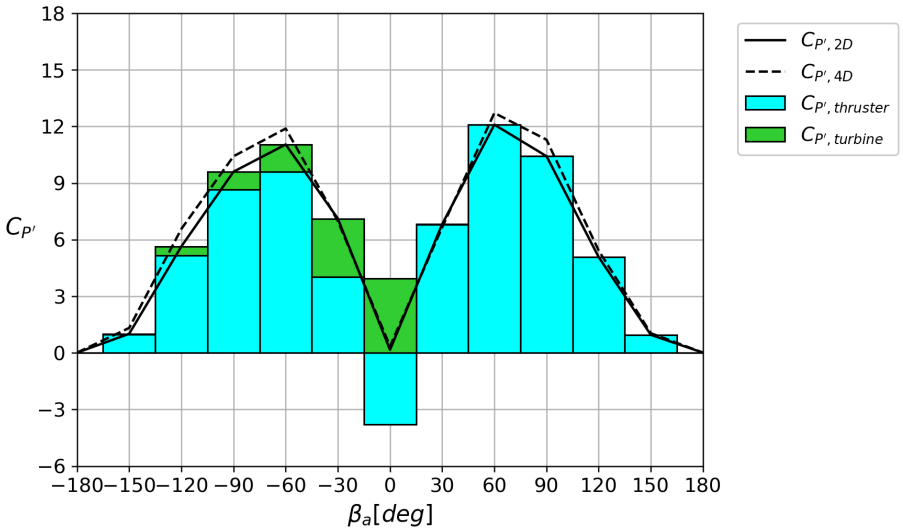

Figure 5.53: VAWT thruster and turbine equivalent propulsive power at sea, constant solidity and pitch amplitude (2D) compared, to optimization with all design parameters free (4D)

The difference in optimized design parameters is shown from Figure 5.54 to Figure 5.57. This shows that both the TSR and pitch phase are similar for both the 4D and 2D optimization cases.

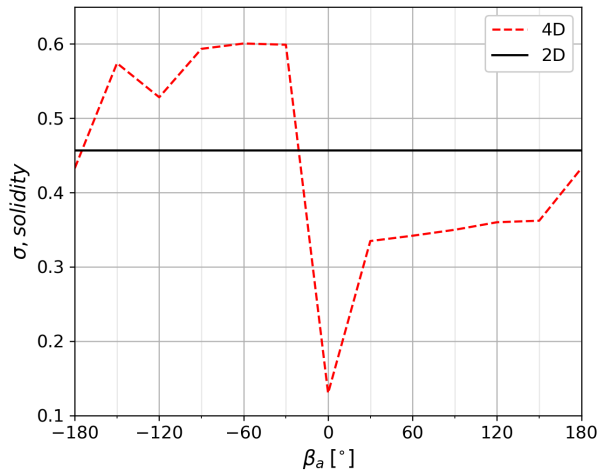

Figure 5.54: Optimized solidity (σ) parameter for different apparent wind directions, comparison of constant solidity and pitch amplitude (2D) and free design parameters (4D)

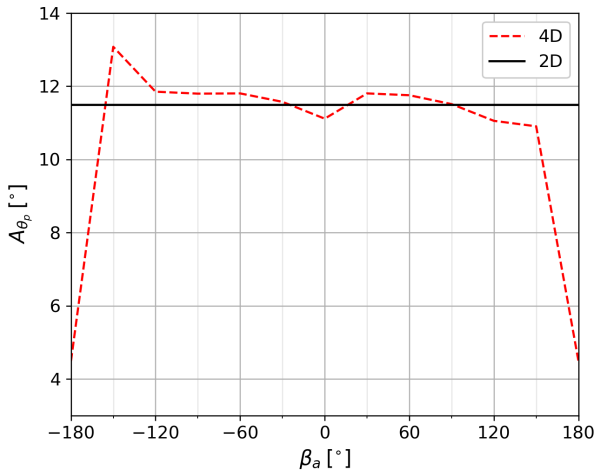

Figure 5.55: Optimized pitch amplitude (A_{θ_p}) parameter for different apparent wind directions, comparison of constant solidity and pitch amplitude (2D) and free design parameters (4D)

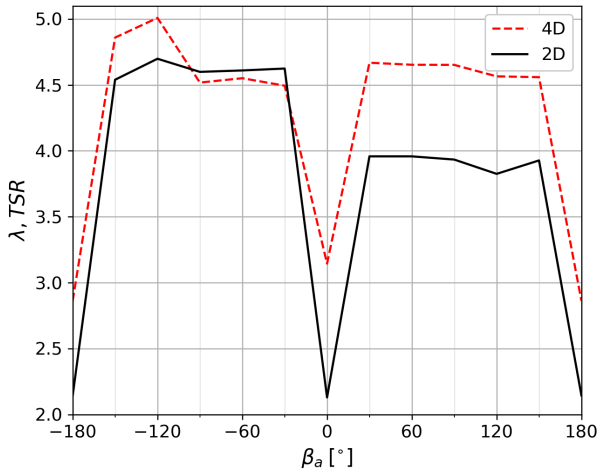

Figure 5.56: Optimized TSR parameter for different apparent wind directions, comparison of constant solidity and pitch amplitude (2D) and free design parameters (4D)

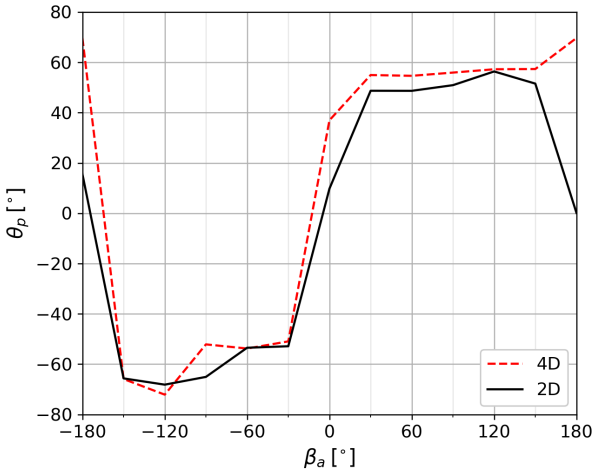

Figure 5.57: Optimized pitch phase (θ_p) parameter for different apparent wind directions, comparison of constant solidity and pitch amplitude (2D) and free design parameters (4D)

The mode where the VAWT is used as a turbine is also optimized for in-port conditions where the objective is to maximize the power coefficient, for the same fixed construction parameters. The comparison of these results is shown in Table 5.8. This shows that the turbine with fixed construction parameters operates at a lower TSR due to the large fixed solidity. The turbine with fixed construction parameters is less efficient as indicated by the power coefficient. The drag of this turbine is also lower and not around 1 which indicates that the turbine operating less efficiently.

Table 5.8: Results of the optimization of a turbine in port with and without fixed construction parameters

Case	σ	$A_{\theta_p}[°]$	TSR	$\theta_p[°]$	C_d	C_l	C_P	$\frac{U_{rel,max}}{U_\infty}$	$\lvert\alpha_{,max}\rvert$ [°]	P_{total}	$\tilde{f}$
2D	0.457	11.5	2.14	15.6	0.815	0.553	0.577	152	32.4	0	-0.577
4D	0.310	7.14	2.95	56.4	1.06	1.10	0.623	41.3	13.1	0	-0.623

The results of this 2D optimization are compared to the previous results of the 4D optimization in Figure 5.53. This shows a reduction in performance for fixed construction parameters (2D) of 4.77% for the conditions at sea. The performance for in-port conditions is reduced by 7.20% for fixed construction parameters. The total performance of the VAWT in combined conditions is reduced by 4.87% for fixed construction parameters. The performance of these different cases is presented in Table 6.1.

5.6 Fine computational settings

All simulations up to here used the converged computational settings. To check the sensitivity and evaluate the results for more accurate model settings, results of the combined objective optimization with fixed construction parameters (2D) is repeated using the fine2 computational settings from Table 4.8. The difference in performance parameters is presented in Figure 5.58 and Figure 5.59 This shows that the lift coefficient is mainly similar with some discrepancy for $-150 < \beta_a < -60$. However, there are differences in the evaluated the power coefficient for all wind directions. This indicates that power is less accurately predicted using the converged settings. This has a minor influence on the performance as most performance is attained using the lift force.

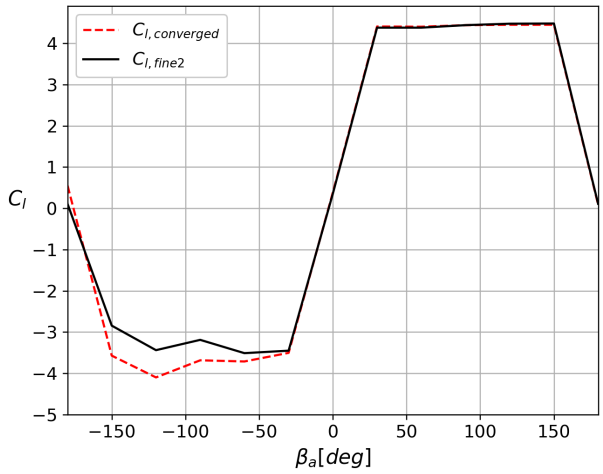

Figure 5.58: C_l comparison for converged and fine2 computational settings, for 2D optimized combined mode at sea

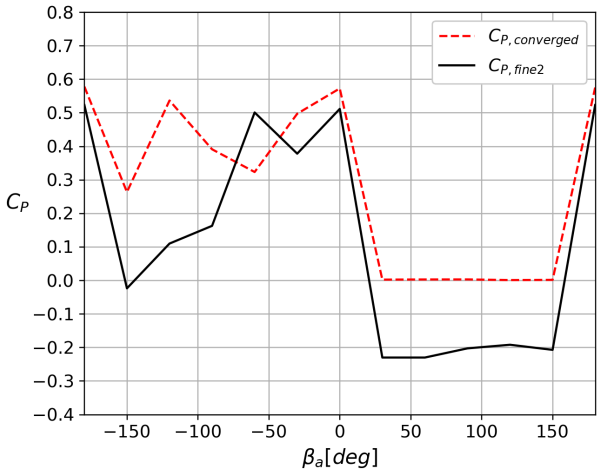

Figure 5.59: C_P comparison for converged and fine2 computational settings, for 2D optimized combined mode at sea

This comparison is presented in Figure 5.60 which shows a reduction in performance of 8.48% for the conditions at sea. The performance is reduced by 13.6% for the conditions in port, and 8.67% reduction in total performance. Note that fine2 settings show some negative power for the cases where $\beta_a > 0$. This indicates that the turbine is driven in these conditions.

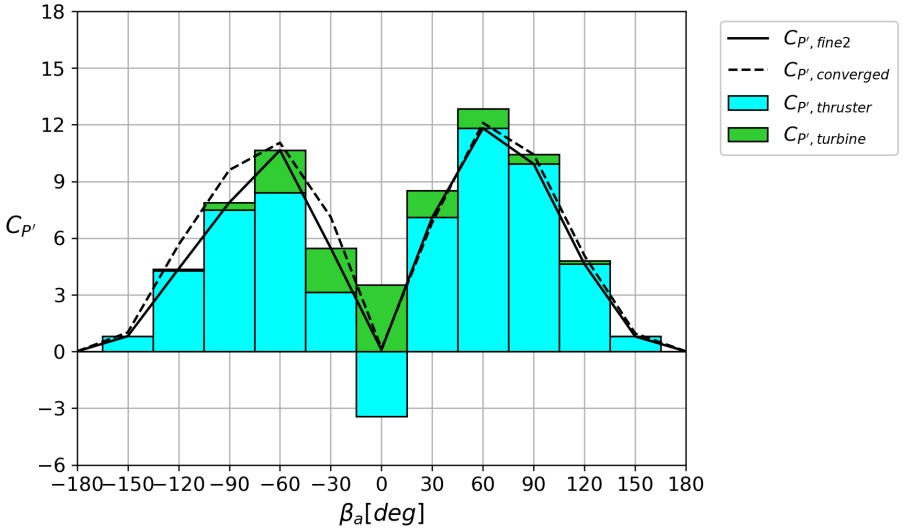

Figure 5.60: VAWT thruster and turbine equivalent propulsive power at sea, constant solidity and pitch amplitude (2D), compared to simulations with the fine2 computational settings

The results of the fine2 computational settings indicate a lower in performance compared to the converged computational settings. This difference can be explained because the converged settings over-predict the performance and because the design space can be different for the fine2 settings. Therefore the optimum design evaluated by the converged settings might not be an optimum design using the fine2 settings. The performance obtained from the fine2 settings might be increased if the entire optimization used the fine2 settings. However, this is deemed infeasible as a single function evaluation around the optimum for the fine2 settings requires 10 to 20 hours, and about 100 evaluations are required to obtain the optimum for a single wind condition of a specific operational mode. Therefore running all simulations using the fine2 settings would require more than 10 years of simulation time.

Chapter 6

Comparison to existing concepts

To evaluate if the VAWT concept could provide an alternative to the current WASP systems, the propulsive performance of the optimized designs is compared to existing WASP concepts. The concepts used for comparison are a rigid wingsail and a suction sail. These concepts are compared for the same wing area as the swept area for the turbine. The relation between the equivalent propulsive power coefficient and the power coefficient of a stationary wind turbine is also discussed.

6.1 Stationary wind turbine

The equivalent power coefficient is used to express the performance of the turbine. This is directly related to the power coefficient of a stationary wind turbine. Therefore the CP' values can be used to compare the performance of a wind turbine on a ship to a stationary wind turbine at sea. Equation 5.7 simplifies to C_P which Burton [40, p. 99] indicates to be around 0.47 for a 3D HAWT.
The average $C_{P'}$ value of the VAWT used as a turbine at sea ($C_{P'} = 0.544$) is 12.6% lower than the evaluated $C_P (= 0.623)$ for a stationary optimized VAWT. This indicates that if the VAWT is only used as a wind turbine for ship propulsion, the average performance is worse on a moving ship compared to a stationary turbine.

6.2 Rigid wingsail

A rigid wingsail like the system from Figure 2.4 is a relatively simple WASP concept and similar to high-performance sailing systems. Therefore this concept with a NACA0015 airfoil section is used to compare the performance. The polars from this system are obtained subsection 4.5.5 for a Reynolds number of $Re = 2e6$. The angle of attack is the only design parameter, therefore this is optimized using the optimizer tool of Excel, to find the best angle of attack setting for each wind condition. The resulting parameters and performance is presented in Appendix F, Table F.7.
The rigid wingsail has a slight negative power in headwind conditions due to the drag of the system even if $\alpha = 0[^\circ]$. In stern wind conditions, this system can only use the drag force to provide propulsion. Because the apparent wind speed is low in these conditions, the equivalent propulsive power is also low. Because the wingsail is a lifting system, most power can be attained for beam wind conditions with maximum power at $\beta_a \pm 60[^\circ]$ due to the increased apparent wind speed in this condition.

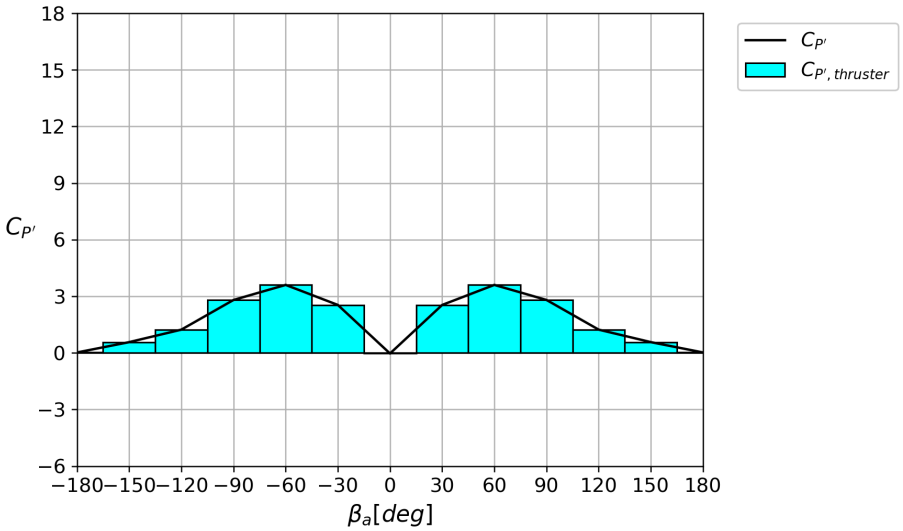

Figure 6.1: NACA0015 wingsail propulsive power at sea

6.3 Suction sail

The performance of the suction sail concept from Figure 2.6 is also used to compare the performance. This system is capable of generating large lift coefficients when boundary layer suction is applied. This suction requires power to be put into the system whereby the required suction power increases for larger apparent wind speeds. The force coefficients and required suction power are obtained from the 2D CFD results from Lagendijk [56, Figure C.25, 26]. The angle of attack is optimized using Excel to find the best angle of attack setting for each wind condition. To prevent stall, the maximum angle of attack is limited to $\alpha \leq 25[°]$. The resulting parameters and performance is presented in Appendix F, Table F.8.
As this is a lift-driven system, maximum power can be attained for beam wind conditions and slightly upwind as the apparent wind speed is larger in these conditions. The thrust force is in all wind conditions sufficient to overcome the power requirement of this system. The suction sail is assumed to be folded down in headwind conditions such that the negative propulsion from the drag force in a headwind is set to $C_{P'} = 0$. Otherwise this would have a performance into a direct headwind ($\beta_a = 0[°]$) of $C_{P'} = -0.342$. This is a substantial negative performance as the headwind condition is frequently encountered. Therefore this system should be retractable.

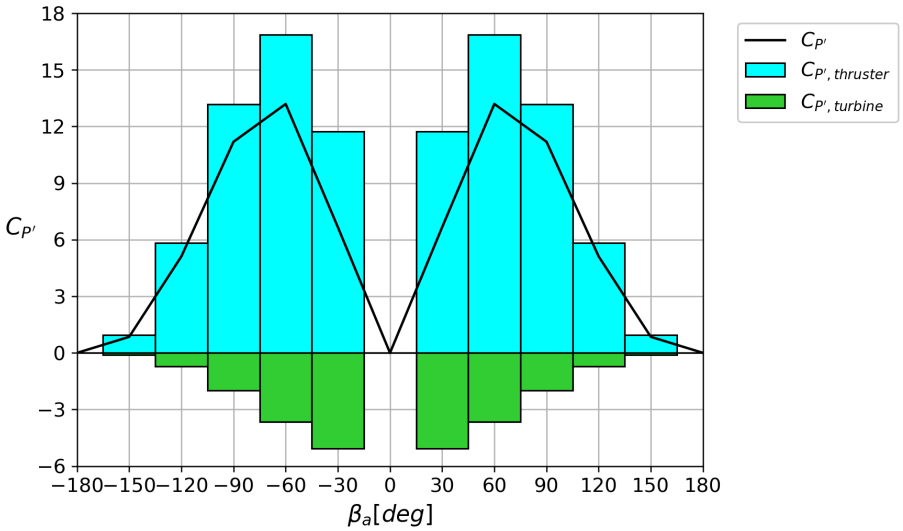

Figure 6.2: Suction sail propulsive power at sea

6.4 Performance comparison

The performance of different systems is compared to the conditions in port, the average performance at sea, and the total average performance. The total average equivalent power coefficient is a result of the weighted averaging of the performance in different conditions, including the conditions (10%) where no power can be produced. These results are presented in Table 6.1. All results per wind condition are presented in Appendix F. This comparison uses the results of the optimized VAWT design in combined mode for fixed construction parameters (2D), using the fine 2 computational settings. These results are used because the combined mode performs best overall, the configurations with fixed construction parameters can realistically be built, and because the fine2 settings provide the most reliable results.
For all systems, the results show that relatively low power can be attained in port, due to thrusting systems not being able to provide thrust propulsion in port and the relatively low wind speed in these conditions. Most power can be attained at sea as the true wind speed is larger in these conditions and because the ship's velocity mostly increases the apparent wind speed. The comparison of the systems is based on the total average performance as this indicates the total effectiveness of a system type.

The performance of the VAWT is compared in different modes of operation. To equally compare the performance, the results of the optimized designs with all design variables (4D) are used for this comparison. These results are presented in Table 6.1. These results indicate that only the turbine and combined mode can provide power in port.
The performance at sea for the thruster and combined mode at sea are similar where the thruster mode registers slightly better performance due to variations in local optima. This difference is therefore within the uncertainty of the optima. The thruster and combined mode at sea provide almost 9 times more equivalent propulsive power compared to the turbine at sea. This is because the thruster mode is most effective at sea. The total average performance of the thruster and combined modes at sea is almost 7 times better compared to the turbine mode. In total, the combined mode just outperforms the thruster mode as the combined mode can produce power in port and in headwind conditions. Therefore the combined mode is used for the comparison with the performance of existing systems.

Table 6.1: Average equivalent propulsive power for various systems in different situations

Case	NACA0015	Suction sail	VAWT turbine mode	VAWT thruster mode	VAWT combined mode		
			4D	4D	4D	2D	2D fine2
$C_{P'port}$	0.00	0.00	0.231	0.00	0.231	0.215	0.185
$C_{P'average,sea}$	1.47	4.70	0.544	4.79	4.75	4.52	4.14
$C_{P'average,total}$	0.733	2.35	0.365	2.40	2.47	2.35	2.14

The results of Table 6.1 indicate that a wingsail on a ship outperforms a stationary wind turbine at sea, as well as the total average performance of a VAWT, used as a turbine. Therefore lifting systems are on average more effective in providing propulsive power compared to turbines even though the lifting systems cannot be used in port. This confirms the findings by Bose [4, p. 157] from section subsection 2.2.2 that wind turbine propulsion performs better in headwind conditions but traditional sailing systems perform better on other courses.
The suction sail can attain large peak performance at sea as shown in Figure 6.3. In total, the suction sail outperforms the VAWT in combined mode (2D fine2) which provides 8.94% less performance for $C_{P'}average, total$. Therefore for the same swept or wing area, the suction sail would be the best performing system. However, the optimization for the combined mode with fixed parameters shows equal total averaged performance to the suction sail ($C_{P'}average, total = 2.35$). As the design space for the fine2 settings might be different to the design space of the converged computational settings, more power might be attained for the VAWT in combined mode for the 2D fine2 settings if the design optimization would use fine2 settings. Therefore both the suction sail and the VAWT in combined mode are roughly matching in performance.
As discussed in subsection 2.2.3, the size of conventional WASP systems is often limited by the sightline regulations. This study compares different systems of the same size. As the VAWT system the semi-transparent when rotating and has relatively small blades when not in operation, the sightline regulations might be less of a problem for VAWT systems which could therefore be larger and therefore the VAWT in combined mode could be more beneficial as this allows for the installation of larger systems.

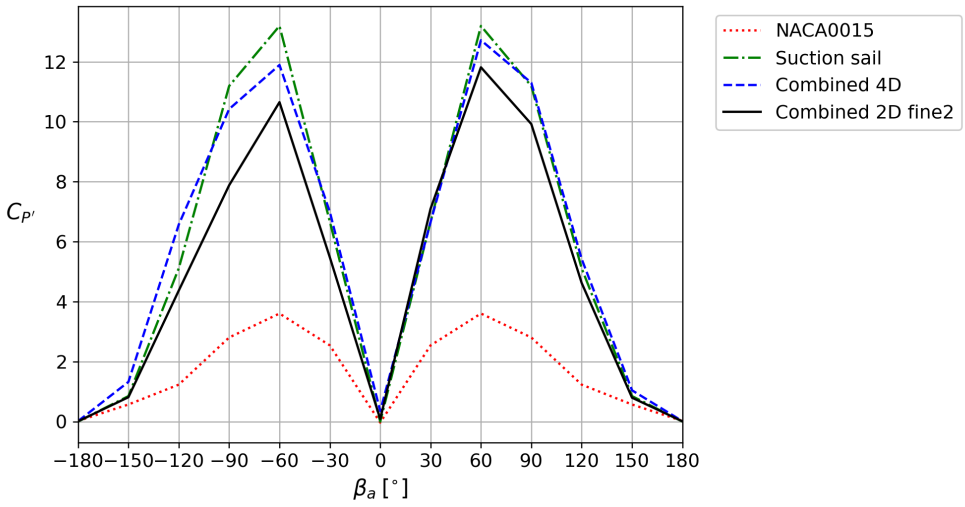

Figure 6.3: Equivalent propulsion power comparison of different propulsion concepts at sea

It should be noted that these results are based on 2D simulations and force parameters. This neglects the finite span effects of induced drag and the downwash effect on lift, which respectively increases the drag and reduces the lift due to the trailing vortices. The performance of lifting devices is therefore overestimated and the actual performance of 3D systems would be lower as these would perform less well in upwind conditions due to the increased lift-over drag ratio. These upwind conditions are frequently encountered and therefore contribute to a substantial part of the total performance. The performance of the suction sail might

therefore be overestimated with respect to the VAWT in combined mode. Because the performance in upwind conditions might be less negatively effected if finite span is accounted for. The VAWT in combined mode can still produce power in upwind conditions whereas the maximum upwind angle where a lifting device can be used is reduced with finite span. The power generating performance of a stationary turbine would also be lower in 3D operation.

Chapter 7

Conclusions and recommendations

The aerodynamic performance of VAWT for ship propulsion has been investigated and optimized for different modes of operation and wind conditions, using a self-developed and validated 2D free wake vortex model. A modified NMS optimization algorithm has been developed to obtain optimum solutions in the 4D design space. The performance of the optimized VAWTs is compared to existing WASP concepts to evaluate the potential of this novel ship propulsion concept. This chapter describes the main findings of this investigation, discusses the uncertainties, and provides recommendations for the design of VAWTs for ship propulsion and regarding further research.

7.1 Conclusions

The optimization of a VAWT for different modes of ship propulsion has resulted in a better understanding of the working principles and the potential performance of a VAWT used for ship propulsion. This knowledge has been obtained through various phases of the project.
A 2D lifting line vortex model which models the free wake is found to be a suitable modeling method to evaluate the performance of a VAWT used for energy generation as well as thrusting. Such a model is developed and sufficiently refined numerical settings for the model are evaluated. This model is validated by comparing the results with 6 different established 2D VAWT models. Using this model, the turbine performance and feasible regions in the design space have been evaluated to provide insight into the design characteristics and performance dependency on design parameters. The model is coupled to a newly developed optimization algorithm to efficiently search for the optimal designs in different modes of operation, at sea, and in port conditions. The results of this optimization are compared to existing WASP concepts.

The main findings of this study are related to performance power generating and thrusting performance of the turbine in port as well as at sea.
The application of sinusoidal pitch variation has been found to increase the power generation of a stationary turbine by 6.13%. The main difference in optimum designs with and without pitch variation is the lower TSR and larger solidity for turbines with pitch variation.
It has been found that it is possible to provide effective propulsion using the VAWT as a turbine to provide power to the propeller in headwind conditions. Even when accounting for the driving efficiency of the drive train and propeller losses, it is possible to sail directly into a headwind using a turbine to provide power.
Even though the VAWT can provide propulsion in any apparent wind direction, it has been found that it is more effective to use thrusting devices as WASP system compared to a turbine system. These thrusting systems provide larger peak propulsion performance in beamwind and slightly upwind conditions. Therefore the VAWT optimized for the combined operational mode of power generation and thrusting, mainly uses the thrusting capabilities to provide propulsion at sea. This thrust is mainly provided using a lift force from the turbine. It has been found that the lifting capabilities of the VAWT depend on the direction of rotation as described in subsubsection 5.2.1.5.
A low TSR is desirable not only for safety and fatigue but also such that the performance is less sensitive for the pitch phase setting and therefore the accuracy of the local wind condition measurement on the ship as concluded in subsubsection 5.2.1.3. The VAWT system has been found to be less sensitive to the correct

pitch phase setting compared to the sensitivity of the angle of attack setting of a wing-like WASP system. This makes the VAWT thruster turbine concept less sensitive for accurate measurements of the local wind direction, which can be difficult to accurately measure onboard a ship.
Part of the optimization is done using 4 design parameters to optimize the designs for one specific operating condition. To evaluate the performance of a design that works efficiently in all conditions, the construction parameters of solidity and pitch amplitude are fixed at a weighted average optimum setting. The operational parameters of TSR and the pitch phase for this design are optimized using 2D optimization. The performance of the realistic 2D optimized turbine performs similarly and with a 4.87% lower performance than the wind condition specific turbine designs using 4D optimization.
An interesting conclusion of this study is that a WASP system on a ship is approximately 8 times more effective compared to a stationary wind turbine of the same swept area operating at $C_P \approx 0.5$. Therefore wind propulsion systems on ships can be considered a promising technology.

Lastly: ideas can be simple however, understanding, modeling, and optimization can be complex yet has been found to be even more rewarding.

7.2 Discussion

The results of this study depend on the reliability of the model and the capabilities of the optimization algorithm to find the optimum. Even though the model is validated in section 4.7, the model shows some discrepancies with other models, and the optimized designs are different from the designs used in the validation case. This is partially but not entirely due to the computational settings. The reliability also depends on the model simplifications.
The wind conditions are assumed to be 2D undisturbed steady flow whereby no interaction between the ship and the turbine or the interaction between multiple turbines on one ship is accounted for. Only one specific characteristic wind speed is used at sea and in port. In reality, this is a spectrum of wind conditions. Also, one characteristic ship speed is used. It would be more accurate to optimize the results based on a statistical distribution of multiple wind conditions which depends on the intended operating region and the characteristic speed of a specific ship.
Some models might increase the accuracy of the modeled blade forces such as a dynamic stall model which is not included. The application of such a stall model might increase the reliability of the results but is not required as most efficiently operating turbines do not approach stalled conditions. Some stall effects are already included in the model by the airfoil polar. Also, no flow curvature correction is included in the model, this might influence the performance, especially for turbines with blades of a large relative chord length. No finite span correction or 3D simulations are done. This might influence the performance of the turbine, especially for turbines with a small $\frac{H}{2R}$ ratio. Finite span also reduces the performance of the existing concepts of the wingsail and the suction sail used to compare the performance. The upwind performance of these lift-driven systems will reduce which reduces the total performance of these systems as upwind conditions are frequently encountered at sea.
The model is only validated for turbine applications, therefore the lifting performance is less reliable even though this is largely unaffected by the computational settings. The feasible design space is non-convex and the model is found not to be smooth for variable solidity. Therefore, the optimization algorithm does not always converge to the global optimum and can converge to a local optimum due to the non-convex and non-smooth design space. The optimized designs with fixed construction parameters might not be the actual optimum as it would require 2 nested 2D optimizations to find the actual best-performing design parameters.
The TSR at which the thrusting configurations can attain maximum performance is substantially larger than what was expected when developing the numeric settings. This meant that a single function evaluation required substantially more computational time. Where an average run time of around 5 minutes was expected, the simulations for thruster configurations required in the order of 1-hour computational time. Because a single optimized design point requires around 100 function evaluations, the optimization process was slower than expected.

7.3 Recommendations

The investigation of a VAWT used for ship propulsion and the answers provided by this report call up new questions regarding many aspects of the VAWT concept used for ship propulsion. This section lists items

that might provide interesting research topics to improve the accuracy of the results and improve the design of the turbine.

- Investigate dependence on ship characteristic speed and the wind speed probability distribution. The resulting design might depend on the characteristic speed of a ship and the wind conditions which are encountered in a specific operating region.
- The flow conditions are assumed to be steady and uniform. However, it might be interesting to investigate the influence of the ship's structure disturbing the wind conditions and the effect of wind shear and wind veer. When multiple VAWTs are installed on a ship, it would be interesting to investigate the interaction between multiple of these systems.
- Investigate the potential benefit of driving the turbine to produce a larger thrust force at the cost of some power.
- Investigate the influence of the variation of the number of blades to indicate the influence on interaction losses as a turbine and potential change in lifting capabilities.
- Investigate the performance benefit of an optimized pitch variation pattern that is not prescribed as a sin-wave.
- Investigate the ratio in blade loading of the upwind and the downwind blades, and how much power is produced by the upwind blades and how much by the downwind blades.
- Investigate the potential benefit of allowing larger solidity turbines. This might require a different modeling method that accounts for the flow curvature effect.
- Investigate 3D effects and influence of the turbine aspect ratio ($\frac{H}{2R}$).
- Investigate the structural design requirements concerning peak loading and fatigue.
- Investigate the efficiency of the MNMS algorithm for different objective functions.
- As the VAWT can produce large lift forces, even without being driven, this might provide an interesting application for Short Take-Off and Landing (STOL) aircraft where the blades could be rotating at take-off and stationary in cruise conditions.

Bibliography

[1] Dykstra Naval Architects. Wasp (ecoliner). `https://www.dykstra-na.nl/designs/wasp-ecoliner/`, March 2022. Sailing cargo ship.

[2] Giovanni Bordogna. *AERODYNAMICS OF WIND-ASSISTED SHIPS*. PhD thesis, Delft University of Technology, January 2020.

[3] Marc Borren. The assessment of aerodynamic interaction between ventifoil suction wings. Masters thesis, TU Delft, April 2022.

[4] Neil Bose. Windmills - propulsion for a hydrofoil trimaran. *Symposium on wind propulsion of commercial ships*, 11, 1980. The Royal Institution of Naval Architects.

[5] Eirik Bøckmann and Sverre Steen. Wind turbine propulsion of ships. *Second International Symposium on Marine Propulsors*, June 2011.

[6] Marco Casini. Small vertical axis wind turbines for energy efficiency of buildings. *Journal of Clean Energy Technologies*, 4(1), January 2016.

[7] Mustafa Cavcar. The international standard atmosphere (isa). *Anadolu University, Turkey*, 30(9):1–6, 2000.

[8] Marine Environment Protection Committee. Mepc.1/circ.896, December 2021.

[9] The SciPy community. scipy.stats.qmc.latinhypercube. `https://docs.scipy.org/doc/scipy/reference/generated/scipy.stats.qmc.LatinHypercube.html`, 2022.

[10] Marine & Offshore Division. Sys-neq-osv, March 2016. Rule Note NR 633 DT R00 E.

[11] Frank Reed Eldridge. *Wind Machines*. Van Nostrand Reinhold Company, New York, second edition, 1980.

[12] Alessandro Bianchini et al. Virtual incidence effect on rotating airfoils in darrieus wind turbines. *Energy Conversion and Management*, 111:329–338, March 2016.

[13] Bengamin I. Moat et al. Quantifying the airflow distortion over merchant ships. *Journal of Atmospheric and Oceanic Technology*, 23(3):351–360, March 2006.

[14] Carlos González Gutiérrez et al. An empirical analysis on the operational profile of liquefied natural gas carriers with steam propulsion plants. *Journal of Navigation*, 74(2):1–20, December 2020.

[15] Carlos Simão Ferreira et al. Comparison of aerodynamic models for vertical axis wind turbines. *Journal of Physics*, 524, June 2014. Conference Series 524.

[16] Carlos Xisto et al. Numerical modelling of geometrical effects in the performance of a cycloidal rotor. *11th World Conference on Computational Mechanics*, July 2014.

[17] Charlotte Banks et al. Understanding ship operating profiles with an aim to improve energy efficient ship operations. Online, 2013. Lecture slides.

[18] Chi-Jeng Bai et al. System integration of the horizontal-axis wind turbine. *Energies*, 7(11):7773–7793, November 2014. Figure 5c.

[19] Chien-Chang Chen et al. What happens to the betz limit in vawt system? *The 13th International Conference on Wind Engineering*, July 2011.

[20] Christos Galinos et al. Vertical axis wind turbine design load cases investigation and comparison with horizontal axis wind turbine. *Energy Procedia*, 94:319–328, January 2016.

[21] Davi Santos et al. Design and implementation of a control system for a sailboat robot. *Robotics*, 5(1), February 2016.

[22] F. F. Rodrigues et al. Novel propulsion system for vtol aircraft based on cycloidal rotors coupled with wings. *Proceedings of Fluids Engineering Division Summer Meeting*, 12:16, July 2020. FEDSM2020-20292.

[23] Gary A. Flandro et al. *Basic Aerodynamics Incompressible Flow*. Cambridge University Press, Cambridge, first edition, 2012.

[24] Helge Aagaard Madsen et al. Analysis of vawt aerodynamics and design using the actuator cylinder flow model. *Journal of Physics*, 555(1), December 2014.

[25] Hicham Bidaoui et al. Wind speed data analysis using weibull and rayleigh distribution functions, case study: Five cities northern morocco. *Procedia Manufacturing*, 32:786–793, 2019.

[26] Hiromichi Akimoto et al. A conformal mapping technique to correlate the rotating flow around a wing section of vertical axis wind turbine and an equivalent linear flow around a static wing. *Environmental Research Letters*, 8(044040), December 2013.

[27] Hu Yu et al. The analysis of cyclogyro using unsteady vortex lattice method. *25th Congress of the International Council of the Aeronautical Sciences*, 2006.

[28] J. H. Strickland et al. A vortex model of the darrieus turbine: An analytical and experimental study. *Journal of Fluids Engineering*, 101(4), May 2015.

[29] Jasper Faber et al. Regulated slow steaming in maritime transport. Technical report, CE Delft, Delft, February 2012.

[30] Jasper Faber et al. Fourth imo ghg study 2020 - full report and annexes. Technical report 4, International Maritime Organization, London, 2021.

[31] John M. Rainbird et al. On the influence of virtual camber effect on airfoil polars for use in simulations of darrieus wind turbines. *Energy Conversion and Managemen*, 106:373–384, December 2015.

[32] José C. Páscoa et al. A novel look at the performance of the cyclorotor propulsion system for air vehicles. *Proceedings of the ASME 2012 International Mechanical Engineering Congress and Exposition*, November 2012. IMECE2012-85544.

[33] Kenneth Loenbaek et al. Optimal relationship between power and design driving loads for wind turbine rotors using 1d models. *Wind Energy Science Discussions*, pages 1–29, July 2019.

[34] M. Elkhoury et al. Experimental and numerical investigation of a three-dimensional vertical-axis wind turbine with variable-pitch. *Journal of Wind Engineering and Industrial Aerodynamics*, 139:111–123, April 2015.

[35] Marcel Ruiz Forns et al. Voith-schneider. `https://frr.wikipedia.org/wiki/Voith-Schneider`, September 2019.

[36] Martin Kaltschmitt et al. *Renewable Energy*. Springer, Berlin, first edition, 2007.

[37] P. Deglaire et al. Analytical solutions for a single blade in vertical axis turbine motion in two-dimensions. *European Journal of Mechanics B/Fluids*, 28:506–520, 2009.

[38] P. G. Migliore et al. Flow curvature effects on darrieus turbine blade aerodynamics. *Journal of Energy*, 4(2):49–55, April 1980.

[39] S. Brusca et al. Design of a vertical-axis wind turbine: how the aspect ratio affects the turbine's performance. *International Journal of Energy and Environmental Engineering*, 5(4):1–8, August 2014.

[40] Tony Burton et al. *Wind Energy Handbook*. Wiley, London, third edition, 2021.

[41] Carlos Ferreira. Rotor wake aerodynamics. Course content, 2019. Lecture slides.

[42] Carlos José Simão Ferreira. *The near wake of the VAWT*. PhD thesis, Delft University of Technology, October 2009. 2D and 3D views of the VAWT aerodynamics.

[43] Nancy Hall. Downwash effects on lift. `https://www.grc.nasa.gov/www/k-12/airplane/downwash.html`, May 2021.

[44] Nancy Hall. Induced drag coefficient. `https://www.grc.nasa.gov/www/k-12/airplane/induced.html`, May 2021.

[45] Siegfried Heier. *Grid Integration of Wind Energy*. Wiley, Chichester, third edition, 2014.

[46] Mazharul Islam. *Analysis of fixed-pitch straight-bladed VAWT with asymmetric airfoils*. PhD thesis, University of Windsor, 2008. Mechanical, Automotive, and Materials Engineering.

[47] Jr. John D. Anderson. *Fundementals of Aerodynamics*. McGraw-Hill, Avenue of the Americas, New York, fifth edition, 2010.

[48] Hannes Johnson and Linda Styhre. Increased energy efficiency in short sea shipping through decreased time in port. *Transportation Research Part A: Policy and Practice*, 71:167–178, January 2015.

[49] Jr. Joseph P. Hennessey. A comparison of the weibull and rayleigh distributions for estimating wind power potential. *Wind Engineering*, 2(3):156–164, 1978.

[50] Fawzi A. L. Jowder. Weibull and rayleigh distribution functions of wind speeds in kingdom of bahrain. *WIND ENGINEERING*, 30(5):439–446, October 2006.

[51] Ersan Kabalci. *Hybrid Renewable Energy Systems and Microgrids*. Elsevier, London, first edition, 2021.

[52] Austin A. Kana. Design of complex specials. Course content, 2020. Lecture slides, Analytic Hierarchy Process.

[53] Joseph Katz and Allen Plotkin. *Low-Speed Aerodynamics*. Cambridge University Press, 32 Avenue of the Americas, New York, second edition, 2001.

[54] Wessel Jan Tonnis Keijer. 3d aerodynamic effects and circulation control of vertical axis wind turbines. Masters thesis, TU Delft and DTU, July 2020.

[55] Rody Kemp. Airfoil optimization. Masters thesis, Delft University of Technology, March 2015.

[56] Laurens-Jan Lagendijk. Performance investigation of ventifoil ship propulsion. Masters thesis, Delft University of Technology, December 2018.

[57] Bruce P. LeBlanc and Carlos Simão Ferreira. Overview and design of pitch vawt, vertical axis wind turbine with active variable pitch for experimental and numerical comparison. *Wind Energy Symposium*, January 2018.

[58] J. Gordon Leishman. *Principles of Helicopter Aerodynamics*. Cambridge University Press, New York, second edition, 2006.

[59] Ang Li. Double actuator cylinder (ac) model of a tandem vertical axis wind turbine (vawt) counter-rotating rotor concept operating in different wind conditions. Masters thesis, Delft University of Technology and Technical University of Denmark, July 2017.

[60] Helge Aagaard Madsen. *The Actuator Cylinder*. PhD thesis, Technical University of Denmark, January 1982. A Flow Model for Vertical Axis Wind Turbines.

[61] A.C. Mandail and J.D. Burton. The effects of dynamic stall and flow curvature on the aerodynamics of darrieus turbines applying the cascade model. *Wind Engineering*, 18(6):267–282, 1994.

[62] James F. Manwell, Jon G. McGowan, and Anthony L. Rogers. *Wind Energy Explained*. Wiley, Chichester, second edition, 2010.

[63] Marin. Blue route. `https://blueroute.application.marin.nl`, 2022.

[64] MSW. Drehflügel – cyclogyro. `https://weaponsandwarfare.com/2020/04/19/drehflugel-cyclogyro/`, April 2020.

[65] United Nations. Paris agreement, 2015.

[66] Frank Nieuwenhuis. Econowind. `https://www.econowind.nl/`, February 2022. Images for marketing purposes.

[67] Panos Y. Papalambros and Donald C. Graham. *Principles of Optimal Design*. Cambridge University Press, Cambridge, second edition, 2000.

[68] R.C.T. Rainey. The wind turbine ship. *Symposium on wind propulsion of commercial ships*, 8, 1980. The Royal Institution of Naval Architects.

[69] Mehdi Habibnia Rami and Jose Carlos Pascoa. Performance optimization of forward-flight and lift-up phases in a cycloidal rotor using an active control mechanism. *Journal of Aerospace Engineering*, 34(4), January 2012.

[70] Mehdi Habibnia Rami and Jose Carlos Pascoa. Coupled active control technique for oscillating blades in a cycloidal rotor using cfd and ann analysis by including 3d end wall effects. *Journal of Aerospace Engineering*, August 2021.

[71] Hannes Riegler. Hawt versus vawt. *Italy reports*, 2003. Ropatec AG.

[72] Jr. Roy L. Clough. Rotor-sailing ship. *Popular Mechanics*, 120(2):124–127, August 1963.

[73] R.W. Saaty. The analytic hierarchy process - what it is and how it is used. *Mathematical Modelling*, 9(3-5):161–176, 1987.

[74] H. Schneekluth and V. Bertram. *Ship Design for Efficiency and Economy*. Butterworth-Heinemann, Oxford, second edition, 1998.

[75] Meinhard Schwaiger and David Wills. D-dalus vtol – efficiency increase in forward flight. *Aircraft Engineering and Aerospace Technology*, 88(5):594–604, September 2016.

[76] Germanischer Lloyd SE. Rules for classification and construction, July 2012. Ship Technology, Seagoing Ships.

[77] V. B. Shavrov. *History of aircraft construction in the USSR until 1938*. Mashinostroenie, fifth edition, 2002.

[78] R. E. Sheldahl and P. C. Klimas. Aerodynamic characteristics of seven symmetrical airfoil sections through 180-degree angle of attack for use in aerodynamic analysis of vertical axis wind turbines. Technical report, Sandia National Labs, Albuquerque, NM (USA), March 1981.

[79] Herbert J Sutherland. A summary of the fatigue properties of wind turbine materials. *WIND ENERGY*, 3:1–34, 2000.

[80] D.A.M. De Tavernier. *Aerodynamic advances in vertical-axis wind turbines*. PhD thesis, Delft University of Technology, February 2021.

[81] Delphine De Tavernier, Carlos Ferreira, and Anders Goude. *Handbook of Wind Energy Aerodynamics*. Springer, first edition, January 2022. Vertical-Axis Wind Turbine Aerodynamics.

[82] Contributors to Wikimedia projects. Cyclogyro. `https://en.wikipedia.org/wiki/Cyclogyro`, September 2021.

[83] Contributors to Wikimedia projects. Flettner rotor. `https://en.wikipedia.org/wiki/Flettner_rotor`, January 2022.

[84] Airfoil Tools. Naca 0015. `http://airfoiltools.com/airfoil/details?airfoil=naca0015-il`, 2022.

[85] Unknown. Rotoplan. `http://www.rotoplan.narod.ru/history_e.htm`, June 2013.

[86] Gerard J.W. van Bussel. Variability. `http://mstudioblackboard.tudelft.nl/duwind/Wind%20energy%20online%20reader/Static_pages/variability.htm`, October 2008.

[87] Nico van der Kolk. Sailing efficiency and course keeping ability of wind assisted ships. Masters thesis, TU Delft, June 2020.

Appendices

Appendix A

Global wind probability distribution

Global wind probability distribution along shipping routes from MEPC [8].

U_{wind} [m/s] \ β_t [°]	0	5	10	15	20	25	30	35	40	45	50	55
0.5	0.0001	0.0001	0.0001	0.0001	0.0001	0.0001	0.0001	0.0001	0.0001	0.0001	0.0001	0.0001
1.5	0.0005	0.0005	0.0005	0.0005	0.0005	0.0005	0.0005	0.0005	0.0005	0.0005	0.0005	0.0005
2.5	0.0009	0.0009	0.0009	0.0009	0.0008	0.0008	0.0008	0.0008	0.0008	0.0008	0.0008	0.0008
3.5	0.0013	0.0013	0.0013	0.0013	0.0012	0.0012	0.0012	0.0012	0.0011	0.0011	0.0011	0.0011
4.5	0.0017	0.0017	0.0017	0.0016	0.0016	0.0015	0.0015	0.0015	0.0014	0.0014	0.0013	0.0013
5.5	0.0021	0.002	0.002	0.0019	0.0018	0.0018	0.0017	0.0016	0.0016	0.0015	0.0015	0.0014
6.5	0.0022	0.0022	0.0021	0.002	0.002	0.0019	0.0018	0.0017	0.0017	0.0016	0.0015	0.0014
7.5	0.002	0.002	0.002	0.0019	0.0019	0.0018	0.0017	0.0016	0.0016	0.0015	0.0014	0.0014
8.5	0.0017	0.0017	0.0017	0.0016	0.0016	0.0016	0.0015	0.0014	0.0014	0.0013	0.0013	0.0012
9.5	0.0013	0.0013	0.0013	0.0013	0.0013	0.0013	0.0012	0.0012	0.0011	0.0011	0.001	0.001
10.5	0.001	0.001	0.001	0.001	0.0009	0.0009	0.0009	0.0009	0.0009	0.0008	0.0008	0.0008
11.5	0.0007	0.0007	0.0007	0.0007	0.0007	0.0006	0.0006	0.0006	0.0006	0.0006	0.0006	0.0005
12.5	0.0004	0.0005	0.0005	0.0005	0.0004	0.0004	0.0004	0.0004	0.0004	0.0004	0.0004	0.0003
13.5	0.0003	0.0003	0.0003	0.0003	0.0003	0.0003	0.0003	0.0003	0.0003	0.0002	0.0002	0.0002
14.5	0.0002	0.0002	0.0002	0.0002	0.0002	0.0002	0.0002	0.0002	0.0002	0.0002	0.0002	0.0002
15.5	0.0001	0.0001	0.0001	0.0001	0.0001	0.0001	0.0001	0.0001	0.0001	0.0001	0.0001	0.0001
16.5	0.0001	0.0001	0.0001	0.0001	0.0001	0.0001	0.0001	0.0001	0.0001	0.0001	0.0001	0.0001
17.5	0.0001	0.0001	0.0001	0.0001	0.0001	0.0001	0.0001	0	0	0	0	0
18.5	0	0	0	0	0	0	0	0	0	0	0	0
19.5	0	0	0	0	0	0	0	0	0	0	0	0
20.5	0	0	0	0	0	0	0	0	0	0	0	0
21.5	0	0	0	0	0	0	0	0	0	0	0	0
22.5	0	0	0	0	0	0	0	0	0	0	0	0
23.5	0	0	0	0	0	0	0	0	0	0	0	0
24.5	0	0	0	0	0	0	0	0	0	0	0	0
25.5	0	0	0	0	0	0	0	0	0	0	0	0

U_{wind} [m/s] \ β_t [°]	60	65	70	75	80	85	90	95	100	105	110	115
0.5	0.0001	0.0001	0.0001	0.0001	0.0001	0.0001	0.0001	0.0001	0.0001	0.0001	0.0001	0.0001
1.5	0.0005	0.0005	0.0005	0.0005	0.0005	0.0005	0.0005	0.0005	0.0005	0.0005	0.0005	0.0005
2.5	0.0008	0.0008	0.0008	0.0008	0.0008	0.0008	0.0008	0.0008	0.0008	0.0008	0.0008	0.0008
3.5	0.0011	0.0011	0.0011	0.001	0.001	0.001	0.001	0.0011	0.0011	0.0011	0.0011	0.0011
4.5	0.0013	0.0012	0.0012	0.0012	0.0012	0.0012	0.0013	0.0013	0.0013	0.0013	0.0013	0.0013
5.5	0.0014	0.0014	0.0014	0.0013	0.0014	0.0014	0.0014	0.0014	0.0014	0.0014	0.0015	0.0015
6.5	0.0014	0.0014	0.0014	0.0014	0.0014	0.0014	0.0014	0.0014	0.0015	0.0015	0.0015	0.0015
7.5	0.0013	0.0013	0.0013	0.0013	0.0013	0.0013	0.0013	0.0013	0.0013	0.0014	0.0014	0.0014
8.5	0.0012	0.0011	0.0011	0.0011	0.0011	0.0011	0.0011	0.0011	0.0011	0.0011	0.0012	0.0012
9.5	0.001	0.0009	0.0009	0.0009	0.0009	0.0009	0.0009	0.0008	0.0008	0.0008	0.0009	0.0009
10.5	0.0008	0.0007	0.0007	0.0007	0.0007	0.0006	0.0006	0.0006	0.0006	0.0006	0.0006	0.0006
11.5	0.0005	0.0005	0.0005	0.0005	0.0005	0.0004	0.0004	0.0004	0.0004	0.0004	0.0004	0.0004
12.5	0.0003	0.0003	0.0003	0.0003	0.0003	0.0003	0.0003	0.0003	0.0003	0.0002	0.0002	0.0002
13.5	0.0002	0.0002	0.0002	0.0002	0.0002	0.0002	0.0002	0.0002	0.0002	0.0002	0.0002	0.0002
14.5	0.0001	0.0001	0.0001	0.0001	0.0001	0.0001	0.0001	0.0001	0.0001	0.0001	0.0001	0.0001
15.5	0.0001	0.0001	0.0001	0.0001	0.0001	0.0001	0.0001	0.0001	0.0001	0.0001	0.0001	0.0001
16.5	0.0001	0.0001	0.0001	0.0001	0.0001	0.0001	0.0001	0.0001	0.0001	0.0001	0.0001	0.0001
17.5	0	0	0	0	0	0	0	0	0	0	0	0
18.5	0	0	0	0	0	0	0	0	0	0	0	0
19.5	0	0	0	0	0	0	0	0	0	0	0	0
20.5	0	0	0	0	0	0	0	0	0	0	0	0
21.5	0	0	0	0	0	0	0	0	0	0	0	0
22.5	0	0	0	0	0	0	0	0	0	0	0	0
23.5	0	0	0	0	0	0	0	0	0	0	0	0
24.5	0	0	0	0	0	0	0	0	0	0	0	0
25.5	0	0	0	0	0	0	0	0	0	0	0	0

U_{wind} [m/s] \ β_t [°]	120	125	130	135	140	145	150	155	160	165	170	175
0.5	0.0001	0.0001	0.0001	0.0001	0.0001	0.0001	0.0001	0.0001	0.0001	0.0001	0.0001	0.0001
1.5	0.0005	0.0005	0.0005	0.0005	0.0005	0.0005	0.0005	0.0005	0.0005	0.0005	0.0005	0.0005
2.5	0.0008	0.0008	0.0008	0.0008	0.0008	0.0009	0.0009	0.0009	0.0009	0.0009	0.0009	0.0009
3.5	0.0011	0.0011	0.0012	0.0012	0.0012	0.0013	0.0013	0.0013	0.0013	0.0013	0.0013	0.0013
4.5	0.0014	0.0014	0.0015	0.0015	0.0016	0.0016	0.0017	0.0017	0.0017	0.0017	0.0017	0.0017
5.5	0.0015	0.0016	0.0017	0.0017	0.0018	0.0019	0.002	0.002	0.0021	0.0021	0.0021	0.0021
6.5	0.0016	0.0016	0.0017	0.0018	0.0019	0.002	0.0021	0.0021	0.0022	0.0022	0.0023	0.0022
7.5	0.0015	0.0015	0.0016	0.0017	0.0017	0.0018	0.0019	0.002	0.002	0.0021	0.0021	0.0021
8.5	0.0012	0.0012	0.0013	0.0014	0.0014	0.0015	0.0016	0.0016	0.0016	0.0017	0.0017	0.0017
9.5	0.0009	0.0009	0.001	0.001	0.0011	0.0011	0.0012	0.0012	0.0012	0.0013	0.0013	0.0013
10.5	0.0006	0.0006	0.0007	0.0007	0.0007	0.0008	0.0008	0.0008	0.0009	0.0009	0.0009	0.001
11.5	0.0004	0.0004	0.0004	0.0005	0.0005	0.0005	0.0005	0.0006	0.0006	0.0006	0.0006	0.0007
12.5	0.0003	0.0003	0.0003	0.0003	0.0003	0.0003	0.0004	0.0004	0.0004	0.0004	0.0004	0.0004
13.5	0.0002	0.0002	0.0002	0.0002	0.0002	0.0002	0.0002	0.0002	0.0003	0.0003	0.0003	0.0003
14.5	0.0001	0.0001	0.0001	0.0001	0.0001	0.0002	0.0002	0.0002	0.0002	0.0002	0.0002	0.0002
15.5	0.0001	0.0001	0.0001	0.0001	0.0001	0.0001	0.0001	0.0001	0.0001	0.0001	0.0001	0.0001
16.5	0.0001	0.0001	0.0001	0.0001	0.0001	0.0001	0.0001	0.0001	0.0001	0.0001	0.0001	0.0001
17.5	0	0	0	0	0	0	0	0	0	0	0.0001	0.0001
18.5	0	0	0	0	0	0	0	0	0	0	0	0
19.5	0	0	0	0	0	0	0	0	0	0	0	0
20.5	0	0	0	0	0	0	0	0	0	0	0	0
21.5	0	0	0	0	0	0	0	0	0	0	0	0
22.5	0	0	0	0	0	0	0	0	0	0	0	0
23.5	0	0	0	0	0	0	0	0	0	0	0	0
24.5	0	0	0	0	0	0	0	0	0	0	0	0
25.5	0	0	0	0	0	0	0	0	0	0	0	0

U_{wind} [m/s] \ β_t [°]	180	185	190	195	200	205	210	215	220	225	230	235
0.5	0.0001	0.0001	0.0001	0.0001	0.0001	0.0001	0.0001	0.0001	0.0001	0.0001	0.0001	0.0001
1.5	0.0005	0.0005	0.0005	0.0005	0.0005	0.0005	0.0005	0.0005	0.0005	0.0005	0.0005	0.0005
2.5	0.0009	0.0009	0.0009	0.0009	0.0008	0.0008	0.0008	0.0008	0.0008	0.0008	0.0008	0.0008
3.5	0.0013	0.0013	0.0013	0.0013	0.0012	0.0012	0.0012	0.0012	0.0011	0.0011	0.0011	0.0011
4.5	0.0017	0.0017	0.0017	0.0016	0.0016	0.0015	0.0015	0.0015	0.0014	0.0014	0.0013	0.0013
5.5	0.0021	0.002	0.002	0.0019	0.0018	0.0018	0.0017	0.0016	0.0016	0.0015	0.0015	0.0014
6.5	0.0022	0.0022	0.0021	0.002	0.002	0.0019	0.0018	0.0017	0.0017	0.0016	0.0015	0.0014
7.5	0.002	0.002	0.002	0.0019	0.0019	0.0018	0.0017	0.0016	0.0016	0.0015	0.0014	0.0014
8.5	0.0017	0.0017	0.0017	0.0016	0.0016	0.0016	0.0015	0.0014	0.0014	0.0013	0.0013	0.0012
9.5	0.0013	0.0013	0.0013	0.0013	0.0013	0.0013	0.0012	0.0012	0.0011	0.0011	0.001	0.001
10.5	0.001	0.001	0.001	0.001	0.0009	0.0009	0.0009	0.0009	0.0009	0.0008	0.0008	0.0008
11.5	0.0007	0.0007	0.0007	0.0007	0.0007	0.0006	0.0006	0.0006	0.0006	0.0006	0.0006	0.0005
12.5	0.0004	0.0005	0.0005	0.0005	0.0004	0.0004	0.0004	0.0004	0.0004	0.0004	0.0004	0.0003
13.5	0.0003	0.0003	0.0003	0.0003	0.0003	0.0003	0.0003	0.0003	0.0003	0.0002	0.0002	0.0002
14.5	0.0002	0.0002	0.0002	0.0002	0.0002	0.0002	0.0002	0.0002	0.0002	0.0002	0.0002	0.0002
15.5	0.0001	0.0001	0.0001	0.0001	0.0001	0.0001	0.0001	0.0001	0.0001	0.0001	0.0001	0.0001
16.5	0.0001	0.0001	0.0001	0.0001	0.0001	0.0001	0.0001	0.0001	0.0001	0.0001	0.0001	0.0001
17.5	0.0001	0.0001	0.0001	0.0001	0.0001	0.0001	0.0001	0	0	0	0	0
18.5	0	0	0	0	0	0	0	0	0	0	0	0
19.5	0	0	0	0	0	0	0	0	0	0	0	0
20.5	0	0	0	0	0	0	0	0	0	0	0	0
21.5	0	0	0	0	0	0	0	0	0	0	0	0
22.5	0	0	0	0	0	0	0	0	0	0	0	0
23.5	0	0	0	0	0	0	0	0	0	0	0	0
24.5	0	0	0	0	0	0	0	0	0	0	0	0
25.5	0	0	0	0	0	0	0	0	0	0	0	0

U_{wind} [m/s] \ β_t [°]	240	245	250	255	260	265	270	275	280	285	290	295
0.5	0.0001	0.0001	0.0001	0.0001	0.0001	0.0001	0.0001	0.0001	0.0001	0.0001	0.0001	0.0001
1.5	0.0005	0.0005	0.0005	0.0005	0.0005	0.0005	0.0005	0.0005	0.0005	0.0005	0.0005	0.0005
2.5	0.0008	0.0008	0.0008	0.0008	0.0008	0.0008	0.0008	0.0008	0.0008	0.0008	0.0008	0.0008
3.5	0.0011	0.0011	0.0011	0.001	0.001	0.001	0.001	0.0011	0.0011	0.0011	0.0011	0.0011
4.5	0.0013	0.0012	0.0012	0.0012	0.0012	0.0012	0.0013	0.0013	0.0013	0.0013	0.0013	0.0013
5.5	0.0014	0.0014	0.0014	0.0013	0.0014	0.0014	0.0014	0.0014	0.0014	0.0014	0.0015	0.0015
6.5	0.0014	0.0014	0.0014	0.0014	0.0014	0.0014	0.0014	0.0014	0.0015	0.0015	0.0015	0.0015
7.5	0.0013	0.0013	0.0013	0.0013	0.0013	0.0013	0.0013	0.0013	0.0013	0.0014	0.0014	0.0014
8.5	0.0012	0.0011	0.0011	0.0011	0.0011	0.0011	0.0011	0.0011	0.0011	0.0011	0.0012	0.0012
9.5	0.001	0.0009	0.0009	0.0009	0.0009	0.0009	0.0009	0.0008	0.0008	0.0008	0.0009	0.0009
10.5	0.0008	0.0007	0.0007	0.0007	0.0007	0.0006	0.0006	0.0006	0.0006	0.0006	0.0006	0.0006
11.5	0.0005	0.0005	0.0005	0.0005	0.0005	0.0004	0.0004	0.0004	0.0004	0.0004	0.0004	0.0004
12.5	0.0003	0.0003	0.0003	0.0003	0.0003	0.0003	0.0003	0.0003	0.0003	0.0002	0.0002	0.0002
13.5	0.0002	0.0002	0.0002	0.0002	0.0002	0.0002	0.0002	0.0002	0.0002	0.0002	0.0002	0.0002
14.5	0.0001	0.0001	0.0001	0.0001	0.0001	0.0001	0.0001	0.0001	0.0001	0.0001	0.0001	0.0001
15.5	0.0001	0.0001	0.0001	0.0001	0.0001	0.0001	0.0001	0.0001	0.0001	0.0001	0.0001	0.0001
16.5	0.0001	0.0001	0.0001	0.0001	0.0001	0.0001	0.0001	0.0001	0.0001	0.0001	0.0001	0.0001
17.5	0	0	0	0	0	0	0	0	0	0	0	0
18.5	0	0	0	0	0	0	0	0	0	0	0	0
19.5	0	0	0	0	0	0	0	0	0	0	0	0
20.5	0	0	0	0	0	0	0	0	0	0	0	0
21.5	0	0	0	0	0	0	0	0	0	0	0	0
22.5	0	0	0	0	0	0	0	0	0	0	0	0
23.5	0	0	0	0	0	0	0	0	0	0	0	0
24.5	0	0	0	0	0	0	0	0	0	0	0	0
25.5	0	0	0	0	0	0	0	0	0	0	0	0

U_{wind} [m/s] \ β_t [°]	300	305	310	315	320	325	330	335	340	345	350	355
0.5	0.0001	0.0001	0.0001	0.0001	0.0001	0.0001	0.0001	0.0001	0.0001	0.0001	0.0001	0.0001
1.5	0.0005	0.0005	0.0005	0.0005	0.0005	0.0005	0.0005	0.0005	0.0005	0.0005	0.0005	0.0005
2.5	0.0008	0.0008	0.0008	0.0008	0.0008	0.0009	0.0009	0.0009	0.0009	0.0009	0.0009	0.0009
3.5	0.0011	0.0011	0.0012	0.0012	0.0012	0.0013	0.0013	0.0013	0.0013	0.0013	0.0013	0.0013
4.5	0.0014	0.0014	0.0015	0.0015	0.0016	0.0016	0.0017	0.0017	0.0017	0.0017	0.0017	0.0017
5.5	0.0015	0.0016	0.0017	0.0017	0.0018	0.0019	0.002	0.002	0.0021	0.0021	0.0021	0.0021
6.5	0.0016	0.0016	0.0017	0.0018	0.0019	0.002	0.0021	0.0021	0.0022	0.0022	0.0023	0.0022
7.5	0.0015	0.0015	0.0016	0.0017	0.0017	0.0018	0.0019	0.002	0.002	0.0021	0.0021	0.0021
8.5	0.0012	0.0012	0.0013	0.0014	0.0014	0.0015	0.0016	0.0016	0.0016	0.0017	0.0017	0.0017
9.5	0.0009	0.0009	0.001	0.001	0.0011	0.0011	0.0012	0.0012	0.0012	0.0013	0.0013	0.0013
10.5	0.0006	0.0006	0.0007	0.0007	0.0007	0.0008	0.0008	0.0008	0.0009	0.0009	0.0009	0.001
11.5	0.0004	0.0004	0.0004	0.0005	0.0005	0.0005	0.0005	0.0006	0.0006	0.0006	0.0006	0.0007
12.5	0.0003	0.0003	0.0003	0.0003	0.0003	0.0003	0.0004	0.0004	0.0004	0.0004	0.0004	0.0004
13.5	0.0002	0.0002	0.0002	0.0002	0.0002	0.0002	0.0002	0.0002	0.0003	0.0003	0.0003	0.0003
14.5	0.0001	0.0001	0.0001	0.0001	0.0001	0.0002	0.0002	0.0002	0.0002	0.0002	0.0002	0.0002
15.5	0.0001	0.0001	0.0001	0.0001	0.0001	0.0001	0.0001	0.0001	0.0001	0.0001	0.0001	0.0001
16.5	0.0001	0.0001	0.0001	0.0001	0.0001	0.0001	0.0001	0.0001	0.0001	0.0001	0.0001	0.0001
17.5	0	0	0	0	0	0	0	0	0	0	0.0001	0.0001
18.5	0	0	0	0	0	0	0	0	0	0	0	0
19.5	0	0	0	0	0	0	0	0	0	0	0	0
20.5	0	0	0	0	0	0	0	0	0	0	0	0
21.5	0	0	0	0	0	0	0	0	0	0	0	0
22.5	0	0	0	0	0	0	0	0	0	0	0	0
23.5	0	0	0	0	0	0	0	0	0	0	0	0
24.5	0	0	0	0	0	0	0	0	0	0	0	0
25.5	0	0	0	0	0	0	0	0	0	0	0	0

Appendix B

Global wind probability distribution

Wind probability distribution in major ports along the global shipping routes from MEPC [8].

Table B.1: Probabilities of true wind speeds in global ports

range U_t [m/s]	0-3.3	3.4-7.9	8-13.8	13.9-20.7	20.8-24.4
$\overline{U_t}$ [m/s]	1.65	5.65	10.9	17.3	22.6
St. Petersburg	0.2547	0.6523	0.0924	0.0004	0
Rotterdam	0.1441	0.5989	0.2461	0.0106	0
Lisbon	0.3986	0.5798	0.0214	0	0
Istanbul	0.3266	0.6114	0.0617	0	0
Hamburg	0.355	0.615	0.0302	0	0
Lagos (Nigeria)	0.1304	0.8276	0.0418	0	0
Durban	0.2886	0.6064	0.1046	0.0003	0
Djibouti	0.531	0.4661	0.0028	0	0
New York	0.5253	0.4671	0.0073	0	0
Houston	0.4185	0.5207	0.06	0.0007	0
Panama	0.6703	0.3296	0	0	0
Seattle	0.7794	0.2197	0.0006	0	0
Los Angeles	0.8348	0.165	0	0	0
Buenos Aires	0.3516	0.6278	0.0207	0	0
Singapore	0.2917	0.6728	0.0355	0	0
Tianjin	0.2109	0.6869	0.1014	0.0007	0
Shanghai	0.2919	0.586	0.1202	0.002	0
Hongkong	0.1305	0.6605	0.2046	0.0037	0
Busan	0.1668	0.6005	0.2271	0.0057	0
Tokio	0.6035	0.376	0.0203	0.0003	0
Doha	0.2721	0.6044	0.1229	0.0002	0
Melbourne	0.2382	0.6197	0.1411	0.0005	0
Brisbane	0.5556	0.4434	0.0007	0	0
Average	0.3813	0.5451	0.07232	0.001091	0

Appendix C

Design space investigation

All figures of the design space investigation using 2D slices.

C.1 TSR and solidity

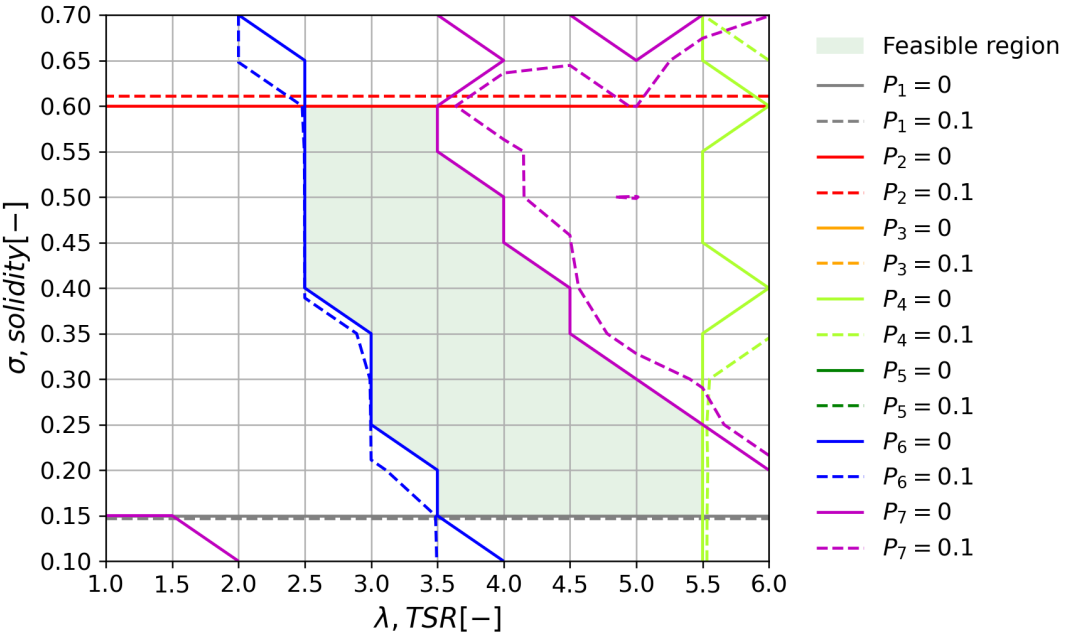

Figure C.1: Penalties from different constraints, $TSR = 2.5$, $\theta_p = 0[^\circ]$

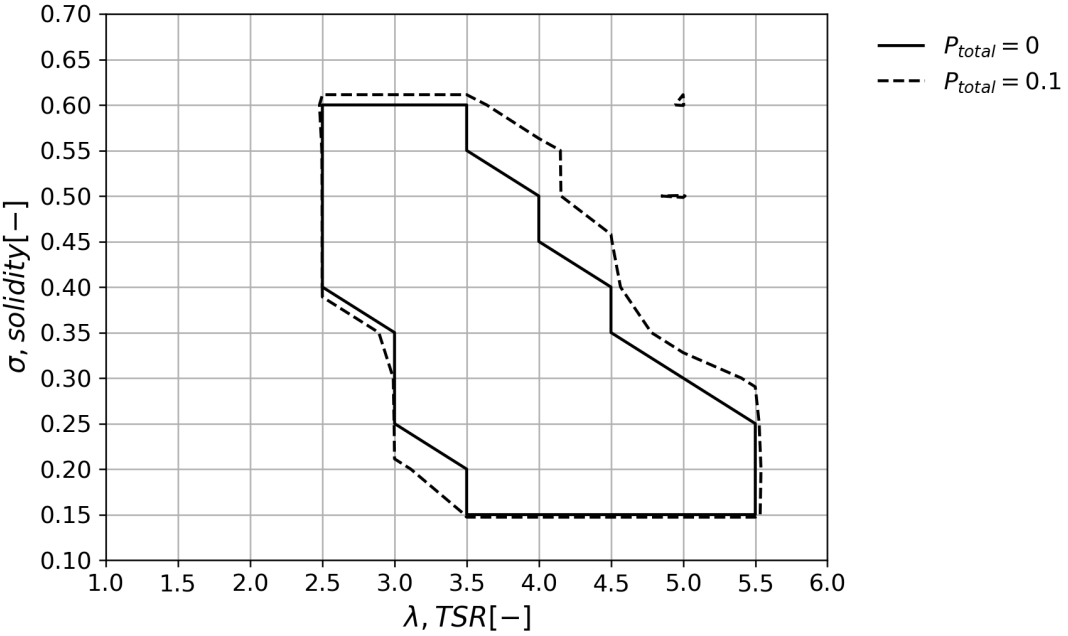

Figure C.2: Total penalty from constraints showing the feasible design region, $TSR = 2.5$, $\theta_p = 0[^\circ]$

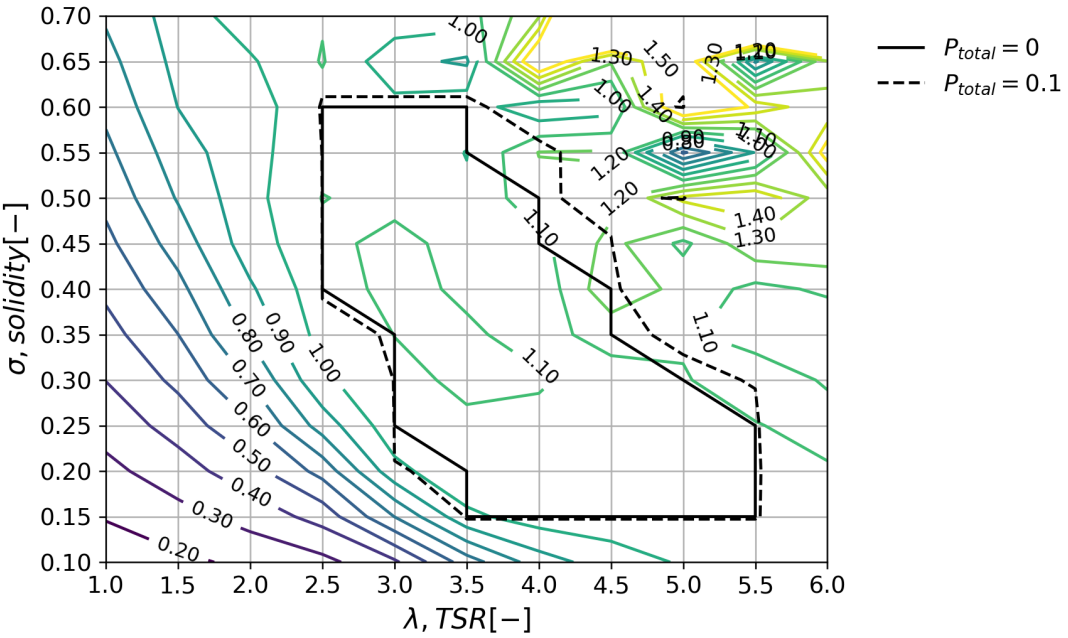

Figure C.3: C_d for different designs and the total penalty showing the feasible design region, $TSR = 2.5$, $\theta_p = 0[^\circ]$

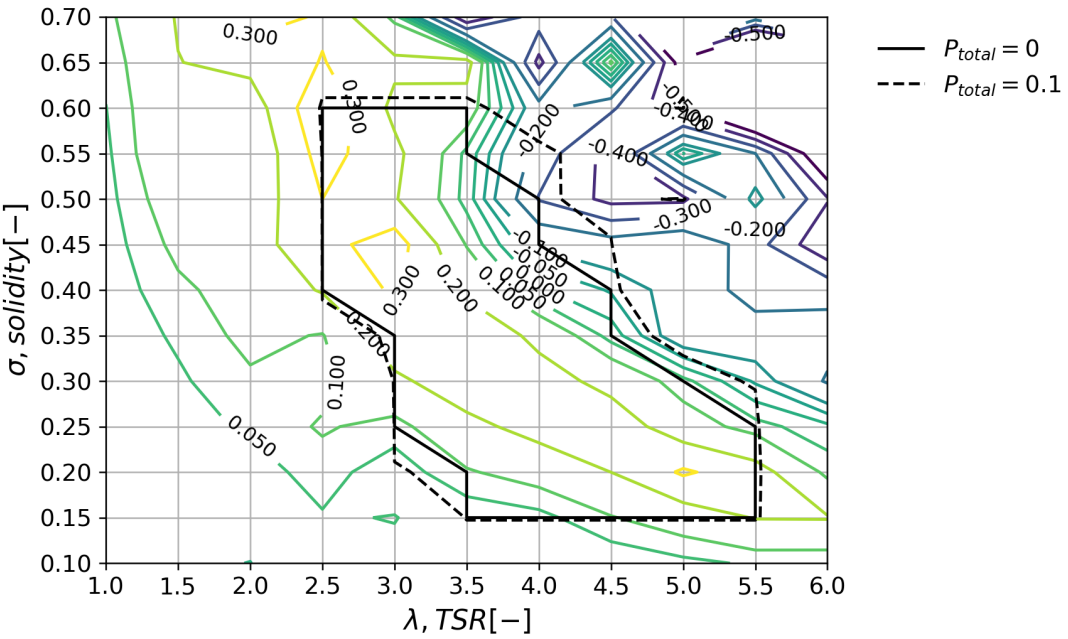

Figure C.4: C_l for different designs and the total penalty showing the feasible design region, $TSR = 2.5$, $\theta_p = 0[°]$

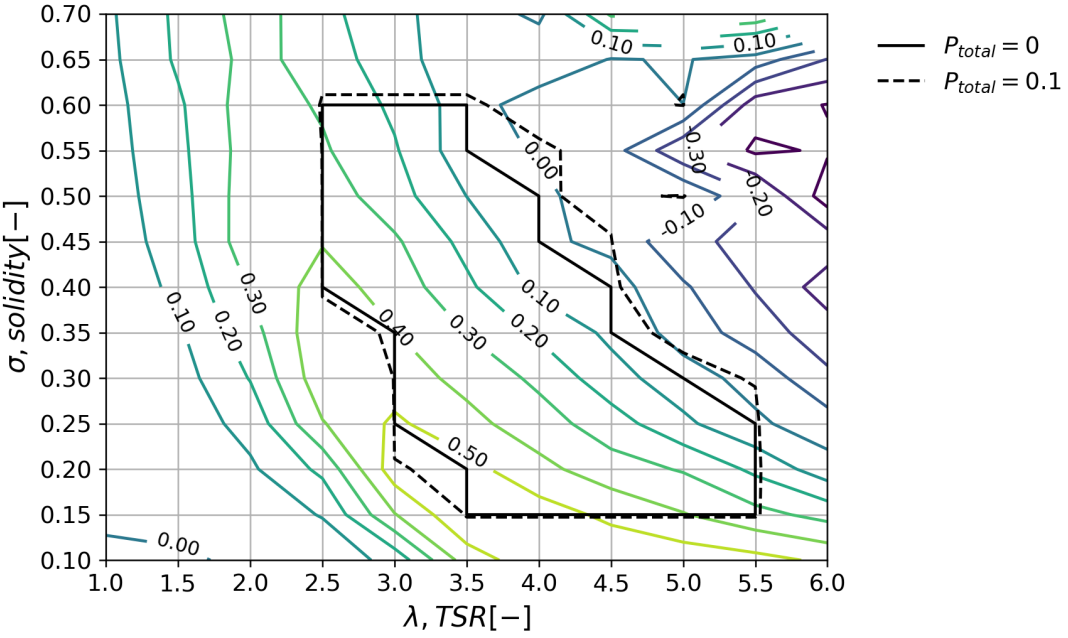

Figure C.5: C_P for different designs and the total penalty showing the feasible design region, $TSR = 2.5$, $\theta_p = 0[°]$

C.2 Solidity and pitch amplitude

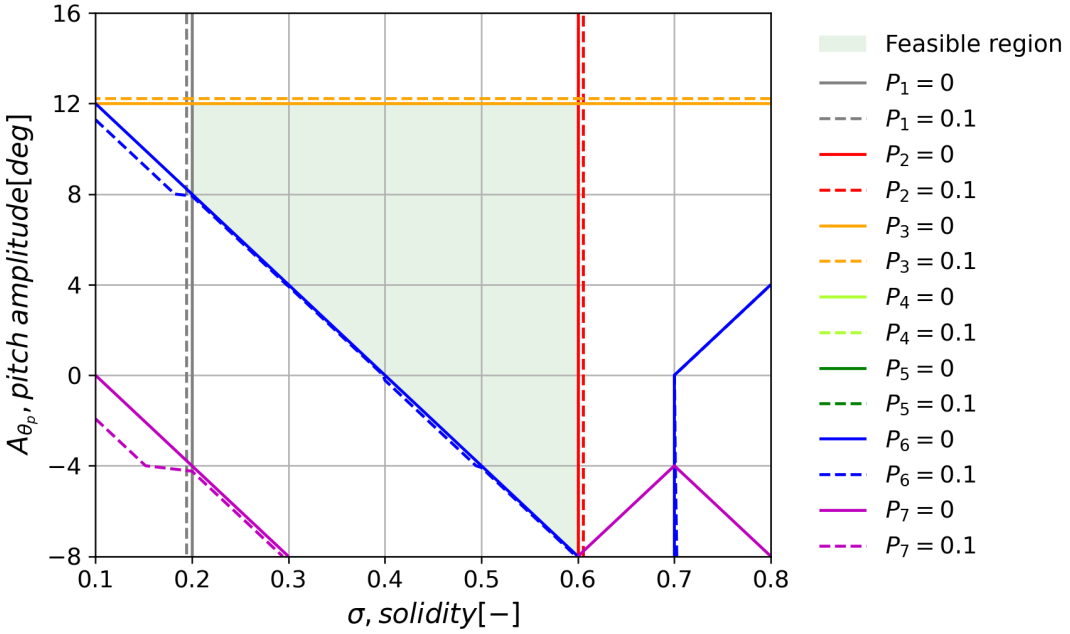

Figure C.6: Penalties from different constraints, $TSR = 2.5$, $\theta_p = 0[^\circ]$

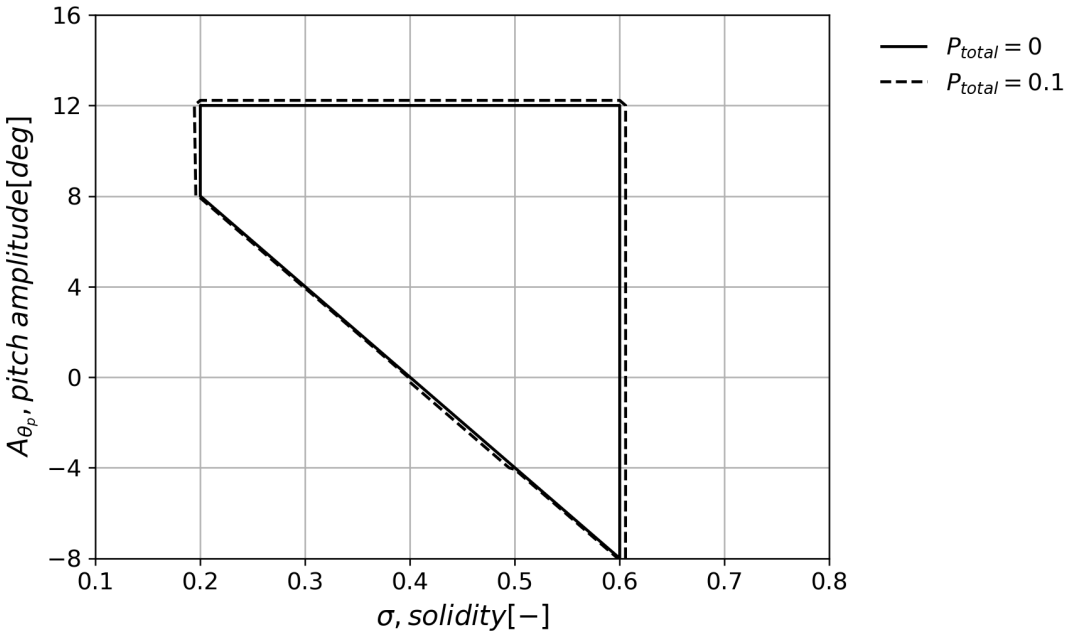

Figure C.7: Total penalty from constraints showing the feasible design region, $TSR = 2.5$, $\theta_p = 0[^\circ]$

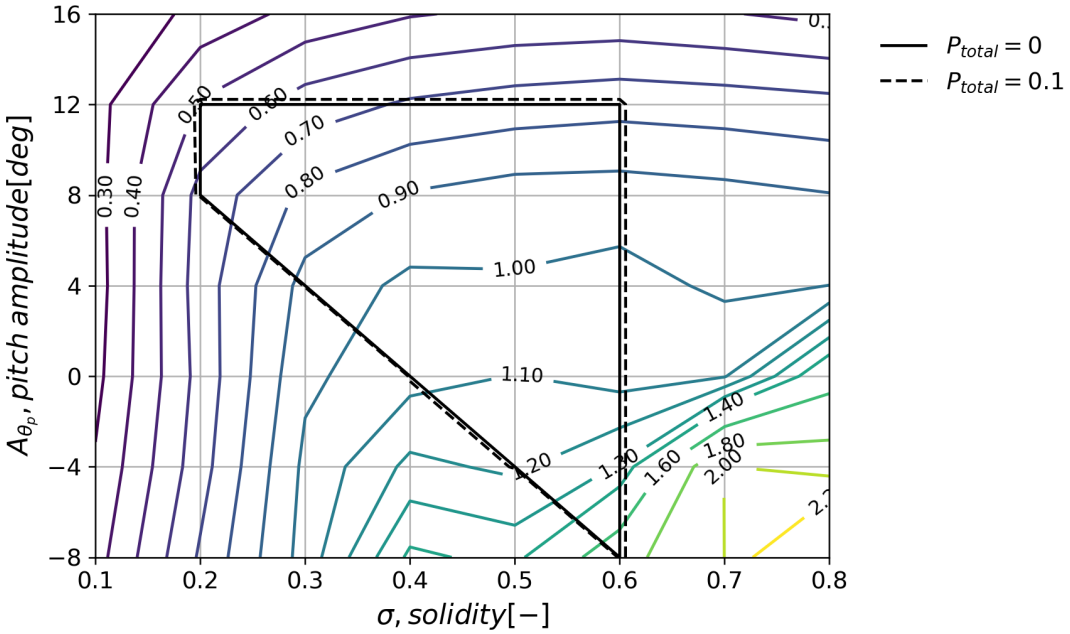

Figure C.8: C_d for different designs and the total penalty showing the feasible design region, $TSR = 2.5$, $\theta_p = 0[°]$

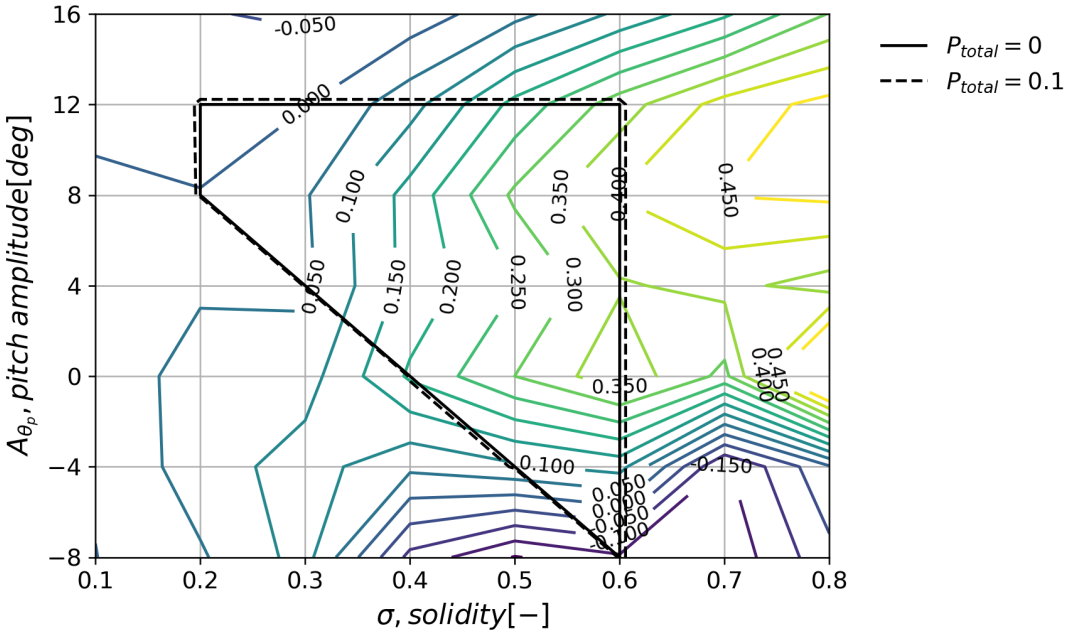

Figure C.9: C_l for different designs and the total penalty showing the feasible design region, $TSR = 2.5$, $\theta_p = 0[°]$

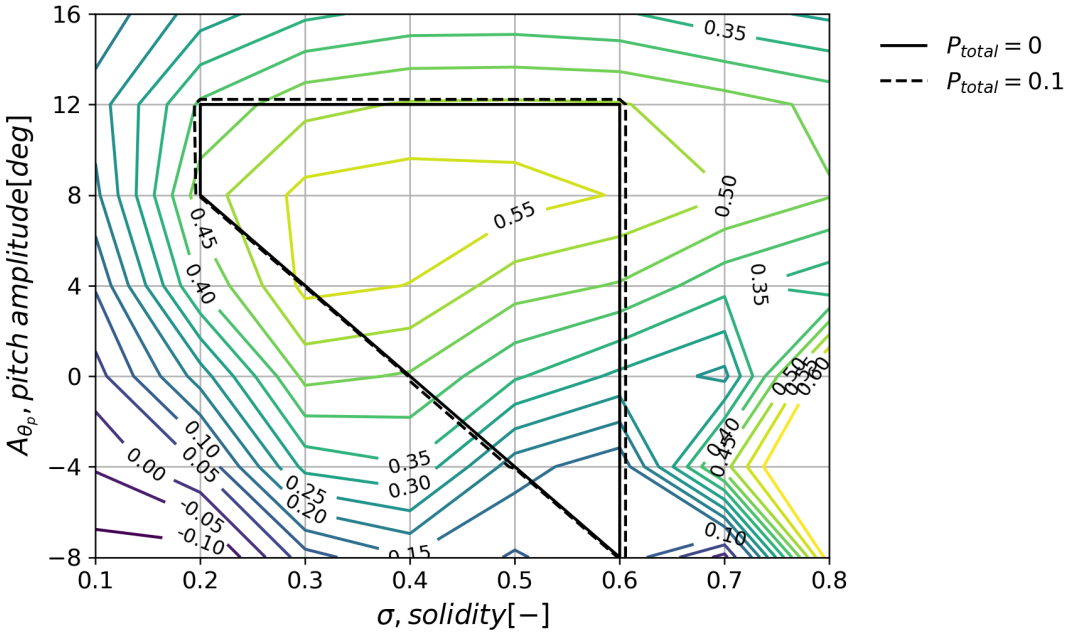

Figure C.10: C_P for different designs and the total penalty showing the feasible design region, $TSR = 2.5$, $\theta_p = 0[^\circ]$

C.3 Solidity and pitch phase

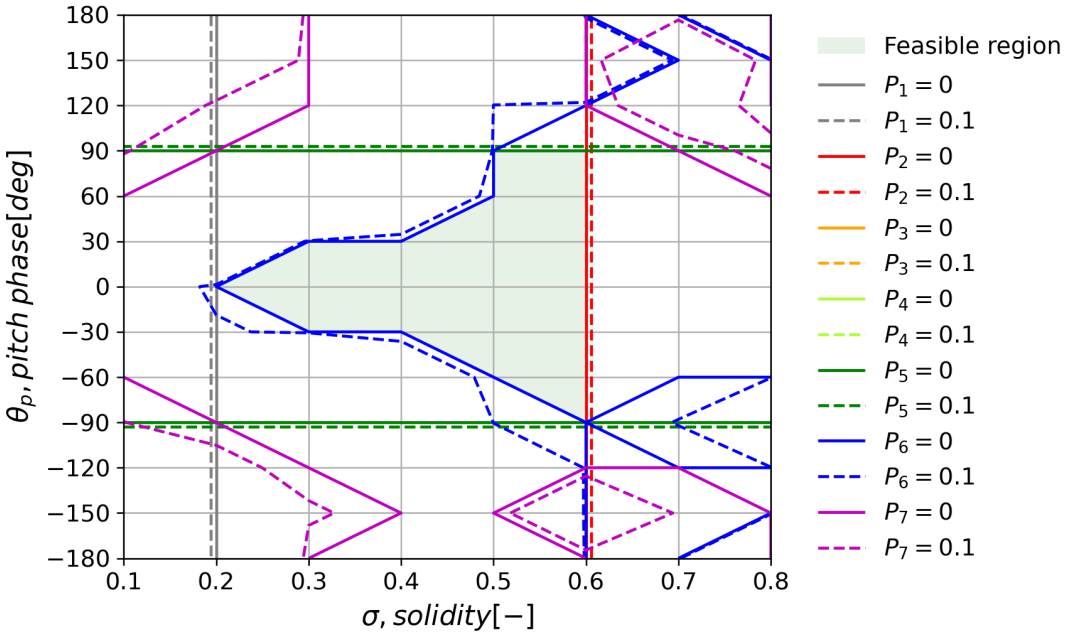

Figure C.11: Penalties from different constraints, $A_{\theta_p} = 8[°]$, $TSR = 2.5$

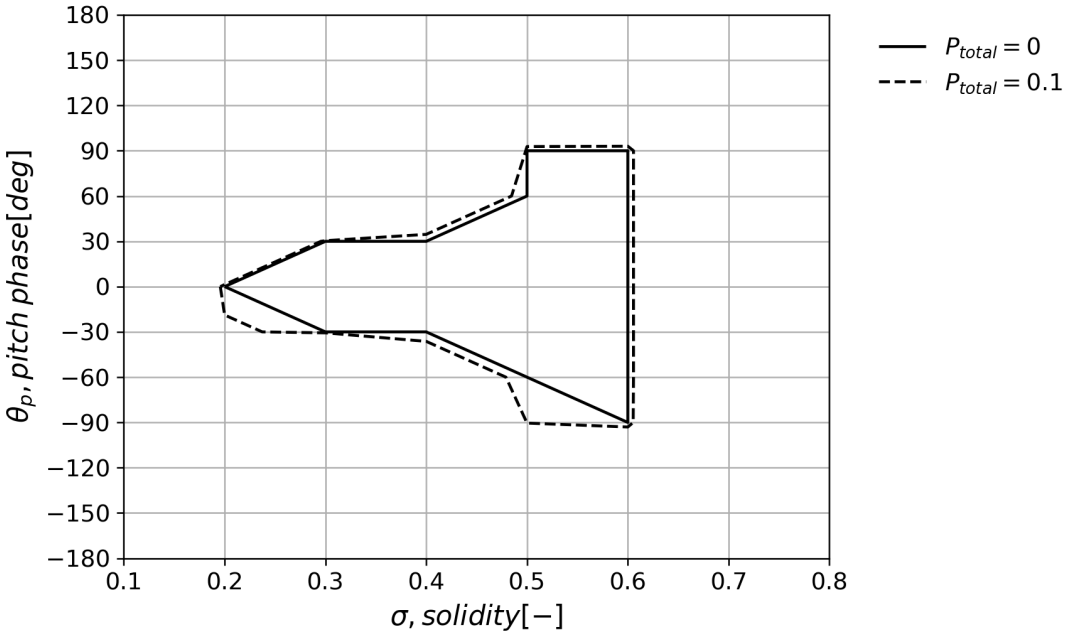

Figure C.12: Total penalty from constraints showing the feasible design region, $A_{\theta_p} = 8[°]$, $TSR = 2.5$

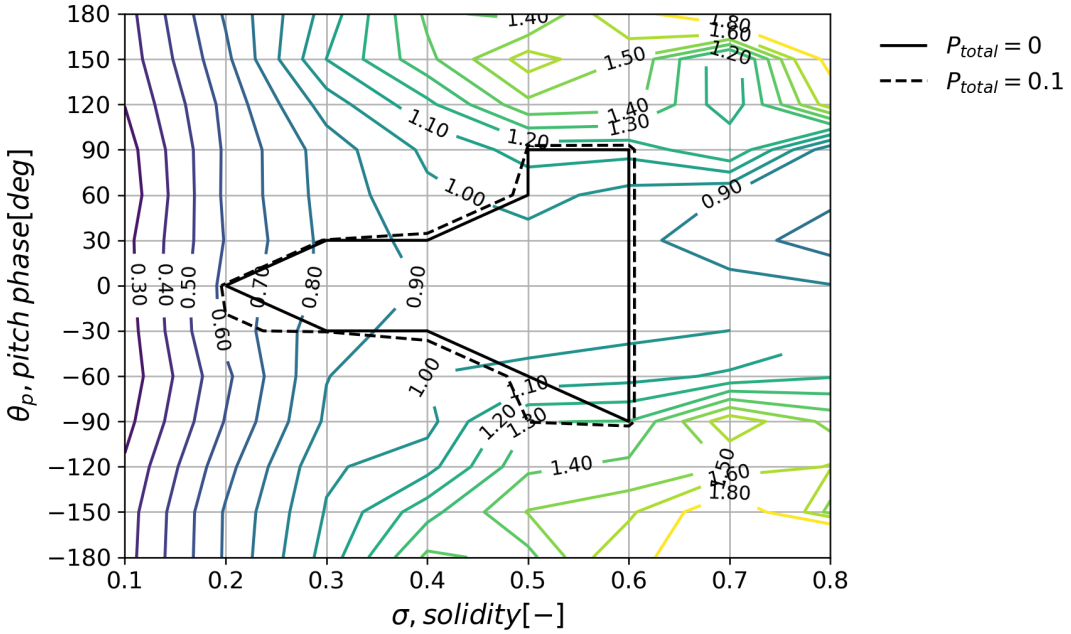

Figure C.13: C_d for different designs and the total penalty showing the feasible design region, $A_{\theta_p} = 8[°]$, $TSR = 2.5$

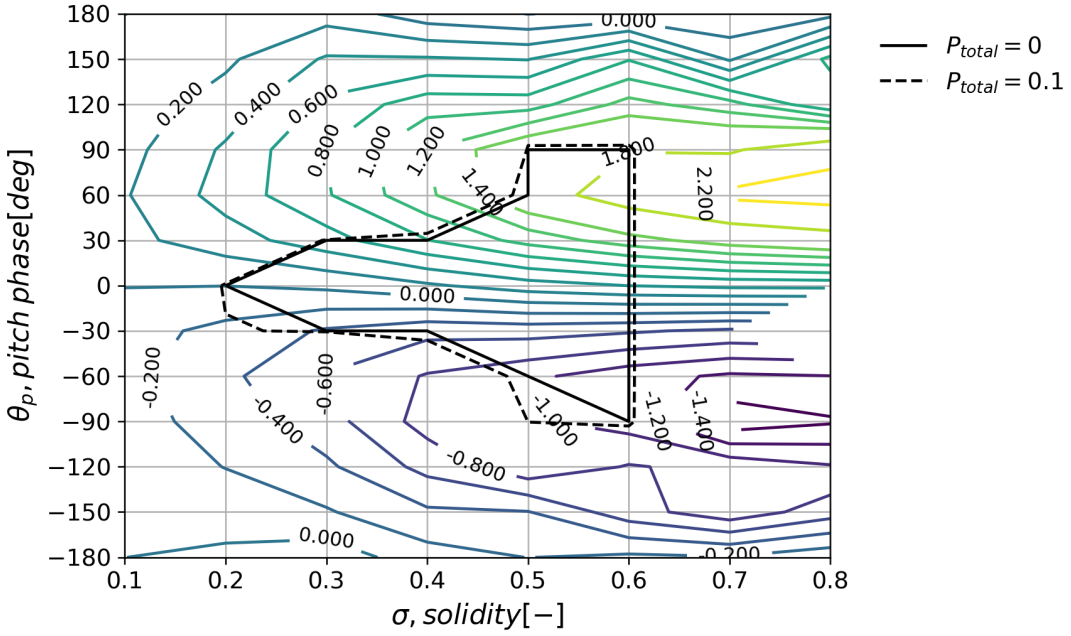

Figure C.14: C_l for different designs and the total penalty showing the feasible design region, $A_{\theta_p} = 8[°]$, $TSR = 2.5$

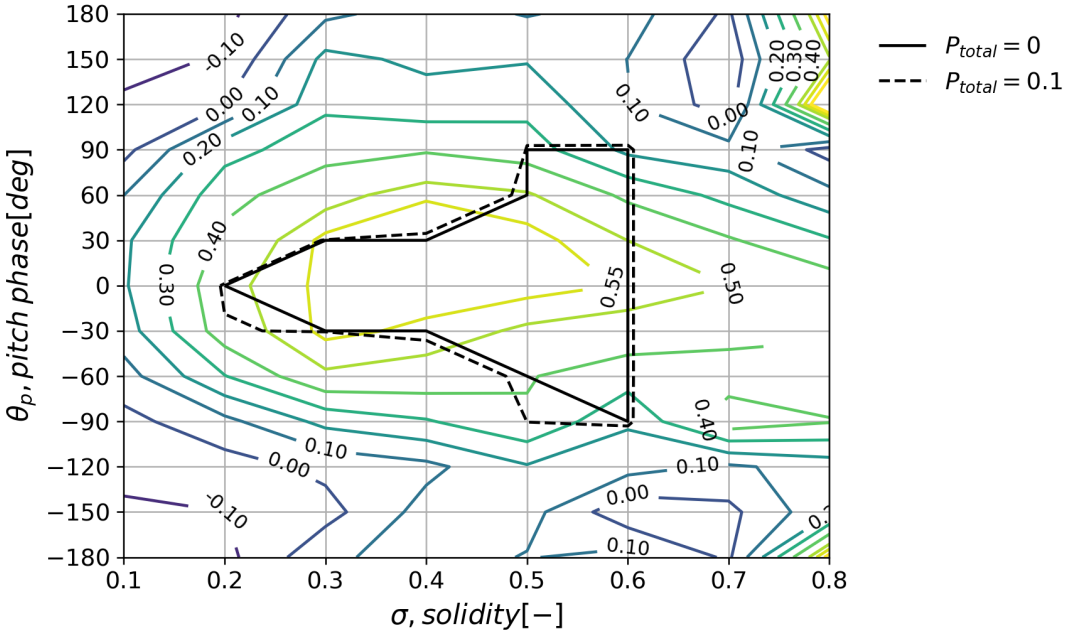

Figure C.15: C_P for different designs and the total penalty showing the feasible design region, $A_{\theta_p} = 8[^\circ]$, $TSR = 2.5$

C.4 TSR and pitch amplitude

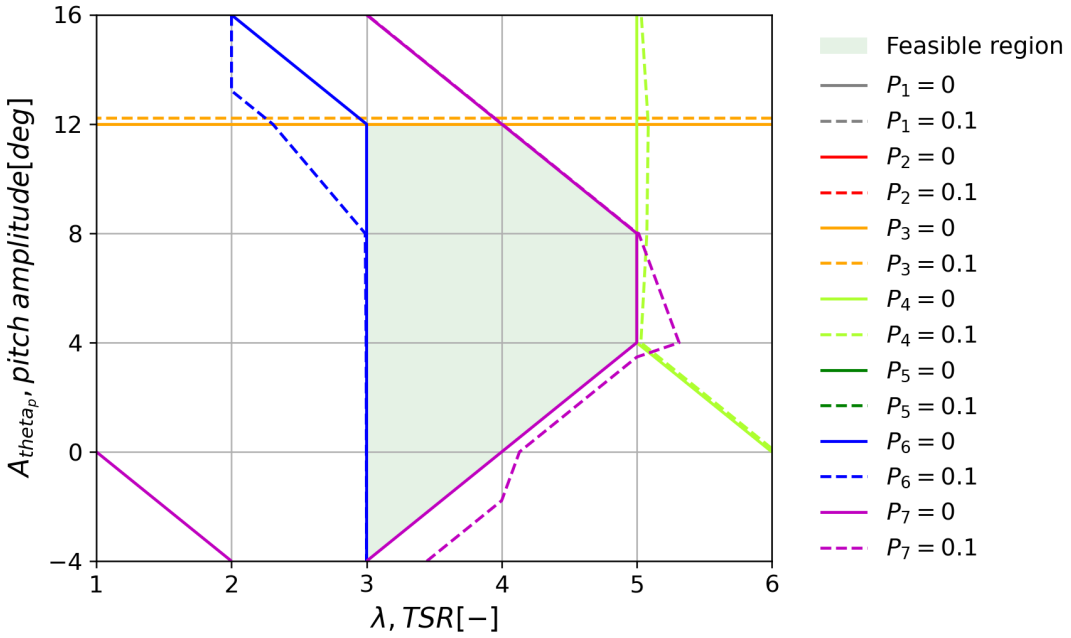

Figure C.16: Penalties from different constraints, $\sigma = 0.4$, $\theta_p = 0[°]$

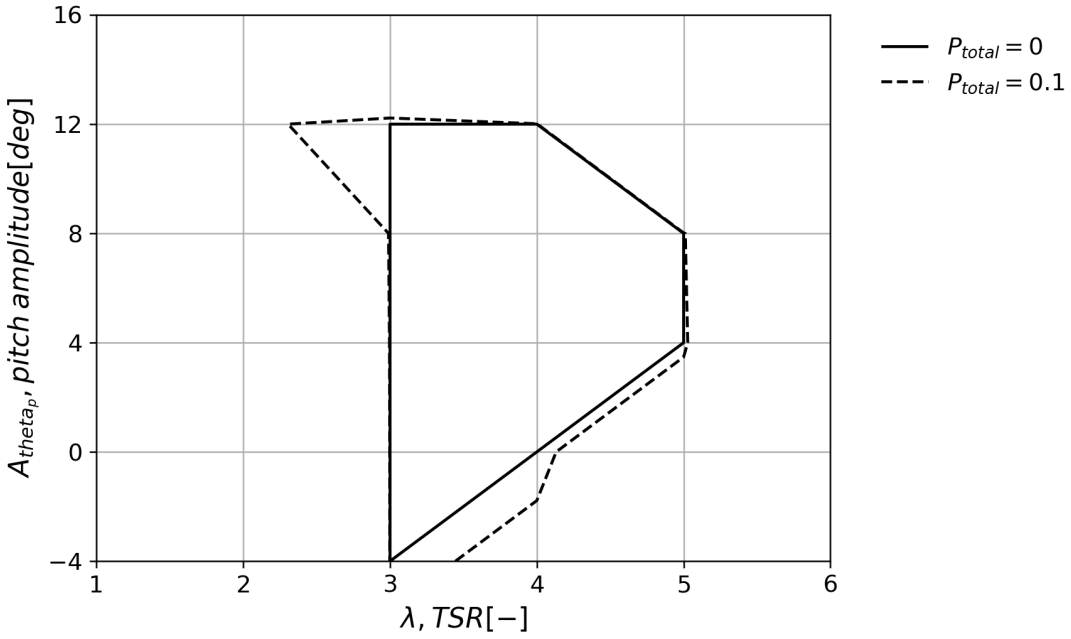

Figure C.17: Total penalty from constraints showing the feasible design region, $\sigma = 0.4$, $\theta_p = 0[°]$

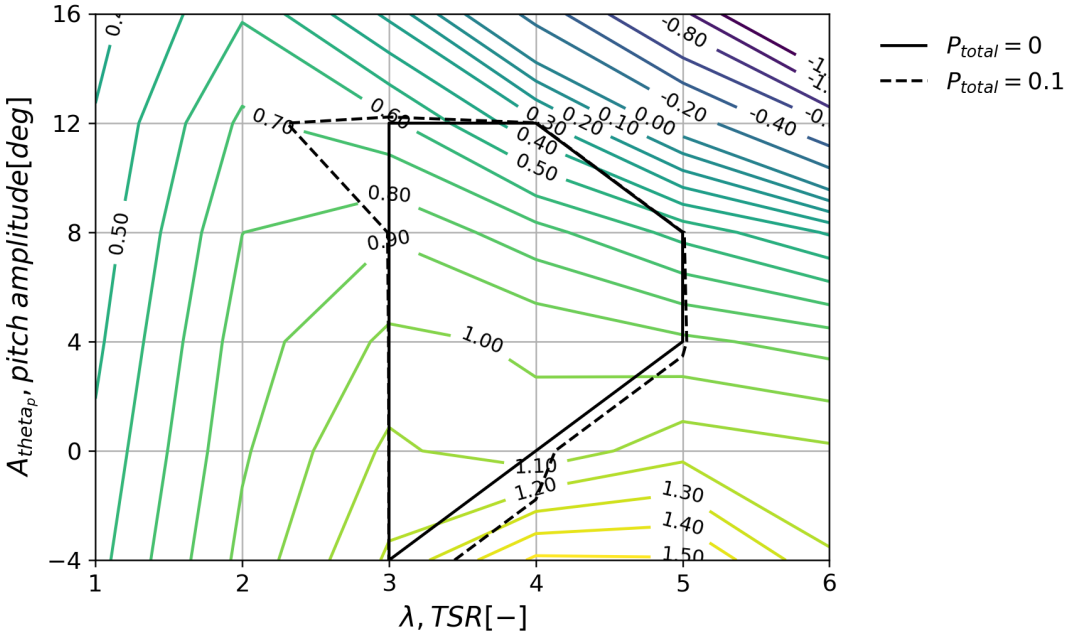

Figure C.18: C_d for different designs and the total penalty showing the feasible design region, $\sigma = 0.4$, $\theta_p = 0[^\circ]$

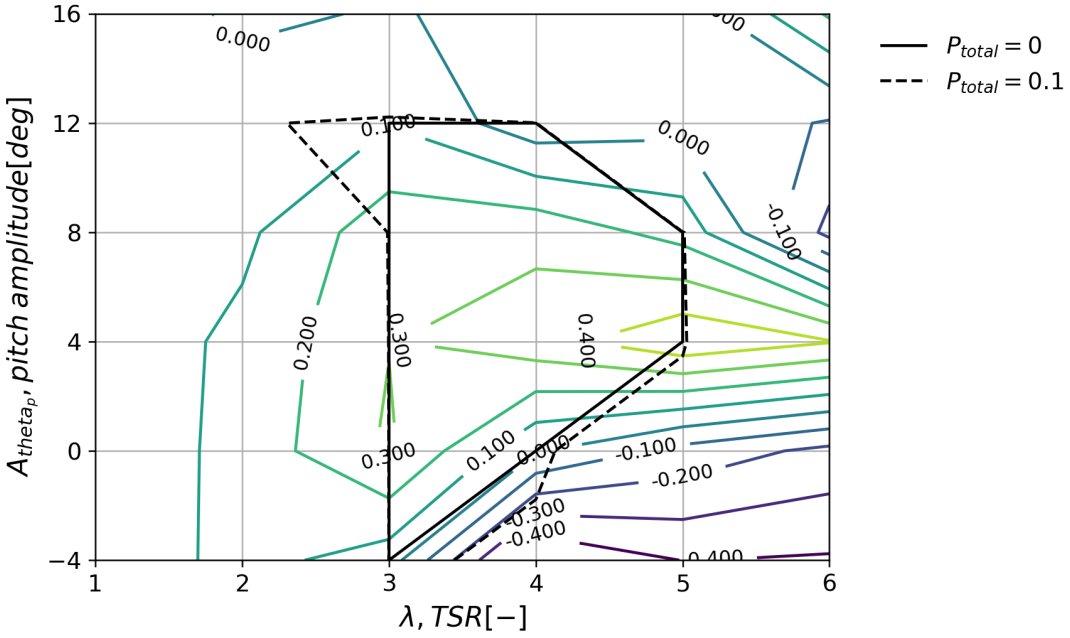

Figure C.19: C_l for different designs and the total penalty showing the feasible design region, $\sigma = 0.4$, $\theta_p = 0[^\circ]$

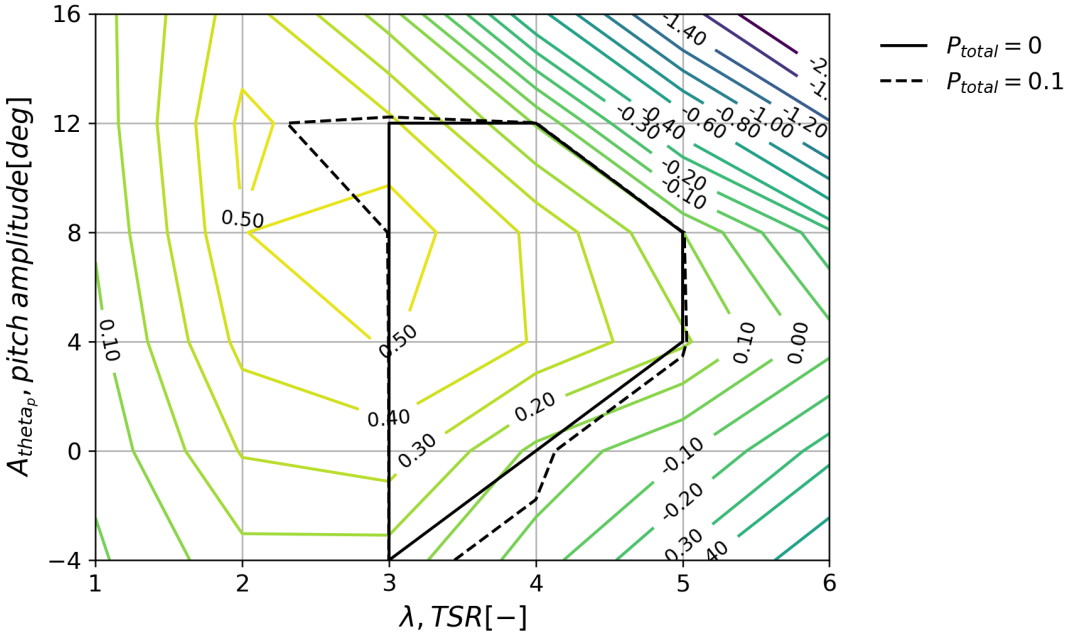

Figure C.20: C_P for different designs and the total penalty showing the feasible design region, $\sigma = 0.4$, $\theta_p = 0[^\circ]$

C.5 TSR and pitch phase

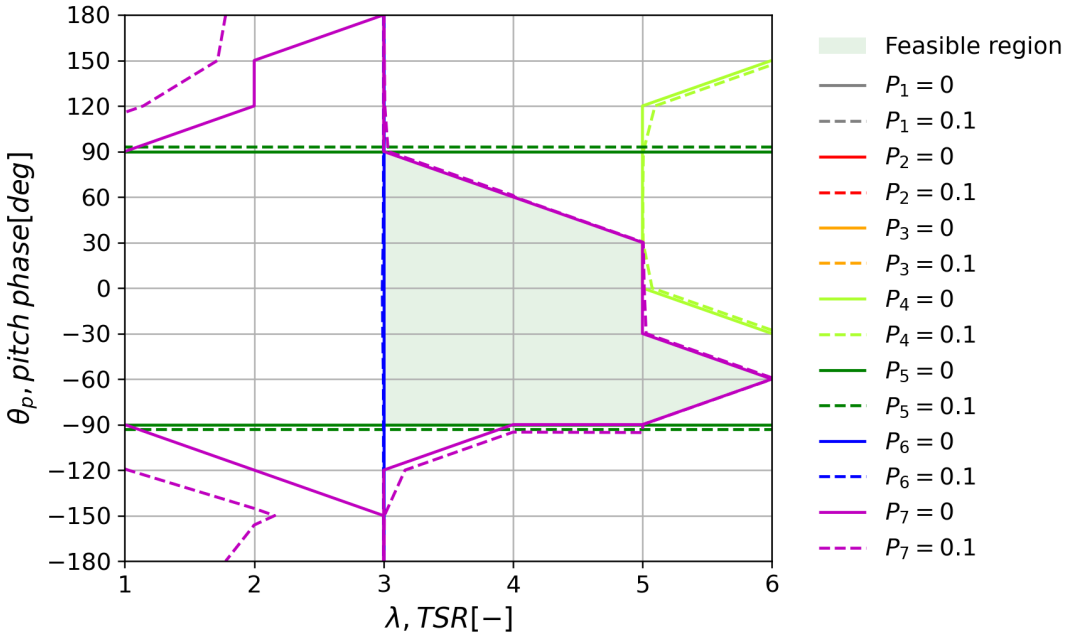

Figure C.21: Penalties from different constraints, $\sigma = 0.4$, $A_{\theta_p} = 8[^\circ]$

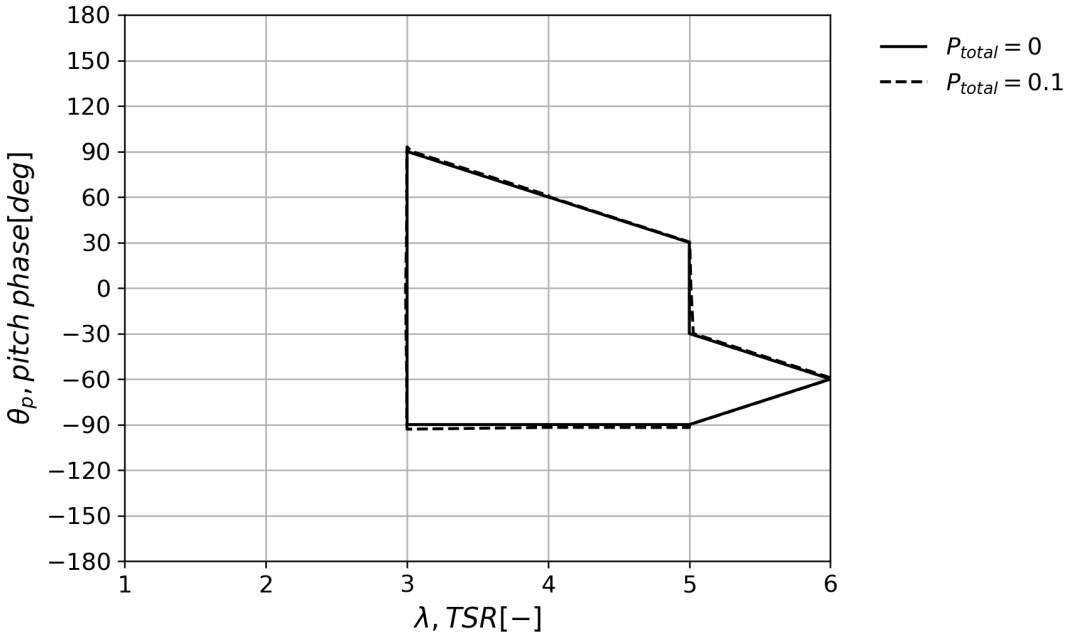

Figure C.22: Total penalty from constraints showing the feasible design region, $\sigma = 0.4$, $A_{\theta_p} = 8[^\circ]$

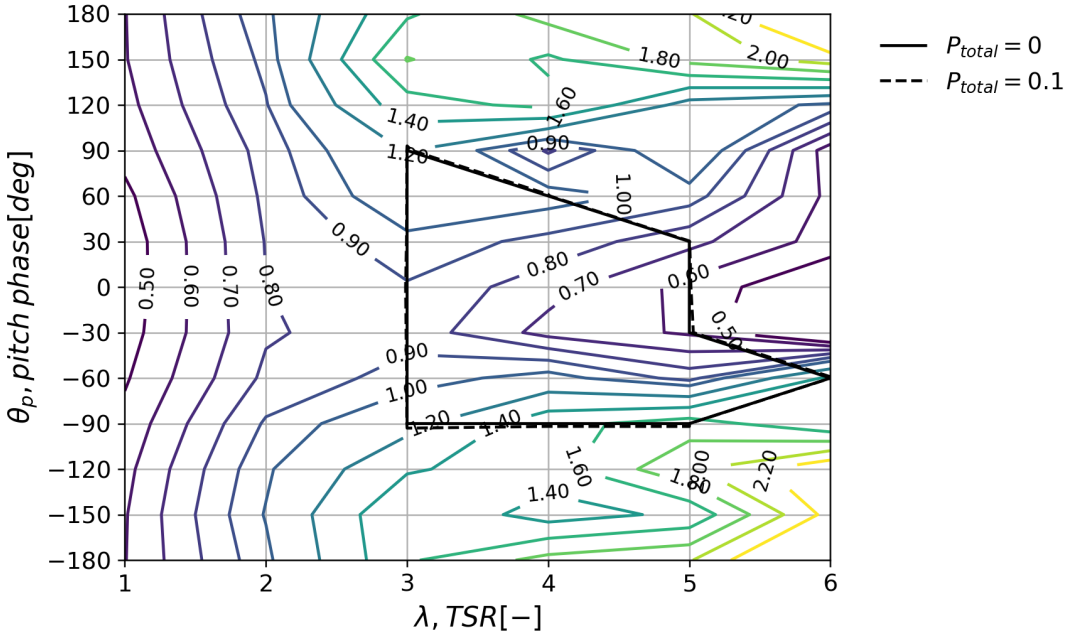

Figure C.23: C_d for different designs and the total penalty showing the feasible design region, $\sigma = 0.4$, $A_{\theta_p} = 8[^\circ]$

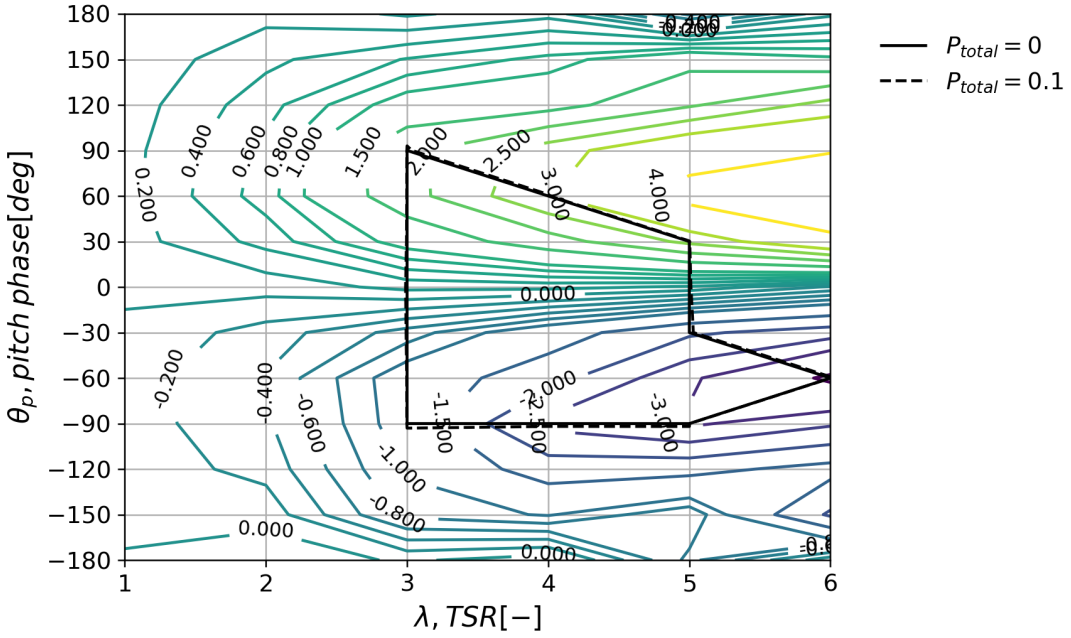

Figure C.24: C_l for different designs and the total penalty showing the feasible design region, $\sigma = 0.4$, $A_{\theta_p} = 8[^\circ]$

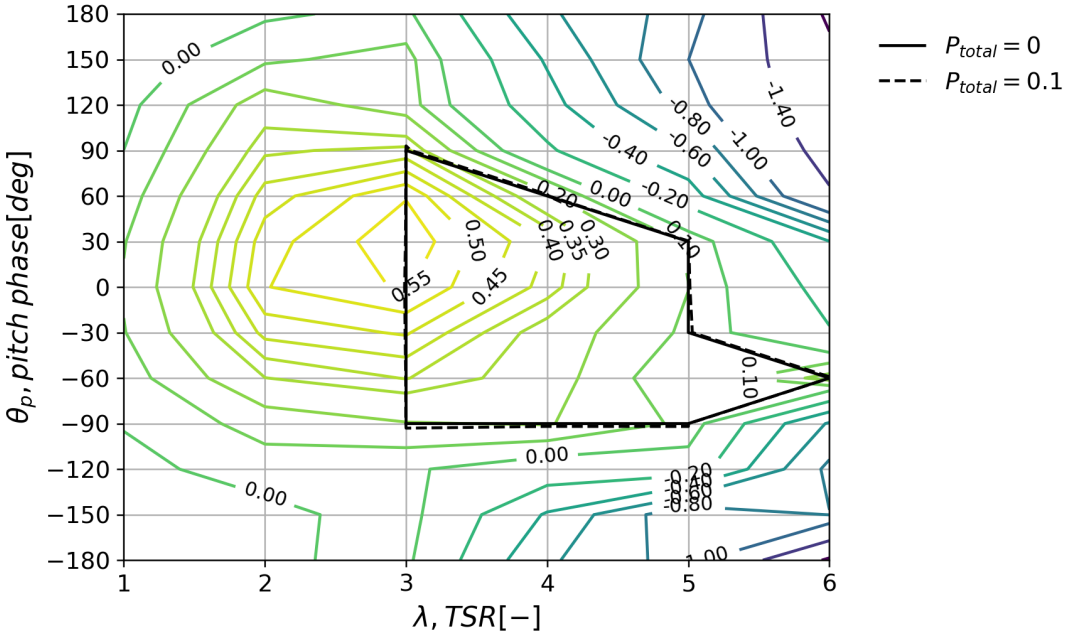

Figure C.25: C_P for different designs and the total penalty showing the feasible design region, $\sigma = 0.4$, $A_{\theta_p} = 8[^\circ]$

C.6 Pitch amplitude and pitch phase

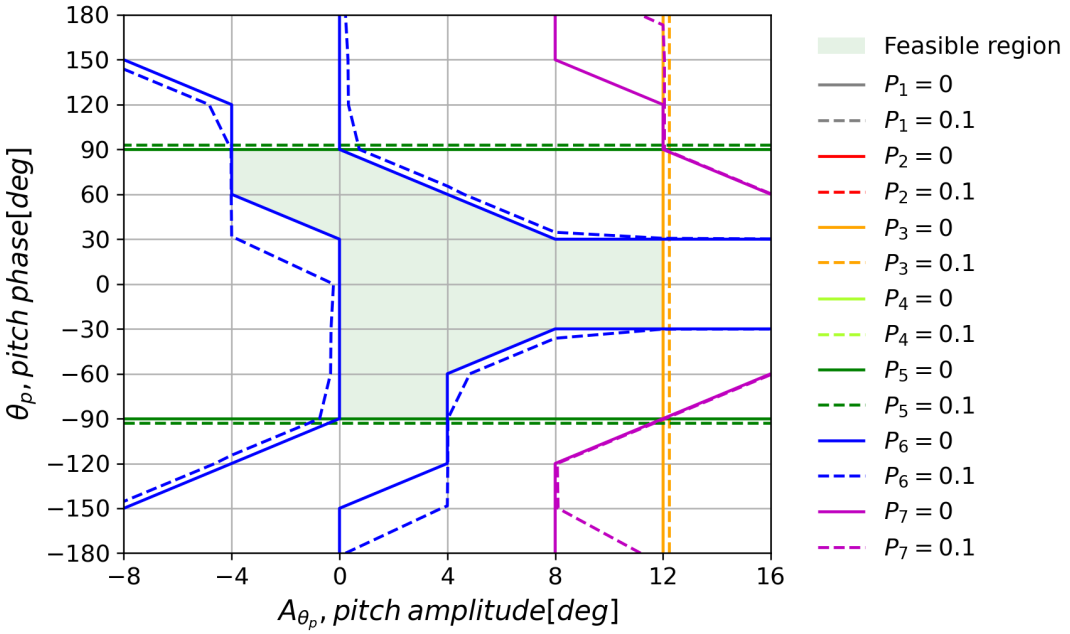

Figure C.26: Penalties from different constraints, $\sigma = 0.4$, $TSR = 2.5$

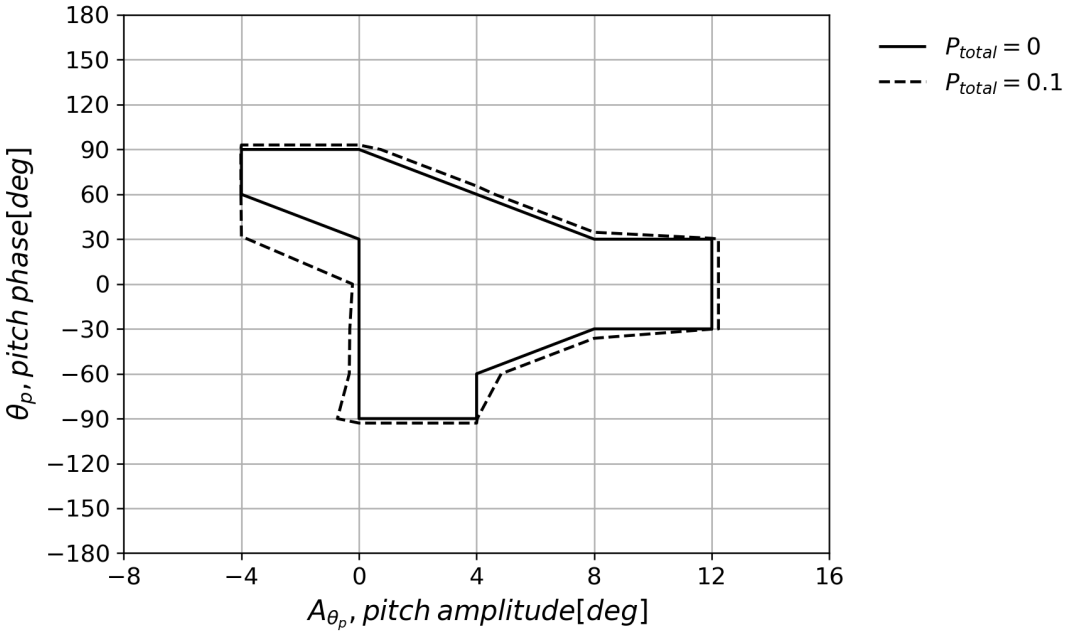

Figure C.27: Total penalty from constraints showing the feasible design region, $\sigma = 0.4$, $TSR = 2.5$

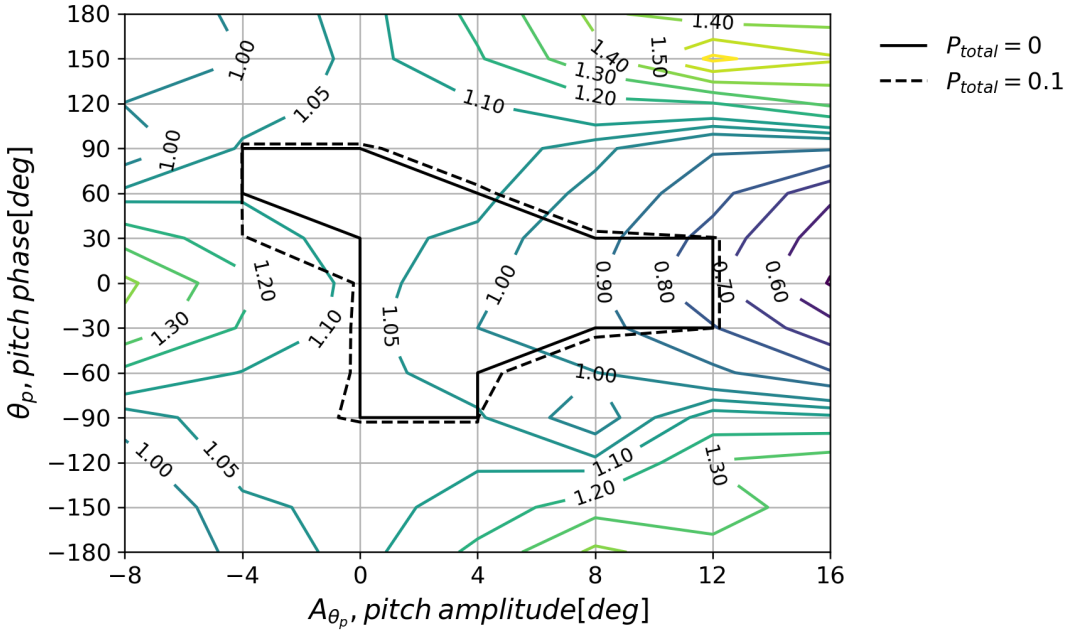

Figure C.28: C_d for different designs and the total penalty showing the feasible design region, $\sigma = 0.4$, $TSR = 2.5$

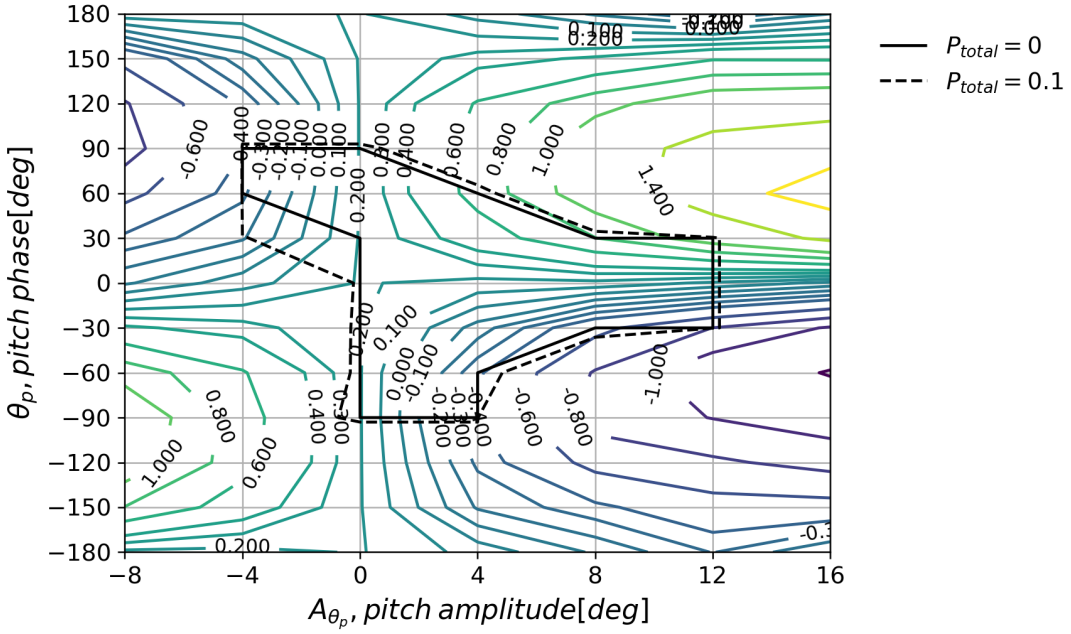

Figure C.29: C_l for different designs and the total penalty showing the feasible design region, $\sigma = 0.4$, $TSR = 2.5$

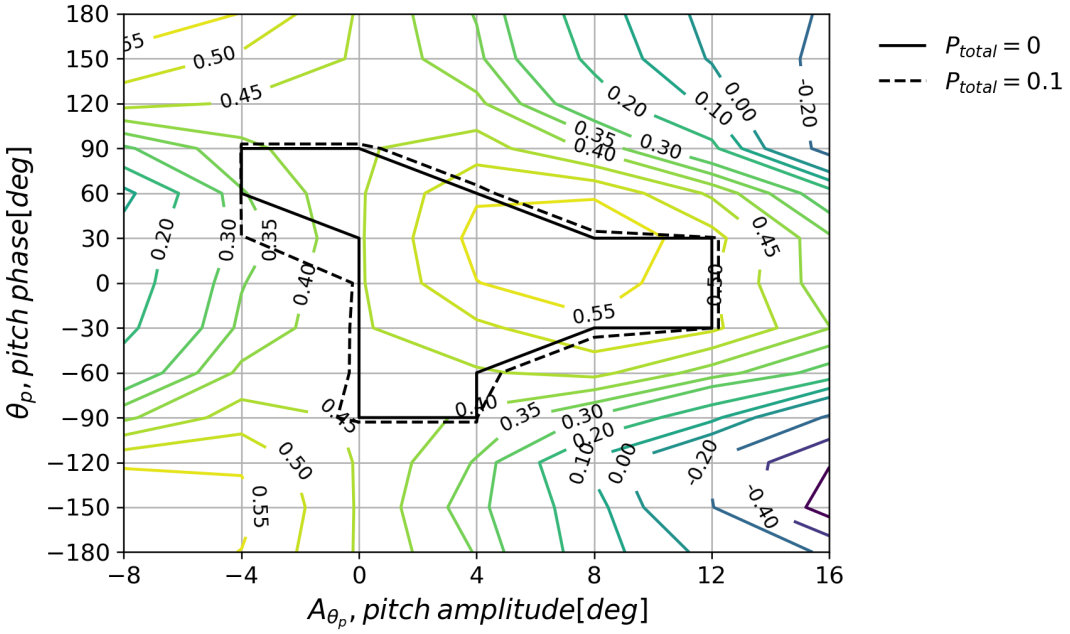

Figure C.30: C_P for different designs and the total penalty showing the feasible design region, $\sigma = 0.4$, $TSR = 2.5$

Appendix D

Sensitivity analysis

D.1 Solidity

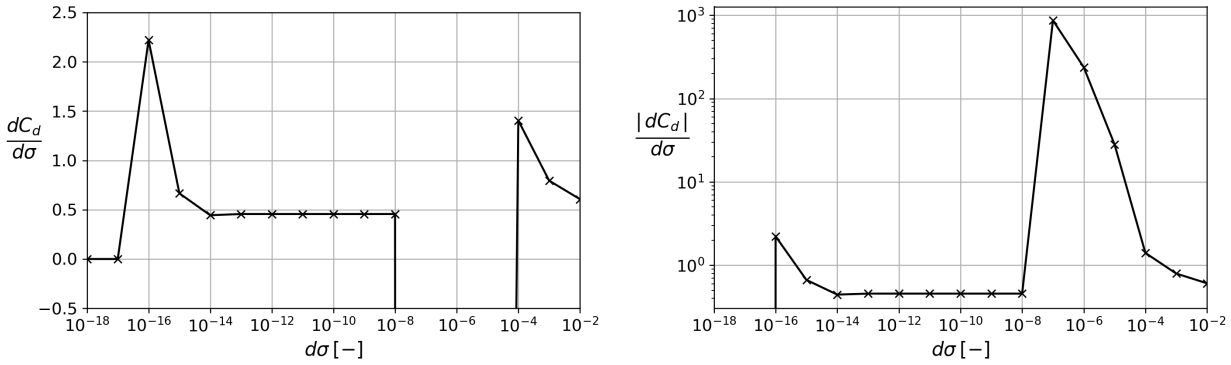

Figure D.1: Drag coefficient response sensitivity of σ at $\sigma = 0.4$, $A_{\theta_p} = 8[deg]$, $TSR = 2.5$, $\theta_p = 0[deg]$

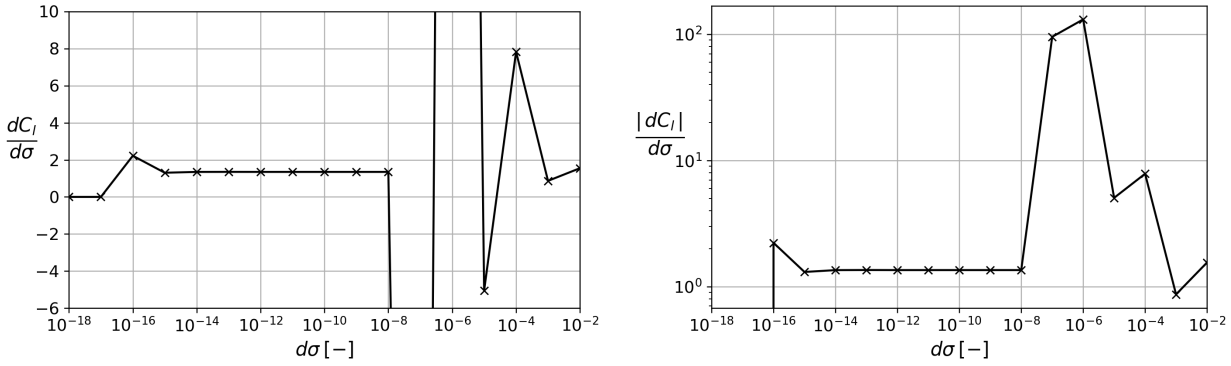

Figure D.2: Lift coefficient response sensitivity of σ at $\sigma = 0.4$, $A_{\theta_p} = 8[deg]$, $TSR = 2.5$, $\theta_p = 0[deg]$

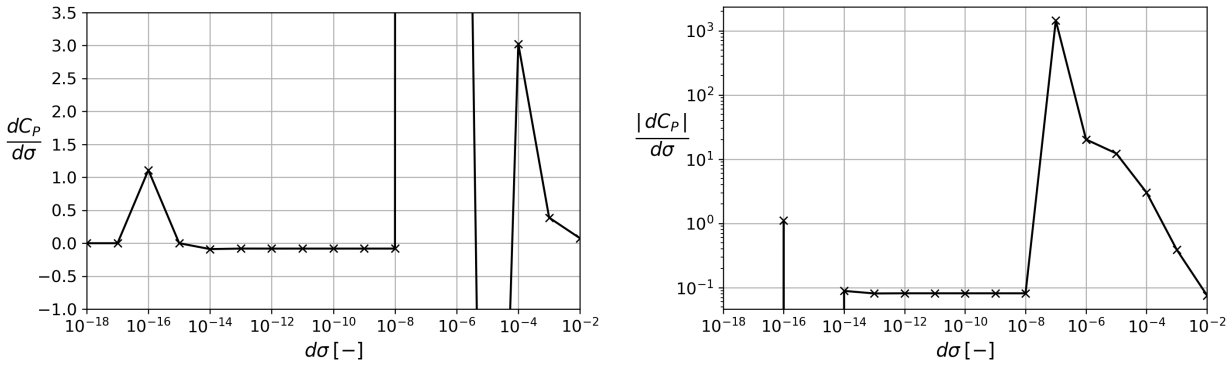

Figure D.3: Power coefficient response sensitivity of σ at $\sigma = 0.4$, $A_{\theta_p} = 8[deg]$, $TSR = 2.5$, $\theta_p = 0[deg]$

D.2 Pitch amplitude

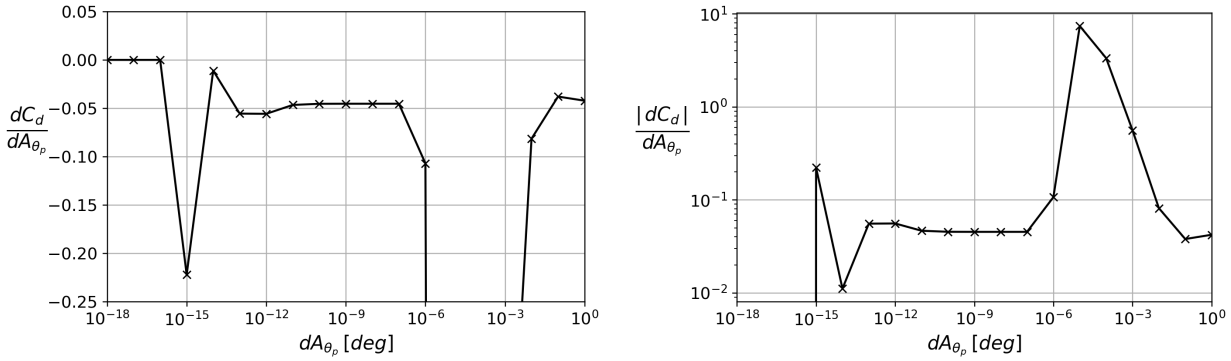

Figure D.4: Drag coefficient response sensitivity of A_{θ_p} at $\sigma = 0.4$, $A_{\theta_p} = 8[deg]$, $TSR = 2.5$, $\theta_p = 0[deg]$

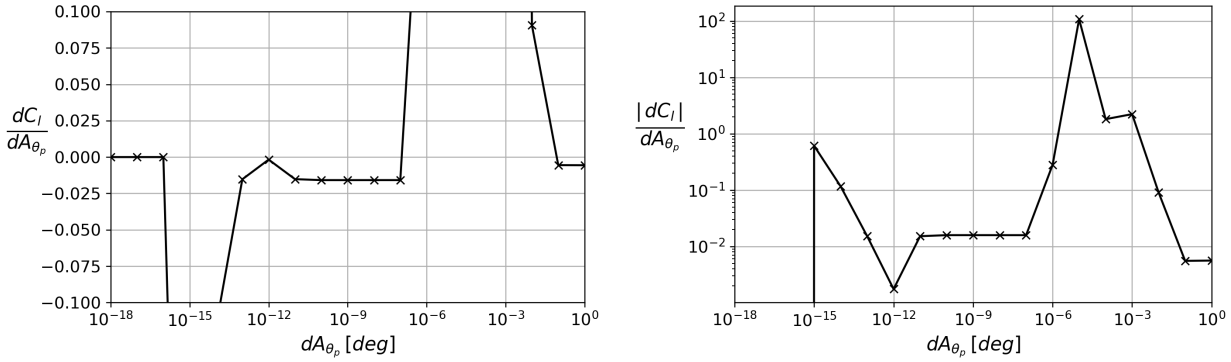

Figure D.5: Lift coefficient response sensitivity of A_{θ_p} at $\sigma = 0.4$, $A_{\theta_p} = 8[deg]$, $TSR = 2.5$, $\theta_p = 0[deg]$

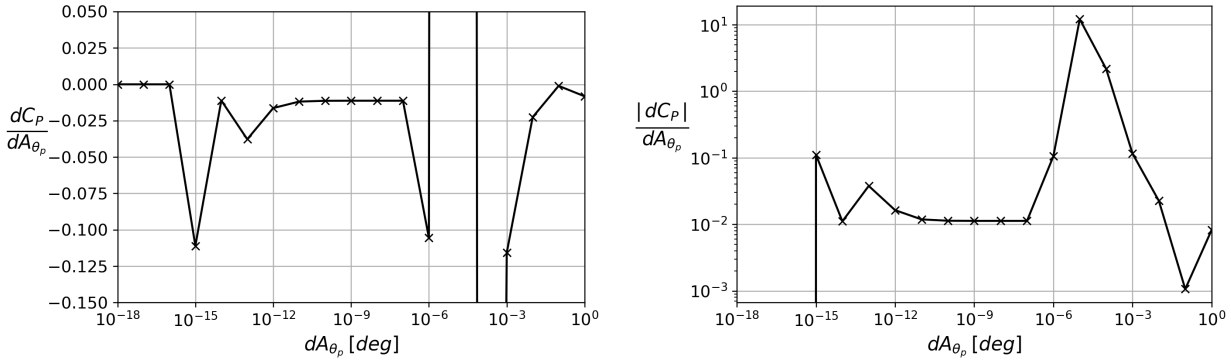

Figure D.6: Power coefficient response sensitivity of A_{θ_p} at $\sigma = 0.4$, $A_{\theta_p} = 8[deg]$, $TSR = 2.5$, $\theta_p = 0[deg]$

D.3 Tip speed ratio

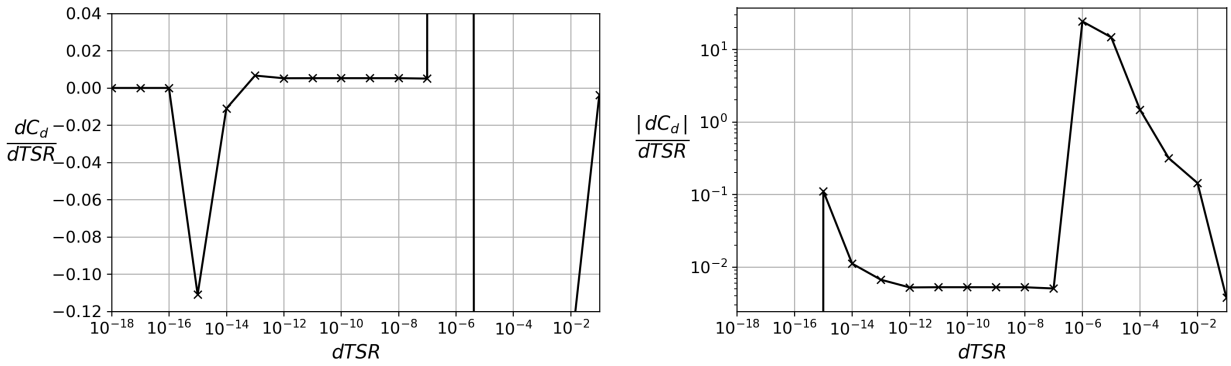

Figure D.7: Drag coefficient response sensitivity of TSR at $\sigma = 0.4$, $A_{\theta_p} = 8[deg]$, $TSR = 2.5$, $\theta_p = 0[deg]$

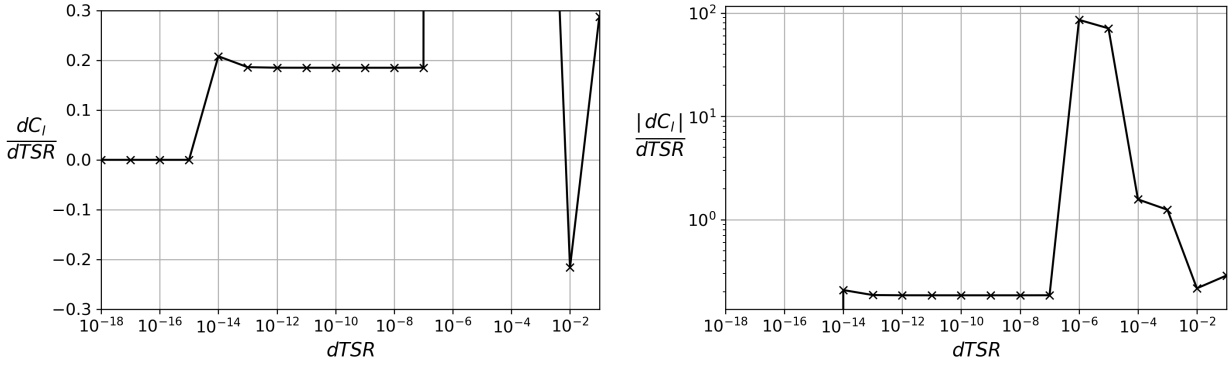

Figure D.8: Lift coefficient response sensitivity of TSR at $\sigma = 0.4$, $A_{\theta_p} = 8[deg]$, $TSR = 2.5$, $\theta_p = 0[deg]$

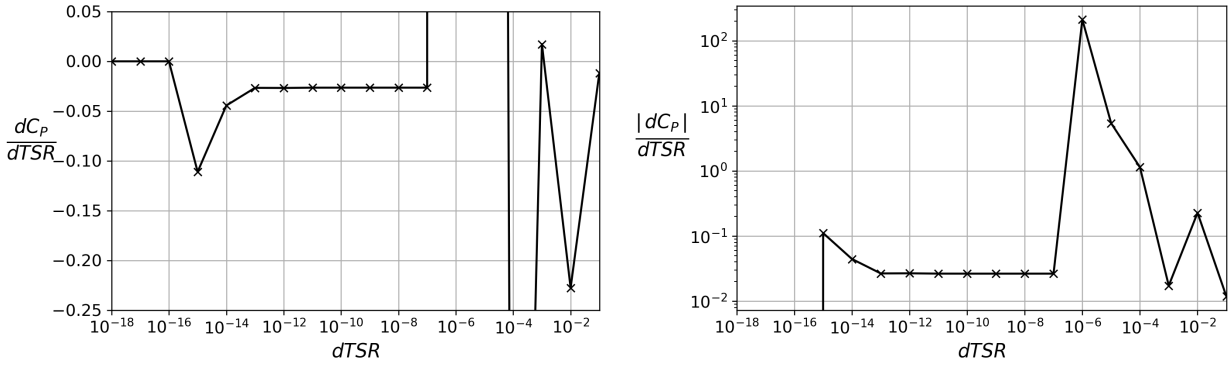

Figure D.9: Power coefficient response sensitivity of TSR at $\sigma = 0.4$, $A_{\theta_p} = 8[deg]$, $TSR = 2.5$, $\theta_p = 0[deg]$

D.4 Pitch phase

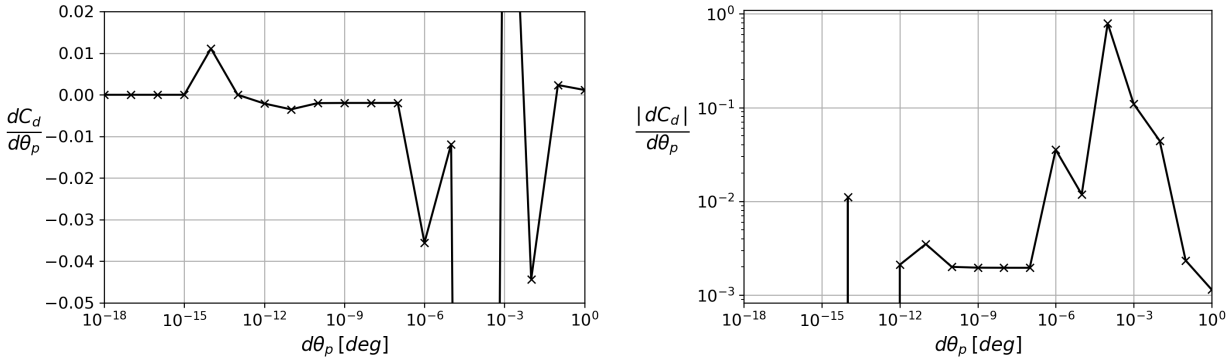

Figure D.10: Drag coefficient response sensitivity of θ_p at $\sigma = 0.4$, $A_{\theta_p} = 8[deg]$, $TSR = 2.5$, $\theta_p = 0[deg]$

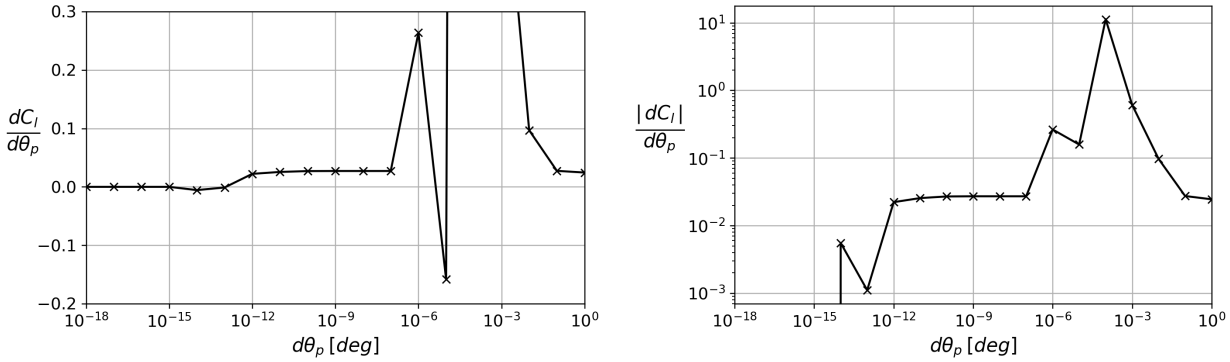

Figure D.11: Lift coefficient response sensitivity of θ_p at $\sigma = 0.4$, $A_{\theta_p} = 8[deg]$, $TSR = 2.5$, $\theta_p = 0[deg]$

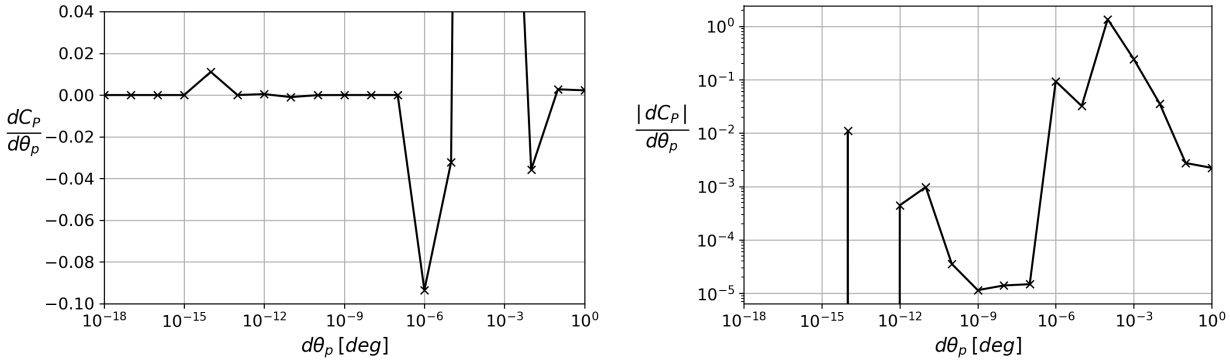

Figure D.12: Power coefficient response sensitivity of θ_p at $\sigma = 0.4$, $A_{\theta_p} = 8[deg]$, $TSR = 2.5$, $\theta_p = 0[deg]$

Appendix E

Smoothness

E.1 Solidity

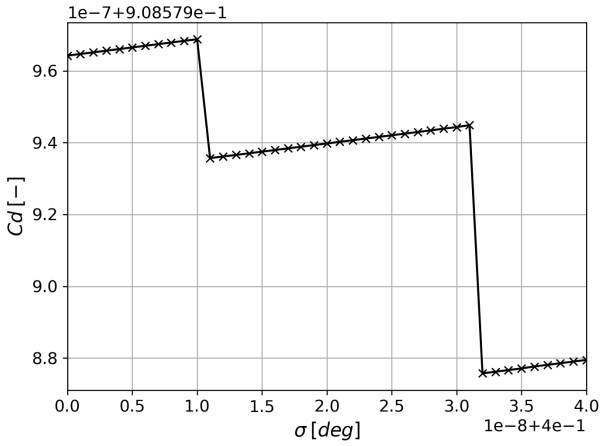

Figure E.1: Smoothness of C_d for variable solidity (σ), step size $d\sigma = 1e-9$

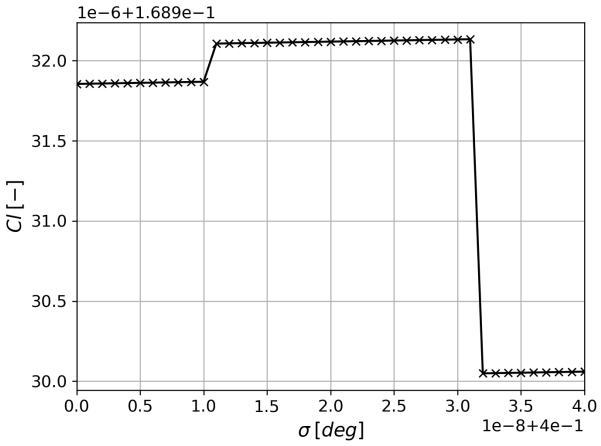

Figure E.2: Smoothness of C_l for variable solidity (σ), step size $d\sigma = 1e-9$

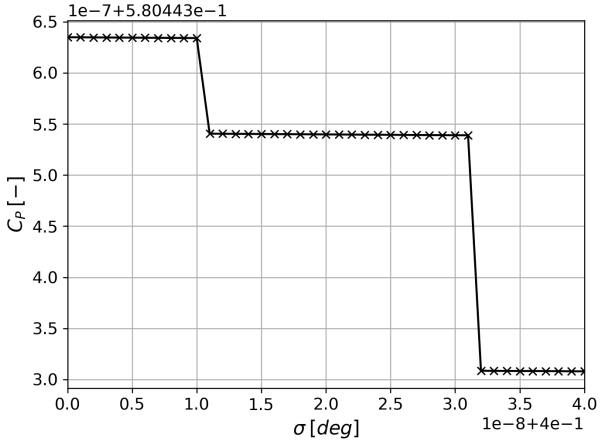

Figure E.3: Smoothness of C_P for variable solidity (σ), step size $d\sigma = 1e-9$

E.2 Pitch amplitude

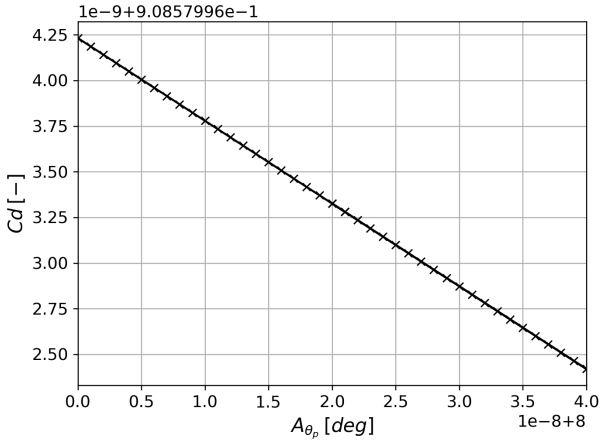

Figure E.4: Smoothness of C_d for variable solidity (A_{θ_p}), step size $dA_{\theta_p} = 1e-9$

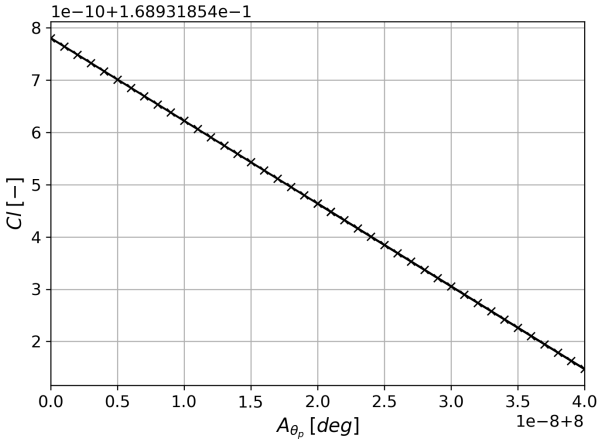

Figure E.5: Smoothness of C_l for variable solidity (A_{θ_p}), step size $dA_{\theta_p} = 1e-9$

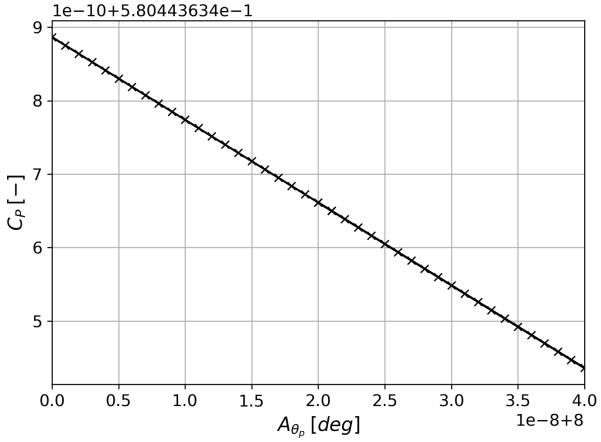

Figure E.6: Smoothness of C_P for variable solidity (A_{θ_p}), step size $dA_{\theta_p} = 1e-9$

E.3 Tip speed ratio

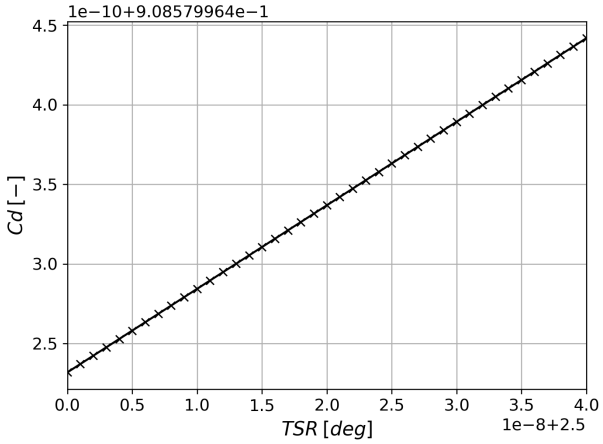

Figure E.7: Smoothness of C_d for variable solidity (TSR), step size $dTSR = 1e-9$

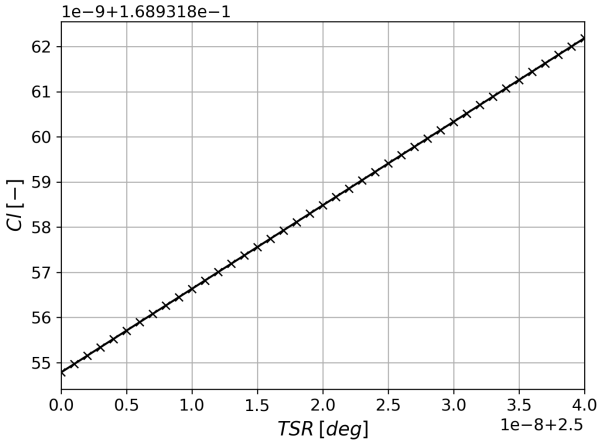

Figure E.8: Smoothness of C_l for variable solidity (TSR), step size $dTSR = 1e-9$

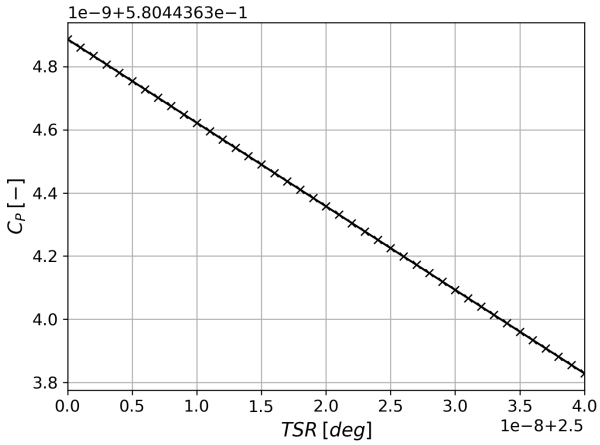

Figure E.9: Smoothness of C_P for variable solidity (TSR), step size $dTSR = 1e-9$

E.4 Pitch phase

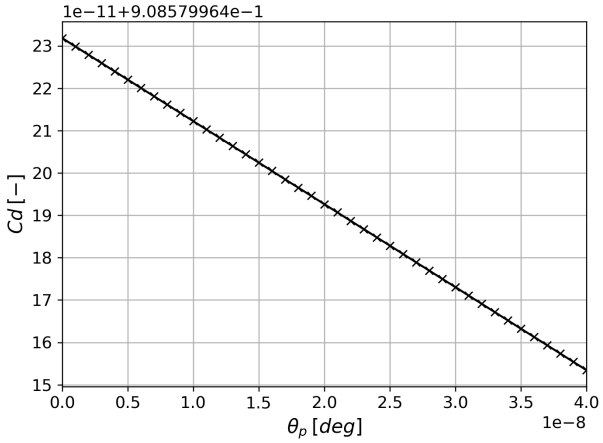

Figure E.10: Smoothness of C_d for variable solidity (θ_p), step size $d\theta_p = 1e-9$

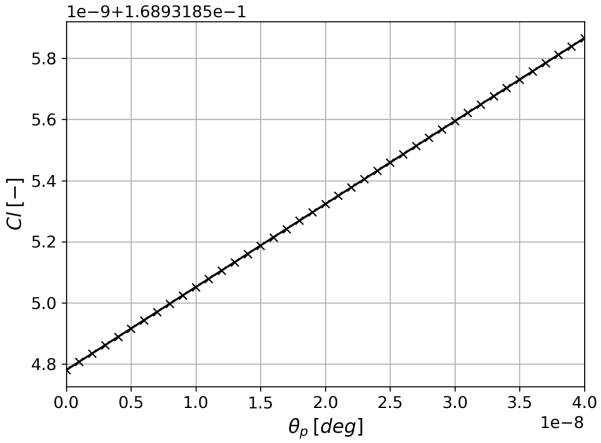

Figure E.11: Smoothness of C_l for variable solidity (θ_p), step size $d\theta_p = 1e-9$

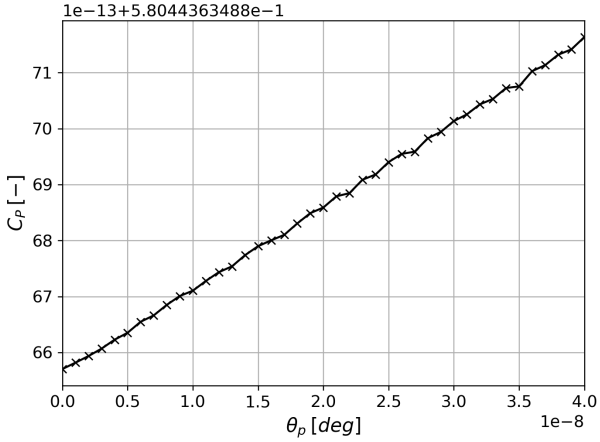

Figure E.12: Smoothness of C_P for variable solidity (θ_p), step size $d\theta_p = 1e-9$

Appendix F

Optimization results

F.1 4D turbine

F.1.1 At sea

Table F.1: Results for 4D optimization for turbine objective

Condition	$\beta_a[^\circ]$	$U_a[m/s]$	σ	$A_{\theta_p}[^\circ]$	TSR	$\theta_p[^\circ]$	C_d	C_l	C_P	$C_{P'}$
Sea	-180	0.640	0.460	4.69	3.08	72.2	1.17	1.35	0.355	0.0144
Sea	-150	3.33	0.377	5.62	2.96	65.4	1.17	1.25	0.556	0.398
Sea	-120	6.34	0.332	6.39	2.88	59.7	1.10	1.08	0.618	1.19
Sea	-90	8.95	0.298	9.32	3.20	65.5	1.09	1.71	0.619	1.52
Sea	-60	11.0	0.298	9.74	3.21	44.6	0.930	1.47	0.592	1.02
Sea	-30	12.2	0.326	12.6	2.77	26.3	0.669	1.02	0.483	0.476
Sea	0	12.6	0.341	13.3	2.59	14.0	0.605	0.59	0.453	0.292
Sea	30	12.2	0.326	12.6	2.77	26.3	0.669	1.02	0.483	0.476
Sea	60	11.0	0.298	9.74	3.21	44.6	0.930	1.47	0.592	1.02
Sea	90	8.95	0.298	9.32	3.20	65.5	1.09	1.71	0.619	1.52
Sea	120	6.34	0.332	6.39	2.88	59.7	1.10	1.08	0.618	1.19
Sea	150	3.33	0.377	5.62	2.96	65.4	1.17	1.25	0.556	0.398
Sea	180	0.640	0.460	4.69	3.08	72.2	1.17	1.35	0.355	0.0144
Port	—	4.77	0.310	7.14	2.95	56.4	1.06	1.10	0.623	0.231

F.1.2 In port

Table F.2: Results for 4D optimization for power coefficient objective in port

Condition	$\beta_a[^\circ]$	$U_a[m/s]$	σ	$A_{\theta_p}[^\circ]$	TSR	$\theta_p[^\circ]$	C_d	C_l	C_P	$C_{P'}$
Port	—	4.77	0.166	0.00	3.40	0.00	1.00	0.0187	0.587	—
Port	—	4.77	0.310	7.14	2.95	56.4	1.06	1.10	0.623	—

F.2 4D thruster

Table F.3: Results for 4D optimization for thruster objective

Condition	$\beta_a[^\circ]$	$U_a[m/s]$	σ	$A_{\theta_p}[^\circ]$	TSR	$\theta_p[^\circ]$	C_d	C_l	C_P	$C_{P'}$
Sea	-180	0.640	0.502	3.90	3.07	76.3	1.13	1.17	0.257	0.0135
Sea	-150	3.33	0.608	12.4	4.88	-72.4	2.44	-4.76	0.454	1.46
Sea	-120	6.34	0.520	12.0	5.03	-72.8	2.29	-4.70	0.406	6.14
Sea	-90	8.95	0.582	12.3	4.95	-73.7	2.19	-4.92	0.212	11.5
Sea	-60	11.0	0.582	12.0	4.76	-63.3	0.885	-4.49	0.00195	12.1
Sea	-30	12.2	0.603	12.0	4.77	-64.3	0.942	-4.84	0.127	7.01
Sea	0	12.6	—	—	—	—	—	—	0.00	0.00
Sea	30	12.2	0.338	11.9	4.66	54.4	0.926	4.75	-0.0292	6.87
Sea	60	11.0	0.362	11.2	4.58	57.1	0.973	4.83	-0.0358	13.0
Sea	90	8.95	0.350	11.4	4.66	56.4	0.986	4.86	-0.0314	11.4
Sea	120	6.34	0.363	11.0	4.56	57.4	0.999	4.77	-0.0121	5.45
Sea	150	3.33	0.378	10.4	4.46	59.3	1.05	4.53	0.00420	1.03
Sea	180	0.640	0.502	3.90	3.07	76.3	1.13	1.17	0.257	0.0135
Port	—	4.77	—	—	0.00	—	—	—	—	0.000

F.3 4D combined

Table F.4: Results for 4D optimization for combined objective

Condition	$\beta_a[^\circ]$	$U_a[m/s]$	σ	$A_{\theta_p}[^\circ]$	TSR	$\theta_p[^\circ]$	C_d	C_l	C_P	$C_{P'}$
Sea	-180	0.640	0.433	4.49	2.86	69.7	1.19	1.13	0.473	0.0147
Sea	-150	3.33	0.574	13.1	4.86	-65.9	1.95	-4.62	0.207	1.32
Sea	-120	6.34	0.528	11.9	5.01	-72.1	1.92	-5.06	0.307	6.57
Sea	-90	8.95	0.593	11.8	4.52	-52.1	1.16	-4.10	0.329	10.4
Sea	-60	11.0	0.601	11.8	4.55	-53.8	1.39	-4.12	0.405	11.9
Sea	-30	12.2	0.599	11.6	4.49	-50.9	1.22	-4.10	0.427	6.99
Sea	0	12.6	0.130	11.1	3.14	37.0	0.447	0.541	0.354	0.351
Sea	30	12.2	0.335	11.8	4.67	55.0	0.954	4.72	-0.00769	6.65
Sea	60	11.0	0.342	11.8	4.65	54.7	0.942	4.76	-0.0227	12.7
Sea	90	8.95	0.350	11.5	4.65	55.9	0.978	4.86	-0.0362	11.3
Sea	120	6.34	0.360	11.1	4.56	57.3	1.00	4.73	0.000275	5.42
Sea	150	3.33	0.362	10.9	4.56	57.4	1.01	4.69	0.00110	1.04
Sea	180	0.640	0.433	4.49	2.86	69.7	1.19	1.13	0.473	0.0147
Port	—	4.77	0.310	7.14	2.95	56.4	1.06	1.10	0.623	0.231

F.4 2D combined

Table F.5: Results for 2D optimization for combined objective with fixed construction parameters

Condition	$\beta_a[^\circ]$	$U_a[m/s]$	σ	$A_{\theta_p}[^\circ]$	TSR	$\theta_p[^\circ]$	C_d	C_l	C_P	$C_{P'}$
Sea	-180	0.640	0.457	11.5	2.14	15.6	0.815	0.553	0.578	0.0103
Sea	-150	3.33	0.457	11.5	4.54	-65.7	1.42	-3.57	0.263	1.01
Sea	-120	6.34	0.457	11.5	4.70	-68.2	1.67	-4.10	0.536	5.64
Sea	-90	8.95	0.457	11.5	4.60	-65.1	1.51	-3.69	0.391	9.60
Sea	-60	11.0	0.457	11.5	4.61	-53.5	0.969	-3.71	0.323	11.0
Sea	-30	12.2	0.457	11.5	4.62	-52.9	0.959	-3.51	0.497	7.12
Sea	0	12.6	0.457	11.5	2.13	9.78	0.809	0.383	0.572	0.162
Sea	30	12.2	0.457	11.5	3.96	48.7	0.745	4.41	0.00213	6.82
Sea	60	11.0	0.457	11.5	3.96	48.7	0.747	4.41	0.00259	12.1
Sea	90	8.95	0.457	11.5	3.93	50.9	0.815	4.44	0.00273	10.4
Sea	120	6.34	0.457	11.5	3.83	56.4	0.904	4.45	0.00079	5.08
Sea	150	3.33	0.457	11.5	3.93	51.6	0.833	4.45	0.00142	0.957
Sea	180	0.640	0.457	11.5	2.14	0.151	0.825	0.0904	0.575	0.0104
Port	—	4.77	0.457	11.5	2.14	15.6	0.815	0.553	0.578	0.215

F.5 2D combined fine2 settings

Table F.6: Results for 2D optimization for combined objective with fixed construction parameters and fine2 computational settings

Condition	$\beta_a[^\circ]$	$U_a[m/s]$	σ	$A_{\theta_p}[^\circ]$	TSR	$\theta_p[^\circ]$	C_d	C_l	C_P	$C_{P'}$
Sea	-180	0.640	0.457	11.5	2.14	0.151	0.761	0.108	0.523	0.00960
Sea	-150	3.33	0.457	11.5	4.54	-65.7	1.26	-2.85	-0.0239	0.813
Sea	-120	6.34	0.457	11.5	4.70	-68.2	1.29	-3.44	0.110	4.37
Sea	-90	8.95	0.457	11.5	4.60	-65.1	1.21	-3.19	0.163	7.88
Sea	-60	11.0	0.457	11.5	4.61	-53.5	1.30	-3.51	0.501	10.7
Sea	-30	12.2	0.457	11.5	4.62	-52.9	1.17	-3.45	0.378	5.48
Sea	0	12.6	0.457	11.5	2.13	9.78	0.736	0.36	0.511	0.0851
Sea	30	12.2	0.457	11.5	3.96	48.7	0.274	4.38	-0.230	7.10
Sea	60	11.0	0.457	11.5	3.96	*48.7*	0.274	4.38	-0.230	11.8
Sea	90	8.95	0.457	11.5	3.93	50.9	0.336	4.44	-0.203	9.92
Sea	120	6.34	0.457	11.5	3.83	56.4	0.375	4.48	-0.192	4.62
Sea	150	3.33	0.457	11.5	3.93	51.6	0.343	4.48	-0.207	0.798
Sea	180	0.640	0.457	11.5	2.14	0.151	0.761	0.108	0.523	0.00960
Port	—	4.77	0.457	11.5	2.14	15.6	0.718	0.519	0.499	0.185

F.6 1D wingsail angle of attack optimization

Table F.7: Results for wingsail performance

Condition	$\beta_a[°]$	$U_a[m/s]$	α	C_d	C_l	C_P	$C_{P'}$
Sea	-180	0.640	90.0	1.80	0.0900	0.00	0.0216
Sea	-150	3.33	70.0	1.67	0.630	0.00	0.570
Sea	-120	6.34	14.0	0.0195	1.20	0.00	1.23
Sea	-90	8.95	14.0	0.0195	1.20	0.00	2.80
Sea	-60	11.0	14.0	0.0195	1.20	0.00	3.60
Sea	-30	12.2	13.0	0.0177	1.19	0.00	2.54
Sea	0	12.6	0.00	0.00700	0.00	0.00	-0.0327
Sea	30	12.2	13.0	0.0177	1.19	0.00	2.54
Sea	60	11.0	14.0	0.0195	1.20	0.00	3.60
Sea	90	8.95	14.0	0.0195	1.20	0.00	2.80
Sea	120	6.34	14.0	0.0195	1.20	0.00	1.23
Sea	150	3.33	70.0	1.67	0.630	0.00	0.570
Sea	180	0.640	90.0	1.80	0.0900	0.00	0.0216
Port	port	4.77	—	—	—	0.00	0.00

F.7 1D suction sail angle of attack optimization

Table F.8: Results for suction sail performance

Condition	$\beta_a[°]$	$U_a[m/s]$	α	C_d	C_l	C_P	$C_{P'}$
Sea	-180	0.640	25.0	0.141	5.62	-0.000731	0.00
Sea	-150	3.33	25.0	0.141	5.62	-0.103	0.849
Sea	-120	6.34	25.0	0.141	5.62	-0.712	5.11
Sea	-90	8.95	25.0	0.141	5.62	-2.00	11.2
Sea	-60	11.0	25.0	0.141	5.62	-3.66	13.2
Sea	-30	12.2	25.0	0.141	5.62	-5.08	6.67
Sea	0	12.6	0.00	0.0730	3.15	0.00	0.00
Sea	30	12.2	25.0	0.141	5.62	-5.08	6.67
Sea	60	11.0	25.0	0.141	5.62	-3.66	13.2
Sea	90	8.95	25.0	0.141	5.62	-2.00	11.2
Sea	120	6.34	25.0	0.141	5.62	-0.712	5.11
Sea	150	3.33	25.0	0.141	5.62	-0.103	0.849
Sea	180	0.640	25.0	0.141	5.62	-0.000731	0.00
Port	port	4.77	—	—	—	0.00	0.00